Complementary Workflows for Analyzing Multiphase Flowback and Post-flowback Production Data In Unconventional Reservoirs

by

Obinna Daniel Ezulike

A THESIS SUBMITTED IN PARTIAL FULFILLMENT OF
THE REQUIREMENTS FOR THE DEGREE OF

DOCTOR OF PHILOSOPHY

in

Petroleum Engineering

Department of Civil and Environmental Engineering

UNIVERSITY OF ALBERTA

Abstract

The application of horizontal drilling and hydraulic fracturing techniques has resulted in the economic production of previously inaccessible hydrocarbon trapped in very-low permeability reservoirs such as Shale gas/oil, tight gas and tight oil. Although the economic production of these reservoirs supplement the decreasing hydrocarbon supply from conventional reservoirs to meet the world's growing energy demand, modeling fluid flow in such complex reservoirs to minimize environmental pollution remains challenging.

There have been improvements in the quality and frequency of rate and pressure measurements during fluid production from multi-stage fractured wells and in the ability of existing transient models to interpret multiphase flowback and post-flowback production data. However, the existing models either make many simplistic assumptions or are too complex. The simplistic nature of some of these models could result in overestimation or underestimation of reservoir parameters and hydrocarbon forecasts. The complexity of some of these models introduces high uncertainty in the estimates of resulting parameters such as fracture pore-volume, half-length and permeability.

This study presents complementary workflows for the qualitative and quantitative analysis of flowback and post-flowback production data. The data are obtained from multifractured horizontal wells completed in low permeability reservoirs with a significant amount of reactivated natural fractures. The workflows are based on three key models proposed in the study, namely — flowback tank model, flowback analysis model and quadrilinear flow model. The main results from this work are summarized in the following paragraphs.

The occurrence of pseudo-steady state flow regime during intermediate flowback periods suggests a "*pressure supercharge*" effect in the fracture network. Rate and pressure data from this flow regime can be analyzed to estimate key fracture properties (e.g. effective pore-volume and initial average gas saturation in the active fracture network) and drive mechanisms (i.e. fracture closure, gas expansion and water depletion). Fracture closure effects play a significant role in the physics of fluid flow during early flowback periods. However, fluid expansion becomes the dominant drive mechanism towards the end of flowback in gas wells. Flowback data from tight oil wells are dominated by single phase, water depletion during early time periods (about 100 hours). This is unlike many Shale gas wells, which show immediate gas and water production.

The concept of dynamic-relative-permeability was proposed to capture the transient, multiphase, fluid saturations in the effective fracture network during flowback. The resulting model enables complementary, 2-phase flowback and post-flowback production data analysis. Qualitative production data analysis show that there is a general correlation between: load recovery and flowback sequence; effective fracture pore volume and flowback sequence; and cumulative water production and effective fracture pore volume. The restriction of comparative load recovery analysis to wells completed in the same formation produces better correlations. Also, this qualitative analysis provides a way to estimate the percentage of the total injected volume left inside and outside the active fracture network respectively. Quantitative production data analysis provides estimates of the pore-volume of active fracture networks, effective half-length and initial gas volume in hydraulic fractures during flowback. This analysis shows that the gas desorption effects from the matrix and the communication interface between secondary fractures and hydraulic fractures, significantly increases as production progresses from flowback to post-flowback periods.

Production data from tight reservoirs with significant reactivated natural fractures now be appropriately analyzed using the proposed quadrilinear flow model. This is achieved by providing type-curves and analysis equations (from flow regimes). The application of a wrong model for production data analysis could result in the overestimation or underestimation of reservoir parameters (e.g. half-lengths of hydraulic fractures and intensity of secondary fractures). This study proposes a criterion (based on spacing aspect ratio) for selecting the appropriate model when interpreting production data from multifractured horizontal wells in tight reservoirs. Uncertainty in parameters estimated from production data analysis can be reduced by using the results from flowback data analysis as inputs (or initial guesses) for post-flowback production data analysis. Also, this can be achieved by comparing the parameters independently estimated using analysis equations from individual flow regimes.

Preface

All or parts of Chapters 2 to 7 have been published as peer reviewed, journal papers. I was responsible for model development, computer programming, writing and editing these papers. My co-authors were responsible for providing relevant data from their respective companies, providing useful comments and discussions on field practices, reviewing the manuscript drafts and securing company approvals for these publication.

The necessary approvals to include the journal papers as chapters in this work are provided in sequential order in the Copyright Permissions section. The reference style from the Society of Petroleum Engineers[1] was used in this study.

[1]Society of Petroleum Engineers, Style Guide (2015-2016 Edition). http://www.spe.org/authors/docs/styleguide.pdf (last accessed 15-11-2016).

Dedication

This is to God Almighty for supplying the Grace, Strength and Wisdom. Also, not forgetting all who have invested and are still investing in my life — *among whom my godly and praying mother shines like the star in the deepest, darkest night*

Acknowledgments

I would like to thank my supervisor, Dr. Hassan Dehghanpour, for giving me the opportunity and support to be his first PhD student — *he ensured that I exercised my potentials and stretched my preconceived boundaries every step of the way.* Also, I thank my supervisory committee members (Dr. Juliana Leung and Dr. Alireza Nouri) for their persistent demand for excellence throughout this work.

I am grateful to Alberta Innovates Technology Futures, Canadian Discovery Limited, Daylight Energy Limited, FMC Technologies, Lightstream Resources Limited, Natural Resources Canada, Natural Sciences and Engineering Research Council of Canada, Newfield Exploration, Nexen ULC, Trican Well Services and Vanier Canada Graduate Scholarship for providing field data and funding this study.

I would like to appreciate my colleagues (Yingkun Fu, Yanmin Xu, Ali Habibi, Ashkan Zolfaghari, Mahmood Yassin, Momotaj Begum, Ali Javaheri, Tobi Adefidipe, Mingxiang Xu, Sara Eghbali, Hamidreza Yarveicy) for their insightful contributions and fruitful discussions. Also, I appreciate the help of some administrative staff members of the civil and environmental engineering department (Anne Jones, Arlene Figley, Jomana Haymour and Trina Cattral). They were willing to listen and help at all times — *God bless you all.*

Table of Contents

Appendices

List of Tables

List of Figures

Chapter 1

General Introduction

1.1 Overview

This part of the chapter briefly describes the key terminologies and field procedures mentioned in relevant chapters and places this work in proper perspective.

1.1.1 Unconventional Reservoirs

In this study, "*unconventional*" refers to the tightness (low porosity and permeability) of the rock matrix (Fig. 1.1).

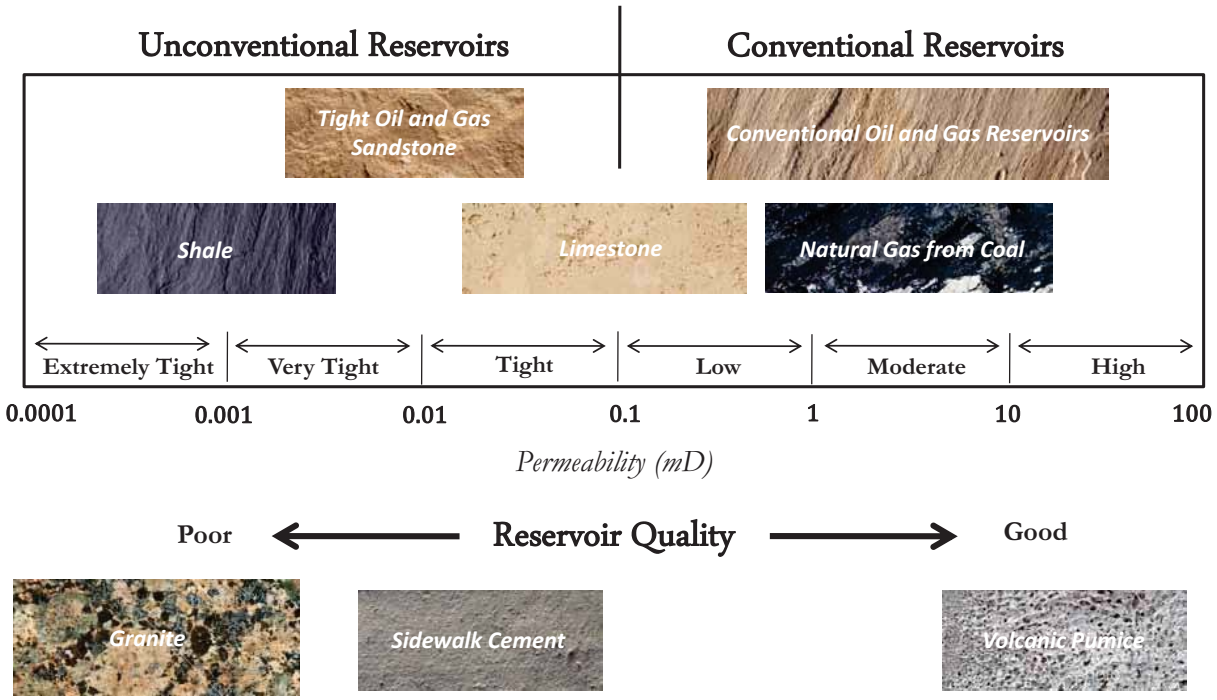

Fig. 1.1: Comparative analysis of rock properties found in various unconventional reservoirs.[2]

[2] http://www.csur.com/sites/default/files/Understanding_TightOil_FINAL.pdf (last accessed 09-01-2017).

Unconventional reservoirs include tight sandstone, Shale etc. (Fig. 1.2). Due to the nature of their rock fabric, these reservoirs do not naturally and readily allow trapped hydrocarbons to flow toward a well drilled into them[3]. Instead, they require special operating procedures beyond the conventional practices to achieve economic flow rates (Holditch, 2003). These special procedures include horizontal technology and hydraulic fracturing.

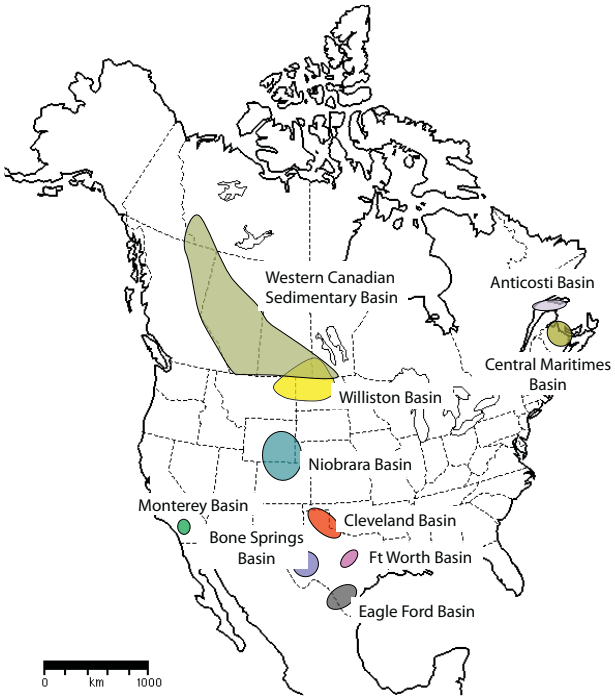

Fig. 1.2: Major Basins in North America having unconventional reservoirs.[4]

1.1.2 Horizontal Well Technology and Multi-Well Pad Drilling

The economic exploitation of unconventional reservoirs has become possible with the combination of horizontal well technology (Fig. 1.3) and multi-well pad drilling (Fig. 1.4). Especially for thin pay zones, horizontal wells increase the contact area between well and reservoir; while multi-well pad drilling minimizes costs (e.g. site monitoring) and reduces the associated environmental impacts (e.g. access roads and surface disturbances).

[3] https://www.aer.ca/about-aer/spotlight-on/unconventional-regulatory-framework/what-is-unconventional-oil-and-gas (last accessed 06-01-2017).

[4] http://www.csur.com/sites/default/files/Understanding_TightOil_FINAL.pdf (last accessed 09-01-2017).

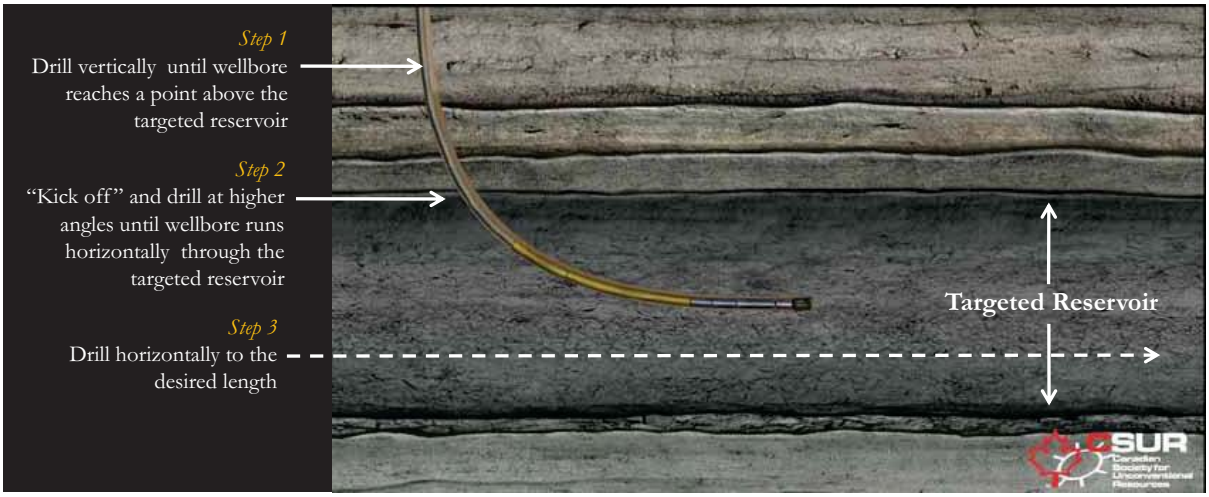

Fig. 1.3: Horizontal Well Technology.[5]

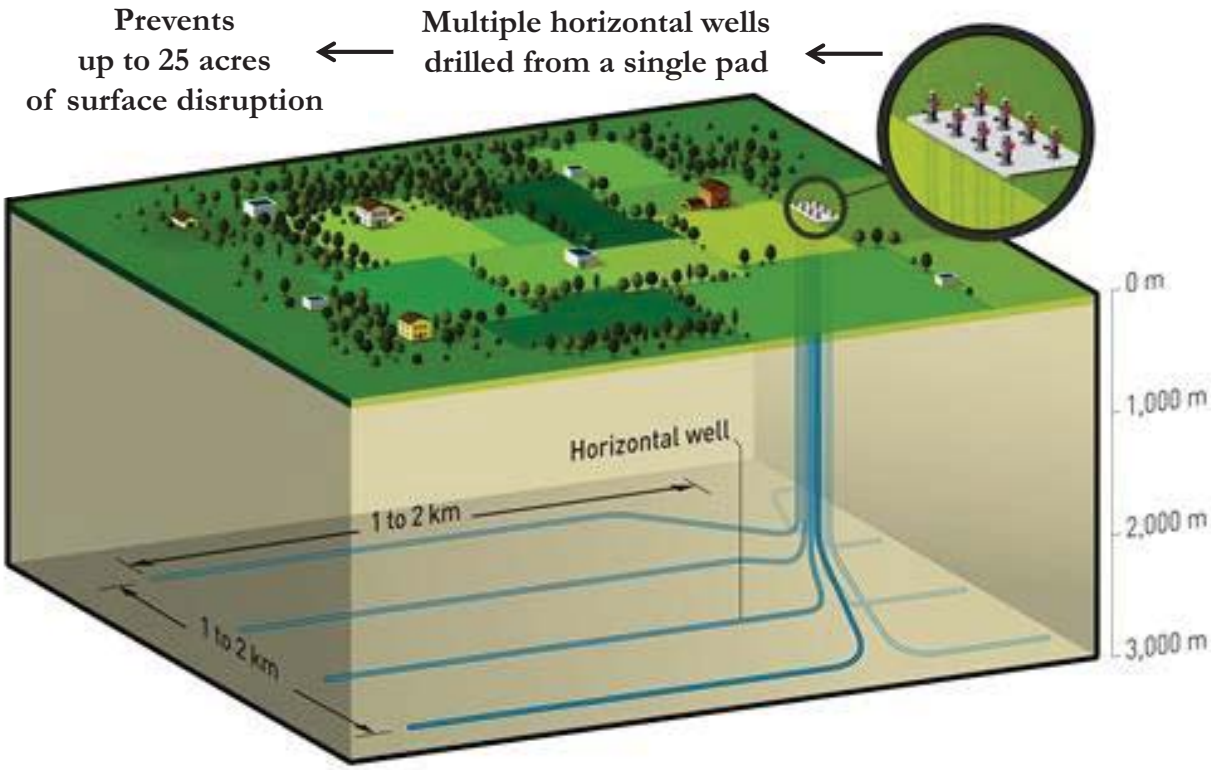

Fig. 1.4: Multi-Well Pad Drilling.[6]

[5] http://www.csur.com/sites/default/files/Understanding_TightOil_FINAL.pdf (last accessed 09-01-2017).

[6] https://bollocks2012.files.wordpress.com/2013/02/shale-gas-well-clusters_500x333.jpg (last accessed 09-01-2017).

1.1.3 Multistage Hydraulic Fracturing and Flowback Operations

Despite the combination of horizontal well technology and multi-well pad drilling, many unconventional reservoirs still do not produce hydrocarbons at economic flow rates.

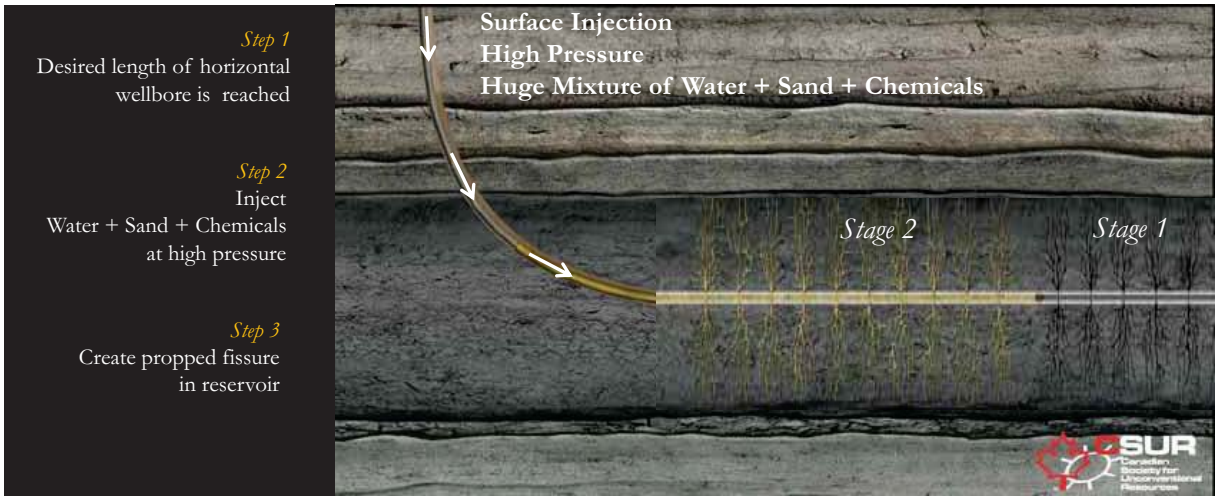

(a)

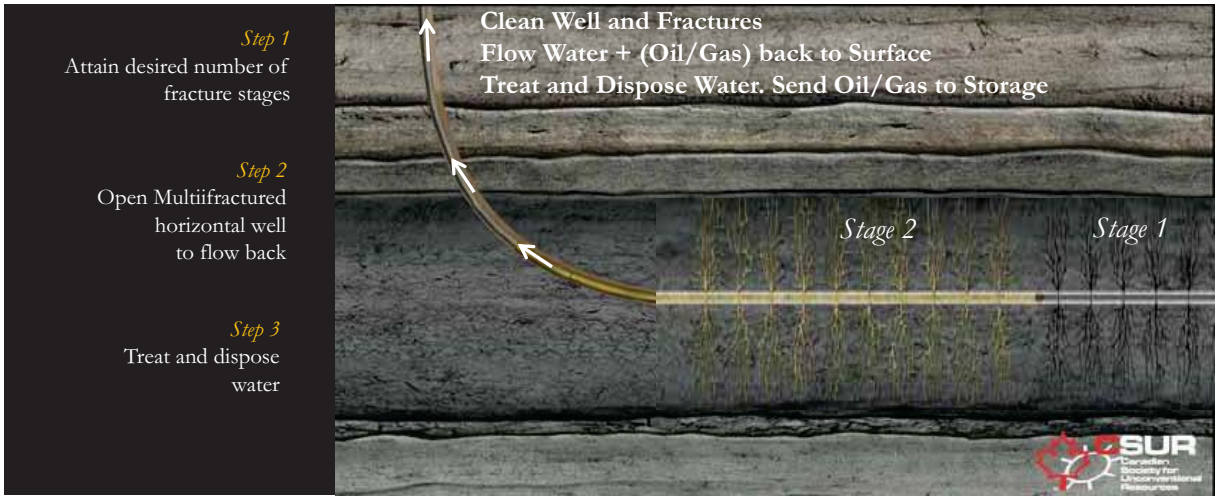

(b)

Fig. 1.5: Horizontal well drilled in a unconventional reservoir. (a) Hydraulic fracturing with multiple stages (b) Flowback after hydraulic fracturing.[7]

To achieve these rates, the horizontal wells need to be hydraulically fractured (Fig. 1.5a) in multiple stages to create additional pathways (different from the in-situ pore networks) for hydrocarbon flow. Also, the hydraulic fractures connect the well with the existing

[7] http://www.csur.com/sites/default/files/Understanding_TightOil_FINAL.pdf (last accessed 09-01-2017).

natural fractures/cleats. Each fracture stage is isolated using flow control devices such as packers or plugs to contain the injected fracturing fluid. Also, these devices ensure that the resulting fractures propagate in the planned direction with the desired length. A fracture stage could comprise single or multiple perforation clusters. These clusters may be matched to natural fracture locations depending on the available knowledge about stresses along the well and behavior of the hydraulic fracture.

The in-situ stress field of the reservoir determines the size and orientation of a hydraulic fracture, and the amount of pressure required to create it (Fig. 1.6).

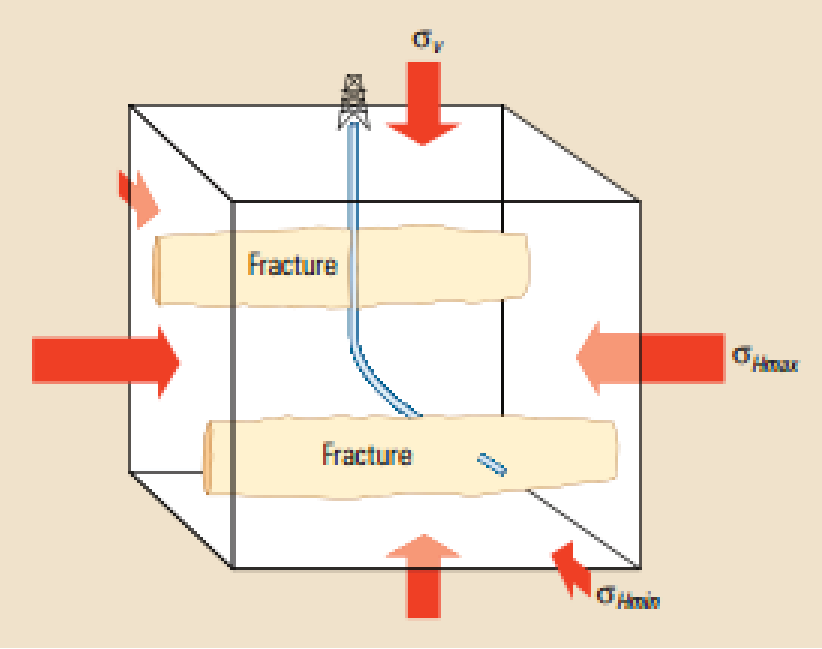

Fig. 1.6: In situ stresses and hydraulic fracture propagation. The three principal compressive stresses (red arrows) are a vertical stress (σ_V) and a maximum and minimum horizontal stress (σ_{Hmax} and σ_{Hmin}) respectively. Hydraulic fractures open in the direction of the least principal stress and propagate in the plane of the greatest and intermediate stresses.[8]

To create the hydraulic fractures, a mixture of fracturing fluids, chemical additives and proppants are injected into well perforations at pressures higher than the breakdown pressure of the reservoir[9]. The breakdown pressure is generally believed to be the sum of in-situ stress and tensile strength of the reservoir[10].

Once the formation is broken down and the fracture created, the fracture can then be extended at a pressure called the fracture-propagation pressure (Cholet, 2008). This

[8] http://www.slb.com/~/media/Files/resources/oilfield_review/ors13/sum13/defining_hydraulics.pdf (last accessed 09-01-2017).

[9] http://https://www.spec2000.net/10-closurestress.htm (last accessed 09-01-2017).

[10] http://petrowiki.org/Fracturing_fluids_and_additives (last accessed 09-01-2017).

fracture-propagation pressure is the sum of in-situ stress, pressure drop down the fracture as a result of viscous fluid flow in it, any pressure increase due to fracture tip effects, pressure drop of the viscous fluid flowing through well perforations and/or pressure drop resulting from tortuosity between the well and propagating fracture (Fig. 1.7).

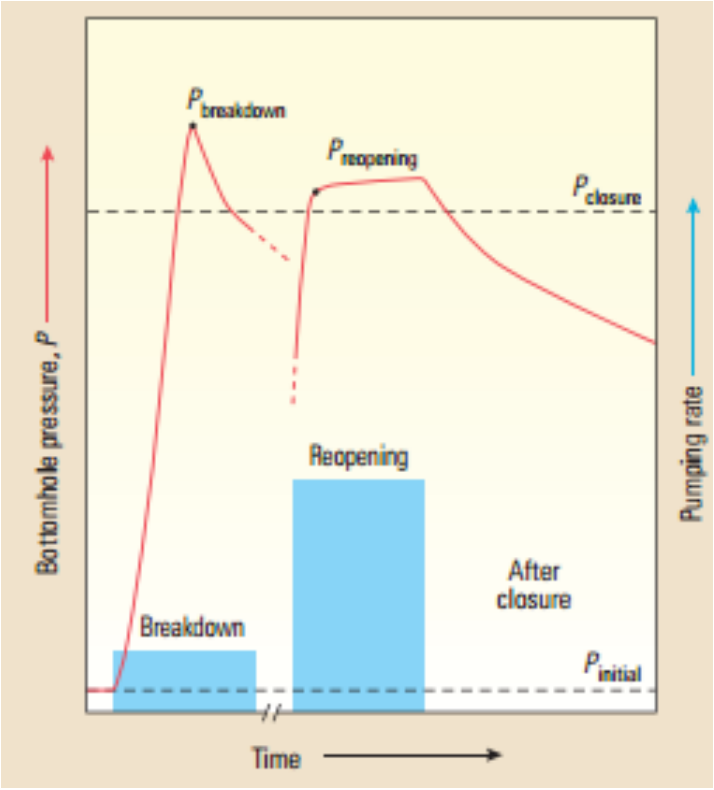

Fig. 1.7: Fracture pressures. During a stimulation treatment, engineers pump fluid into the targeted stimulation zone at a prescribed rate (blue polygons), and pressure (red line) builds to a peak at the breakdown pressure, then it drops, indicating the rock around the well has failed. Pumping stops and pressure decreases to below the closure pressure. During a second pumping cycle, the fracture opens again at its reopening pressure, which is higher than the closure pressure. After pumping, the fracture closes and the pressure subsides. The initial pore pressure is the ambient pressure in the reservoir zone.[11]

Generally, the volume of hydraulic fracture created is estimated as the percentage of the total volume of injected fluid which does not leak off into the reservoir. Since unconventional reservoirs have very low permeabilities, this leak-off percentage is expected to be at a minimum.

After hydraulic fracturing, there is usually a period of soaking (or shut-in) before opening the well for flowback operations. The duration of this soaking depends on the knowledge about leak-off rates of water into the reservoir matrix and how long it takes to

[11] http://www.slb.com/~/media/Files/resources/oilfield_review/ors13/sum13/defining_hydraulics.pdf (last accessed 09-01-2017).

prepare surface facilities for production. Flowback is the cleanup process which recovers as much injected fluid as possible from the well (Fig. 1.5b) and prepares it for optimal, long-term hydrocarbon production. This is usually a process of short duration which could involve some proppant production. The flow of these recovered proppants through tubing can damage control devices like valves, chokes and probes. Although optimal well management during flowback affects long term well performance, best practices depend on geology, fracturing fluid and completion.

1.1.3.1 Fracturing Fluids

The properties of fracturing fluids are important for optimal creation and propagation of hydraulic fractures. A good fracturing fluid should have the following properties:

- Transportation of proppants in the fracture.
- Compatibility with the formation rock and fluid to prevent damage due to fine plugging, wash outs etc.
- Generation of enough pressure to create fractures of appropriate width and expected length.
- Minimization of pressure losses as a result of friction during injection.
- Ability to subsequently break into a low-viscosity fluid with sufficient density for cleanup (flowback) after the fracturing operations.
- Cost effective.

Table 1.1: Fracturing fluids and conditions for their use.[12]

Base	Fluid Type	Main Composition	Uses
Water	Linear	Guar, HPG, HEC, CMHPG	Short fractures, low temperature
	Micellar	Electrolyte + Surfactant	Moderate length fractures, moderate temperature
	Crosslinked	Crosslinker + Guar, HPG, CMHEC or CMHPG	Long fractures, high temperature
Foam	Water based	Foamer + N_2 or CO_2	Low pressure Formations
	Acid based	Foamer + N_2	Low pressure, carbonate Formations
	Alcohol based	Methanol + Foamer + N_2	Low pressure, water-sensitive Formations
Oil	Linear	Gelling agent	Short fractures, water-sensitive Formations
	Water emulsion	Water + Oil + Emulsifier	Moderate length fractures, good fluid loss control
	Crosslinked	Gelling agent + Crosslinker	Long fractures, water-sensitive Formations
Acid	Linear	Guar or HPG	Short fractures, carbonate Formations
	Oil emulsion	Acid + Oil + Emulsifier	Moderate length fractures, carbonate Formations
	Crosslinked	Crosslinker + Guar or HPG	Longer, wider fractures; carbonate Formations

[12] http://petrowiki.org/Fracture_treatment_design (last accessed 10-01-2017).

Although fracturing fluid could be oil, acid or foam based (or a combination); water is the common base fluid used for exploiting many unconventional reservoirs (Table 1.1, Fig. 1.8).

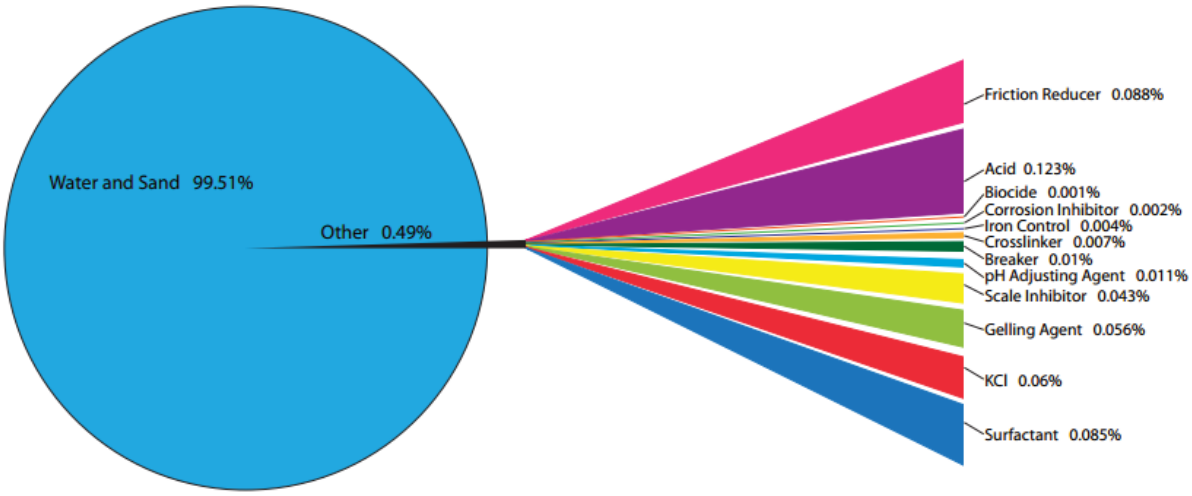

Fig. 1.8: Typical volumetric composition of a water-based fracturing fluid.[13]

Also, there is usually a trade-off between reservoir or fracture damage and proppant concentration in the choice of fracturing fluid (Fig. 1.9).

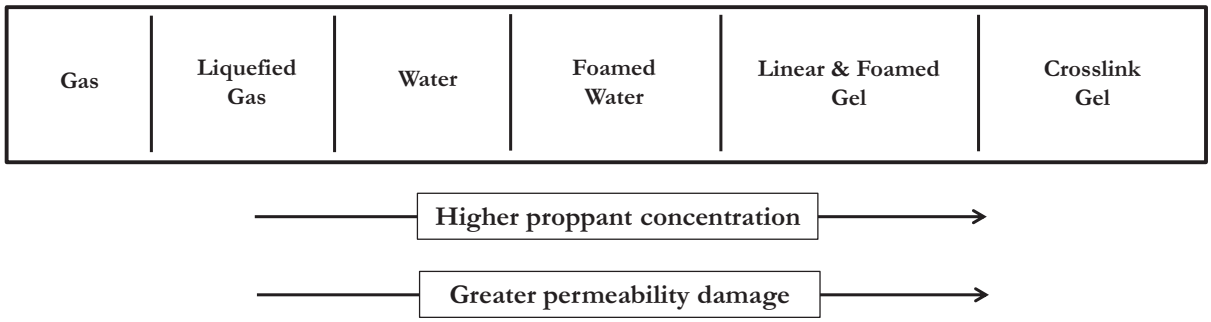

Fig. 1.9: Sample tradeoff in selection of optimal fracturing fluid.[14]

While viscosity of the fracturing fluid primarily determines the nature of the hydraulic fractures, its density determines the surface injection pressure/rate. Generally, fracturing fluids with low viscosity are injected at higher rates (often 60-100 bbl/minute) to generate narrow, complex fractures with low proppant concentrations (0.2 to 5 lbm proppant

[13] http://www.csur.com/images/CSUG_publications/CSUG_HydraulicFrac_Brochure.pdf (last accessed 12-01-2017).

[14] https://www.netl.doe.gov/File%20Library/Research/Oil-Gas/Natural%20Gas/shale%20gas/09122-02-final-report.pdf (last accessed 09-01-2017).

added per gallon), small widths (less than 0.5 in) and short half-lengths[15]. These complex fractures could comprise primary hydraulic fractures which are connected to secondary orthogonal fractures and tertiary parallel fractures (Fisher et al., 2002). One advantage of creating complex fractures is that they provide higher contact area between well and reservoir; therefore improving hydrocarbon recovery.

The volume of fracturing fluid used to stimulate a well depends on the size or number of treatment operations and reservoir geology. For example, multistage fracture treatments in deep horizontal wells could use up to 15000 m^3 of water while those in shallow zones might require less than 50 m^3 of water[16].

1.1.3.2 Chemical Additives

The optimal combination of chemical additives used in fracturing unconventional reservoirs is determined by the local environmental regulations, choice of fracturing fluid and reservoir geology. Table 1.2 provides a quick summary of the roles played by chemical additives during hydraulic fracturing.

Table 1.2: Typical chemical additives used during hydraulic fracturing.[17]

Additive	Function	Typical Product
Biocide	Kill bacteria	Gluteraldehyde carbonate
Breaker	Reduce viscosity	Acid, oxidizer. enzyme breaker
Buffer	Control pH	Sodium bicarbonate, fumaric acid
Clay stabilizer	Prevent clay swelling	KCl, NHCl, KCl substitutes
Diverting agent	Divert fluid flow	Ball sealers, rock salt, boric acid
Fluid loss additive	Improve fluid efficiency	Diesel, particulates, fine sand
Friction reducer	Reduce friction	Polyacrylamide derivatives
Iron controller	Keep iron in solution	Acetic and citric acid
Surfactant	Modify surface tension and wettability	Fluorocarbon, Isopropanol
Gel stabilizer	Reduce thermal degradation	MEOH, sodium thiosulphate
Scale Inhibitors	Reduce scale formation	Inorganic and organic phosphates

[15] http://petrowiki.org/Fracturing_fluids_and_additives (last accessed 09-01-2017).
[16] http://www.csur.com/images/CSUG_publications/CSUG_HydraulicFrac_Brochure.pdf (last accessed 12-01-2017).
[17] http://petrowiki.org/Fracturing_fluids_and_additives (last accessed 09-01-2017).

The most chemical additives used in water-based fracturing fluids for unconventional reservoirs is the friction reducer. This is because the high pump rates used for these treatments require up to 70% reduction in friction pressure to moderate the pumping pressure to a manageable level during proppant injection. Typically, the performance of friction reducers in water-based treatments decreases as salinity increases.

1.1.3.3 Proppants

Proppants are materials injected into fractures (created by hydraulic fracturing) to keep them open. These materials (Liang et al., 2016) could be natural or artificial, sand or non-sand based, coated or uncoated, smooth or rough, light or heavy etc. (Fig. 1.10). The optimal choice of type, size, density and concentration of proppant depends on reservoir geology, properties of fracturing fluid, prevailing stress and temperature regimes in pay zone of interest, target fracture widths etc.

Fig. 1.10: Several proppant types. (a) High-strength bauxite (b) Resin-coated silica (c) Lightweight ceramic.[18]

In many situations, proppants of different properties are used sequentially or simultaneously with the fracturing fluid to control proppant embedment and achieve optimal fracture conductivity (product of width and permeability)[19]. Generally, proppants with larger particle sizes are expected to provide higher fracture conductivity in the hydraulic fractures, whereas proppants with smaller particle sizes can access and prop finer fractures (e.g. preexisting natural fractures). Therefore, a typical fracture treatment will start with proppants of smaller particle size followed by those with larger particle size to maximize the near wellbore conductivity.

Most proppants used for hydraulic fracturing in unconventional reservoirs generally fall between 8 (2.38 mm) and 140 (0.105 mm) mesh sizes (Liang et al., 2016). Table 1.3 shows a summary of the ASTM International sieve series for proppant sizes.

[18] http://www.slb.com/~/media/Files/resources/oilfield_review/ors13/sum13/defining_hydraulics.pdf (last accessed 09-01-2017).

[19] https://www.netl.doe.gov/File%20Library/Research/Oil-Gas/Natural%20Gas/shale%20gas/09122-02-final-report.pdf (last accessed 09-01-2017).

Table 1.3: ASTM International sieve series for proppant sizes (Roberts, 2009).

US Mesh	**Sieve opening** (mm)
5	4.0000
6	3.3600
7	2.8300
8	2.3800
10	2.0000
12	1.6800
14	1.4100
16	1.1900
18	1.0000
20	0.8400
25	0.7100
30	0.5890
35	0.5000
40	0.4200
45	0.3510
50	0.2970
60	0.2500
70	0.2100
80	0.1770
100	0.1490
120	0.1240
140	0.1040
170	0.0880
200	0.0740

1.1.4 Natural Fractures

For this study, natural fractures (Fig. 1.11) are macroscopic planar discontinuities in a rock due to deformation or diagenesis (Nelson, 2001). Typically, it is assumed that they were initially open and may have been subsequently deformed or mineralized. Generally, they could be open, partially filled with minerals or sealed (Gale et al., 2014). The sealing or filling in these fractures depends on the nature of the host rock. For example, natural fractures in Shales are prone to sealing because of the diagenetically reactive nature of Shales (Gale et al., 2014).

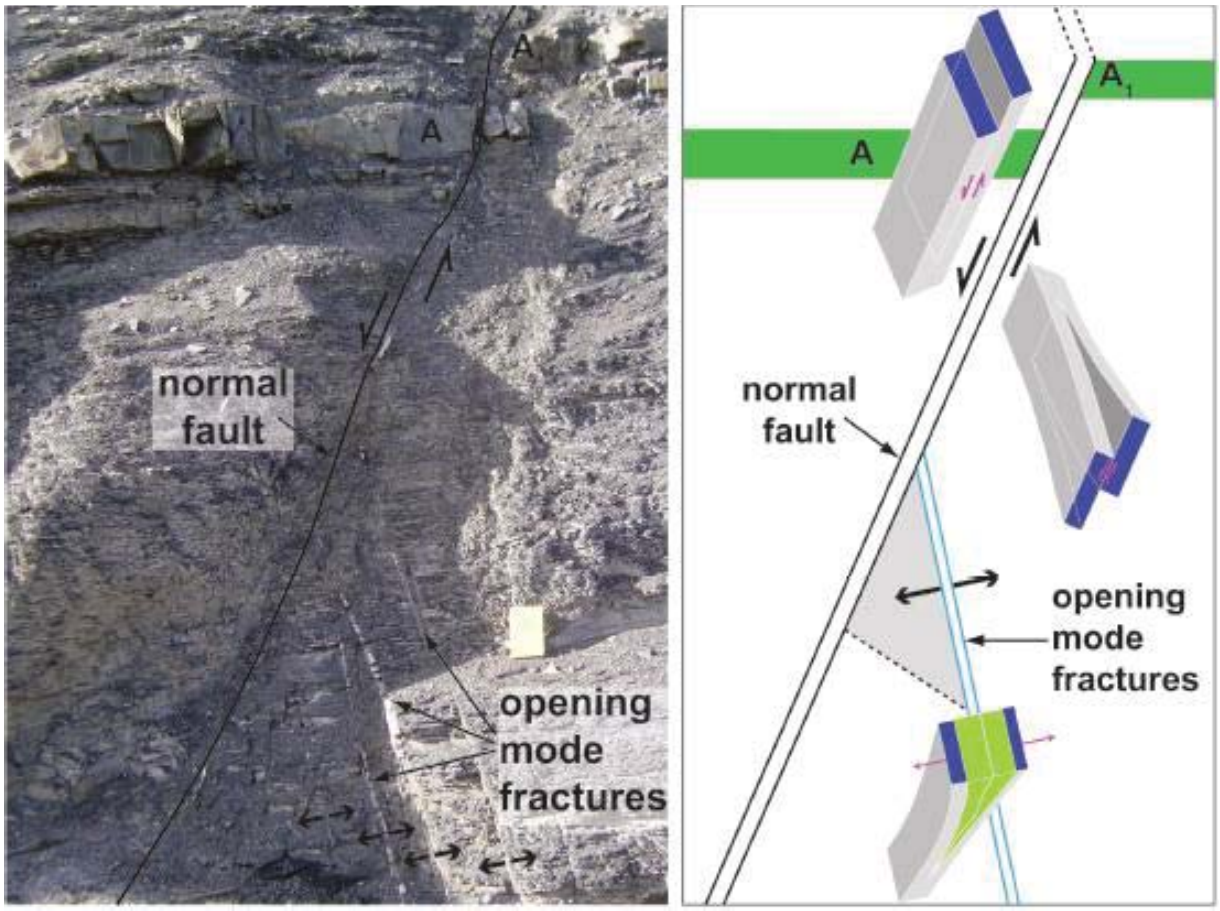

Fig. 1.11: Normal fault showing opening-mode natural fractures on the left side (scale of field book beside the fractures is 19 x 12 cm). Interpretative diagram on the right side showing sense of displacement for different fractures from the right side (Gale et al., 2014).

Natural fractures are not induced by drilling, contain cement or mineral fillings unrelated to the drilling fluid, form at least one parallel set, generally do not require microscopy to detect, and represent the local state of stress at the time of fracturing (Gale et al., 2007; Nelson, 2001; Taal-van Koppen, 2008). However, natural fractures could be reactivated as a result of drilling and hydraulic fracturing operations; as the fracturing fluid increases their pore pressure and decreases the effective normal stress on the fracture plane causing slippage and shear dilation (Moradian et al., 2016). This reactivation could enhance hydrocarbon recovery (Nelson, 2001) by increasing the connectivity between hydraulic fractures and reservoir matrix. On the other hand, it could reduce target length of hydraulic fractures by allowing the natural fractures to capture most of the injected fracturing fluids (Gale et al., 2014). This happends because hydraulic fractures tend to initiate more easily in areas of low stresses and in most areas of natural fractures.

Generally, natural fractures (Gale et al., 2007) are narrow (typically less than 0.05

mm) and could have high length to width aspect ratios (typically greater than 1000). Their porosities, permeabilities and compressibilities depend on the interplay between the net stress on them and the amount of secondary mineralization within them. Although, mineralization can act as an efficient, natural propping agent for natural fractures, the minerals could be crushed by high in-situ stresses leading to reduction in fracture permeability (Aguilera, 2006).

Natural fractures could occur on a regional or local scale depending on: the orientation and magnitudes of stresses responsible for creating them; the number of superimposed, separate stress events; bedding thickness; and properties of the host rock (Lorenz et al., 1996). Regional natural fractures tend to have a relatively regular orientation, be extensive, have simple geometry, and are parallel to sub-parallel features over wide areas within relatively undeformed strata (Lorenz et al., 1996; Taal-van Koppen, 2008). Regional natural fractures are created by anisotropic stress fields under high pore pressures, and tend to be unidirectional, least stress sensitive and poorly interconnected (Lorenz and Warpinski, 1992). The high pore pressures effectively de-stresses the rock such that rock failure happens at smaller deviatoric stresses. These regional fractures can be induced when the maximum horizontal in-situ stress increases (e.g. near a thrust belt), minimum horizontal in-situ stress decreases (e.g. in an extensional environment) and pore pressure increases (e.g. due to gas generation). Also, they are generally considered to have originated in extension normal to the fracture plane, rather than in shear (Lorenz et al., 1996). On the other hand, local natural fractures generally form random sets with no significant consistent trend and are typically caused by non-regional factors like diagenesis.

1.2 Research Motivation

There are several existing techniques for analyzing post-flowback production data independent of flowback data. Some of these techniques are discussed in the introduction sections of the relevant chapters. However, this section focuses on the key drawback of the existing techniques and the intended contributions of this work.

Unlike conventional reservoirs where hydraulic fracturing is mainly an enhanced recovery strategy, it is required as part of the primary recovery strategy in unconventional reservoirs. This is because if the horizontal well is not combined with hydraulic fractures in unconventional reservoirs, the nature of their pore structures prevents them from producing fluids at economic flow rates.

After fracturing the reservoir, the stimulated horizontal well undergoes a period of flowback before being put on long-term production. Since water (not hydrocarbon) is

the main fluid recovered during flowback, many operators do not record the flow rates. Therefore, many wells only have a record of post-flowback data. As a result, the missing flowback data from most wells makes reservoir characterization and reliable hydrocarbon prediction quite challenging (Alkouh et al., 2014).

Flowback data provides an early opportunity to characterize the hydraulic fractures, evaluate the stimulation job and predict well performance. Therefore, this study investigates how flowback data analysis can complement post-flowback data analysis to improve reservoir and fracture characterization, reduce uncertainty in parameter estimation and enhance hydrocarbon forecasts. Also, it explores how the fluid physics during flowback changes as production transitions into post-flowback periods.

1.3 Research Objectives

This research has a three-fold objective:

- to develop robust mathematical models to analyze flowback rate and pressure data from multistage, hydraulically fractured wells. These models would account for the rapid saturation changes and multiphase flow in the fracture networks.
- to develop robust mathematical models to analyze post-flowback rate and pressure data from multistage hydraulically fractured wells. These models would account for the possibility of reactivating preexisting natural fractures during hydraulic fracturing.
- to design integrated workflows for complementary flowback and post-flowback data to improve reservoir and fracture characterization, reduce uncertainty in parameter estimation and enhance hydrocarbon forecasts.

1.4 Organization of Thesis

This work is divided into eight chapters, all of which (except the first and last) have been published as peer-reviewed journal papers. Therefore, there might be some repetition of texts or figures in the chapters. Although each chapter forms a distinct unit of study with its own nomenclature, the chapters can still be read sequentially without loss of coherence.

Chapter 1 gives a general introduction, sets the study in appropriate perspective, and provides the motivation and objectives of the research. Chapters 2 to 7 can be classified under two broad headings, namely: accounting for multiphase flow and rapid

saturation changes in fracture networks during flowback; and accounting for secondary fracture networks during post-flowback.

Chapters 2 to 4 describe two flowback analysis models (closed-tank and dual-porosity based frameworks) which handles the rapid saturation changes in the fractures during pseudo-steady and transient flow regimes. Also, it shows how the results from these flowback models can be used to complement the analysis of post-flowback data.

Chapters 5 to 7 describe a quadrilinear flow model which relaxes the sequential fluid transfer in existing models to allow simultaneous fluid transfer from matrix to both primary and secondary fracture networks. Also, it presents simplified equations by splitting the flow model based on key flow regime. In addition, it compares the flow model performance against some existing models to propose a criterion for selecting the appropriate model when interpreting production data from multi-fractured horizontal wells in tight reservoirs.

Chapter 8 provides key conclusions from this study and some recommendations for future studies.

The references from all chapters are combined together and presented after Chapter 8. Similarly, the appendices from all chapters are combined together and presented after the references.

Chapter 2

Fracture Closure during Flowback: A Key Factor for Estimating Effective Pore-Volume

2.1 Introduction

The economic exploitation of tight oil and gas reservoirs has become possible with the use of multi-fractured horizontal wells. A major challenge in exploiting these unconventional resources is the reliable characterization of their complex fracture network using existing flow models. In the past, fluid rate and pressure data obtained during the post-stimulation "*flowback*" period was generally ignored. However, such data presents the earliest opportunity for characterizing hydraulic fractures and gaining insights into the effectiveness of the stimulation operation; as well as generating long-term production forecasts. Recent advances in probe technology have enhanced the frequency and quality of fluid rate and pressure measurements during flowback. This has led to the development of transient models which capture more flowback physics and provide improved data interpretation. A number of research studies have introduced diverse approaches to the analysis of flowback data. However, many of these approaches are unable to properly capture the transient saturation changes in the hydraulic fractures (due to single phase flow assumption) or produce high uncertainty in output reservoir parameters (due to model complexity).

Crafton (1998) and Crafton and Gunderson (2006, 2007) championed the use of high frequency, single phase data for estimating fracture permeability and conductivity. Abbasi et al. (2014) proposed a similar methodology which utilizes an early-time single phase region, which occurs during the first few hours of flowback in tight oil and gas wells. They developed a flowing material-balance model to estimate fracture permeability and a storage coefficient by history-matching early-time flowback data. However, flowback is a multiphase flow process; and as such, it cannot be accurately analyzed by single phase models. This is specifically the case in wells with extended shut-in period(s) prior to flowback operations (Adefidipe et al., 2014; Xu et al., 2015).

Clarkson's research group analyzed two-phase flowback data using numerical simulation and pressure transient techniques originally developed for coal bed methane (CBM) reservoirs. Their methodology takes advantage of a proposed similarity between the two-phase flowback production in hydraulically fractured reservoirs and the simultaneous flow of gas and water during long-term production from naturally fractured, coal reservoirs (Clarkson and McGovern, 2005; Clarkson, 2012). They expanded their work by introducing stochastic history-matching and multiphase type-curve matching techniques to deal with uncertainties in characterizing fractures from flowback data (Clarkson and Williams-Kovacs, 2013; Williams-Kovacs and Clarkson, 2013a). Although this stochastic approach handles uncertainty in output parameter from the flowback model, the fluid physics taking place in CBM reservoirs is slightly different from that during flowback process. During flowback, water in the hydraulic fracture network is generally displaced by hydrocarbon influx from the matrix as opposed to the additional matrix desorption mechanism taking place in CBM reservoirs (Ezulike et al., 2013).

Ezulike and Dehghanpour (2014b,c) extended the linear dual-porosity model (Bello and Wattenbarger, 2010a) to analyze flowback data as a transient two-phase displacement process. The model introduces an explicit dynamic-relative-permeability (DRP) function of time into the existing dual-porosity model to capture the transient fluid saturations in the fracture network. Ezulike and Dehghanpour (2014b,c) presented an integrated workflow for history-matching flowback from multi-fractured Shale gas wells completed in the Horn River Basin. The integrated workflow involves two tightly coupled steps — the first step is history-matching cumulative water and cumulative gas/oil data during flowback to obtain a representative DRP function; the second step is the history-matching of flowback rate and pressure data with the modified linear dual-porosity model. The authors demonstrated how the workflow can be used to estimate fracture half-length and fluid leak off, and to predict gas recovery during post-flowback periods. While this approach appears robust and adequately captures much flowback physics, it requires a large number of input parameters which must be obtained by independent or complementary analytical methods. This introduces a high degree of uncertainty in the resulting parameter estimates.

Adefidipe et al. (2014) and Xu et al. (2015) presented alternative approaches for analyzing two-phase flowback data. They identified trends in production data which divide flowback data into two distinct regions — early gas production and late gas production. Using a two-phase tank model approach, they developed simplistic material-balance techniques to analyze flowback data (regardless of the fracture geometry) and to estimate the effective fracture pore-volume. While this simplistic approach greatly reduces the number of input parameters and the uncertainties associated with them, it only focuses on a

restricted flow period and utilizes a small fraction of the flowback data and may not be representative of the entire flowback process.

Some authors have approached fracture characterization by numerically simulating the flowback process. Li et al. (2013) carried out simulation studies by varying several fracture parameters to develop a correlation between early gas production and key fracture parameters in a Shale reservoir. Similarly, Almulhim et al. (2014) carried out numerical studies on the impact of water imbibition on flowback behavior. Cheng (2012) found correlations between shut-in time and water rate, and between gas rate and water load recovery. Although simulation studies allow the qualitative and quantitative analysis of flowback data, it is challenging to quantitatively characterize the hydraulic fractures. This is because of the computational power required to assign distinct representative parameters to fractures and matrix cells respectively. As such, the same average values (e.g. of compressibility) are conventionally assigned for all the porous media in the stimulated reservoir volume (Cheng, 2012; Li et al., 2013; Almulhim et al., 2014; Ghanbari and Dehghanpour, 2016). This could lead to misleading history-match results and erroneous production forecast during field data analysis.

Alkouh et al. (2014) went a step further by proposing an alternate semi-analytical approach based on observations from a number of simulation cases mimicking the flowback process. They used diagnostic and specialized plots to compare the results from simulation studies with actual field production data. These comparisons led to certain assumptions which were used to simplify the diffusivity equation. From the simulation analysis, they showed that at water saturations below 70%, the volumetric contribution of gas compressibility ($S_g c_g$) is at least 97% of total compressibility; thus the effects of water expansion and fracture compressibility are negligible. This observation was based on the assumption of an average "formation compressibility" for both matrix and fracture cells. This assumption holds in cases where actual matrix, gas and fracture compressibilities are of the same magnitude. However, since matrix compressibility is usually one to two orders of magnitude less than fracture compressibility (Newman, 1973; Sawabini et al., 1973), that assumption could underestimate the contribution of the fracture compressibility term during flowback.

This chapter proposes a simple two-phase flowback model for quick reservoir parameter estimation and as a complement to existing complex models. The model is developed by minimizing the number of model parameters in the diffusivity equation and using only those which capture most of the flowback physics (fluid saturations, fluid and fracture compressibilities). Also, the model is explicitly independent of fracture geometry and fracture permeability. It accounts for distinct input values for matrix and fracture compressibili-

ties, and shows the importance of this distinction during early time (about 100 hours in this study) of flowback data analysis. The study starts by using rate-normalized-pressure plots to observe changes in the mechanisms of fluid flow in multistage fractured wells. The observation of "*pressure supercharge*" effect in intermediate times (a pseudo-steady state behavior) forms the basis for model development. This model is a simple linear relationship of rate-normalized-pressure against time which interprets two-phase flowback data in wells showing the "*pressure supercharge*" effect. The linear relationship is implemented on a monte-carlo spreadsheet to conduct a sensitivity analysis in resulting parameter estimates. This study investigates the importance of various flowback drive mechanisms (such as fracture closure, gas expansion and water depletion) using quantitative indices similar to those used in conventional reservoir engineering.

2.2 Methodology

This chapter utilizes a data driven approach (using rate-normalized-pressure plots, see Figs. 2.3, 2.6 and 2.9) to observe changes in the physics of fluid flow in multistage fractured wells.

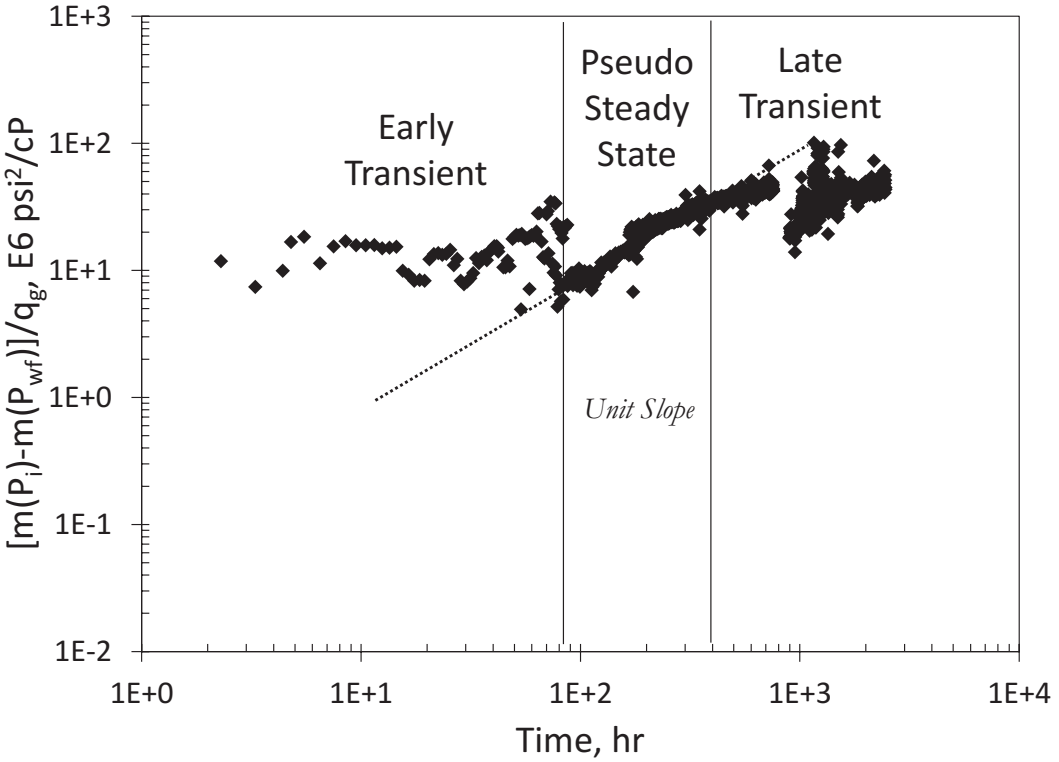

Fig. 2.1: Flowback rate normalized pseudo-pressure versus time plot (log-log axes) for a typical multi-fractured horizontal gas well showing key flow regions. The unit of the vertical axis is in per unit rate (m^3/day) and E represents a power of 10.

In turn, these observations will guide the development of the proposed tank flowback model using the least number of unknown parameters as possible. Fig. 2.1 shows the various flow regimes observed on the rate normalized pseudo-pressure plot from a typical Shale gas well during flowback. Rate normalized pseudo-pressure is used instead of the conventional rate-normalized-pressure to account for real gas behavior (and not slightly compressible liquid behavior) in gas wells. The interpretations of the observations from this plot are summarized below:

- The early flowback period is generally noisy. This could be a result of wellbore storage or data recording challenges. However, the actual flow signature is expected to be transient.
- The intermediate flowback period shows a clear unit slope, representative of pseudo-steady state (PSS) depletion. This cannot just be a result of data noise or wellbore storage. It suggests fluid depletion from a closed tank volume where the rate of pressure drop is fairly constant. Since the fracture network is usually smaller when volumetrically compared to the matrix, this period indicates storage depletion in the fractures.
- The late flowback period generally shows a transient flow signature.

Fig. 2.1 shows that the transient flow regime at the onset of flowback was interrupted by a period of PSS depletion before returning to transient flow again. However, a careful observation of the hydraulic fracturing process (see Fig. 2.2) reveals that a possible reason for the interruption of the transient flow regime by PSS depletion is the "*pressure supercharge*" effect (Jones Jr. et al., 2014). This "*pressure supercharge*" effect can be summarized as follows:

- During the early hours of flowback, the average pressure in the effective fractures created after hydraulic fracturing should still be larger than the average pressure in the matrix ($P_f > P_m$). However, since the bottom hole flowing pressure is less than both the average pressures in the effective fractures and matrix respectively, it is easier for fluids already in the fractures to flow to the surface without necessarily being supported by fluid influx from the matrix. Also from Darcy law, the matrix permeability which is orders of magnitude lower than the pressure difference between fracture and matrix, should not allow significant water transfer from fracture to matrix during this period. Moreover during shut-in after fracturing and before flowback, there is a possibility of the water from the fractures to compress the gas

further into the matrix — forming a kind of water block on the fracture face. Therefore, the observed transient fluid depletion should primarily come from the effective fracture volume.

- During the intermediate hours of flowback, the average pressure in the effective fractures decreases to the point where its rate of change is almost constant (PSS depletion) as a result of the fracture boundary effect.
- This PSS depletion continues until average pressure in the effective fractures is approximately the same as the average pressure in the matrix ($P_f \approx P_m$). At this point, any form of water block on the fracture faces should have significantly dissipated; such that fluid support from the matrix to the effective fractures begins and restores transient depletion.

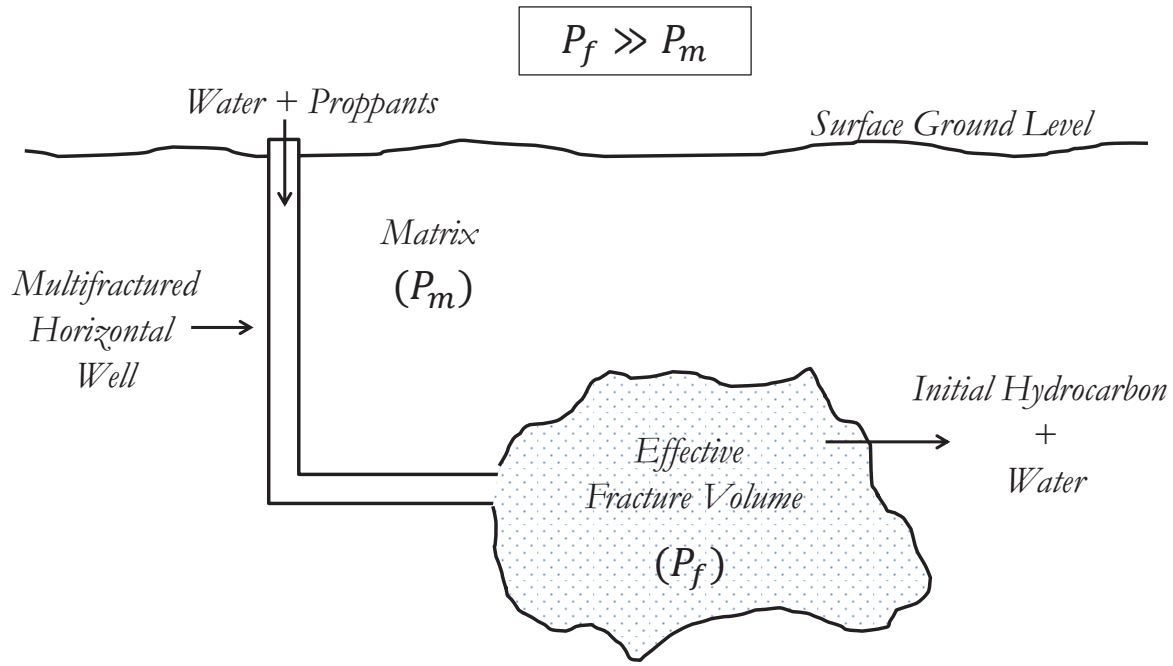

Fig. 2.2: Schematic of the hydraulic fracturing process depicting the pressure supercharge effect before flowback starts. P_f and P_m are the average pressures in the effective fractures and matrix respectively.

The intermediate PSS flow region from this pressure supercharge effect forms the basis for developing the proposed two-phase flowback tank model. The stochastic implementation of this model will be applied for probabilistic parameter estimation from pressure and rate data recorded during flowback.

2.3 Model

The control volume for the proposed model is the effective fracture volume (see Fig. 2.2) which is active during the PSS period of flowback. The key assumptions for developing this flowback model are given below:

- The average fracture pressure is much higher than the matrix pressure ($P_f \gg P_m$) when flowback starts due to the pressure supercharge effect.
- There is negligible fluid influx from matrix to the fractures due to pressure supercharge effect.
- There is negligible gas exsolution from oil at down-hole conditions (for oil wells).
- The average total compressibility for the fracture system is constant during this flow period.
- The pore-volume compressibility term (c_{pe}) of the effective fractures accounts for net porosity reduction as a result of fluid withdrawal during flowback, possible proppant crushing or embedment, compressibility of rock grains and thermal stresses due to temperature difference between fracturing fluid and insitu formation fluids. In this chapter, c_{pe} is subsequently referred to as "*fracture closure*".
- The effects of gas desorption from matrix is negligible for gas wells, since both initial matrix and flowing bottom-hole pressures for these reservoirs are greater than the critical desorption pressure (Ezulike and Dehghanpour, 2015) during this period.

Conducting material balance on the control volume (effective fracture volume in Fig. 2.2), the following equations at reservoir conditions are obtained:

Mass in (from Matrix) − Mass out = Rate of accumulation in fracture system

Water Phase:

$$0 - q_w \rho_w = \frac{\partial}{\partial t} [\rho_w V_w] \tag{2.1}$$

Since isothermal water compressibility can be expressed as

$$c_w = \frac{1}{\rho_w} \frac{\partial \rho_w}{\partial P} \tag{2.2}$$

Substituting Eq. 2.2 into Eq. 2.1 and simplifying it results in

$$-q_w = \frac{\partial V_w}{\partial t} + c_w V_w \frac{\partial P}{\partial t} \tag{2.3}$$

Hydrocarbon Phase (for Gas Well):

$$0 - q_g \rho_g = \frac{\partial}{\partial t} [\rho_g V_g] \tag{2.4}$$

Since effective fracture pore-volume (V_{pe}) is the sum of water and gas volumes in the fracture, Eq. 2.4 becomes

$$-q_g \rho_g = \rho_g \frac{\partial}{\partial t} [V_{pe} - V_w] + V_g \frac{\partial \rho_g}{\partial t} \tag{2.5}$$

$$-q_g \rho_g = \rho_g \frac{\partial V_{pe}}{\partial t} + V_g \frac{\partial \rho_g}{\partial t} - \rho_g \frac{\partial V_w}{\partial t} \tag{2.6}$$

Since isothermal gas compressibility can be expressed as $c_g = \frac{1}{\rho_g} \frac{\partial \rho_g}{\partial P}$, Eq. 2.6 becomes

$$-q_g = \frac{\partial V_{pe}}{\partial P} \frac{\partial P}{\partial t} + c_g V_g \frac{\partial P}{\partial t} - \frac{\partial V_w}{\partial t} \tag{2.7}$$

Since pore-volume compressibility of effective fractures can be expressed as $c_{pe} = \frac{1}{V_{pe}} \frac{\partial V_{pe}}{\partial P}$, Eq. 2.7 becomes

$$-q_g = c_{pe} V_{pe} \frac{\partial P}{\partial t} + c_g V_g \frac{\partial P}{\partial t} - \frac{\partial V_w}{\partial t} \tag{2.8}$$

Adding Water and Hydrocarbon Equations:

$$-q_w + q_g = [c_{pe} V_{pe} + c_g V_g + c_w V_w] \frac{\partial P}{\partial t} \tag{2.9}$$

$$-q_t = V_{pe} \left[c_{pe} + c_g \frac{V_g}{V_{pe}} + c_w \frac{V_w}{V_{pe}} \right] \frac{\partial P}{\partial t} \tag{2.10}$$

$$-q_t = V_{pe} [c_{pe} + c_g S_g + c_w S_w] \frac{\partial P}{\partial t} \tag{2.11}$$

Replacing the bracketed terms with an total compressibility term, Eq. 2.11 becomes

$$-q_t = V_{pe} c_t \frac{\partial P}{\partial t} \tag{2.12}$$

Using the pressure and time range for PSS, integrating both sides with respect to time results in

$$-q_t \int_0^t dt = V_{pe} c_t \int_{P_i}^{P_{wf}} dP \tag{2.13}$$

Eq. 2.13 holds under the assumption that the values of effective fracture pore-volume and total compressibility used here are average values representative of the PSS period

$$q_t \times t = V_{pe} \times c_t \times (P_i - P_{wf}) \tag{2.14}$$

$$\frac{P_i - P_{wf}}{q_t} = \frac{1}{V_{pe} c_t} \times t \tag{2.15}$$

The left hand side of Eq. 2.15 is the rate-normalized-pressure (RNP), therefore

$$RNP = \frac{1}{V_{pe} c_t} \times t \tag{2.16}$$

The model relationship shown in Eq. 2.16 is a straight line equation, which must pass through the origin, when RNP is plotted against production time on Cartesian axes. The slope (m) of this line is the inverse of the product of effective fracture pore-volume and total average compressibility as shown in Eq. 2.17.

$$m = \frac{1}{V_{pe} c_t} \tag{2.17}$$

$$\text{For gas wells, } \; c_t = c_{pe} + c_g S_g + c_w S_w \tag{2.18}$$

$$\text{For oil wells, } \; c_t = c_{pe} + c_w \tag{2.19}$$

Eq. 2.16 reveals that the drive mechanisms for flowback during this PSS period are within the total average compressibility term (c_t). The general field observation is that both gas and water are produced during the early flowback period for gas wells, while only water is produced during this same period for oil wells. Therefore the total compressibility term for oil wells (Eq. 2.19) lacks the hydrocarbon term present in the total compressibility term for gas wells (Eq. 2.18).

The total compressibility term in this model can be split into various terms representing flowback drive indices. For a general case, dividing both sides of Eq. 2.18 by the total average compressibility gives,

$$\frac{c_{pe}}{c_t} + \frac{c_g S_g}{c_t} + \frac{c_w S_w}{c_t} = 1 \tag{2.20}$$

$$CDI + HDI + WDI = 1 \tag{2.21}$$

$$CDI + EDI = 1 \tag{2.22}$$

Eq. 2.21 shows three key drive mechanisms in this flowback model namely; compaction drive index (CDI), hydrocarbon drive index (HDI) and water drive index (WDI). As pressure in the fractures fall: CDI, HDI and WDI represents the portion of fluid recovery due to reduction in effective fracture pore-volume, gas or (and) oil expansion, and water expansion respectively. Eq. 2.22 shows that the expansion drive index (EDI = HDI + WDI) is a summation of both hydrocarbon and water drive indices.

In general, the slope of the Cartesian RNP versus time plot can provide estimates of five unknown parameters ($V_{pe}e, c_{pe}, c_g, c_w, S_g/S_w$) for gas wells and three unknown parameters (V_{pe}, c_{pe}, c_w) for oil wells. In practical terms, as more parameters can be estimated from complementary studies (e.g. effective volume from microseismic, compressibility from core or fluid experiments), the less the unknown parameters left to be estimated from the straight line slope.

2.4 Application

The straight line relationship (see Eq. 2.16) for the proposed model is implemented on a monte-carlo spreadsheet. The objective function of this spreadsheet is to minimize the difference between the straight line slope from Cartesian RNP field data plot and that calculated using estimates of unknown reservoir parameters (see Eq. 2.17). Mathematically, the objective function can be expressed as:

$$\left| m - \frac{1}{V_{pe} c_t} \right| \longrightarrow 0 \tag{2.23}$$

The monte-carlo spreadsheet is designed using a combination of generalized reduced gradient (GRG) and evolutionary algorithms. The GRG algorithm traverses the possible search spaces to estimate one possible, optimal combination of unknown parameters that

best satisfies the objective function. Subsequently, the evolutionary algorithm is used to generate the corresponding probability density function (PDF) and cumulative distribution function (CDF) associated with the estimated unknown parameters.

This chapter uses the proposed model to interpret pressure and rate data from three well groups — Group 1 comprises eight Shale gas wells, Group 2 comprises four Shale gas wells, and Group 3 comprises three tight oil wells. Table 2.1 summarizes the completion and geologic data for these well groups.

Table 2.1: Completion and geologic data for the three well groups. Each group is numbered according to flowback sequence. X_e = horizontal well, n_F = fracture stages, n_{CL} = cluster per fracture stage, TIV = Total Injected Volume.

Well	**Formation**	X_e **(m)**	n_F	n_{CL}	**TIV** (m^3)
		Well Group 1			
W_{11}	Muskwa	1400	15	1	69373
W_{12}	Muskwa	1700	17	4	66246
W_{13}	Otter-Park	1900	20	1	75504
W_{14}	Otter-Park	1500	15	4	60590
W_{15}	Muskwa	1500	15	4	53927
W_{16}	Otter-Park	1970	20	4	54217
W_{17}	Otter-Park	1900	20	1	58678
W_{18}	Muskwa	1600	17	1	54217
		Well Group 2			
W_{21}	Muskwa	2008	16	5	56522
W_{22}	Otter-Park	1942	16	5	52968
W_{23}	Muskwa	1855	15	5	50156
W_{24}	Muskwa	1835	15	5	54217
		Well Group 3			
W_{31}	Woodford	1082	12	6	27621
W_{32}	Woodford	1932	14	4	16600
W_{33}	Meramec	2263	49	4	28398

The search spaces (range of values) for unknown parameters used in this chapter are given from Eq. 2.24 to Eq. 2.28; where TIV represents total injected volume of fracturing fluid. The end point values of the search space for effective fracture pore-volume are

chosen to fall within the typical load recovery during flowback and TIV. The end point values of the search spaces for the average gas and average water compressibilities are obtained from the Benedict-Webb-Rubin and Meehan correlations (Fekete, 2014). The end point values of the search space for the average fracture compressibility are obtained from relevant studies done at similar reservoir conditions (Newman, 1973; Sawabini et al., 1973). This average fracture compressibility is a simplistic attempt to account for the spatial and temporal variations in primary (hydraulic) and secondary (reactivated natural and micro) fractures that make up the effective fracture network.

$$20\%\, TIV \leq V_{pe} \leq 100\%\, TIV \tag{2.24}$$

$$c_{g(PSS\ start)} \leq c_g \leq c_{g(PSS\ end)} \tag{2.25}$$

$$c_{w(PSS\ start)} \leq c_w \leq c_{w(PSS\ end)} \tag{2.26}$$

$$0.00001\ psi^{-1} \leq c_{pe} \leq 0.001\ psi^{-1} \tag{2.27}$$

$$0 \leq S_g \leq 0.15 \tag{2.28}$$

The flowback data from these well groups will now be analyzed one after the other using the procedure outlined below:

- Plot RNP (gas rate-normalized pseudo-pressure for gas wells and water rate-normalized-pressure for oil wells) against production time on log-log axes
- Identify the unit slope (PSS flow regime) on this log-log plot of RNP against time
- Plot the unit slope data portion on a Cartesian graph of RNP against time
- Draw a line of best fit which must pass through the origin of this Cartesian plot
- Select the appropriate ranges for the unknown reservoir parameters from complementary studies (e.g. correlations, core analysis etc)
- Input these ranges as the search spaces for the monte-carlo spreadsheet run
- Run the particular test case until the objective function (see Eq. 2.23) is satisfied

- Generate the PDF and CDF for each parameter estimate using the resulting mean and standard deviation values from the monte-carlo spreadsheet run

2.4.1 Well Group 1

This group comprises eight multi-fractured horizontal Shale gas wells completed in the Muskwa and Otter Park members of the Horn River formation respectively. However, only four of these wells show distinct unit slopes of reasonable duration. This is possibly due to data noise issues.

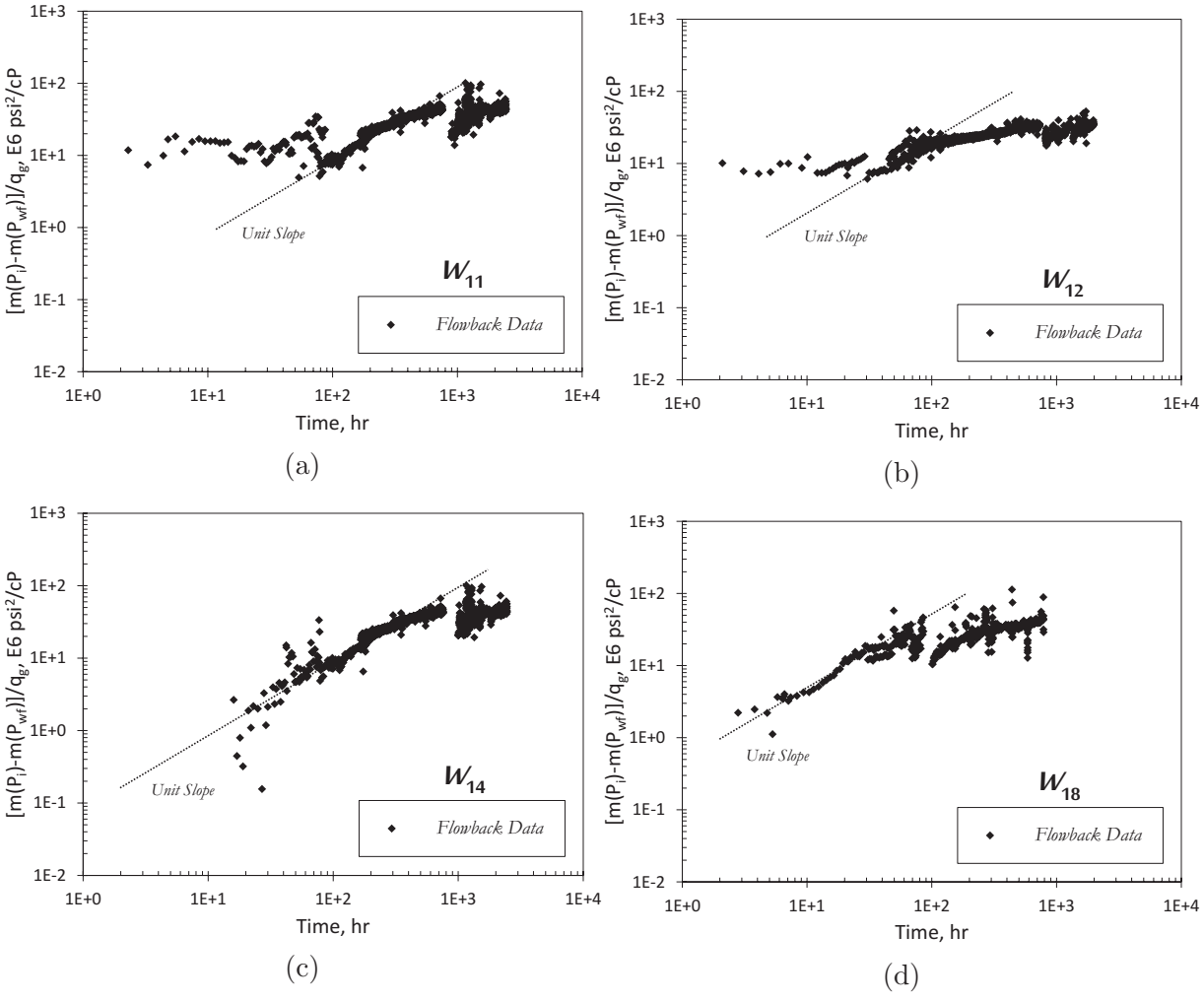

Fig. 2.3: Flowback gas rate-normalized pseudo-pressure plots for well group 1 showing pseudo-steady state flow region (unit slope). The unit of the vertical axis is in per rate.

Fig. 2.3 shows the PSS flow regime (unit slope) from the log-log RNP against produc-

tion time plot. The duration of PSS in some of these wells is less than one log cycle. This could be due to data masking as a result of noise, strong transient flow regime before PSS and quick unblocking of any existing water blocks around the matrix–fracture interface.

Fig. 2.4 shows the Cartesian RNP against production time plot of the unit slope data from Fig. 2.3.

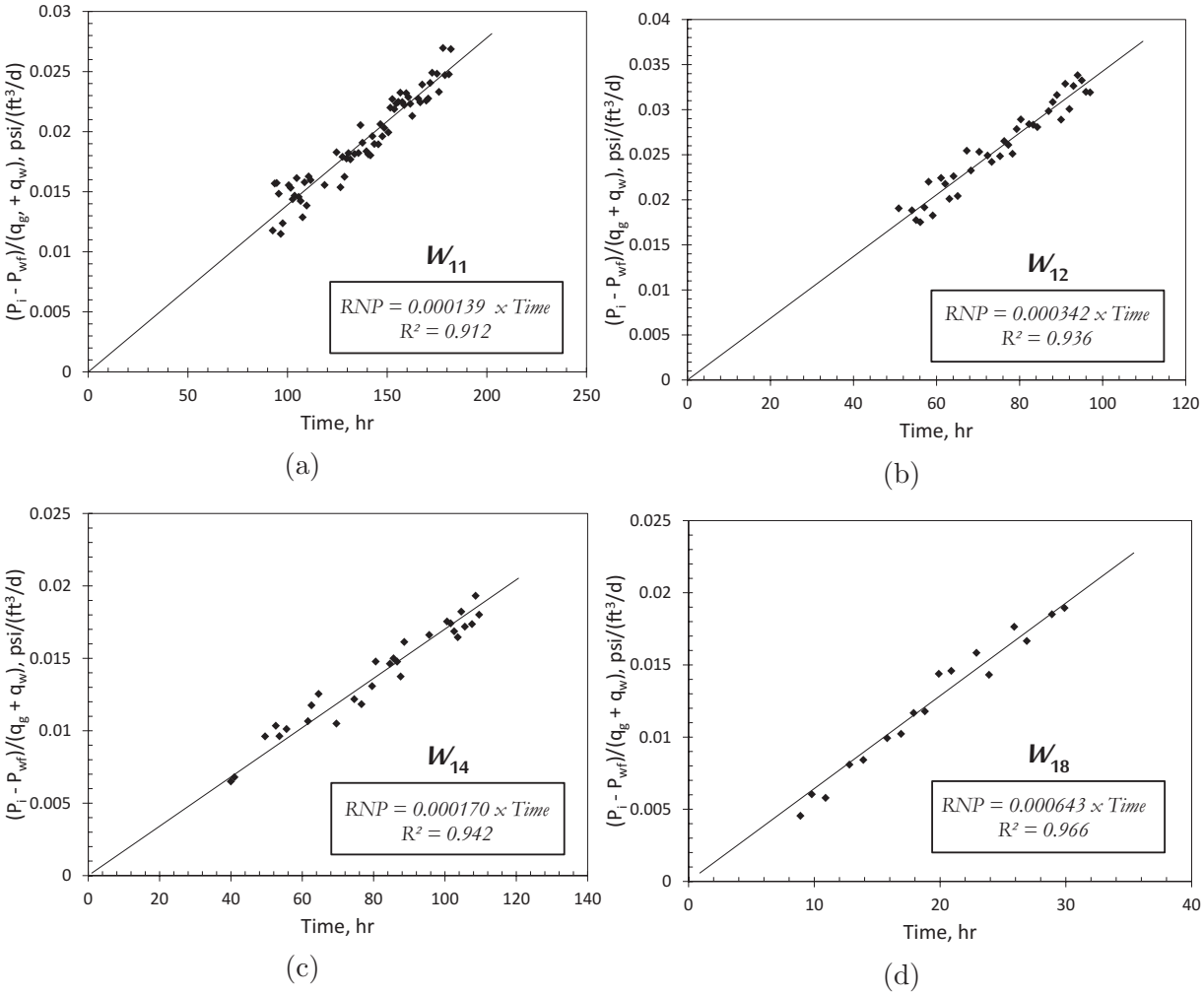

Fig. 2.4: Flowback rate-normalized pressure versus time plots for the pseudo-steady state flow region of well group 1.

The objective functions (see Eq. 2.23) for the wells studied in this group equal zero. Tables 2.2, 2.3 and 2.4 list the optimal values of the effective fracture pore-volume (V_{pe}), average fracture pore-volume compressibility (c_{pe}), average gas compressibility (c_g), average water compressibility (c_w) and average gas saturation (S_g). A continuous normal distribution is used to generate the PDF and CDF using data from Tables 2.2, 2.3 and 2.4. For this well group, only results for well W_{11} are shown in Fig. 2.5 due to space restrictions.

Table 2.2: Estimates of effective fracture pore-volume for well group 1. $S.D$ = Standard Deviation.

Well	Input (psi^{-1})		Guess (psi^{-1})	Optimal (psi^{-1})	Uncertainty (psi^{-1})	
	Min.	Max.			Mean	S.D
W_{11}	13875	69373	41624	43643	43603	15150
W_{12}	13250	66246	39747	35863	39296	14513
W_{14}	12137	60590	36354	42348	35756	13535
W_{18}	10843	57157	32530	47797	25471	10490

Table 2.3: Estimates of average values of fracture, gas and water compressibilities for well group 1. $S.D$ = Standard Deviation.

Well	Input (psi^{-1})		Guess (psi^{-1})	Optimal (psi^{-1})	Uncertainty (psi^{-1})	
	Min.	Max.			Mean	S.D
Average Fracture Compressibility						
W_{11}	1.0×10^{-5}	2.0×10^{-3}	1.0×10^{-3}	1.5×10^{-4}	1.2×10^{-4}	5.3×10^{-5}
W_{12}	1.0×10^{-5}	2.0×10^{-3}	1.0×10^{-3}	5.2×10^{-5}	1.1×10^{-4}	5.4×10^{-5}
W_{14}	1.0×10^{-5}	2.0×10^{-3}	1.0×10^{-3}	1.5×10^{-4}	1.0×10^{-3}	5.6×10^{-4}
W_{18}	1.0×10^{-5}	2.0×10^{-3}	5.1×10^{-4}	2.9×10^{-5}	3.0×10^{-4}	2.2×10^{-4}
Average Gas Compressibility						
W_{11}	2.0×10^{-4}	5.0×10^{-4}	3.5×10^{-4}	3.3×10^{-4}	3.4×10^{-4}	9.0×10^{-5}
W_{12}	2.0×10^{-4}	5.0×10^{-4}	3.5×10^{-4}	3.4×10^{-4}	3.5×10^{-4}	9.0×10^{-5}
W_{14}	2.0×10^{-4}	5.0×10^{-4}	3.5×10^{-4}	3.1×10^{-4}	3.5×10^{-4}	8.0×10^{-5}
W_{18}	2.0×10^{-4}	5.0×10^{-4}	3.5×10^{-4}	2.1×10^{-4}	3.6×10^{-4}	8.0×10^{-5}
Average Water Compressibility						
W_{11}	3.6×10^{-6}	3.9×10^{-6}	3.75×10^{-6}	3.83×10^{-6}	3.8×10^{-6}	8.0×10^{-8}
W_{12}	3.6×10^{-6}	3.9×10^{-6}	3.75×10^{-6}	3.83×10^{-6}	3.8×10^{-6}	8.0×10^{-8}
W_{14}	3.6×10^{-6}	3.9×10^{-6}	3.75×10^{-6}	3.83×10^{-6}	3.8×10^{-6}	8.0×10^{-8}
W_{18}	3.6×10^{-6}	3.9×10^{-6}	3.75×10^{-6}	3.83×10^{-6}	3.8×10^{-6}	7.0×10^{-8}

Table 2.4: Estimates of average gas saturation for well group 1. $S.D$ = Standard Deviation.

Well	**Input** (psi^{-1})		**Guess** (psi^{-1})	**Optimal** (psi^{-1})	**Uncertainty** (psi^{-1})	
	Min.	**Max.**			**Mean**	**S.D**
W_{11}	0	0.15	0.075	0.126	0.075	0.044
W_{12}	0	0.15	0.075	0.119	0.074	0.043
W_{14}	0	0.15	0.075	0.047	0.072	0.043
W_{18}	0	0.15	0.075	0.023	0.071	0.036

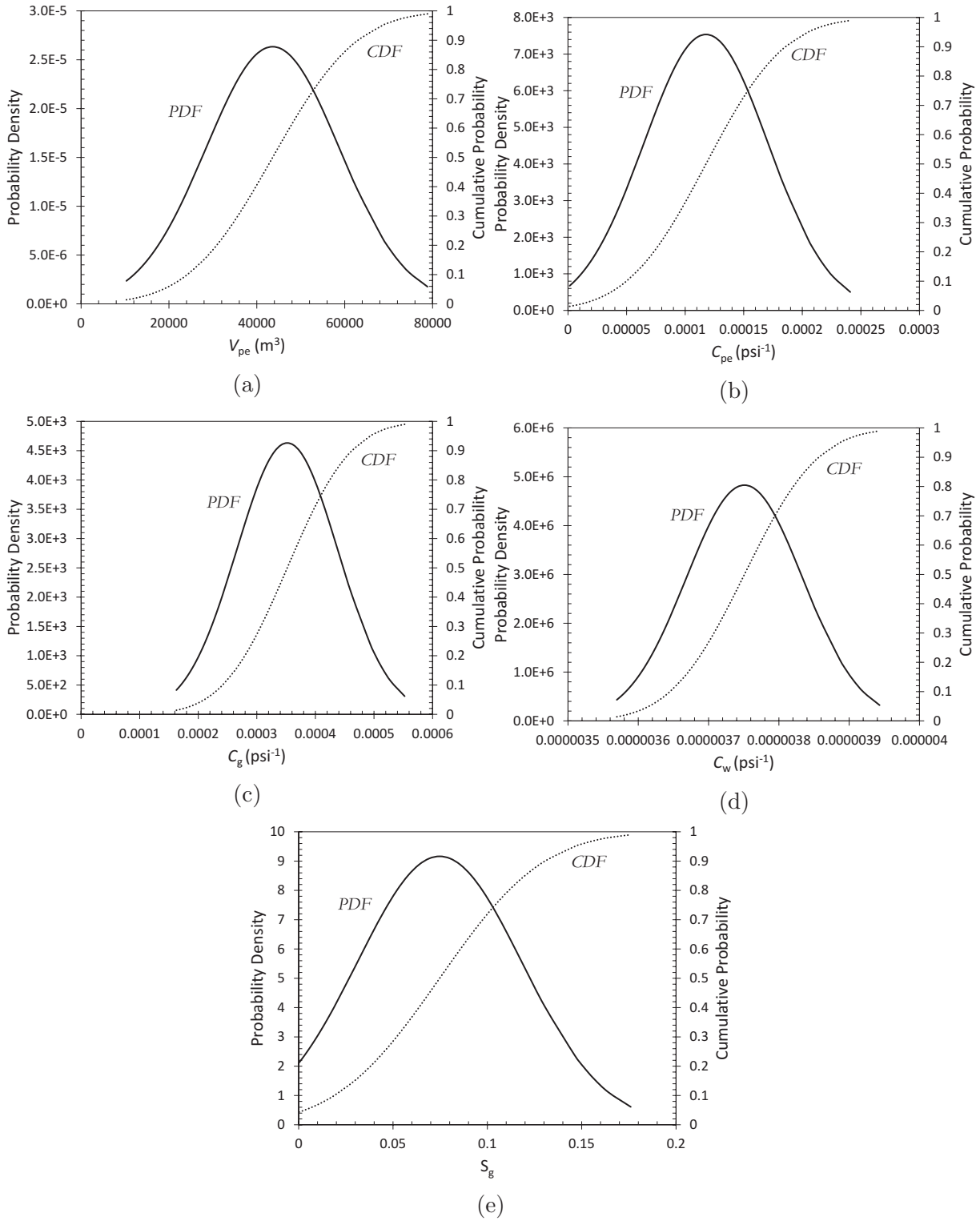

Fig. 2.5: Probability density and cumulative distribution functions (PDF and CDF) of reservoir estimates for well group 1 (W_{11} case study).

2.4.2 Well Group 2

This group comprises four multi-fractured horizontal Shale gas wells completed in the Muskwa and Otter Park members of the Horn River formation respectively. However, only two of these wells show distinct unit slopes of reasonable duration. This is possibly due to data noise issues.

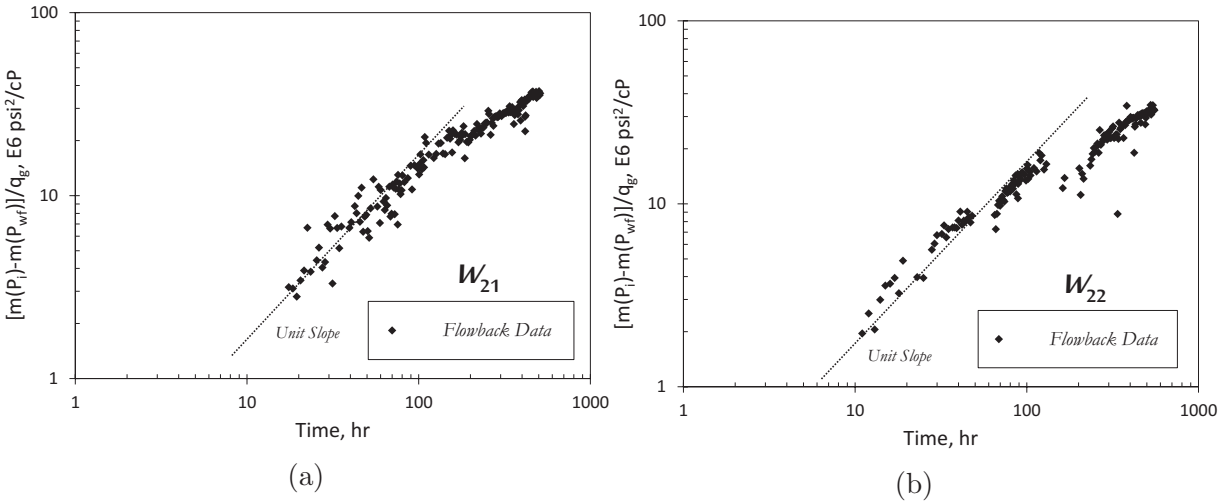

(a) (b)

Fig. 2.6: Flowback gas rate-normalized pseudo-pressure plots for well group 2 showing pseudo-steady state flow region (unit slope). The unit of the vertical axis is in per rate.

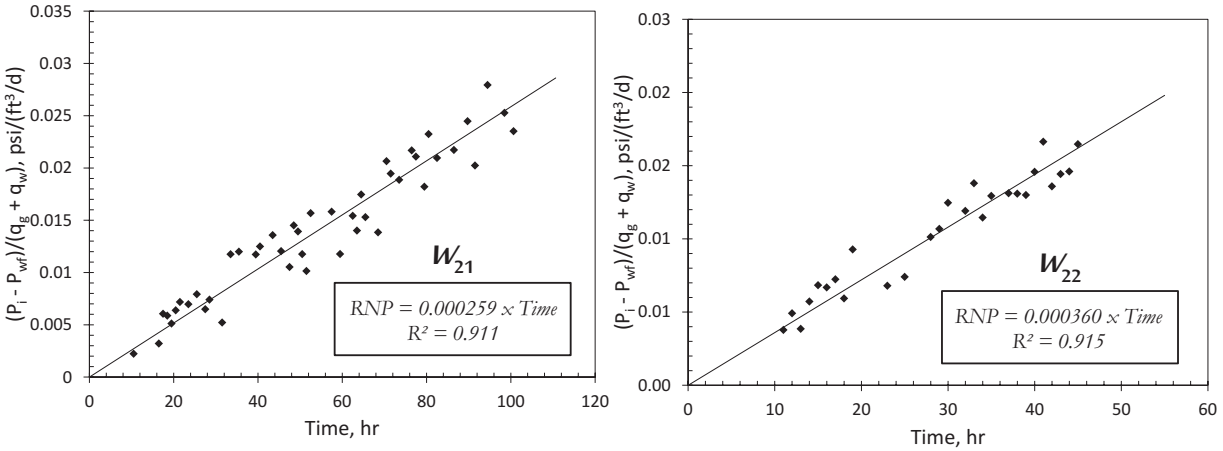

(a) (b)

Fig. 2.7: Flowback rate-normalized pressure versus time plots for the pseudo-steady state flow region of well group 2.

Fig. 2.6 shows the PSS flow regime (unit slope) from the log-log RNP against production time plot. The duration of PSS in some of these wells is less than one log cycle. This

could be due to data masking as a result of noise, strong transient flow regime before PSS and quick unblocking of any existing water blocks around the matrix–fracture interface.

Fig. 2.7 shows the Cartesian RNP against production time plot of the unit slope data from Fig. 2.6.

Table 2.5: Estimates of effective fracture pore-volume for well group 2. $S.D$ = Standard Deviation.

Well	**Input** (psi^{-1})		**Guess** (psi^{-1})	**Optimal** (psi^{-1})	**Uncertainty** (psi^{-1})	
	Min.	**Max.**			**Mean**	**S.D**
W_{21}	11304	56522	33913	39936	35609	12461
W_{22}	10594	52968	31781	43629	33489	8684

Table 2.6: Estimates of average values of fracture, gas and water compressibilities for well group 2. $S.D$ = Standard Deviation.

Well	**Input** (psi^{-1})		**Guess** (psi^{-1})	**Optimal** (psi^{-1})	**Uncertainty** (psi^{-1})	
	Min.	**Max.**			**Mean**	**S.D**
Average Fracture Compressibility						
W_{21}	1.0×10^{-5}	2.0×10^{-3}	1.0×10^{-3}	8.2×10^{-5}	1.1×10^{-4}	5.2×10^{-5}
W_{22}	1.0×10^{-5}	2.0×10^{-3}	1.0×10^{-3}	5.2×10^{-5}	9.4×10^{-5}	3.6×10^{-5}
Average Gas Compressibility						
W_{21}	1.5×10^{-4}	3.0×10^{-4}	2.3×10^{-4}	2.3×10^{-4}	2.3×10^{-4}	4.0×10^{-5}
W_{22}	1.5×10^{-4}	2.0×10^{-4}	1.8×10^{-4}	1.9×10^{-4}	1.8×10^{-4}	1.0×10^{-5}
Average Water Compressibility						
W_{21}	3.5×10^{-6}	3.6×10^{-6}	3.51×10^{-6}	3.53×10^{-6}	3.51×10^{-6}	3.0×10^{-8}
W_{22}	3.7×10^{-6}	3.8×10^{-6}	3.74×10^{-6}	3.73×10^{-6}	3.74×10^{-6}	1.0×10^{-8}

The objective functions (see Eq. 2.23) for the wells studied in this group equal zero. Tables 2.5, 2.6 and 2.7 list the optimal values of V_{pe}, c_{pe}, c_g, c_w and S_g. A continuous normal distribution is used to generate the PDF and CDF using data from Tables 2.5, 2.6

and 2.7. For this well group, only results for well W_{21} are shown in Fig. 2.8 due to space restrictions.

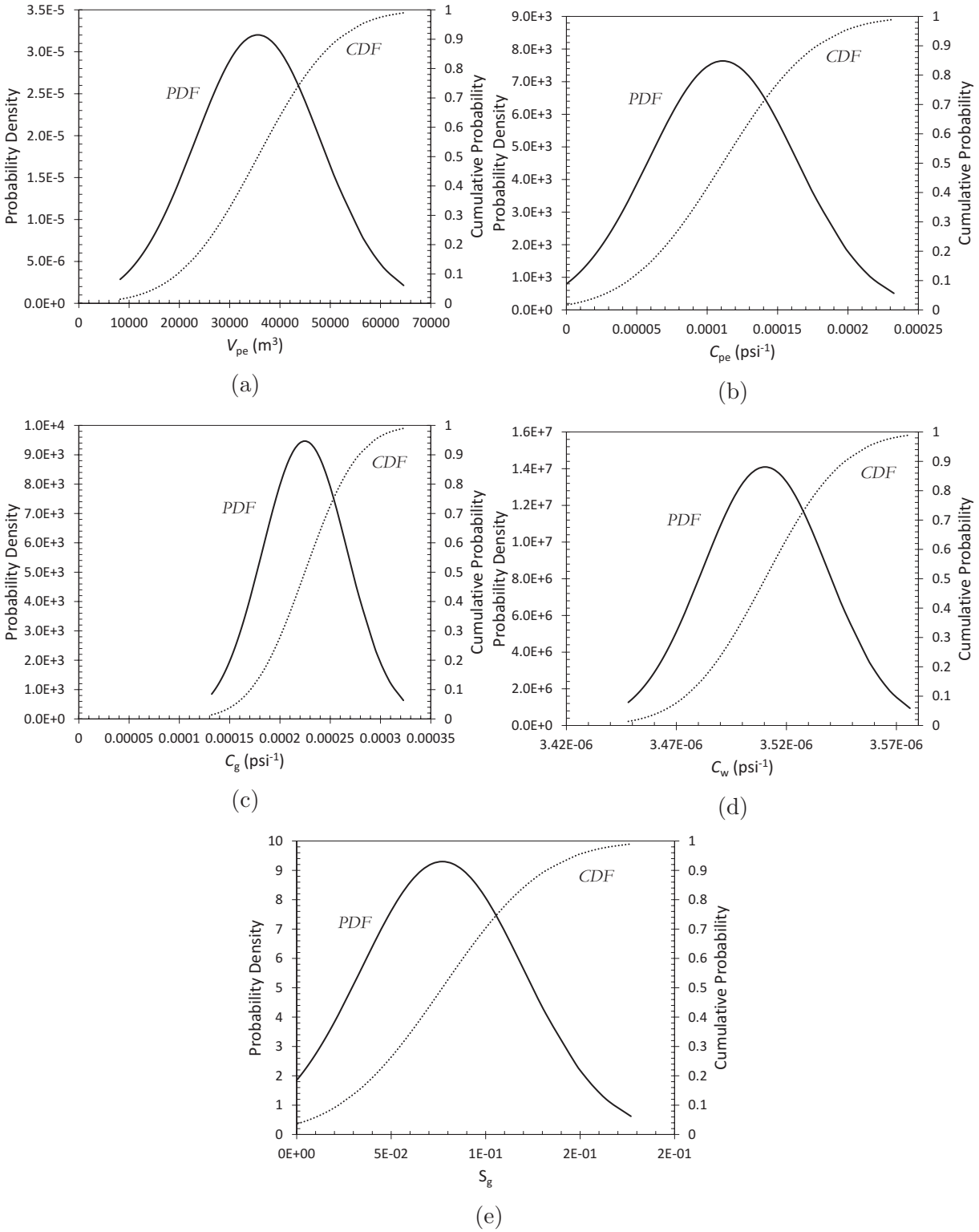

Fig. 2.8: Probability density and cumulative distribution functions (PDF and CDF) of reservoir estimates for well group 2 (W_{21} case study).

Table 2.7: Estimates of average gas saturation for well group 2. $S.D$ = Standard Deviation.

Well	Input (psi^{-1})		Guess (psi^{-1})	Optimal (psi^{-1})	Uncertainty (psi^{-1})	
	Min.	Max.			Mean	S.D
W_{21}	0	0.15	0.075	0.125	0.077	0.042
W_{22}	0	0.15	0.075	0.104	0.081	0.036

2.4.3 Well Group 3

This group comprises three multi-fractured horizontal tight oil wells completed in the Woodford and Meramec Formations of the Anadarko Basin.

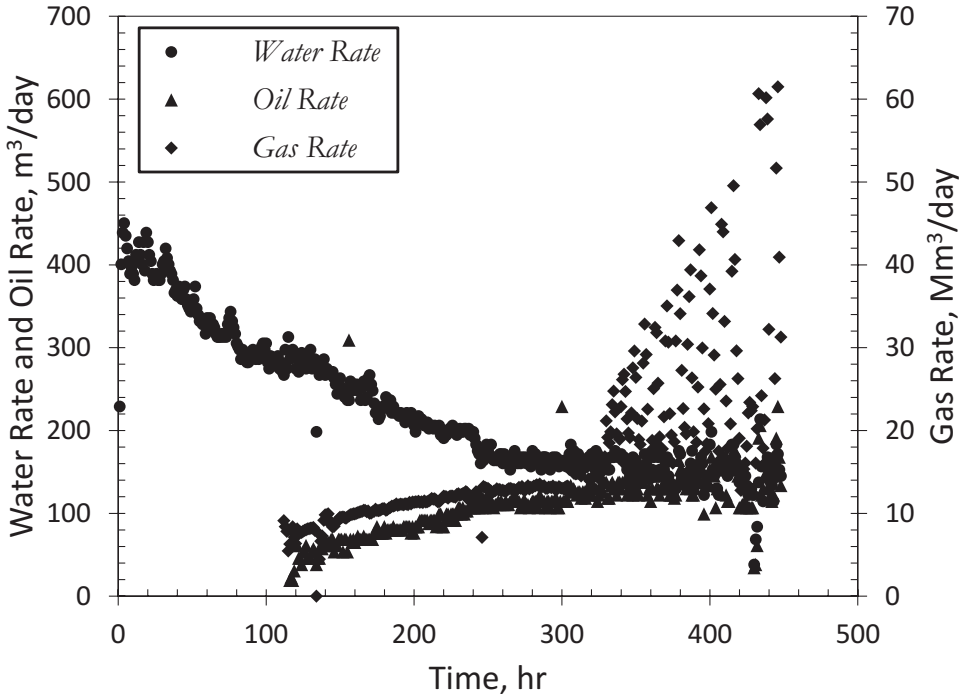

Fig. 2.9: Typical flowback water, gas and oil rate plot for well group 3 (W_{32} case study).

Fig. 2.9 shows typical water, gas and oil flow rate profiles during flowback of this well group. It can be seen that water is the dominant fluid recorded at the surface during the first 100 hours (even though oil and gas might have broken through into the fractures from the matrix). This single phase phenomenon appears unique to well group 3 (tight oil wells) because well groups 1 and 2 (Shale gas wells) show immediate water and gas production at the onset of flowback (see Figs. 2.4 and 2.7).

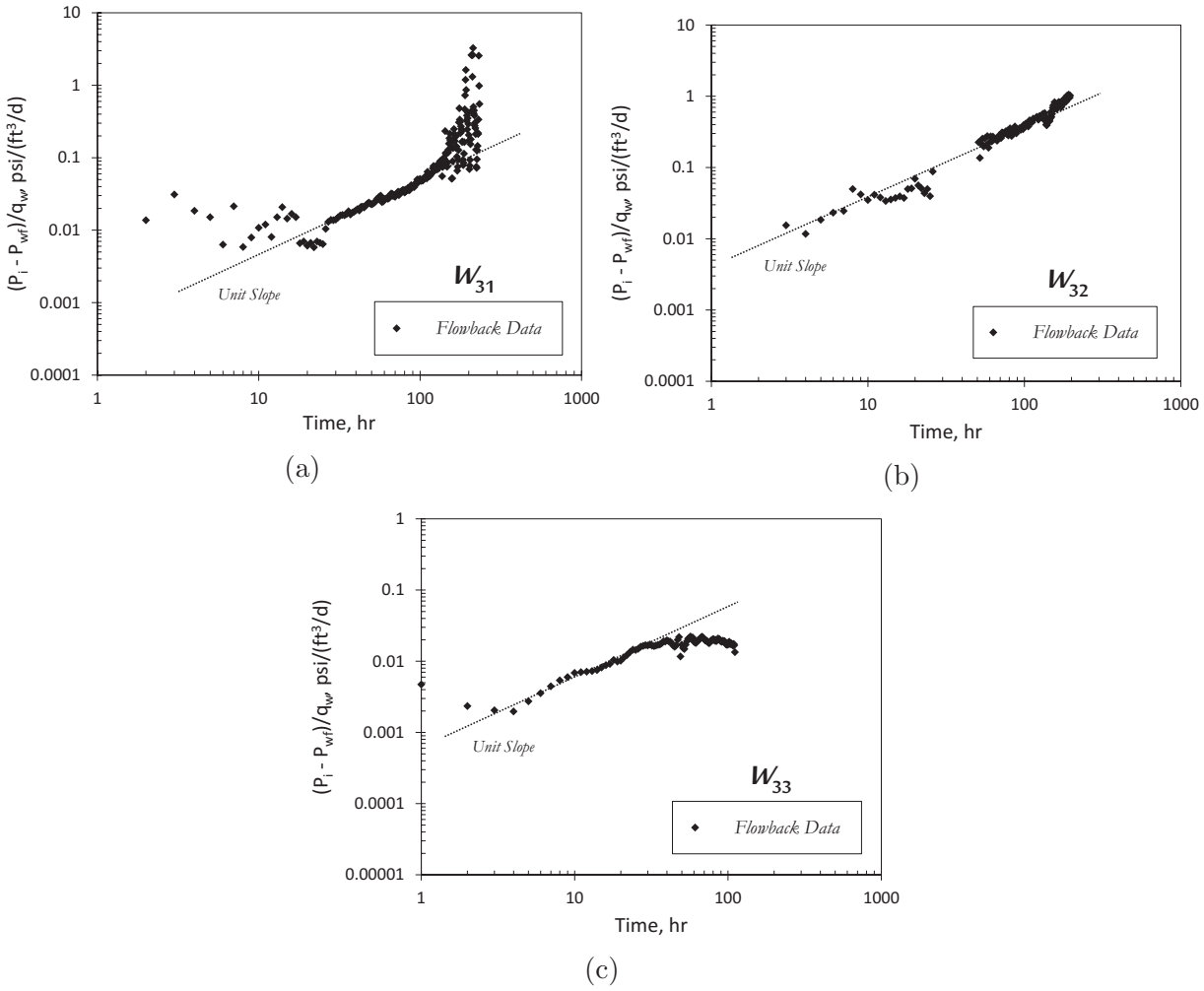

Fig. 2.10: Flowback gas rate-normalized pressure plots for well group 3 showing pseudo-steady state flow region (unit slope).

Fig. 2.10 shows the PSS flow regime (unit slope) from the log-log RNP against production time plot. The duration of PSS in all of these wells is approximately one log cycle. Fig. 2.10 shows the Cartesian plots of the unit slope data from Fig. 2.10. The objective functions (see Eq. 2.23) for all wells in this group equals zero. Tables 2.8 and 2.9 list the optimal values of c_{pe}, c_{pe} and c_w. A continuous normal distribution is used to generate the PDF and CDF using data from Tables 2.8 and 2.9. For this well group, only results for well W_{31} are shown in Fig. 2.12 due to space restrictions.

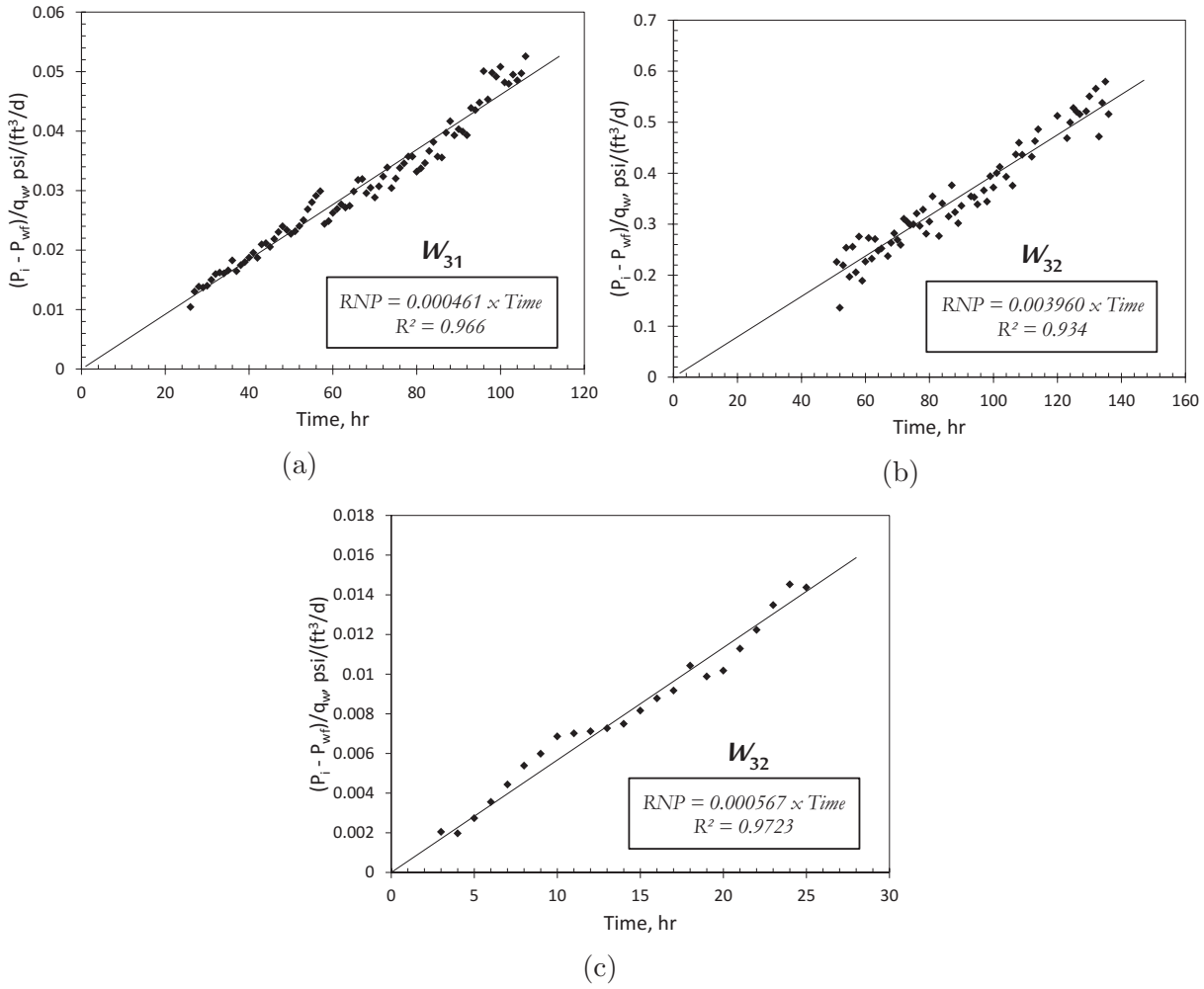

Fig. 2.11: Flowback rate-normalized pressure versus time plots for the pseudo-steady state flow region of well group 3.

Table 2.8: Estimates of effective fracture pore-volume for well group 3. $S.D$ = Standard Deviation.

Well	**Input** (psi^{-1})		**Guess** (psi^{-1})	**Optimal** (psi^{-1})	**Uncertainty** (psi^{-1})	
	Min.	**Max.**			**Mean**	**S.D**
W_{31}	5524	27621	16573	21798	16874	6352
W_{32}	3320	16600	9960	10951	9996	3771
W_{33}	5680	28398	17038	14301	15707	2364

Table 2.9: Estimates of average values of fracture and water compressibilities for well group 3. $S.D$ = Standard Deviation.

Well	**Input** (psi^{-1})		**Guess** (psi^{-1})	**Optimal** (psi^{-1})	**Uncertainty** (psi^{-1})	
	Min.	**Max.**			**Mean**	**S.D**
Average Fracture Compressibility						
W_{31}	1.0×10^{-5}	2.0×10^{-3}	1.0×10^{-3}	1.2×10^{-4}	1.1×10^{-4}	5.4×10^{-5}
W_{32}	1.0×10^{-5}	2.0×10^{-3}	1.0×10^{-3}	1.5×10^{-4}	1.1×10^{-4}	5.4×10^{-5}
W_{33}	1.0×10^{-5}	2.0×10^{-3}	1.0×10^{-3}	1.4×10^{-4}	1.3×10^{-4}	1.8×10^{-5}
Average Water Compressibility						
W_{31}	2.8×10^{-6}	2.9×10^{-6}	2.86×10^{-6}	2.85×10^{-6}	2.86×10^{-6}	1.0×10^{-8}
W_{32}	2.7×10^{-6}	2.8×10^{-6}	2.76×10^{-6}	2.74×10^{-6}	2.75×10^{-6}	1.0×10^{-8}
W_{33}	2.6×10^{-6}	2.7×10^{-6}	2.65×10^{-6}	2.62×10^{-6}	2.64×10^{-6}	2.0×10^{-8}

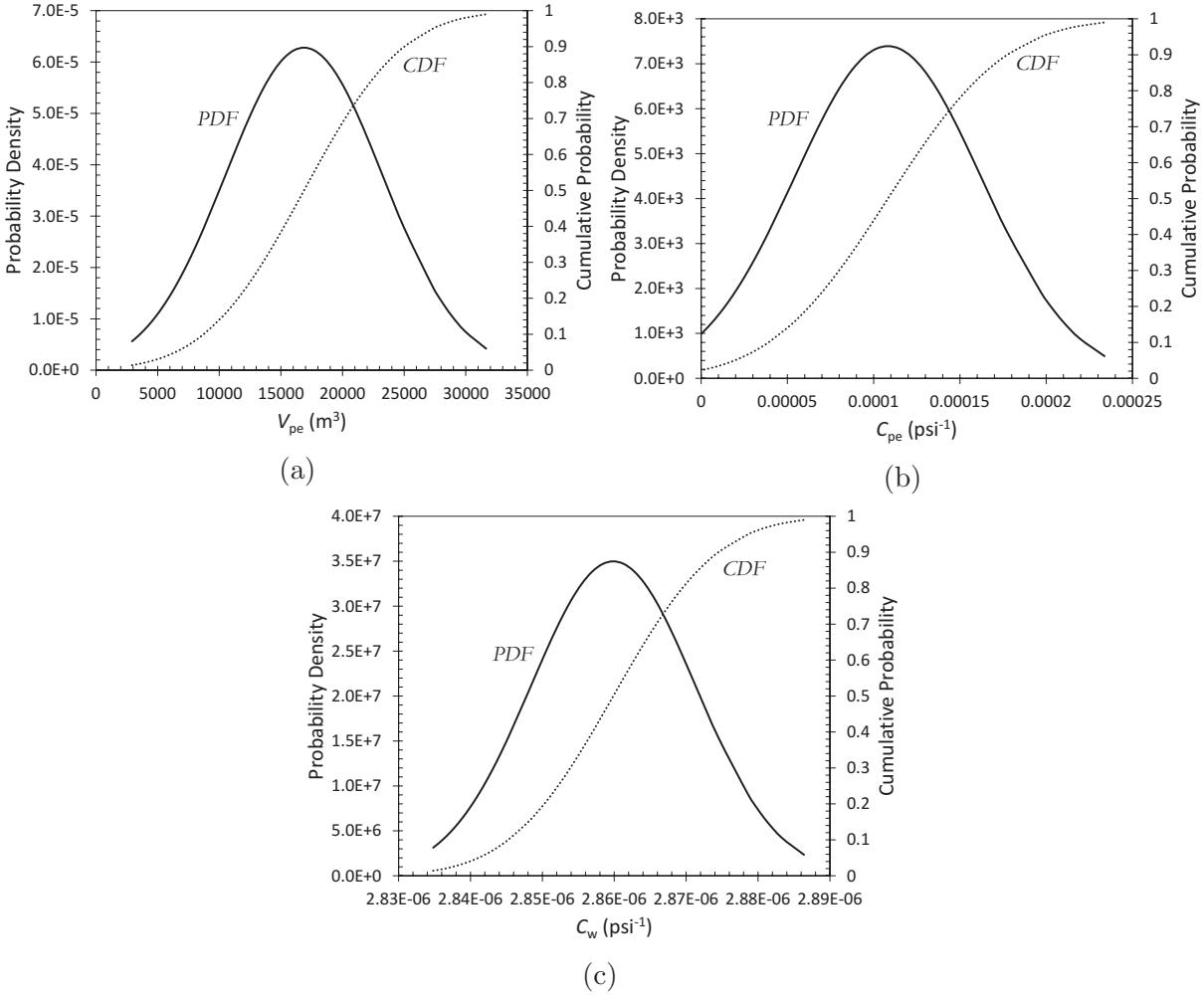

Fig. 2.12: Probability density and cumulative distribution functions (PDF and CDF) of reservoir estimates for well group 3 (W_{31} case study).

2.4.4 Discussions

This part deals with the guidelines for the appropriate application of the proposed model on flowback data. Also, it compares the key flowback drive mechanisms to determine the dominant one(s). Where applicable, the key observations from this chapter will be compared with those from existing models. Alkouh et al. (2014) will be the representative model of comparison here.

2.4.4.1 Appropriate Model Selection

The application of the proposed model should be limited to flowback data which shows PSS (unit slope) depletion during early periods. This is because PSS depletion could also happen during later periods such as post-flowback production (when depletion reaches the stimulated reservoir volume boundaries).

Considering the left hand side of Eq. 2.13, if q_t is included in the integral then Eq. 2.16 will take the form of:

$$P_i - P_{wf} = \frac{1}{V_{pe} c_t} \times N_t \tag{2.29}$$

Further studies should compare the current results which uses Eq. 2.16 against those which will be obtained using Eq. 2.29.

2.4.4.2 Search Space Selection

In this chapter, search space is a combination of the lower limit and upper limit of the unknown reservoir parameter. It determines the duration of model run and uncertainty associated with the output parameter. This uncertainty can be reduced using good engineering judgment. Results from appropriate complementary studies (such as core analysis, micro-seismic etc.) should be used as inputs for some unknown parameters in the proposed model. This will reduce the number of unknown parameters left to be estimated by this model, and the corresponding uncertainty in the parameter estimates. On the other hand, parameter estimates from relevant off-set wells or geologic information should guide the selection of appropriate search space for the remaining unknown parameters. This would help reduce model run time.

The gas compressibility values are obtained from the Benedict-Webb-Rubin and Meehan correlations (Fekete, 2014). The input values for gas compressibility in the analysis correspond to the values at the start and end of the PSS region. Based on the proposed model, what is required for analysis is one single value of average gas compressibility repre-

sentative of the physics in the PSS period. This is the reason average gas compressibility (and not actual gas compressibility) appears as an optimization parameter. Flowback sequence in the well pads considered in this chapter causes a near-order variation in the magnitude of output parameter estimates. Therefore, wells which are flowed back early have slightly different output parameters (due to higher reservoir and down-hole pressures respectively) from the wells flowed back later in the pad sequence.

2.4.4.3 Parameter Uncertainty Interpretation

For the purpose of this chapter, all the PDFs and CDFs are generated under the assumption that the output parameters follow a normal distribution. However, an appropriate distribution (Williams-Kovacs and Clarkson, 2013a; Virués et al., 2013) should be selected for each output parameter based on relevant play or field background information. Caution should be exercised when using the PDF and CDF from the proposed model as input guides in complex studies (e.g. numerical flow simulation, fracture network modeling). For example, using a fracture compressibility corresponding to a 90% cumulative probability (P90) as input in a subsequent monte-carlo run will not necessarily produce an effective pore-volume with the same cumulative probability from a previous run. Therefore, parameter values from test runs which satisfy the objective function should be used as groups rather than as individual values.

2.4.4.4 Initial Fracture Saturation and Ultimate Load Recovery

At the start of flowback, all Shale gas wells (well groups 1 and 2) in this chapter show immediate gas and water production, while the tight oil wells (well group 3) show single phase water production. Therefore, the fractures connected to the Shale gas wells appear to be initially saturated with gas and water before flowback; while the tight oil wells are initially saturated with water (and negligible oil). This can be attributed to differences in the mobility ratio between water–oil and water–gas which favors single-phase water production in tight oil wells as flowback starts.

$$S_{gi} = \frac{N_{p(before\ PSS)}}{V_{pe}} + S_{g(during\ PSS)} \tag{2.30}$$

$$ULR = \frac{N_{p(before\ PSS)} + S_{w(during\ PSS)} \times V_{pe}}{TIV} \tag{2.31}$$

Eq. 2.30 estimates the initial gas saturation in the effective fractures. Eq. 2.31 estimates the ultimate load recovery (ULR) for wells with negligible formation water production.

Eqs. 2.30 and 2.31 assumes that the all fluid production before PSS is from the effective fracture volume.

Table 2.10: Estimates of initial fluid saturations in the effective fractures and ultimate load recovery (ULR) for all well groups.

Well Group	Well Name	S_{gi}	S_{oi}	S_{wi}	ULR, %
1	W_{11}	0.21	0	0.79	56
	W_{12}	0.21	0	0.79	48
	W_{14}	0.09	0	0.91	67
	W_{18}	0.21	0	0.79	48
2	W_{21}	0.13	0	0.87	62
	W_{22}	0.11	0	0.89	74
3	W_{31}	0	0	1	79
	W_{32}	0	0	1	66
	W_{33}	0	0	1	50

Table 2.10 summarizes the estimates of initial fluid saturations and ULR from the effective fractures connected to the wells. It shows that the initial hydrocarbon saturation ($S_{gi}+S_{oi}$) for fractured Shale gas wells can be significant, but negligible for fractured tight oil wells.

The actual load recovery (LR, is usually less than 30% within the first year of production) for these wells change with time, as water production increases; therefore it might differ from the ultimate load recovery from the connected fractures. This means that after LR equals ULR, subsequent water production might be coming from sources (e.g. formation water from matrix) outside the effective fracture volume.

2.4.4.5 Pore-Volume Differentiation

Differentiating between the volumes of secondary fractures from that of hydraulic fractures can be done by (i) comparing effective fracture pore-volume estimates from the present study with equivalent hydraulic fracture pore-volume calculated from half-length estimates (Ezulike and Dehghanpour, 2014c, 2015) and (ii) analyzing flowback chemical data (Zolfaghari et al., 2016).

However, it is important to note that one key source of uncertainty in the effective pore-volume estimates would be from the compressibility calculations; since both unpropped secondary fractures and propped hydraulic fractures are treated as single porous medium in this chapter.

2.4.4.6 Key Flowback Mechanisms

This part summarizes and compares the key flowback drive mechanisms (see Eqs. 2.20, 2.21 and 2.22) for the Shale gas and tight oil wells studied in this chapter. Table 2.11 shows that fracture pore-volume closure (CDI) is the primary flowback drive for all well groups. Although gas expansion (HDI) is the secondary drive mechanism for Shale gas wells during flowback, water expansion (WDI) is the secondary drive mechanism for tight oil wells. The tight oil wells experience negligible hydrocarbon expansion (HDI) during flowback. This is because oil in the reservoir matrix has lower mobility compared to gas, and there is negligible oil saturation in the fractures after hydraulic fracturing and before flowback. Therefore, oil needs more time (which might come after the PSS region) before it is able to break into the fractures.

Table 2.11: Flowback drive indices for all well groups. HDI = Hydrocarbon Drive Index and WDI = Water Drive Index.

Well Group	Well Name	Expansion Drive Index		Compaction Drive Index
		HDI	WDI	
1	W_{11}	0.21	0.02	0.77
	W_{12}	0.42	0.04	0.54
	W_{14}	0.09	0.02	0.89
	W_{18}	0.12	0.10	0.78
2	W_{21}	0.26	0.03	0.71
	W_{22}	0.26	0.04	0.70
3	W_{31}	0	0.02	0.98
	W_{32}	0	0.02	0.98
	W_{33}	0	0.02	0.98

Fig. 2.13 compares three flowback drive indices for the three well groups. The CDI

versus EDI plot shows an inverse linear trend, since CDI = 1 − EDI (see Eq. 2.22). It also falls into the top left hand quadrant, meaning that CDI is the main drive mechanism during early flowback periods (about 100 hours) for both the Shale gas and tight oil wells. This disagrees with the simulation observations of dominant gas drive mechanism in Alkouh et al. (2014). This is because the simulation case used an average "formation compressibility" for both matrix and fracture cells — which holds in cases where actual matrix, gas and fracture compressibilities are of the same magnitude. However, matrix compressibility is usually one to two orders of magnitude less than fracture compressibility (Newman, 1973; Sawabini et al., 1973). Therefore, the scenario presented in Alkouh et al. (2014) is justifiable at lower pressures (less than or equal to the pressure at the end of the PSS flow region) when the product of average gas saturation and average gas compressibility in fractures is higher than average fracture compressibility. Therefore, the use of non-representative fluid and rock compressibility values can underestimate the contribution of the fracture compressibility term during flowback.

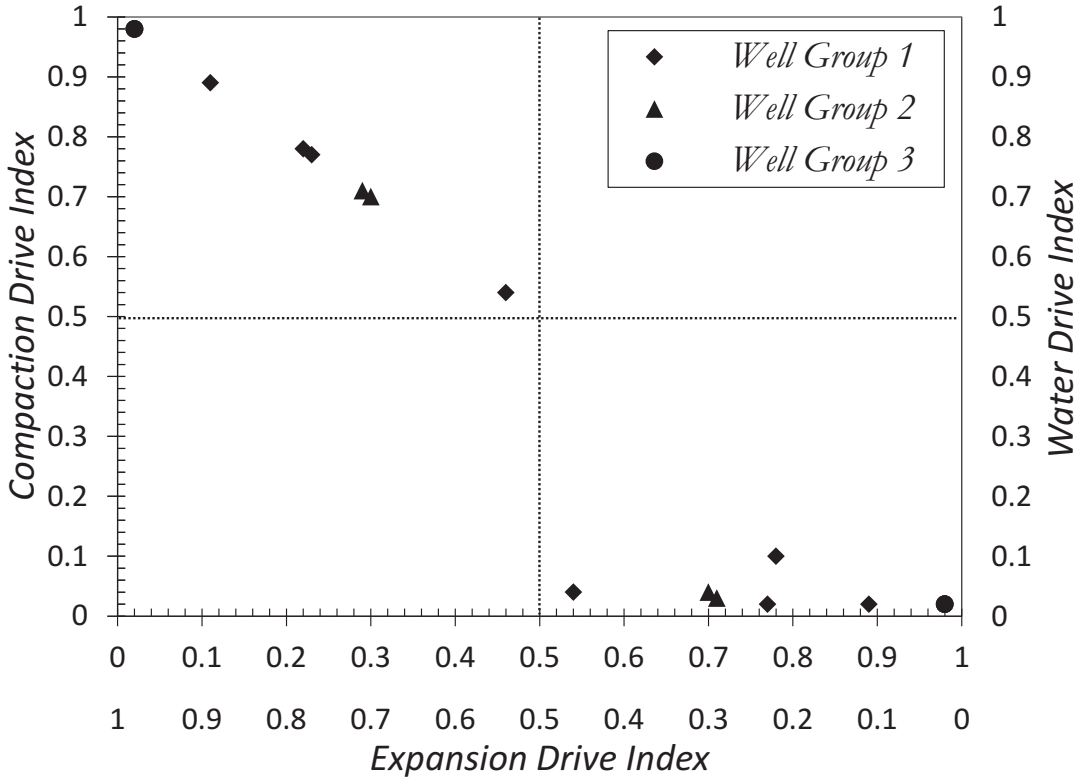

Fig. 2.13: Crossplot of key flowback drive mechanisms for Shale gas (groups 1 and 2) and tight oil wells (group 3). The left vertical axis and upper horizontal axis form the primary axes, and vice versa. The dotted lines divides the plot into four equal quadrants.

The WDI versus EDI plot shows an almost flat profile. It also falls into the bottom right

hand quadrant, which means that water expansion plays a secondary role (see Eqs. 2.21 and 2.22) during flowback, when compared with hydrocarbon expansion. This agrees with the work of Alkouh et al. (2014).

The Shale gas wells (groups 1 and 2) have a broad range of CDI and EDI values. This is mainly due to differences in the values of three key parameters namely; average gas saturation in fracture network, average gas compressibility and average fracture pore-volume compressibility (see Eq. 2.18). Water compressibility is usually orders of magnitutde less than the other compressibilities; hence it plays a negligible role in the flowback of the Shale gas wells. This agrees with the work of Alkouh et al. (2014). Among all well groups, the tight oil wells (group 3) show the highest CDI values and lowest EDI values, determined primarily by the magnitude of fracture pore-volume compressibility. This is because of the absence of hydrocarbon in the fractures during this flowback period (see Eq. 2.20) and a negligible water contribution (WDI = 0.02).

The results suggest that flowback is controlled by the total effective compressibility and not just gas and oil compressibility. The ratio of the effects of fracture closure to those of fluid expansion is between 1 and 10 for Shale gas wells and greater than 45 for tight oil wells. This ratio should increase as hydrocarbon API gravity decreases (less light hydrocarbon components to aid fluid expansion), as fracture proppant density (amount of proppant in a typical fracturing treatment) decreases and as formation in-situ stress increases (high tendency of fracture proppants being compacted). At high reservoir pressures, the fluid expansion plays a secondary role in flowback compared with fracture pore-volume closure. However, as fracture depletion continues and reservoir pressure falls, the fluid (especially gas) compressibility becomes the primary production mechanism. This is because gas compressibility rapidly increases as reservoir pressure decreases.

2.4.4.7 Impact of Control Variables

Although the tight oil and Shale gas wells evaluated in this chapter have slightly different completion parameters (see Table 2.1), the number of wells suitable for analysis were only nine in number (see Table 2.11). This made it unreasonable to do a comparative analysis of the impact of control variables such as fracture treatment type or volume, completion design and reservoir properties. However, a detailed study of control variables using data mining technologies on a large database of flowback data is presented in Zhou et al. (2016).

2.5 Summary

This chapter proposes a two-phase flowback tank model for reducing uncertainty in fracture parameter estimates and calculating fracture pore-volume independent of its geometry. The "*pressure supercharge*" effect in fractures form the basis for developing this model. The implementation of this tank model on a simple monte-carlo spreadsheet is used for parameter estimation and uncertainty analysis. Application of the proposed tank model to flowback data from Shale gas and tight oil wells estimates the effective pore-volume and initial average fluid saturation in the active fractures using probabilistic distributions of their average compressibility, and average fluid saturations respectively. Also, it investigates the effects of key drive mechanisms (i.e. fracture closure, gas expansion and water depletion) on flowback.

The results suggest that flowback is controlled by the total effective compressibility and not just gas and oil compressibility. It also shows that the effective fracture pore-volume is most sensitive to fracture pore-volume compressibility. Therefore fracture closure is the dominant flowback mechanism (compared to fluid expansion) for all wells in this study. The ratio of the effects of fracture closure to those of fluid expansion is between 1 and 10 for Shale gas wells and greater than 45 for tight oil wells. This ratio should increase as hydrocarbon API gravity decreases, as fracture proppant density (amount of proppant in a typical fracturing treatment) decreases and as formation in-situ stress increases. Hence, fracture volume closure (pore-volume compressibility in this study) which plays an important role during early flowback depletion, should not be neglected in modeling flowback data. However, fluid (especially gas) compressibility becomes the primary production mechanism reservoir pressure falls. Parameter estimates (using representative input guesses) from the proposed model could serve as input guides for advanced studies (such as discrete fracture network modeling and transient flowback simulation). This reduces the number of unknown parameters and uncertainty in output results from complex models.

Comparative analysis shows that flowback data from tight oil wells show clear single-phase water depletion during early time periods (about 100 hours) while Shale gas wells show immediate gas and water production.

Nomenclature

Symbols

c	Compressibility, Lt^2M^{-1}, atm^{-1}, [Pa^{-1}, psi^{-1}].
q	Rate, L^3t^{-1}, $m^3.s^{-1}$, [$rb.day^{-1}$].
t	Time, t, s, [hr, day].
L	Distance or length, L, m, [ft].
N	Cumulative production, L^3, m^3, [ft^3].
P	Pressure, $ML^{-1}t^{-2}$, Pa, [psi].
S	Average Saturation, dimensionless.
V	Volume, L^3, m^3, [ft^3].
ρ	Density, ML^{-3}, $kg.m^{-3}$, [$lb.ft^{-3}$].
CDI	Compaction drive index, dimensionless.
EDI	Expansion drive index, dimensionless.
HDI	Hydrocarbon drive index, dimensionless.
WDI	Water drive index, dimensionless.

Subscripts

$_e$	Equivalent or effective.
$_g$	Gas.
$_i$	Initial.
$_o$	Oil.
$_p$	Pore.
$_t$	Total.
$_w$	Water.
$_{wf}$	Bottom-hole flowing.

Chapter 3

Understanding Flowback as a Transient Two-phase Depletion Process

3.1 Introduction

Unconventional (very-low permeability) reservoirs have emerged as a major source of hydrocarbon to supplement the decreasing supply from conventional reservoirs and meet the increasing energy demand of the world (Zahid et al., 2007; Clarkson and Pederson, 2010; Abdelaziz et al., 2011). The economic production of these unconventional reservoirs has been made possible by the combination of horizontal drilling and hydraulic-fracturing techniques.

Multi-stage hydraulic fracturing (Cheng, 2012) involves the injection of millions of gallons of fracturing fluid through a horizontal well to create multiple fractures. These fractures significantly increase the contact area between the well and reservoir. The fracturing fluid pumped through the well into the rock matrix needs to be recovered before placing the stimulated well on production. Hence, flowback is done after hydraulic fracturing operations to clean (get rid of the injected fluid as much as possible) and prepare the fractured horizontal well for a long-term hydrocarbon production (Crafton and Gunderson, 2007).

Careful management of flowback operations is crucial to obtain accurate physical and chemical data measurements, prevent damage to the stimulated well (Crafton, 2008, 2010), improve well clean-up and maximize load recovery (Crafton, 1998). Accurate data measurement during flowback ensures representative volumetric, transient rate/pressure, and chemical (tracer) analyses. These analyses provide key reservoir parameters (Crafton and Gunderson, 2006, 2007), load recovery estimates (the fraction of total injected fracturing fluid still left in the reservoir), an efficient means (Asadi et al., 2008; Sullivan et al., 2004; Willberg et al., 1998; Woodroof et al., 2003; Ghanbari et al., 2013) of differentiating formation water from flowback water (injected + formation water), an optimal fracture clean-up

or load recovery workflow, and indicators of post-flowback well performance (Clarkson, 2012).

Developing an appropriate model for analyzing the rate and pressure data measured during flowback operations requires a proper review of the static framework and flow physics of existing models for unconventional reservoirs. The number of distinct porous regions in a reservoir determines the appropriate conceptual model for simulating fluid flow through it. Examples of these models for single-phase flow in unconventional reservoirs include the radial dual-porosity models (Carlson and Mercer, 1991), linear dual-porosity models (El-Banbi, 1998; Bello, 2009), radial triple-porosity models (Ozkan et al., 2010; Dehghanpour and Shirdel, 2011), linear triple-porosity models (Al-Ahmadi, 2010; Al-Ahmadi and Wattenbarger, 2011; Ali et al., 2013), trilinear flow model (Brown et al., 2011) and quadrilinear flow model (Ezulike, 2013; Ezulike and Dehghanpour, 2014a, 2016a).

Flowback is a process involving rapid saturation changes of fluids with time. Hence, the main challenge of using the existing unconventional reservoir models for flowback data analysis is their inability to handle transient multiphase fluid flow. Similarly, existing models (Martin, 1959; Al-Khalifa et al., 1987, 1989) for analyzing multiphase data from conventional solution-gas drive and high water-saturation reservoirs cannot be applied to flowback data because of the: assumption of radial flow, constant average phase saturation with time, and constant terminal rate or pressure well constraint (Kamal and Pan, 2010); absence of hydraulic fractures (HF) or micro-fractures (MF); challenge of expressing relative permeability as an implicit (not explicit) function of saturation and pressure (Raghavan, 1976); and difficulty in calculating the pseudo-pressure integral (Chu et al., 1992). The application and drawbacks of these methods are discussed below.

Among the existing flowback chemical analysis models (Asadi et al., 2008; Sullivan et al., 2004; Willberg et al., 1998; Woodroof et al., 2003), Gdanski et al. (2007) was one of the few to add a chemistry layer on a 2-D numerical simulator to account for the movement of soluble chemical components (e.g. sodium, potassium, and chloride) during shut-in and production periods. This simulator was used to history-match the ionic composition (e.g. salt concentration) of flowback fluid. Gdanski et al. (2007) concluded that deviation of simulation results from the observed flowback profiles indicates the need for an improved understanding of fluid chemistry and flow physics.

Ilk et al. (2010) proposed a comprehensive workflow for analyzing flowback data using various diagnostic plots to correlate different data types from one well, correlate the same data type from multiple wells, and guide model-driven analysis. Abbasi (2013) applied similar diagnostic plots to analyze flowback data from several gas wells completed in the Horn River Basin.

Crafton (1997, 1998) analyzed flowback rate and pressure data from stimulated vertical gas and oil wells using a modified reciprocal-productivity-index (RPI) method for conventional reservoirs. The drawbacks of the RPI method include the assumption of single-phase flow in homogeneous (conventional) reservoirs and restriction to stimulated vertical wells (not horizontal wells). Recently, two rate transient models (linear + radial) were proposed (Abbasi, 2013; Abbasi et al., 2014) to analyze the early-time portion of flowback data and estimate lumped fracture parameters (e.g. porosity and permeability). Similarly, Clarkson (2012) applied a modified two-phase, coal-bed-methane tank model (Clarkson and McGovern, 2005) on the pseudo-steady state portion of flowback data to estimate fracture permeability and half-length. One limitation of these models (Abbasi (2013); Abbasi et al. (2014); Clarkson (2012)) is the assumption of pseudo-steady fluid depletion in HF which restricts their application to the short fracture-storage period during flowback.

The existing methods for flowback analysis discussed so far have several limitations — the main one being their inability to properly capture the transient multiphase saturation changes in the HF. Hence, we propose a flowback analysis model (FAM) to address some of these limitations. The challenges for developing FAM include finding an explicit relationship between relative-permeability and pressure/time that captures the rapidly changing fluid-phase saturations in HF and incorporating this relationship into the existing model framework (dual- or triple-porosity) for unconventional reservoirs.

In this chapter, we develop FAM by applying the concept of dynamic-relative-permeability (DRP) on the existing linear dual-porosity model (DPM) for production data analysis (Bello, 2009). DRP allows the extension of DPM to FAM by relaxing the restrictive single-phase fluid flow assumption to account for transient two-phase (water + hydrocarbon) clean-up action in the HF during flowback. This is achieved in 3 steps — model development, validation and application. Step 1 derives flow equations which govern transient two-phase (water + hydrocarbon) clean-up of HF during flowback, solves the flow equations using Laplace transforms under variable bottom-hole pressure and rate well constraints, generates type-curves by numerically inverting the Laplace-space solutions to real time, validates the concept of DRP using synthetic data from a commercial simulator. Step 2 tests FAM's convergence to the existing DPM and analyzes its sensitivity to key flowback parameters using type-curves. Step 3 proposes an integrated workflow to analyze flowback rate + pressure data, estimate key reservoir parameters (e.g. effective HF half-length and pore-volume), evaluate flowback performance (e.g. percentage of injected fluid left in HF and matrix respectively) and forecast hydrocarbon recovery.

3.2 Methodology

The methodology used in this chapter includes describing the flowback physics, conceptual "static" framework, governing fluid flow equations and procedure for solving the flow equations.

3.2.1 Flowback Physics

This part uses transient rate and pressure (qualitative and quantitative) studies and existing experimental (imbibition and drainage) data to describe the physics of flowback.

Diagnostic plots of flowback (water, oil and gas) rates reveal three general flow regions: regions 1, 2 and 3 (Abbasi et al., 2014). These flow regions demarcate the i) pre-breakthrough period — when HF are filled with only single-phase fracturing water (for oil wells) or two-phase fluid (water + initial gas released during soaking period before flowback), ii) post-breakthrough period — when hydrocarbon influx from matrix to HF starts, when the relative-permeability of hydrocarbon increases and that of water decreases respectively in HF, and iii) stabilization period — when the relative-permeability of hydrocarbon and water in HF approaches constant maximum and minimum values respectively. The occurrence of "single-phase" region 1 for gas wells is rare even if the wells are flowed back immediately after fracturing. This might be due to the channeling or fingering of gas through water and spontaneous imbibition during soaking period (Abbasi, 2013; Dehghanpour et al., 2012, 2013; Parmar et al., 2012, 2014; Makhanov et al., 2014).

The ongoing discussion reveals that flowback is a multiphase process which involves changing fluid saturations and relative permeability values in the HF. Williams-Kovacs and Clarkson (2013b) proposed a method for capturing transient relative permeability (k_r) for flowback data analysis using the concept of fractional flow theory and corey-style k_r model. However, they did not provide a procedure for incorporating this time dependent k_r into a reservoir model (e.g. dual- or triple-porosity).

Hence, this chapter presents a parametric form of the dynamic-relative-permeability (DRP) as a function of time and cumulative production using a data-driven-analysis of flowback data. DRP simply means relative permeability expressed as a function of time; it does not mean that the relative permeability curve(s) itself for each reservoir case would change with time. Also, this chapter couples DRP with the existing DPM for transient pressure, rate and saturation analysis. The concept of DRP (k_r as an explicit function of time) exploited in this study is analogous to the pressure-dependent effective permeability (Chin et al., 2000; Chacon and Djebbar, 2007; Cho et al., 2013) concept used to model stress-sensitive (conventional, naturally-fractured and tight gas) reservoirs.

3.2.2 Conceptual Model

The conceptual static framework for the proposed model (FAM) is the DPM (Bello, 2009). Fig. 3.1a shows hydraulic fractures (HF) in a given stimulated reservoir volume (SRV). Fig. 3.1b is an idealized static framework of the proposed FAM used to develop fluid flow equations. HF shown in Fig. 3.1a are modeled as straight porous units in Fig. 3.1b. The inset in Fig. 3.1b shows the depletion path from matrix into hydraulic fracture (HF). The proposed model assumes that the SRV after multi-stage hydraulic fracturing can be approximated as a continuum of two contiguous porous media (see Fig. 3.1):

1. Hydraulic fractures denoted by F with maximum permeability.

2. Matrix blocks denoted by m with minimum permeability.

In Fig. 3.1, y_e is the half-length of HF, L_F is the spacing between consecutive HF and X_e is the horizontal well length.

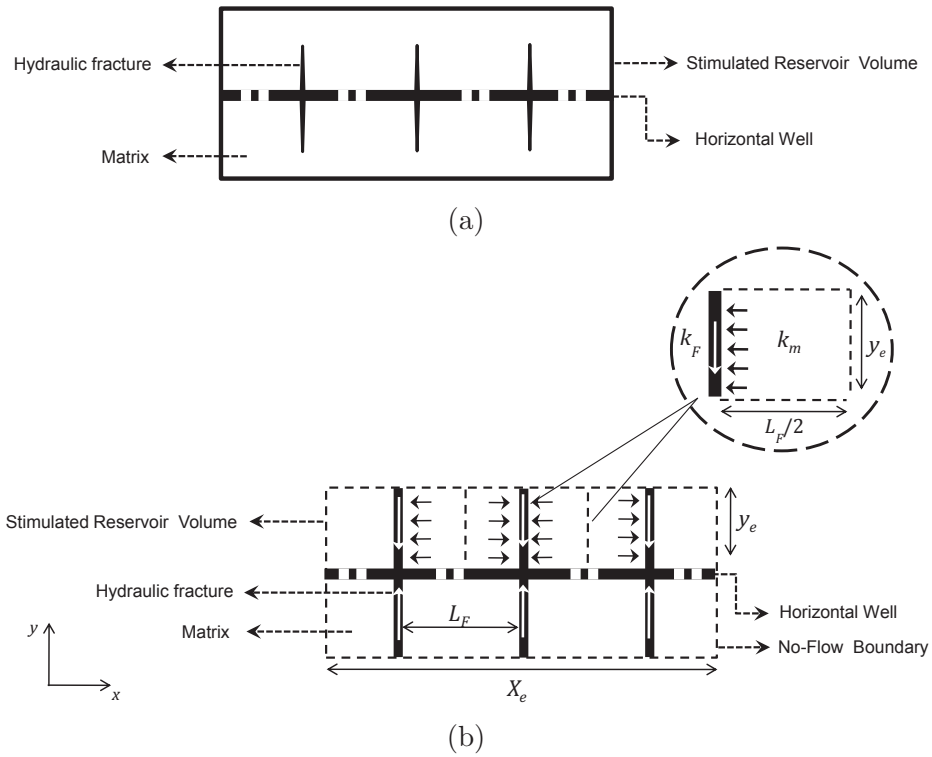

Fig. 3.1: Horizontal cross-section of idealized flowback analysis model (FAM) after multi-stage hydraulic fracturing in tight reservoirs. Solid arrows in the matrix and hydraulic fracture show show fluid flow directions.

The next step involves coupling the dynamic framework (based on DRP derived from flowback physics) with the static framework described here.

3.2.3 Mathematical Formulation

The fluid flow equations for FAM are derived based on the following key assumptions:

- Fully penetrating horizontal well is located at the center of a closed rectangular stimulated reservoir volume (SRV).
- Active secondary (micro and reactivated natural) fractures are negligible.
- Single phase flow of hydrocarbon in the matrix. Leak-off water is trapped in the matrix due to capillarity.
- Transient two-phase (water and hydrocarbon) flow in HF.
- Fluid influx from the SRV boundaries beyond the tips of HF is negligible. Fluid flow from matrix to horizontal well is negligible.
- Saturation and capillary-pressure gradients in space inside the HF is negligible.
- Stress and temperature effects on reservoir parameters are negligible.
- The huge pressure disturbance created near the wellbore as a result of hydraulic fracturing is fairly dissipated during well shut-in before flowback starts. Hence, the initial reservoir pressure during flowback analysis becomes the equilibrated reservoir pressure after this shut-in period.

FAM relaxes the single-phase fluid flow assumption in the existing DPM using the dynamic-relative-permeability of the hydrocarbon phase. The governing equations for fluid flow through matrix and HF are given below:

Diffusivity equation for hydrocarbon phase, initial condition and boundary conditions that control matrix–HF communication are

$$\frac{\partial^2 \Delta P_m}{\partial x^2} = \frac{\mu(\phi c_t)_m}{k_m} \frac{\partial \Delta P_m}{\partial t} \tag{3.1}$$

$$\Delta P_m(x,\ 0) = 0 \tag{3.2}$$

$$\Delta P_m\Big|_{x=\frac{L_F}{2}} = \Delta P_{_F}\Big|_{x=\frac{L_F}{2}} \tag{3.3}$$

$$\left.\frac{\partial \Delta P_m}{\partial x}\right|_{x=0} = 0 \tag{3.4}$$

Diffusivity equation for hydrocarbon phase, initial condition and boundary conditions that control HF–horizontal well communication under variable bottom-hole rate and pressure well constraints and no-flow outer boundary conditions are

$$k_{_F} k_{r_{HC}}(t)\frac{\partial^2 \Delta P_{_F}}{\partial y^2} = \mu(\phi c_t)_{_F}\frac{\partial \Delta P_{_F}}{\partial t} + \left.\frac{k_m}{L_{_F}/2}\frac{\partial \Delta P_m}{\partial x}\right|_{x=\frac{L_F}{2}} \tag{3.5}$$

$$\Delta P_{_F}(y,\ 0) = 0 \tag{3.6}$$

$$q(t) = -\left.\frac{k_{_F} k_{r_{HC}}(t) A_{cw}}{\mu}\frac{\partial \Delta P_{_F}}{\partial y}\right|_{y=0} \tag{3.7}$$

$$\left.\frac{\partial \Delta P_{_F}}{\partial y}\right|_{y=y_e} = 0 \tag{3.8}$$

Eq. 3.1 models fluid flow in the matrix. The left-hand-side (LHS) and first term on the right-hand-side (RHS) of Eq. 3.5 models fluid flow in HF without any external influx. The second term on the RHS of Eq. 3.5 accounts for matrix-HF linear fluid transfer. $k_{r_{HC}}(t)$ is the dynamic-relative-permeability function that incorporates transient multiphase fluid flow into Eq. 3.5. Eqs. 3.2 and 3.6 indicate that the matrix and HF are at initial stabilised reservoir pressure after well shut in (soaking time) and before flowback starts (t=0). Eq. 3.7 includes the inner boundary condition of variable terminal flow-rate and bottom-hole pressure toward the horizontal well. Eq. 3.8 represents negligible fluid flow to the HF tips beyond the SRV. The no-flow boundary conditions represented by Eq. 3.4 denote the line of symmetry for transient matrix depletion into HF. This line of symmetry is at the centre of two consecutive HF. The FAM equations simplify to the existing single-phase DPM at very long times when $k_{r_{HC}}(t \longrightarrow \infty) = k^o_{r_{HC}}$. $k^o_{r_{HC}}$ is the end-point relative-permeability. This happens when the water-saturation in HF is at residual or constant values due to capillary effects.

The porosity and permeability values in this study are bulk estimates (Ezulike and Dehghanpour, 2014a). The notations used in this study are described in the nomenclature section. E as used in figures represents a power of 10.

3.2.4 Solution Methodology

This part proposes a semi-analytical solution method similar to those used in the existing single phase models for unconventional reservoirs. This method comprises these steps:

- Obtain a representative time dependent, relative-permeability function — $k_{r_{HC}}(t)$.
- Make FAM equations dimensionless using parameters similar to those used in previous studies (Bello, 2009; Al-Ahmadi, 2010; Ezulike, 2013). This enables comparison of the resulting dimensionless solutions to the existing solutions.
- Apply Laplace transform (Tranter, 1966) on the resulting dimensionless fluid-flow equations to obtain a solution for the FAM equations.
- Obtain new transfer functions from the resulting analytical solutions in Laplace-space.
- Generate type-curves by numerically inverting the FAM solutions from Laplace-space to time-space using the Gaver-Stefhest algorithm (Davies, 2001; Stehfest, 1970) implemented in MATLAB 2012a.

3.3 Results

A detailed solution of the FAM equations under variable bottom-hole rate and pressure well conditions is given in Appendix A. This part details the derivation of dynamic-relative-permeability (DRP) using a data-driven-analysis of flowback data and summarizes the FAM solution, validation and flow regime sensitivity to flowback parameters. Also, this chapter exploits the ability of dimensionless logarithmic pressure derivative ($\partial P_{_D}/\partial lnt_{_D}$) and dimensionless rate ($q_{_D}$) type-curves to detect subtle flow regime transitions and reduce the non-uniqueness associated with type-curves (Stanislav et al., 1987).

3.3.1 Dynamic Relative Permeability

Assuming there exists negligible water influx from the matrix into the HF during flowback; the transient, average saturation in the HF can be evaluated from material balance as follows:

$$S_{wav}(t) = \frac{V_{p_e} - V_{_{HC_i}}}{V_{p_e}} - \frac{N_w(t)}{V_{p_e}} \tag{3.9}$$

$$S_{wav}(t) = S_{w_i} - \frac{N_w(t)}{V_{p_e}} \tag{3.10}$$

$$\text{where} \quad S_{wav} + S_{HC} = 1 \tag{3.11}$$

Here V_{p_e}, V_{HC_i} and N_w represent effective pore-volume of primary (+ active secondary) fractures, volume of initial hydrocarbon in the fractures at the start of flowback and cumulative water production respectively. Also S_{w_i}, S_{wav} and S_{HC} represent initial water-saturation, transient average water-saturation and transient hydrocarbon-saturation in the fractures respectively. Williams-Kovacs and Clarkson (2013b) used a similar relationship (Eq. 3.10) to estimate transient average water-saturation for flowback analysis.

n_F, n_{CL}, ϕ_F and a_F represent number of fracture stages, number of fracture clusters per stage, average fracture porosity and average fracture aperture or width respectively. Generally, V_{p_e} is not equal to the total injected volume (TIV) because of leak-off (fluid loss to existing secondary fractures and forced or spontaneous imbibition (Dehghanpour et al., 2012, 2013; Makhanov et al., 2014) into the matrix. Similarly, V_{p_e} is used in Eqs. 3.9 and 3.10 instead of total pore-volume created after fracturing because not all fractures might contribute to fluid recovery during flowback. Some of them might be plugged or damaged such that the fluid in them are trapped and cut-off from the fracture network during flowback.

$$y_e(min) = \frac{V_{p_e}}{2n_F n_{CL} h_F a_F \phi_F} \tag{3.12}$$

$$y_e(max) = \frac{2V_{p_e}}{\pi n_F n_{CL} h_F a_F \phi_F} \tag{3.13}$$

V_{p_e} provides an alternate means of estimating HF half-lengths apart from direct application of FAM on flowback data. Using this volumetric analysis method, the effective minimum and maximum HF half-lengths can be estimated using Eqs. 3.12 and 3.13 by approximating HF as a cuboid and an elliptical cylinder respectively. The initial guess for V_{p_e} in this chapter is assumed to be 70% (Rogers et al., 2010) of the TIV for gas wells and 90% of the TIV for oil wells.

S_{w_i} depends on reservoir type and flowback management. $S_{w_i} \neq 1$ when oil and gas wells have long shut-in or soaking periods before being opened for flowback operations. This is because of the possibility of significant counter-current imbibition depending on the Shale or clay content of the matrix and redistribution of injected water with the gas already present in secondary fractures. However, $S_{w_i} \approx 1$ for oil wells due to a lower

chance of counter-current imbibition when compared to gas wells.

N_w in Eq. 3.9 after a long flowback period (constant or residual water saturation in HF, S_w^r) can be approximated as:

$$N_w(t \longrightarrow \infty) = V_{p_e} \times \phi_{_F} \times (S_{wi} - S_w^r) \tag{3.14}$$

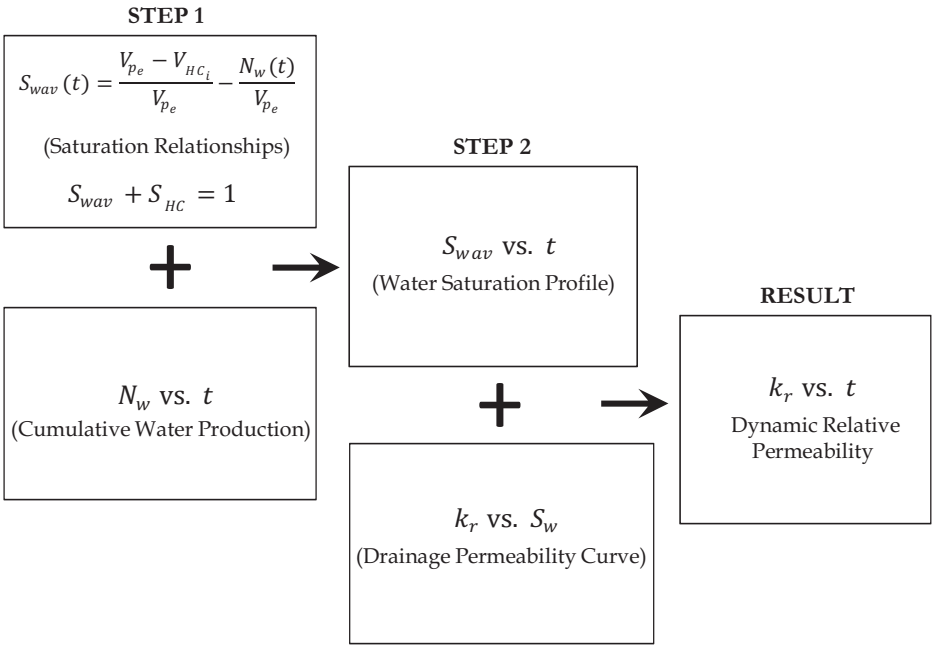

Fig. 3.2: Procedure to estimate $k_r(t)$ profile from field data.

A combination of Eq. 3.10 and relative-permeability curve for HF, $k_r(S_w)$, during flowback yields an average water saturation profile, $S_w(t)$. FAM requires a water-drainage $k_r(S_w)$ curve since flowback behaves like a "hydrocarbon" flooding phenomenon which sweeps water from the HF. Two-phase drainage $k_r(S_w)$ curves adapted for data-driven-analysis of flowback in this chapter are:

$$k_{r_{HC}} = (1 - S_n)^{n_{HC}} \tag{3.15}$$

$$k_{rw} = k_{rw}^o S_n^{n_w} \tag{3.16}$$

$$\text{where} \quad S_n = \frac{S_w - S_{wi}}{1 - S_w^r - S_{HC}^r} \tag{3.17}$$

Assuming that proppants in HF under down hole conditions resemble well-sorted unconsolidated sands (Honarpour et al., 1986), $n_{_{HC}} = n_w = 3$ and values of $k_{rw}^o = 0.2$,

$S_{wi} = S_w^r = 0.3$ and $S_{HC}^r \approx 0.0$ are substituted into Eqs. 3.15 to 3.17.

A combination of $S_w(t)$ profile and $k_r(S_w)$ curve yields a relative permeability profile, $k_r(t)$. The $k_r(t)$ profile could also be a function of cumulative production instead of time. This form is more representative since it directly accounts for shut-in periods (due to limitations in surface facilities). However, it is easier to solve the FAM equations with the k_r profile as a function of time rather than cumulative production.

The 2-step procedure for obtaining $k_r(t)$ profile from flowback data is summarized in Fig. 3.2. Curve-fitting the $k_r(t)$ profile yields the parametric form of DRP for flowback analysis, which can then be substituted directly into FAM equations.

3.3.1.1 DRP Parametric Form

Generally, $k_r(S_w)$ curves are almost sigmoid in shape. A similar shape is expected for $k_r(t)$ profile since it is obtained through a process involving the $k_r(S_w)$ curve as input. Several processes (Weiss, 1997; Birch, 1999; Harris, 1989; Narusawa, 2001; Leibowitz et al., 2010; Buscaglia et al., 2013) have been modeled with sigmoid curves. However, the "leanest" parametric form of DRP obtained from curve-fitting the $k_r(t)$ profile of 15 tight gas, tight oil and Shale gas wells (six are shown in Figs. 3.3 and 3.4) is a 3-parameter function given in Eq. 3.18.

$$k_{r_{HC}}(t) = \frac{\beta_1}{1 + (\beta_2 t)^{-\beta_3}} \tag{3.18}$$

The β terms in Eq. 3.18 are curve-fitting parameters. These parameters could be interpreted as "clean-up" indices because they control how fast the flowback process "cleans" the HF of mobile water (i.e. as $k_{r_{HC}}$ in the fractures approaches to a maximum constant value). The "clean-up" indices in Eq. 3.18 are all dimensionless except β_2 which is in per unit time. β_1, β_2 and β_3 control the maximum value, "half-maximum" and steepness of the $k_r(t)$ profile respectively.

The shape of the curves for tight oil and tight gas (Fig. 3.3) are slightly different from those of the Shale gas (Fig. 3.4). A similar behavior has been observed in diagnostic plots (Abbasi, 2013) of the same well groups. One possible explanation for this behavior can be found from imbibition experiments with the Horn River Shales (Dehghanpour et al., 2012, 2013; Makhanov et al., 2014). Although the Horn River Shales spontaneously imbibe large volumes of water and release gas (mobile or adsorbed), it takes a long time before there is appreciable increase in k_{rg} (which is not the case for tight gas and tight oil reservoirs). This suggests that the imbibed water might be acting as a skin or block.

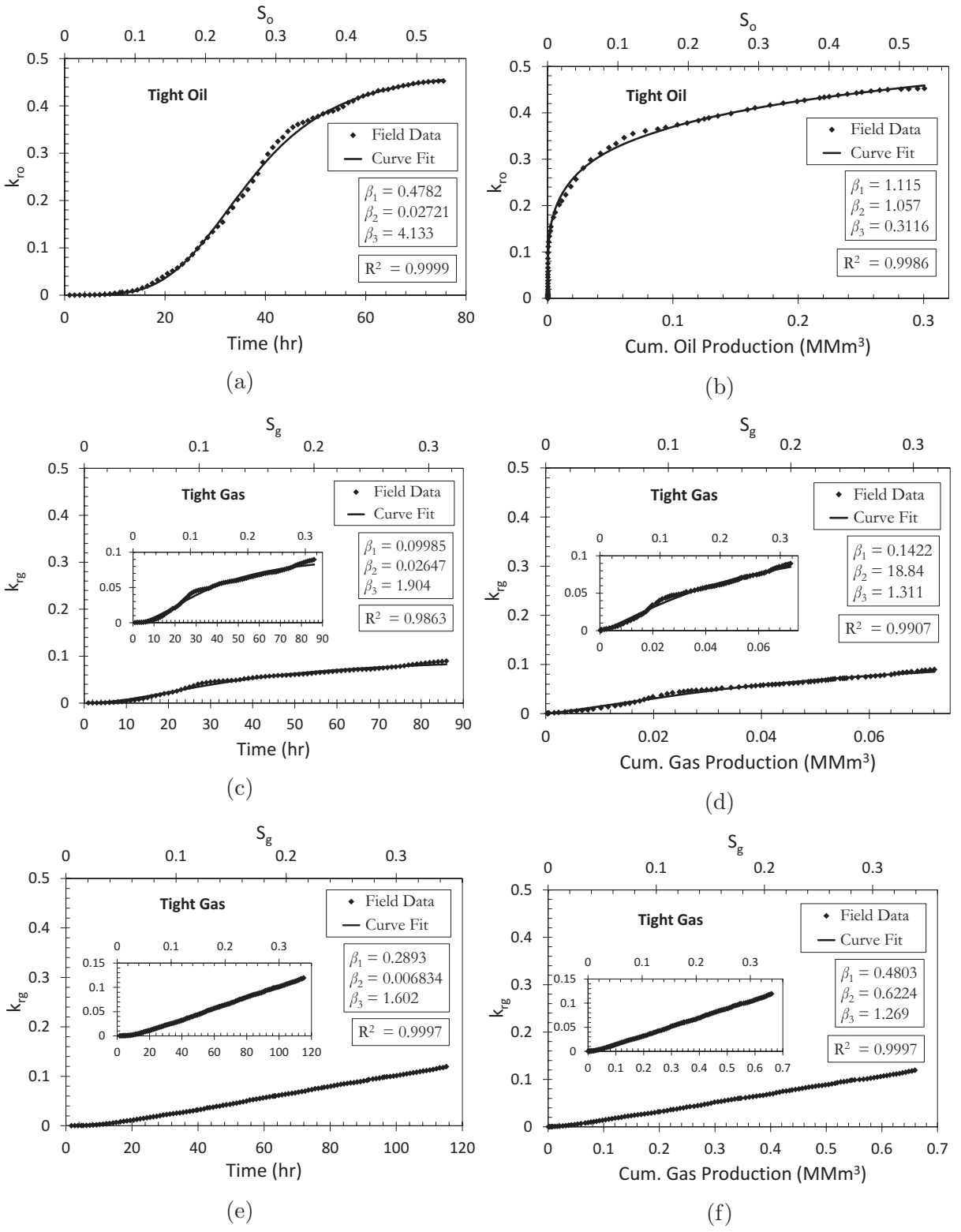

Fig. 3.3: k_r profile curve-fits for three multi-fractured tight oil and tight gas wells completed in the Cardium (a, b, c & d) and Bluesky (e & f) Formations. β_1, β_2 (hr^{-1}) and β_3 are clean-up indices. Insets zoom the curve (near-complete ogive) trends.

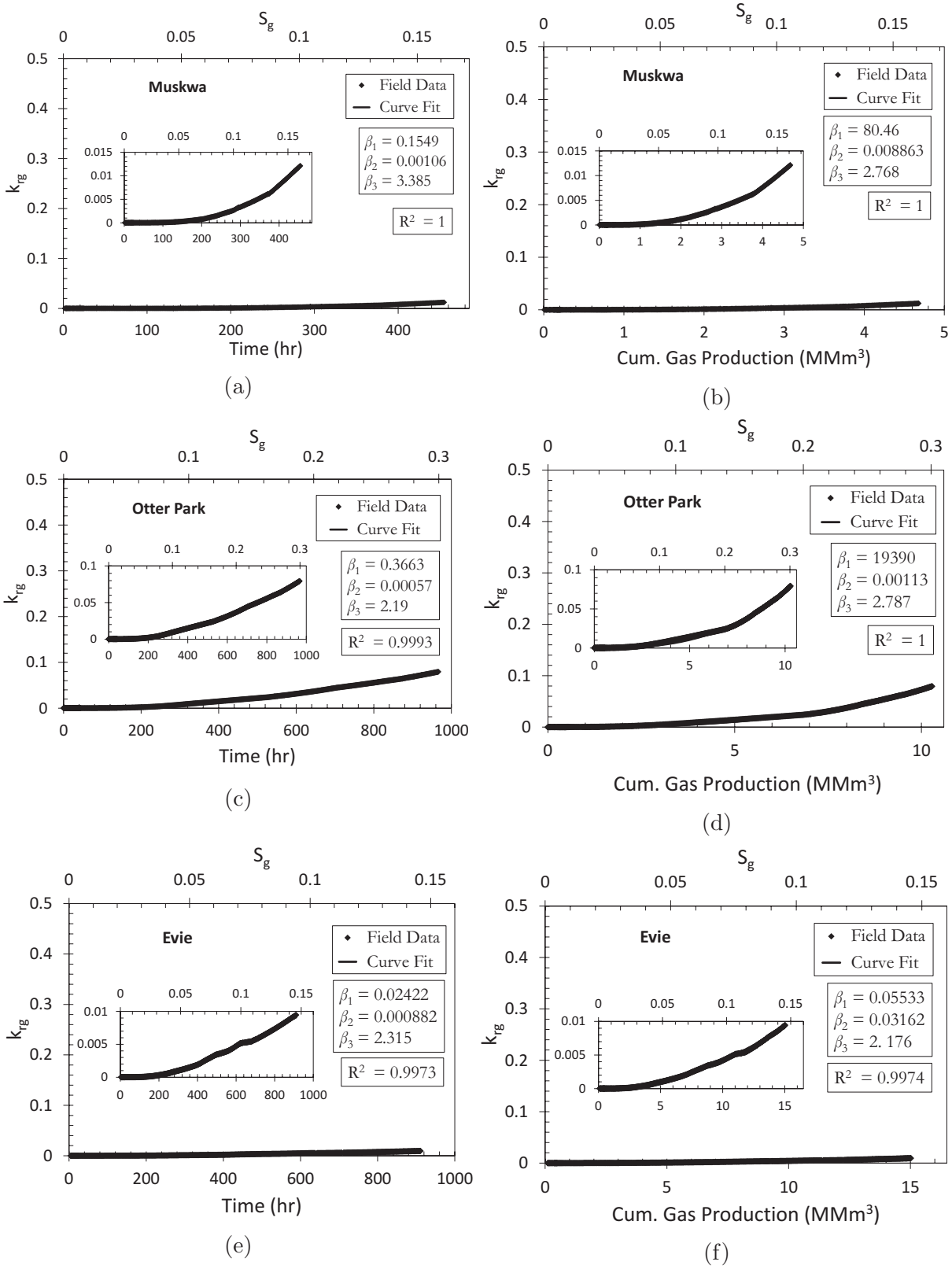

Fig. 3.4: k_r profile curve-fits for three multi-fractured Shale gas wells completed in the Muskwa (a & b), Otter-Park (c & d) and Evie (e & f) Formations. β_1, β_2 (hr^{-1}) and β_3 are clean-up indices. Insets zoom the curve (incomplete ogive) trends.

The curve shapes of the tight gas (Figs. 3.3c to 3.3f) and Shale gas profiles can be considered as subsets of the ogive in the tight oil curve (Fig. 3.3a). Hence, the ogive observed in Fig. 3.3a can be taken as the general shape of the $k_r(t)$ profile.

3.3.1.2 DRP Shape

This part addresses the physics which control the $k_{ro}(t)$ profile. The ogive shape (Fig. 3.3a) of the k_{ro} profile can be explained by considering complementary data plots (Fig. 3.5) from the same tight oil well.

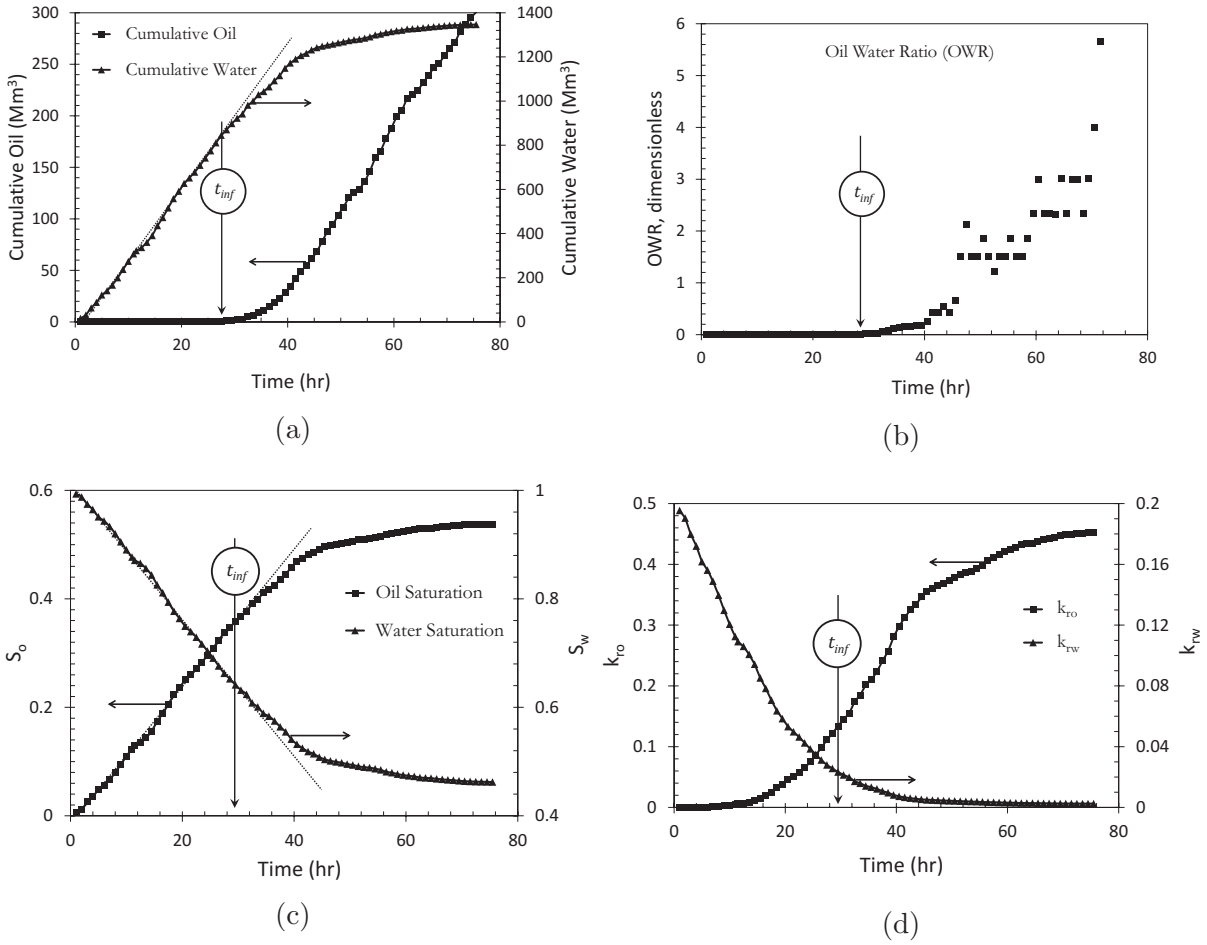

Fig. 3.5: Complementary plots from data-driven-analysis of a multi-fractured tight oil well completed in the Cardium Formation. (a) Cumulative oil and water production (b) Oil-Water-Ratio (c) Saturation profiles (d) Relative-permeability profiles. t_{inf} is the time at which inflexion occurs in the $k_{ro}(t)$ profile.

Although there is little or no oil production at early times during flowback (Figs. 3.5a and 3.5b), oil might already be in the HF. The increase in oil volume in the HF due to influx from the matrix results in an increasing S_o (and k_{ro}) and decreasing S_w (and k_{rw})

respectively (Figs. 3.5c and 3.5d) during this time period.

As flowback continues, oil eventually breaks through at the well. This happens at the time when: the profile of cumulative water production deviates from being a straight line — Fig. 3.5a, oil production starts — Fig. 3.5b, the oil and water saturation profiles deviate from being a straight line — Fig. 3.5c, and inflexion on the k_{ro} profile happens — Fig. 3.5d. Hence, t_{inf} can be taken as the approximate hydrocarbon breakthrough time (t_{bt}). t_{inf} signifies a change in fluid flow physics. One possible reason for this behavior is that t_{inf} marks the time at which $\frac{\partial k_{ro}}{\partial t} = \frac{\partial k_{rw}}{\partial t}$ inside the HF. After this point, both $\frac{\partial k_{ro}}{\partial t}$ and $\frac{\partial k_{rw}}{\partial t}$ decrease as k_{ro} and k_{rw} approach their end-point values.

After the end-point relative permeability values are reached, the physics of fluid flow in the reservoir can be modeled as single-phase flow of oil from matrix through HF to the horizontal well. The low value of k^o_{ro} in Fig. 3.5d might be due to the huge value of V_{pe} input used (assumed to be 70% of the TIV) for this plot.

3.3.1.3 DRP Simplification

Semi-analytical methods (e.g. Laplace transform) are suitable for solving flow equations in existing linear models (Bello, 2009; Al-Ahmadi, 2010; Ali et al., 2013; Ezulike and Dehghanpour, 2014a). However, the introduction of $k_{r_{HC}}(t)$ from Eq. 3.18 into Eq. 3.5's LHS makes solving the flow equations using transform methods challenging. Although the challenge can be overcome using numerical methods, this paper attempts a simplification of Eq. 3.18 based on the inflexion point in k_{ro} profile. This simplification results in an alternative DRP form (compared to Eq. 3.18) suitable to semi-analytical solution methods.

The time of inflexion (t_{inf}) can be estimated from Eq. 3.18 by solving for $\frac{\partial^2 k_{r_{HC}}}{\partial t^2} = 0$ (Hazewinkel, 2002). Mathematically, this results in:

$$t_{inf} \approx \frac{1}{\beta_2} \times \left\{ \frac{-2(1-\gamma) + \sqrt{\beta_3(\beta_3 - 2)}}{2} \right\}^{-\frac{1}{\beta_3}} \tag{3.19}$$

$$\text{where } \gamma = \frac{\beta_3}{\beta_3 + 1} \tag{3.20}$$

Fig. 3.6 shows that the ogive ($k_{ro}(t)$ profile in Fig. 3.3a) can be modeled as two separate curves — pre-inflexion and post-inflexion. The pre-inflexion (Eq. 3.21) and post-inflexion (Eq. 3.2) curves have 2- and 3-parametric functional forms respectively.

$$k_{r_{HC}}(t) = \beta_2 \exp(\beta_3 t) \qquad 0 \leq t \leq t_{inf} \tag{3.21}$$

$$k_{r_{HC}}(t) = \frac{\beta_1}{1 + \beta_2 \exp(-\beta_3 t)} \qquad t > t_{inf} \tag{3.22}$$

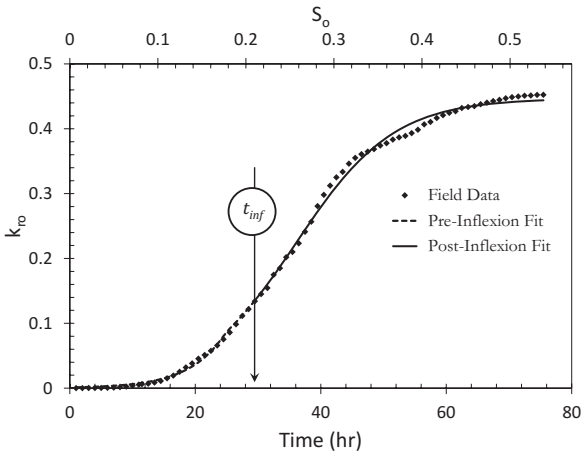

Fig. 3.6: Simplification of the dynamic-relative-permeability function into two regions based on inflexion point: Pre-Inflexion ($\beta_2 = 0.00528$, $\beta_3 = 0.1057$ hr^{-1} and $R^2 = 0.9747$) and Post-Inflexion ($\beta_1 = 0.4692$, $\beta_2 = 14.7$, $\beta_3 = 0.08134$ hr^{-1} and $R^2 = 0.9975$). t_{inf} is the time at which inflexion occurs in the $k_{ro}(t)$ profile.

The β terms in Eqs. 3.21 and 3.22 are fitting parameters. These parameters could be interpreted as "clean-up" indices that control how fast the flowback process "cleans" the HF of mobile water (i.e. as $k_{r_{HC}}$ in the fractures tends to a maximum constant value). β_2 and β_3 in Eq. 3.21 control the initial value and growth rate of the pre-inflexion $k_r(t)$ profile. β_1, β_2 and β_3 in Eq. 3.22 control the end-point value, inflexion point and growth rate of the post-inflexion $k_r(t)$ profile respectively. It is important to note that β_2 and β_3 have different values for the pre-inflexion and post-inflexion $k_r(t)$ profiles. After this simplification in DRP, the "clean-up" indices are all dimensionless except β_3 whose unit is per unit time.

3.3.2 Physical Significance of DRP

This part shows how to use the regions on the DRP profile as a diagnostic tool for improved interpretation of production data plots. There are three possible regions (Fig. 3.7) of interest on the DRP profile — pre-inflexion flowback, post-inflexion flowback and post-flowback production periods. Regions 1 and 2 are still under flowback. They are divided by the time (t_{inf}) at which hydrocarbon breaks through into the well. Flowback is differentiated from "full" hydrocarbon production by the time at which the DRP profile reaches a terminal or constant value (i.e. single-phase flow).

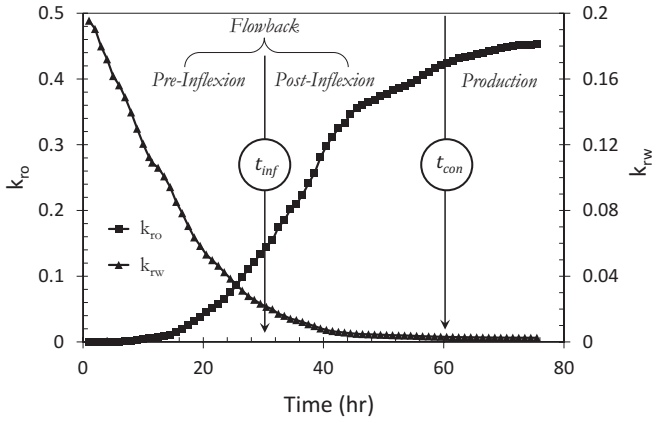

Fig. 3.7: The physical significance of the dynamic-relative-permeability curve. t_{inf} is the time at which inflexion occurs. t_{con} is the time at which the curve approaches a constant value.

3.3.3 FAM Solution

After substituting Eqs. 3.21 and 3.22 into Eq. 3.5, the solution of Eqs. 3.1 and 3.5 using Laplace transform yields the dimensionless wellbore pressure equation in Laplace space under variable rate inner boundary conditions:

$$\overline{P}_{wDL} = \frac{f^*(s)}{\sqrt{f(s)}} \left\{ \coth\left(\sqrt{f(s)} y_{De}\right) + I_D \sqrt{f(s)} \right\} \tag{3.23}$$

$$\text{where } I_D = \frac{r_w}{\sqrt{A_{cw}}} I \tag{3.24}$$

$$\text{and } f(s) = \begin{cases} \dfrac{1}{\beta_2}\left[\omega_F(s+\beta_3^*) + \dfrac{\lambda_{AC,Fm}}{3}\sqrt{f_m(s+\beta_3^*)}\tanh\left(\sqrt{f_m(s+\beta_3^*)}\right)\right] & 0 \le t_{D_{AC}} \le t_{D_{AC\,inf}} \\ \dfrac{1}{\beta_1}\left(\omega_F\left[s+\beta_2(s+\beta_3^{**})\right] + \dfrac{\lambda_{AC,Fm}}{3}\left[\sqrt{f_m(s)}\tanh\left(\sqrt{f_m(s)}\right) + \right.\right. & \\ \left.\left. \beta_2\sqrt{f_m(s+\beta_3^{**})}\tanh\left(\sqrt{f_m(s+\beta_3^{**})}\right)\right]\right) & t_{D_{AC}} > t_{D_{AC\,inf}} \end{cases} \tag{3.25}$$

$$\text{and } f^*(s) = \begin{cases} \frac{1}{\beta_2}\left[\frac{1}{(s+\beta_3^*)}\right] & 0 \leq t_{D_{AC}} \leq t_{D_{AC\,inf}} \\ \frac{1}{\beta_1}\left[\frac{1}{s} + \frac{\beta_2}{(s+\beta_3^{**})}\right] & t_{D_{AC}} > t_{D_{AC\,inf}} \end{cases} \tag{3.26}$$

$$\text{and } f_m(s) = \frac{3s\omega_m}{\lambda_{AC,Fm}} \tag{3.27}$$

Here, I is the convergence skin that accounts for flow distortion (Bello, 2009) from linear to radial around the well, $f_m(s)$ is the transfer-function controlling fluid flow from matrix to HF, $f^*(s)$ is the transfer-function controlling the perturbation caused by the presence of the horizontal well and $f(s)$ is the transfer-function controlling fluid transfer from matrix and HF into the multi-fractured horizontal well.

3.3.4 Model Verification

This part validates the proposed model by testing the convergence of FAM solutions (Eq. 3.23) to the linear dual-porosity model (DPM) and verifying the behavior of DRP using synthetic data from IMEX CMG [20] software.

3.3.4.1 FAM's Convergence to DPM

This convergence is achieved using dimensionless pressure and logarithmic pressure derivative (P_D and $\partial P_D/\partial lnt_D$) curves respectively. These curves are generated by numerically inverting Eq. 3.23 from Laplace space to time space using the Stefhest algorithm (Stehfest, 1970; Davies, 2001). A dimensionless data-set representing possible field operating conditions during flowback operation is substituted into Eq. 3.23.

FAM should converge to DPM during single-phase hydrocarbon flow as the dynamic-relative-permeability in Eqs. 3.21 and 3.22 approaches an end-point value (at residual S_w in HF). Fig. 3.8 shows the data match from the beginning of flowback till "full" production (see Subsection 3.3.2) when the hydrocarbon phase is the dominant mobile phase in the fractures. This demonstrates that FAM converges to the existing DPM as the dynamic-relative-permeability approaches end-point or constant values.

[20] Computer Modeling Group (http://www.cmgl.ca, last accessed 18-11-2016)

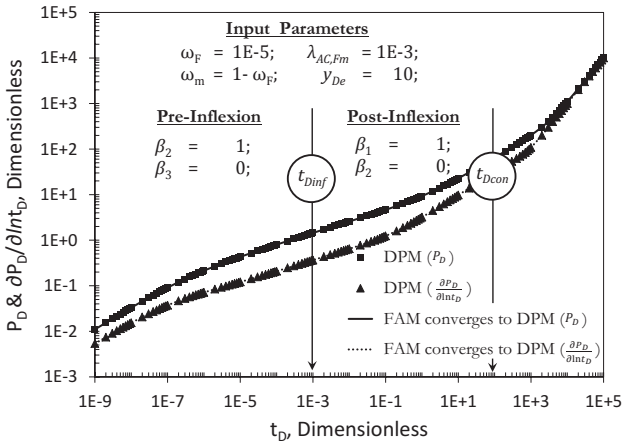

Fig. 3.8: Flowback analysis model converges to linear dual-porosity model (for $I = 0$). t_{Dinf} is the dimensionless inflexion time for $k_r(t)$ profile. t_{Dcon} is the dimensionless time at which the $k_r(t)$ profile approaches a constant value.

3.3.4.2 DRP Behavior Using Synthetic Data from IMEX CMG

IMEX CMG is used to simulate a gas reservoir having matrix and hydraulic fracture as its contiguous porous media. Fig. 3.9 shows the top view for two stages of hydraulic fracture in the reservoir. Table 3.1 shows the fluid, rock and well properties typical of Muskwa Formation. These properties are inputted into the flow simulation. To mimic field operations, the simulation starts with the injection (TIV) of about 346 bbl of water at 7000 psi for 7 days. Afterwards, the well is shut-in for 3 days to allow for water imbibition into the matrix and for gas influx from matrix into the fractures. This shut-in period allows a gradual build-up of free gas saturation in the fractures before the well is opened for 10 days of flowback under a constant bottom-hole pressure of 1500 psi. The average water saturation in the fractures at the start of flowback is about 0.63 (see Fig. 3.11b).

Fig. 3.10 shows the fluid model used to simulate the reservoir. The curve-fit equations for the data points in Fig. 3.10d are $k_{rg} = -1.3021{S_w}^4 + 2.6042{S_w}^3 - 0.57292{S_w}^2 - 1.7292S_w + 1$ and $k_{rw} = -1.3021{S_w}^4 + 2.6042{S_w}^3 - 0.57292{S_w}^2 + 0.27083S_w + 5.329 \times 10^{-13}$ with $R^2 = 1$ respectively. These equations are combined with the saturation profiles in Fig. 3.11b to obtain the DRP in Fig. 3.11d. This DRP from synthetic data has the same form as Eq. 3.18 which was obtained from a data-driven-analysis of actual field data.

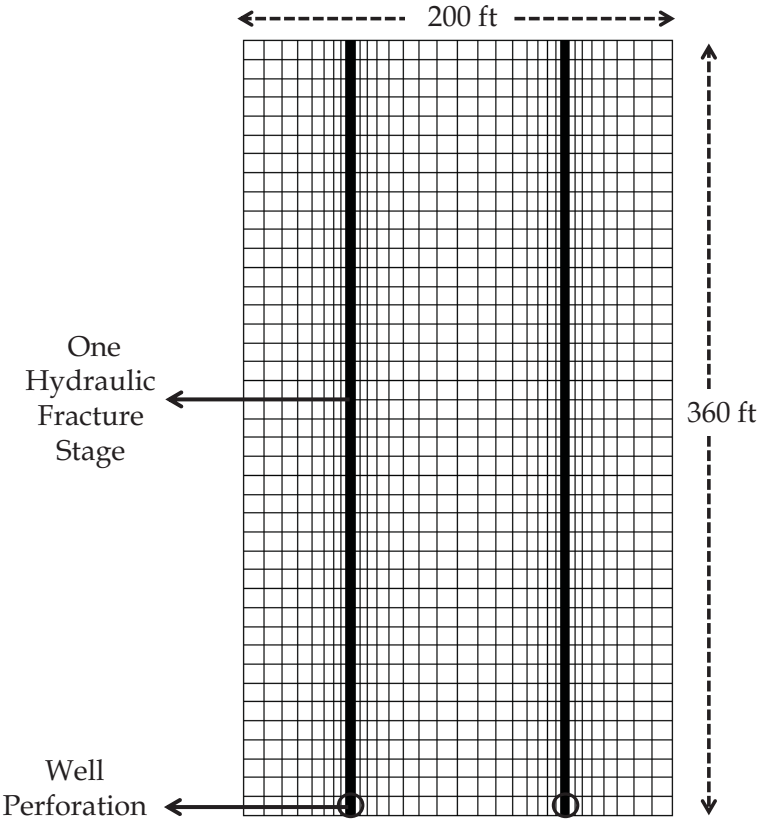

Fig. 3.9: Top view of static framework used for flow simulation in IMEX CMG.

Table 3.1: Input Dataset for IMEX CMG Simulation.

Reservoir Parameter	**Value**	**Units**
h	56	ft
y_e	360	ft
$n_{_F}$	2	—
$L_{_F}$	98	ft
$a_{_F}$	3×10^{-3}	m
k_m^t	0.0005	mD
$k_{_F}^t$	2000	mD
ϕ_m^t	0.08	—
ϕ_F^t	0.6	—
V_{pe}	71	bbl
$(c_t)_m$	3×10^{-6}	psi^{-1}
$(c_t)_{_F}$	3×10^{-6}	psi^{-1}
P_i	3000	psi
P_{wf}	1500	psi
$S_{wi,m}$	0.1	—
$S_{wi,F}$	1	—
TIV	346	bbl
Gas gravity	0.6	—
Reservoir Temperature	278	^oF

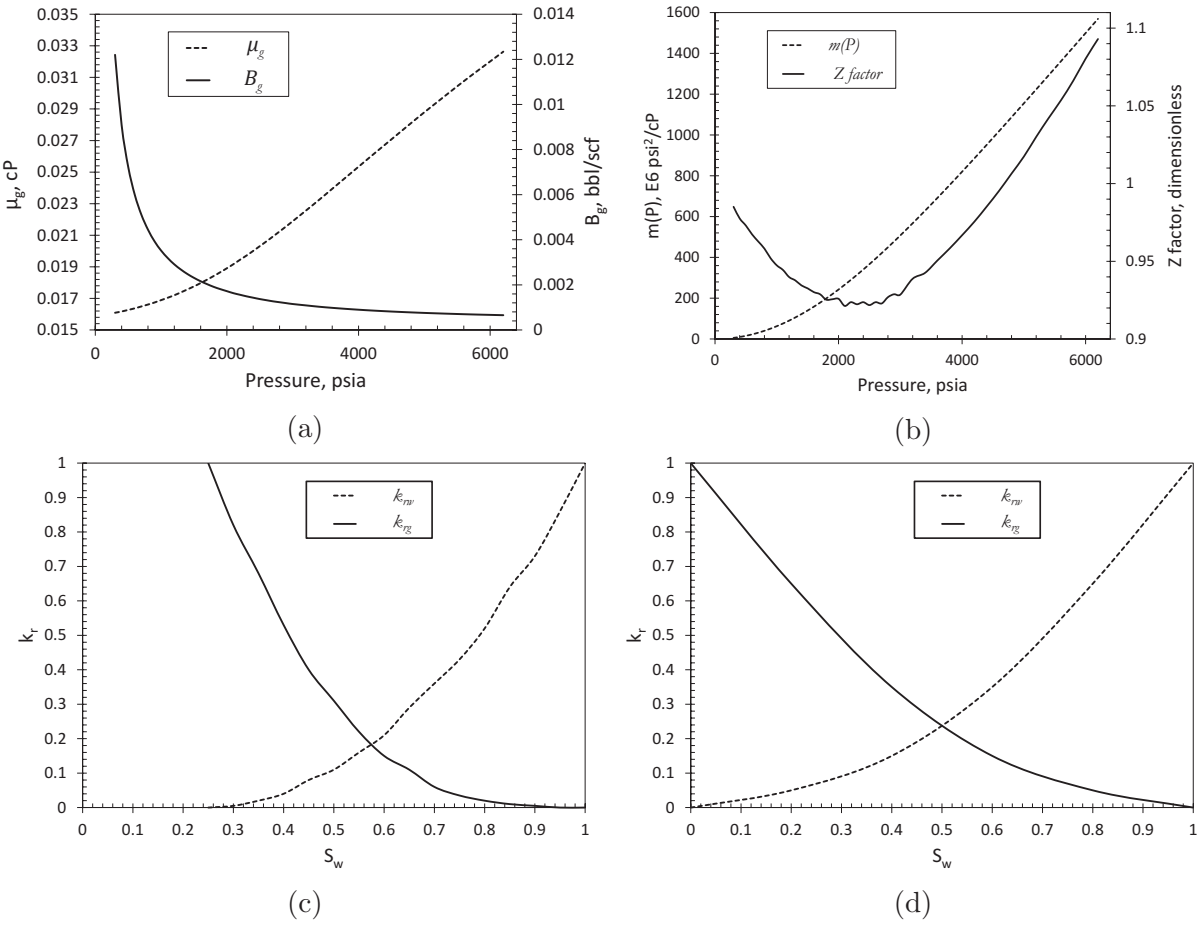

Fig. 3.10: Multiphase correlation models for flow simulation in IMEX CMG. (a) Viscosity and Formation volume factor (b) Pseudo-pressure and Z factor (c) Matrix relative permeability curves and (d) Fracture relative permeability curves.

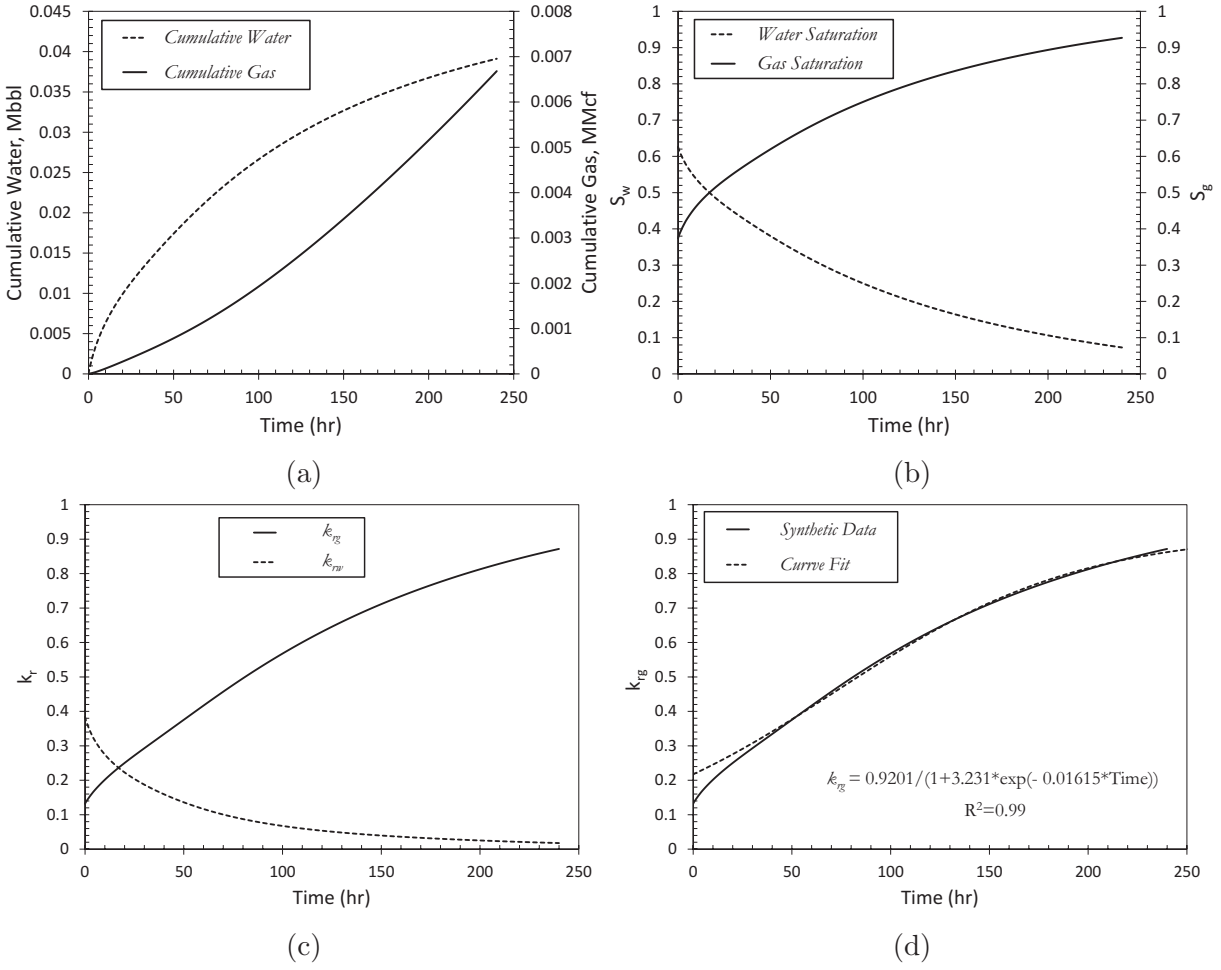

Fig. 3.11: DRP behavior using synthetic data from IMEX CMG (a) Cumulative water and gas flowback data (b) Saturation profiles for water and gas in the fractures using Eq. 3.10 (c) k_{rg} and k_{rw} profiles using the procedure shown in Fig. 3.2. (d) Curve fit of k_{rg} to obtain DRP.

3.3.5 Flow Regimes

Table 3.2 exploits the similarities between dimensionless rate ($q_{_D}$) and logarithmic pressure derivative ($\partial P_{_D}/\partial lnt_{_D}$) type-curves to qualitatively describe the physics behind typical flow regimes observed in FAM.

Table 3.2: Qualitative description of typical flow regimes observed in FAM.

Flow Regime	Slope	Flow regime physics	Interpretation
1	0.5	Early transient linear flow in HF (Al-Ahmadi and Wattenbarger, 2011).	Single phase (water) flow.
2	0.25	Bilinear flow due to simultaneous linear flow in HF and matrix (Bello, 2009).	Two phase (water and hydrocarbon) flow due to hydrocarbon breakthrough from matrix to HF.
3	0.5	Transient linear flow from matrix to HF (Bello and Wattenbarger, 2010b).	Single-phase (hydrocarbon) flow.
4	1	Pseudo-steady state flow (Song et al., 2011; Bello, 2009) as depletion reaches all no-flow boundaries.	Single-phase (hydrocarbon) flow continues.

Fig. 3.12 shows the progression of these flow regimes from flowback to post-flowback production periods. It is possible for other sequences of flow regimes different from those in Fig. 3.12 to occur. This depends on the values of reservoir properties relative to one another. Quantitative flow regime interpretation (which is the subject of a future study) will be done after detailed analyses of FAM's Eq. 3.23.

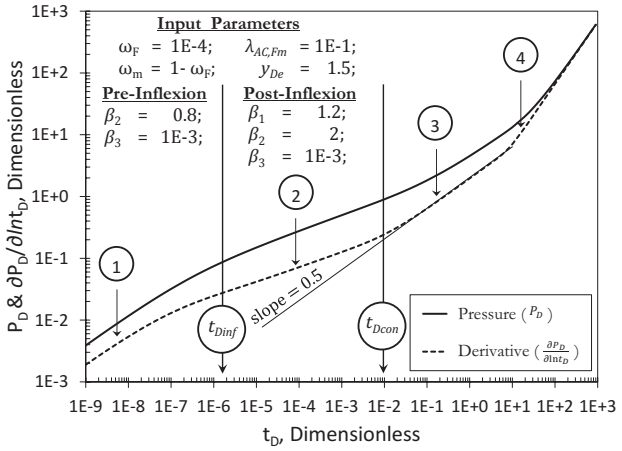

Fig. 3.12: Typical FAM flow regimes (1 to 4) from dimensionless logarithmic pressure derivative (for $I = 0$). t_{Dinf} is the dimensionless inflexion time for $k_r(t)$ profile. t_{Dcon} is the dimensionless time at which $k_r(t)$ approaches a constant value.

3.3.6 Sensitivity Analysis

Sensitivity analysis for FAM focuses on the initial hydrocarbon saturation (S_{HC_i}) in hydraulic fractures before flowback. This part shows how S_{HC_i} can be tuned to history-match the early time two-phase data for fracture characterization.

Table 3.3: Base case dataset for sensitivity analysis on FAM.

Reservoir Parameter	Value	Units
r_w	0.091	m
h	5	m
X_e	1000	m
y_e	150	m
n_F	15	—
n_{CL}	1	—
L_F	62.5	m
a_F	1×10^{-3}	m
k_m^t	0.035	mD
k_F^t	10	mD
ϕ_m^t	0.12	—
ϕ_F^t	0.48	—
$(c_t)_m$	2.209×10^{-6}	kPa^{-1}
$(c_t)_F$	2.209×10^{-9}	kPa^{-1}

The base case dataset shown in Table 3.3 is substituted into Eq. 3.23 to obtain di-

mensionless logarithmic pressure derivative ($\partial P_D/\partial lnt_D$) type-curves. The dimensionless rate (q_D) type-curves are generated by substituting Eq. 3.23 in the relationship provided by Van Everdingen and Hurst (1949).

Initial hydrocarbon saturation (S_{HC_i}) in HF affects both pre- and post-inflexion flowback periods. Fig. 3.13 illustrates this effect on the early- and intermediate-time FAM flow regimes. The late-time flow regimes are not sensitive to changes in S_{HC_i} because the relative permeability gradually converges to constant end-point values at late time periods. Hence, S_{HC_i} only affects the pressure drop (Fig. 3.13a) and flow rate (Fig. 3.13b) of the early- to intermediate-time flow regimes.

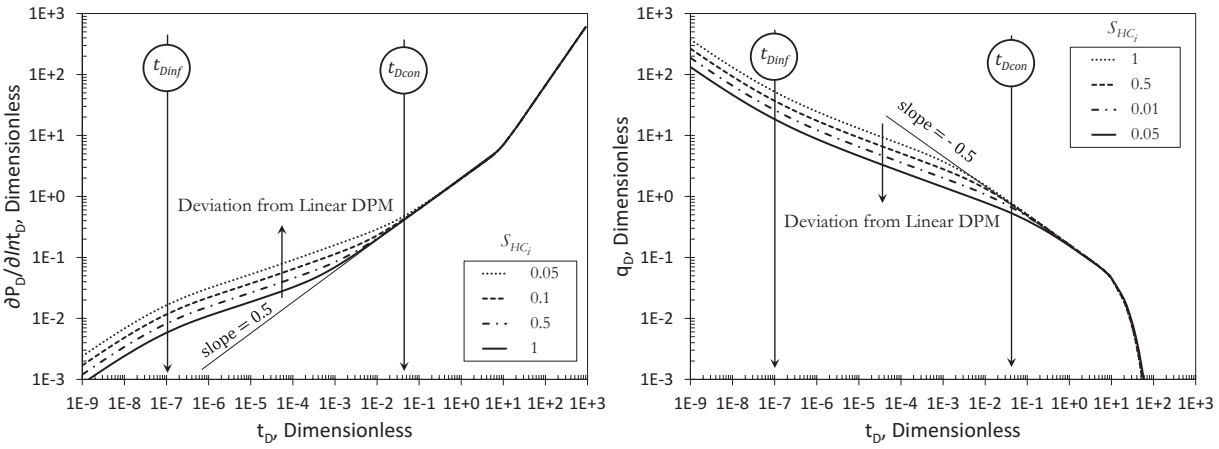

(a) (b)

Fig. 3.13: FAM's sensitivity to initial hydrocarbon saturation (S_{HC_i}) in HF (for $I = 0$). Dimensionless pressure derivative plot and (b) Dimensionless rate plot. t_{Dinf} is the dimensionless time of inflexion on the $k_r(t)$ profile. t_{Dcon} is the dimensionless time at which $k_r(t)$ approaches a constant value.

The reservoir behaves as a linear dual porosity system (DPM) as $S_{HC_i} \longrightarrow 1$. Increasing S_{HC_i} results in increasing hydrocarbon flow rate, decreasing pressure-drop in the early three flow regimes (see Table 3.2) and early occurrence of the matrix–HF transient linear flow. This early occurrence of matrix–HF support is due to the high effective HF permeability resulting from low pressure drop.

3.4 Application

This part presents a workflow for analyzing two-phase flowback (rate + pressure) data, and applies this workflow to a field example from a multi-fractured horizontal well (Well X) to estimate key reservoir parameters. This workflow is implemented as an integrated module called FAMSOLVE v.1.

3.4.1 Workflow

The analysis workflow for interpreting two-phase flowback (rate + pressure) data with the proposed FAM comprises the following steps:

1. Obtain input reservoir parameters using alternate means:
    - Complementary studies (e.g. matrix permeability from laboratory experiments).
    - Well testing (e.g production data analysis) from offset wells.
2. Obtain output reservoir parameters through these steps:
    - Select representative two-phase drainage $k_r(S_w)$ curves for HF.
    - Assume a value of V_{p_e} as a percentage of the total injected volume.
    - Combine cumulative flowback data, "assumed" V_{p_e} and $k_r(S_w)$ curves (see Fig. 3.2).
    - Obtain average hydrocarbon $k_r(t)$ history A in HF.
    - Curve fit $k_r(t)$ history A using the format of Eq. 3.18.
    - Obtain flowback "clean-up" indices (β_1, β_2 and β_3) from the curve-fit.
    - Substitute these "clean-up" indices into Eq. 3.19
    - Estimate the inflexion time (t_{inf}).
    - Apply t_{inf} to curve-fit k_r history A using Eqs. 3.21 and 3.22.
    - Estimate the pre- and post-inflexion values of β_3 from the curve-fit .
    - Input β_3 and other known parameters (reservoir and well) into Eq. 3.23.
    - History-match two-phase flowback rate + pressure data with FAM
    - Estimate β_1, β_2 and other unknown reservoir parameters.
3. Obtain other key parameters through these steps:
    - Obtain $k_r(t)$ history B by putting β_1, β_2 and β_3 from history-match in Eqs. 3.21 and 3.22.
    - Match $k_r(t)$ history A and B by tuning V_{p_e} and V_{HC_i} in Eqs. 3.15, 3.16 and 3.17.
    - Estimate "optimal" V_{p_e} and V_{HC_i} from this tuning.
    - Estimate the range for "final" y_e by inputting V_{p_e} in Eqs. 3.12 and 3.13.
    - Estimate leak-off volume ($= TIV - V_{p_e}$).
    - Estimate current water volume left in HF ($= V_{p_e} - N_w(t)$).
    - Forecast hydrocarbon recovery from the FAM history-match.

3.4.2 Field Example

This part briefly describes the geology and processing required for applying the proposed model to flowback data from Well X.

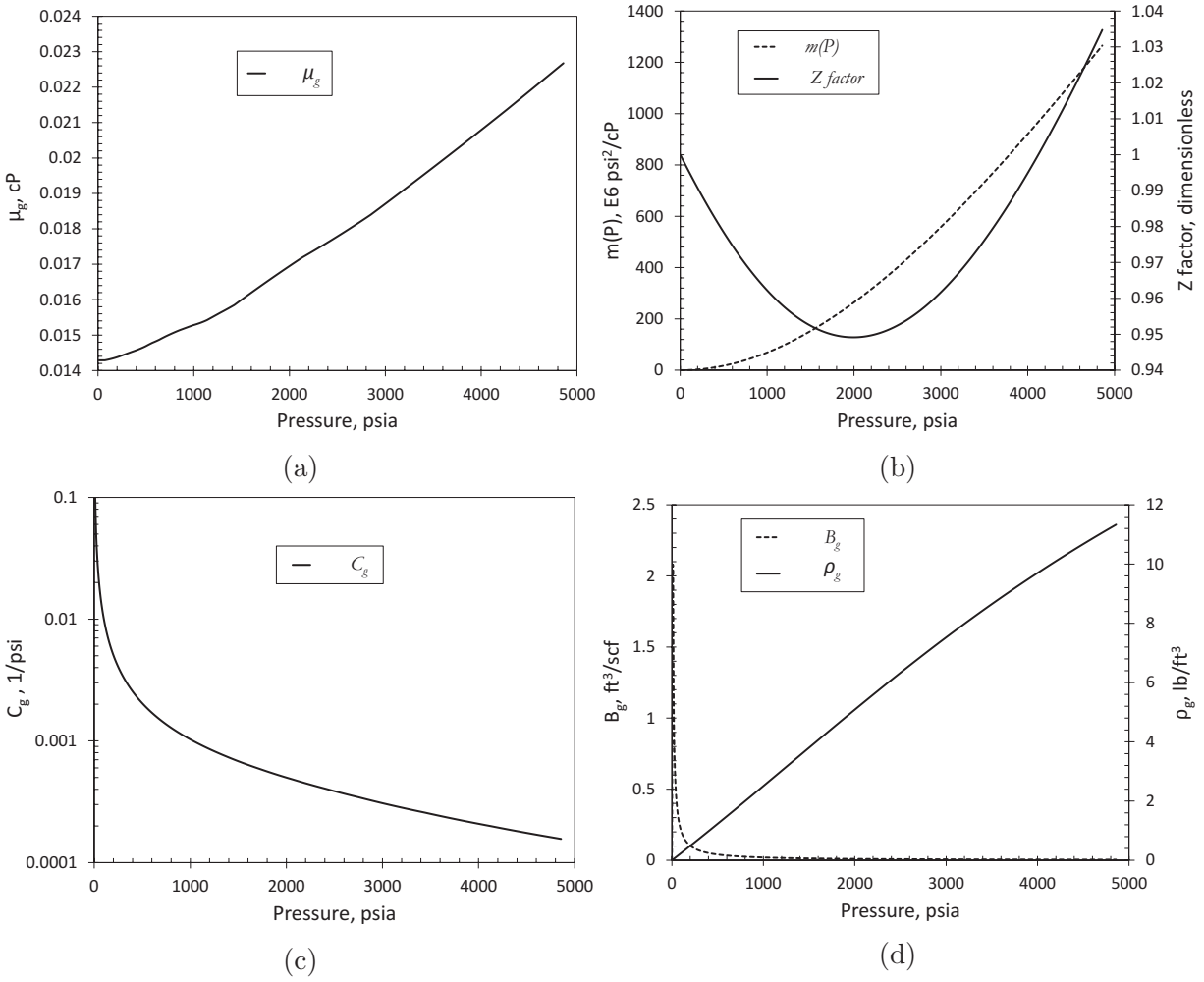

Fig. 3.14: Correlations for converting Well X flowback data from surface to bottom-hole conditions. (a) Viscosity (b) Pseudo-pressure and z factor (c) Compressibility and (d) Formation volume factor and density.

Well X is one of eight multi-fractured horizontal Shale gas wells completed in the Horn River Basin. Due to complex basin history, the Horn River Shales have a high amount of natural fractures that are optimally oriented to the in-situ stress field, making them easily reactivated during hydraulic fracturing (Virués et al., 2013). Figs. 3.14 and 3.15 summarize the conversion of two-phase flowback data recorded at the surface to bottom-hole conditions using IHS Harmony software.

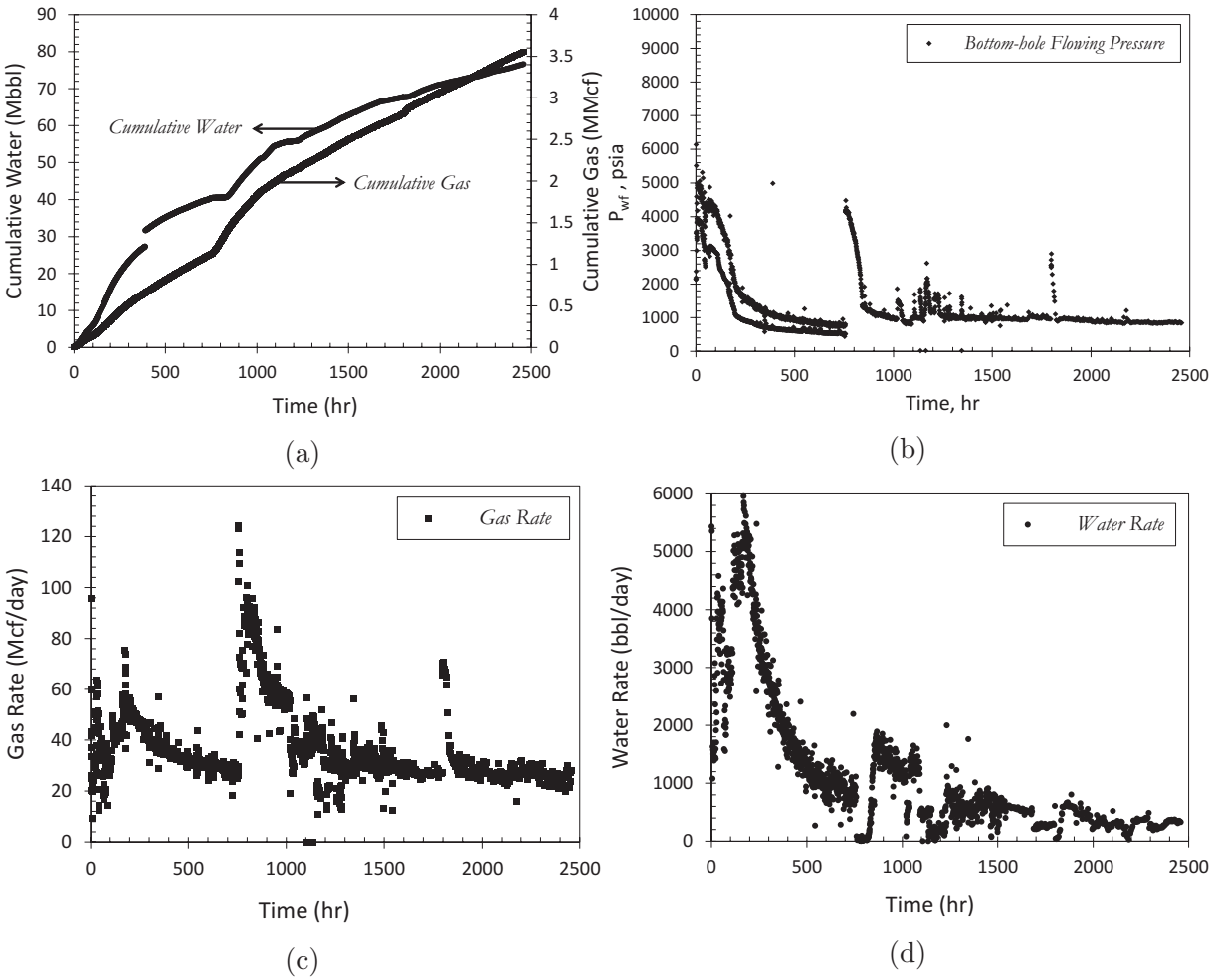

Fig. 3.15: Well X's Flowback data after conversion from surface to down-hole conditions. (a) Cumulative gas and water (b) Bottom-hole pressure (c) Gas rate and (d) Water rate.

3.4.3 Interpretation

This part applies the proposed workflow on two-phase flowback (rate and pressure) data from Well X to estimate half-length, leak-off volume and forecast hydrocarbon production.

3.4.3.1 Input Reservoir Parameters

The input well and reservoir data from microseismic studies, field tests and production data analysis are shown in Table 3.4. The bulk porosity and permeability values in Table 3.4 are estimated using the approximations provided in Ezulike and Dehghanpour (2014a).

Table 3.4: Input Parameters for Flowback Analysis of Well X Data. TIV = total injected volume of water. $(c_t)_F$ is assumed to be $100 \times (c_t)_m$.

Input Parameter	Value	Units
r_w	0.07	m
h	120	m
X_e	1400	m
n_F	15	—
n_{CL}	1	—
L_F	87.5	m
a_F	1×10^{-3}	m
k_m (true)	4.5×10^{-4}	mD
k_m (bulk)	4.5×10^{-4}	mD
k_F (true)	70000	mD
k_F (bulk)	0.8	mD
ϕ_m (true)	0.05	—
ϕ_m (bulk)	0.05	—
ϕ_F (true)	0.5	—
ϕ_F (bulk)	5.7×10^{-6}	—
$(c_t)_m$	9.4×10^{-7}	kPa^{-1}
$(c_t)_F$	9.4×10^{-5}	kPa^{-1}
TIV	69373	m^3

3.4.3.2 Output Reservoir Parameters

The coefficients for well-sorted unconsolidated sands (Honarpour et al., 1986) are substituted in Eqs. 3.15 and 3.16 to obtain two-phase drainage $k_r(S_w)$ curves for HF used for flowback analysis. The initial value of effective fracture pore volume (V_{p_e}) is assumed to be 65% of the total injected volume of water (i.e. 35% leak-off). Also, the volume of the initial hydrocarbon (V_{HCi}) in the fractures is assumed to be zero for this analysis. Future studies will account for the possibility when the fractures are not fully saturated with water ($S_{w_i} \neq 1$) as flowback starts.

Fig. 3.16 shows the average $k_r(t)$ history A in the fractures obtained by combining cumulative flowback data, the "assumed" V_{p_e} and k_r curves. It also shows the pre- and post-inflexion values of β_3 from curve-fitting average gas $k_r(t)$ history A. The value of β_3 from Fig. 3.16 is important because it controls the shape of $k_r(t)$.

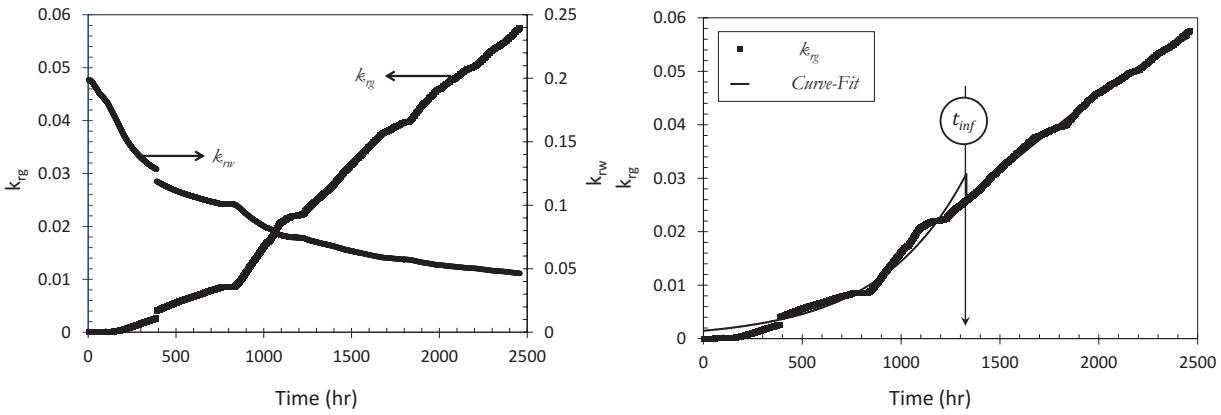

(a) (b)

Fig. 3.16: Initial dynamic relative permeability for Well X obtained by combining cumulative flowback data, "assumed" V_{pe} and k_r curves. (a) Average $k_r(t)$ history A (b) Average gas $k_r(t)$ history A showing inflexion point (t_{inf}) — Pre-Inflexion ($\beta_2 = 0.0015$, $\beta_3 = 0.0023hr^{-1}$ and $R^2 = 0.9615$) and Post-Inflexion ($\beta_1 = 0.0698$, $\beta_2 = 16.2$, $\beta_3 = 0.001715hr^{-1}$ and $R^2 = 0.9972$).

The history-match two-phase flowback rate + pressure data with FAM (Fig. 3.17) is obtained by substituting for β_3 and other known parameters (reservoir + well) into Eq. 3.23. This history-match yields estimates of HF half-length, β_1 and β_2 shown in Table 3.5. Fig. 3.17b is obtained by converting the equivalent dimensionless rate plots to dimensional RNP units for easy understanding.

The low signal to noise ratio in the early 60 hours in Fig. 3.17a could be a result of wellbore storage (due to choke and valve changing operations). However, this chapter focuses on the possible "true" flow regime obtainable in the absence of wellbore storage effects. This explains the discrepancy in the early hours of Fig. 3.17a. Also, the interpretation procedure assumes continuous operations (ignoring the shut-in between 700 – 1000 hours) because shut-in times are not accounted for in this model. It is also important to note that the choice of initial input parameters affects the general match (Table 3.5). However, this match is constrained by ensuring that the input parameters are iterated until there is at least a 90% R^2 match between the $k_{rg}(t)$ history and model (Fig. 3.18). Also, the data noise is not cleaned or filtered in the history-match to see if it will adversely affect the output reservoir parameters.

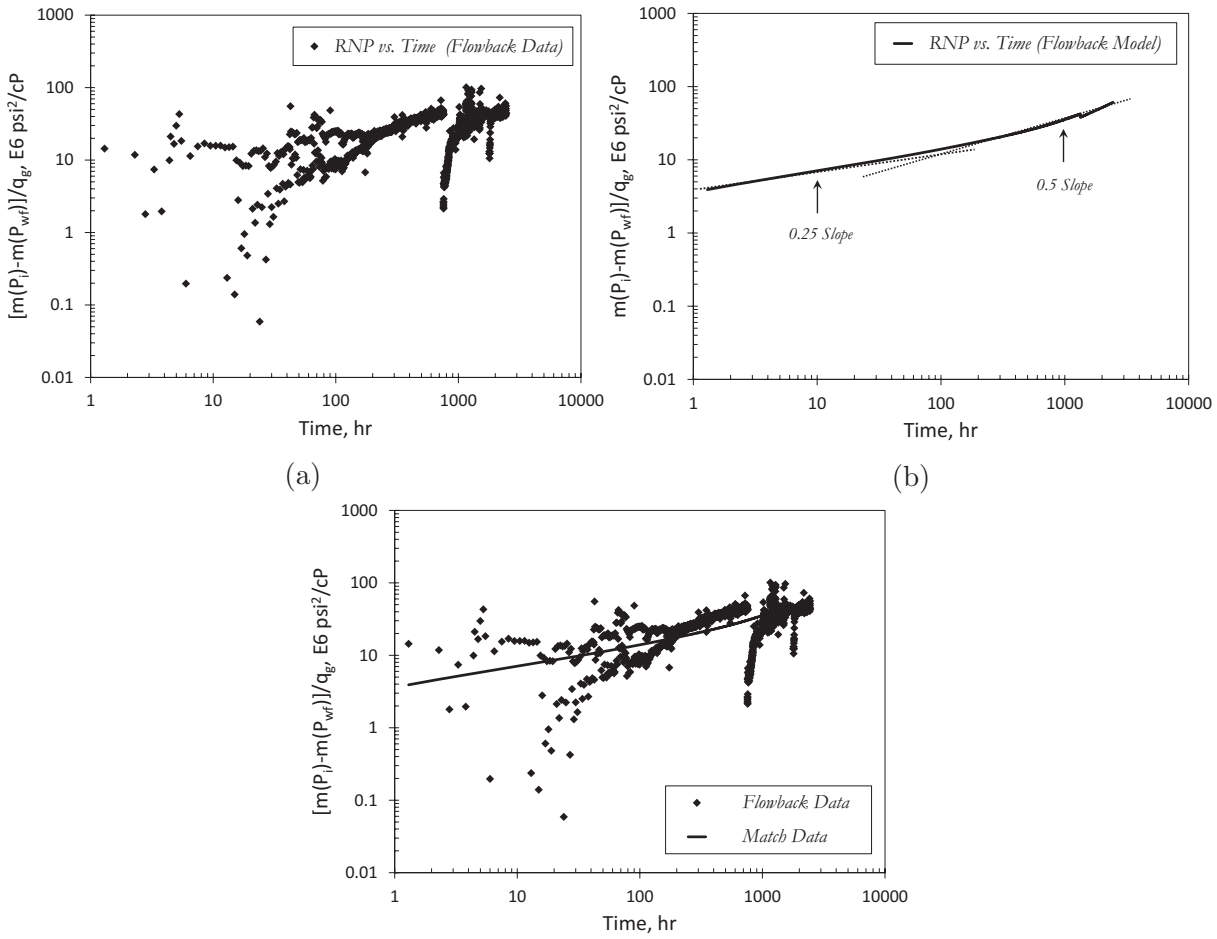

Fig. 3.17: History-match of Well X's flowback data with FAM. Rate normalized pseudo-pressure vs. time (vertical axis is in per unit rate). (a) Field data plot (b) FAM data plot showing flow regime slopes (c) Match of field data and proposed FAM.

Table 3.5: Half-length and dynamic-relative-permeability parameters estimated from history-matching FAM and flowback data for Well X

Parameter	**Guess**	**95% Confidence Interval**		
		Lower Bound	**Optimal Estimate**	**Upper Bound**
y_e	150 m	116.2 m	116.5 m	116.7 m
β_1	0.5	0.326	0.328	0.330
β_2 (pre-inflexion)	5.0×10^{-3}	5.86×10^{-3}	5.89×10^{-3}	5.92×10^{-3}
β_2 (post-inflexion)	10	15.03	15.12	15.21

3.4.3.3 Other Key Parameters

Fig. 3.18a shows the "actual" k_r history for Well X. This is obtained by putting β_1 and β_2 from Table 3.5 and β_3 from Fig. 3.16 in Eqs. 3.21 and 3.22 respectively.

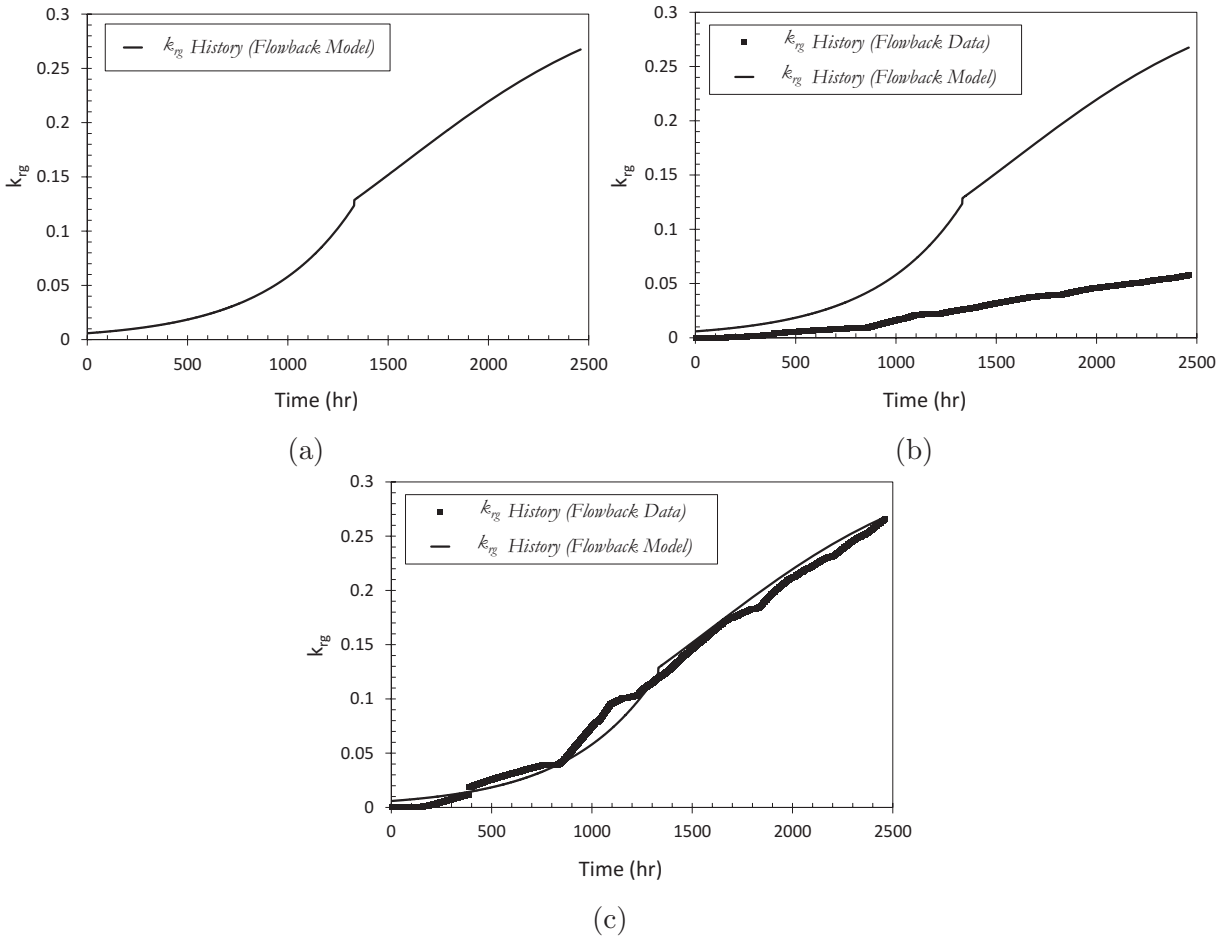

Fig. 3.18: History-match of Well X's k_r history from field data and FAM. (a) k_r history B from application of FAM (b) k_r history from field data and FAM before tuning V_{p_e} (c) Match of k_r history from field data and FAM after tuning V_{p_e}. "Optimal" $V_{p_e} \approx 39\%$ of total injected volume.

Fig. 3.18c shows the match of k_r history A and B obtained by tuning V_{p_e}. This match estimates V_{p_e} to be approximately 39% of the total injected volume of water (i.e. 61% leak-off into matrix, inactive secondary fractures, and isolated hydraulic fractures). Fig. 3.19 shows the "actual" dynamic-relative-permeability profile and average saturation history for the HF created from Well X.

Table 3.6 provides estimates of the leak-off volume ($V_{leak-off}$ = Total Injected Volume - V_{p_e}), the current water volume left in HF ($V_{w_{current}} = V_{p_e} - N_w(t)$) and the current load recovery ($LR_{current} = N_w(t)$ / TIV). The minimum and maximum half-lengths (from

volumetric analysis) estimated by putting V_{p_e} in Eqs. 3.12 and 3.13 are 15000 m and 19000 m respectively. The huge discrepancy of this y_e range of values from that in Tables 3.6 is explained in Section 3.5.

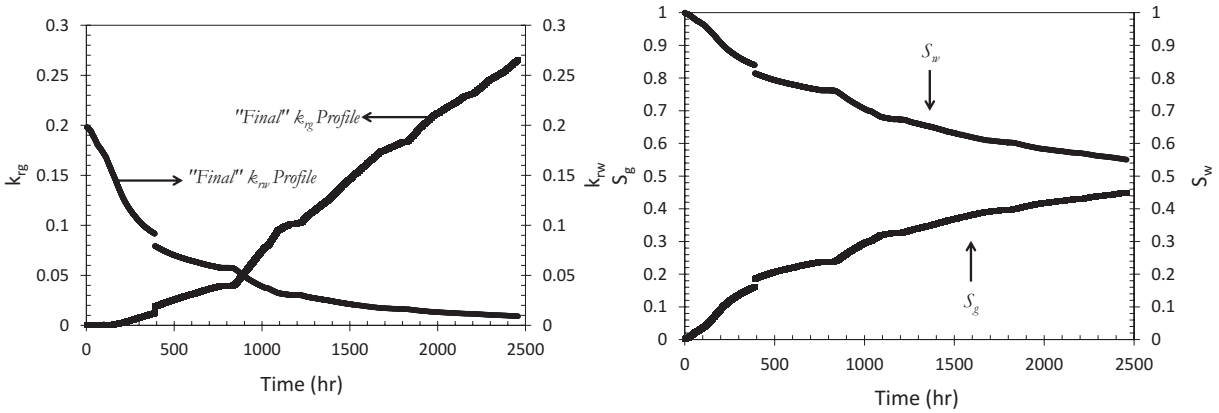

(a) (b)

Fig. 3.19: "Optimal" transient flow history in HF obtained by tuning V_{p_e} in the history-match of Well X's flowback and FAM. (a) Dynamic relative permeability profile (b) Average saturation history.

Table 3.6: Other key parameter estimates from flowback data analysis of Well X.

Output Parameter	Value	Units
TIV	69373	m^3
V_{p_e}	27000	m^3
$V_{leak-off}$	42000	m^3
$V_{w_{current}}$	15000	m^3
$LR_{current}$	18	%

3.4.3.4 Hydrocarbon Production Forecast

Long term, production forecast during post-flowback period is obtained by extending the time range after history-matching the short-period flowback rate and pressure data recorded from the field with FAM (see Eq. 3.23). Fig. 3.20a shows the post-flowback rate-normalized-pressure forecast based on the history-match in Fig. 3.17. Fig. 3.20b shows the

possible gas recovery forecast if Well X continues production at the current bottom-hole pressure (constant $P_{wf} \approx 850$ psia).

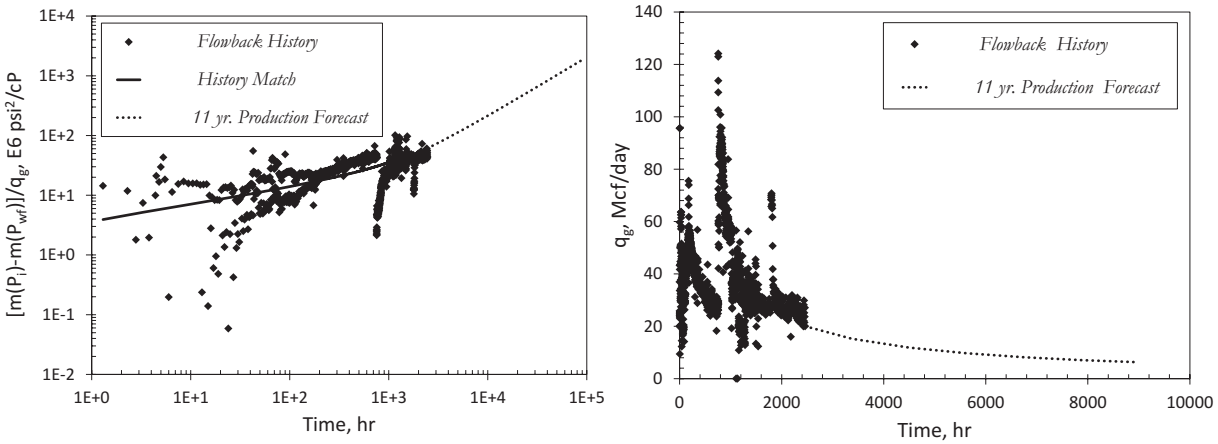

(a) (b)

Fig. 3.20: Production forecast from FAM history-match of two-phase flowback data from Well X. (a) Rate normalized pseudo-pressure plot on logarithmic scale (vertical axis unit is in per unit rate) (b) Gas rate plot on arithmetic scale.

3.5 Discussions

The results of this chapter can be summarized under five points namely: development of a mathematical model for transient two-phase flowback process; derivation of dynamic-relative-permeability as an explicit function of time; proposal of a workflow for flowback data analysis; application of this workflow to history-match flowback rate + pressure data; and prediction of gas recovery during post-flowback period from the history-match.

Result 1 relaxes the single phase assumption in the existing DPM using the concept of dynamic-relative-permeability. It is also significant for evaluating flowback performance and forecasting hydrocarbon recovery in reservoirs with negligible MF (micro-fractures and reactivated natural fractures). However, the assumption of negligible MF has to be confirmed from complementary studies (e.g. image logs and micro-seismic). Result 1 is applicable to two-phase data from Shale gas wells by replacing pressure with the appropriate pseudo-pressure function $[m(P)]$. An example of such pseudo-pressure function (Al-Hussainy and Ramey Jr., 1966) as used in this paper is:

$$m(P) = 2\int_{P_i}^{P} \frac{P}{\mu(P)z(P)}\,\mathrm{d}P$$

Similarly, the pseudo-dimensionless pseudo-pressure adapted for field data application in Section 3.4 is:

$$m_{DL} = \frac{k_F\sqrt{A_{cw}}[m(P_i) - m(P_{wf})]}{q(t)\mu P_i}$$

However for Shale gas wells, desorption plays a key role in the complex gas depletion process from the matrix during post-flowback period. This effect can be accounted for using a desorption compressibility term (Clarkson et al., 2007) for transient flow regime analysis. In this study, the desorption compressibility is implicitly accounted for in the $(c_t)_m$ value.

Result 2 shows that a general non-linear k_r function of time can be used to capture the transient phase saturation in the HF during flowback. This function does not violate the flow physics at key limiting conditions, as it tends to an end-point value ($= \beta_1$ at residual or constant S_w in HF). This ensures that FAM mathematically converges to the existing single-phase DPM at very long times when $k_{r_{HC}}(t \longrightarrow \infty) = \beta_1$ (see Eq. 3.18).

Result 3 proposes a workflow for estimating key reservoir parameters, evaluating flowback performance and forecasting hydrocarbon recovery. The uncertainty in estimated reservoir parameters from this workflow could be reduced if some parameters estimated from other sources (e.g outcrop studies, borehole micro-seismic and image logs from off-set wells) could serve as initial guesses. However, the reservoir parameters estimated from off-set well data or outcrop studies should be applied with caution (engineering judgment) due to the high degree of spatial heterogeneity in unconventional reservoirs. There is high noise to signal ratio in the early portion of the recorded data. This could be a result of wellbore storage due to choke and valve changing operations. This effect can be quantified by including a wellbore storage term in the Laplace-space solution (Ezulike and Igbokoyi, 2012).

Result 4 applies the proposed workflow on two-phase flowback data from multi-fractured Shale gas well. One key observation is the discrepancy in half-length estimates from model history-match (116.5 m) and effective pore-volume analysis ($15000 - 19000$ m) respectively. One key assumption in developing FAM is that there are negligible secondary fractures communicating with the bi-wing hydraulic fractures during flowback. However, it is assumed that the effective volume considered in obtaining DRP is the effective pore-volume (which includes any active secondary fractures). Obviously, this half-length discrepancy shows that the assumption of negligible secondary fractures in FAM might not be necessarily correct. However, the results of this chapter provide interesting observations. It tells us that there is an extra connected pore-volume that is 100 times larger than that

of the primary HF network (excluding the leak-off volume in non-connected hydraulic and secondary fractures and Shale matrix). The most probable source of this extra pore-volume is the induced or reactivated, propped or unpropped, secondary fracture networks (which could include natural fractures). Hence, subsequent studies will investigate the effects of active secondary fractures during flowback and post-flowback periods. Also, FAM's dual-porosity frmework would be extended to the triple-porosity framework proposed by (Ezulike and Dehghanpour, 2014a). Additionally, there is a huge difference in the effective leak-off water volume ($42,000\ m^3$) stored in the matrix and inactive fracture networks compared to the active HF pore-volume ($27,000\ m^3$). This could explain the low load recovery (Cheng, 2012) frequently recorded during post-flowback operations. The other key observation is that water and gas rate plots follow the same decreasing trend (a successful fracturing operation is expected yield increasing gas rate and decreasing water rate). One possible reason is that water could be acting as a plug in the interconnected secondary fractures or/and as a skin at the matrix–HF interface. This effect minimizes gas influx from the matrix. One possible solution to improve gas recovery in this situation is to shut-in the well for some time (based on upscaled imbibition rates from experimental studies) to allow the leak-off water volume to imbibe further away from both active MF and near-matrix-HF interface.

Result 5 predicts long-term post-flowback gas production from history-matching short-period flowback data. This could serve as a well/reservoir management tool for the industry to complement conventional production data analysis for improved fracture characterization. One important point of note is that the predictive capability of the proposed model is dependent on the quality and frequency of available data. For example, the prediction accuracy of flowback analysis from a new well with few data points is expected to be lower than the case with more data points of reliable quality.

3.6 Summary

A mathematical model (FAM) has been developed to analyze transient two-phase flowback data under variable bottom-hole rate and pressure well constraints. FAM is achieved by applying the concept of dynamic-relative-permeability on the existing single-phase DPM to account for the rapidly changing multiphase fluid saturations in the HF network. FAM converges to DPM at long times when the water-saturation in HF reaches a constant/residual value.

This chapter provides an integrated workflow for analyzing two-phase flowback data from multi-fractured horizontal wells, estimating key reservoir parameters, evaluating flow-

back performance and forecasting post-flowback hydrocarbon recovery.

Future studies will focus on the: extension of FAM to explicitly account for the presence of reactivated natural fractures in the static framework and include the effects of fracture closure; and numerical solution of the FAM flow equations using the complete (not simplified) DRP function.

Nomenclature

Symbols

a	Fracture aperture/width, L, m, $[ft]$.
c	Compressibility, Lt^2M^{-1}, atm^{-1}, $[Pa^{-1}$, $psi^{-1}]$.
h	Reservoir thickness, L, m, $[ft]$.
k	Bulk permeability of hydrocarbon phase, L^2, m^2 $[D]$.
l	Characteristic length, L, m, $[ft]$.
n	Number, L, m, $[ft]$.
q	Rate, L^3t^{-1}, $m^3.s^{-1}$, $[rb.day^{-1}]$.
r	Wellbore radius, L, m, $[ft]$.
s	Laplace variable, t^{-1}, s^{-1}, $[hr^{-1}$, $day^{-1}]$.
t	Time, t, s, $[hr$, $day]$.
x, y	Principal reference SRV co-ordinates , L, m, $[ft]$.
z	Gas compressibility factor, dimensionless.
A	Area, L^2, m^2, $[ft^2]$.
B	Formation volume factor, L^3L^{-3}, ft^3scf^{-1}, $[bblstb^{-1}]$.
I	Convergence skin, dimensionless.
L	Distance or length, L, m, $[ft]$.
N	Cumulative Production, L^3, m^3, $[ft^3]$.
P	Pressure of hydrocarbon phase, $ML^{-1}t^{-2}$, Pa, $[psi]$.
S	Saturation, dimensionless.
T	Connection area per unit volume of rock, L^{-1}, m^{-1}, $[ft^{-1}]$.
V	Volume, L^3, m^3, $[ft^3]$.
X	Horizontal well length, L, m, $[ft]$.
α	Interporosity shape factor, L^{-2}, m^{-2}, $[ft^{-2}]$.
β	Clean-up parameter, dimensionless.
ϕ	Bulk porosity, dimensionless.
λ	Interporosity transmissivity ratio.
μ	Viscosity of hydrocarbon phase, $ML^{-1}t^{-1}$, $Pa.s$, $[cP]$.

ω	Storativity ratio, dimensionless.
Δ	Change.

Superscripts

$\bar{}$	Laplace transform.
^{o}	End-Point.
^{r}	Residual.

Subscripts

$_c$	cross-section.
$_e$	equivalent or effective.
$_g$	Gas.
$_i$	Initial.
$_m$	Matrix.
$_n$	Normalized.
$_o$	Oil.
$_p$	Pore.
$_r$	Relative.
$_t$	Total.
$_w$	Well.
$_D$	Dimensionless.
$_F$	Hydraulic fracture.
$_L$	Reference length.
$_{wf}$	Bottom-hole flowing.
$_{CL}$	Fracture clusters per stage.
$_{HC}$	Hydrocarbon.
$_{inf}$	Inflexion point on relative-permeability curve.
$_{wav}$	Average water.

Chapter 4

A Complementary Approach for Uncertainty Reduction in Flowback and Post-flowback Production Data Analysis

4.1 Introduction

Tight reservoirs are formations with very low permeability. Hence they require a process like hydraulic fracturing to produce economic amounts of oil and gas. Multistage hydraulic fracturing (King, 2012; Cheng, 2012) involves injecting millions of gallons of fracturing fluid (a mixture of ≥ 90 % water, proppants and chemical additives) through horizontal wells to create multiple fractures. These fractures significantly increase the contact area between the wells and tight reservoirs.

After hydraulic fracturing, a large portion of the injected fluid remains in the created fractures. To ensure optimal flow rates from the stimulated well, the water in these fractures needs to be recovered before putting the well on a long-term hydrocarbon production (Crafton and Gunderson, 2007). This is achieved through flowback operations. Flowback is a short process where water (and some hydrocarbons) in the fractures is allowed to flow to the surface. The duration of this process varies from well to well and depends on the reservoir geology and operational challenges. Although, the flow rate and pressure of the fluids recovered during flowback are recorded, they are usually of poor quality and typically discarded. However, the industry in recent times have realized that flowback can provide the earliest opportunity to characterize both fracture and reservoir. This has prompted improvements in the quality and frequency of data measurement during flowback. Nevertheless, reliable data recording still faces some practical challenges like sand production (which can damage recording devices), data quality control, inter-well communication and optimal flowback management. Although flowback is a multiphase process, many existing flowback models (Crafton, 1997, 1998; Clarkson, 2012; Abbasi,

2013; Abbasi et al., 2014) either assume single phase flow or do not properly account for the rapid fluid saturation changes in the hydraulic fractures (HF). Some of these limitations are now accounted for in newer models such as Ezulike and Dehghanpour (2014b). However, the frequent well shut-in periods due to operational challenges (e.g. erosion of chokes and valves) still need to be accounted for in flowback models for reliable production forecasts during post-flowback periods

After flowback, water saturation in the active fractures is expected to become negligible such that the stimulated well is ready to be put on production. Although the recovered fluid is mainly hydrocarbon during post-flowback production, flow from the well is still multiphase. However, most of the analytic models available for conventional production data analysis (PDA) are single phase. Examples of such models include the: radial dual-porosity models (Carlson and Mercer, 1991); linear dual-porosity models (El-Banbi, 1998; Bello, 2009); radial triple-porosity models (Ozkan et al., 2010; Dehghanpour and Shirdel, 2011); linear triple-porosity models (Al-Ahmadi, 2010; Al-Ahmadi and Wattenbarger, 2011; Ali et al., 2013); trilinear flow model (Brown et al., 2011); and quadrilinear flow model (Ezulike and Dehghanpour, 2014a).

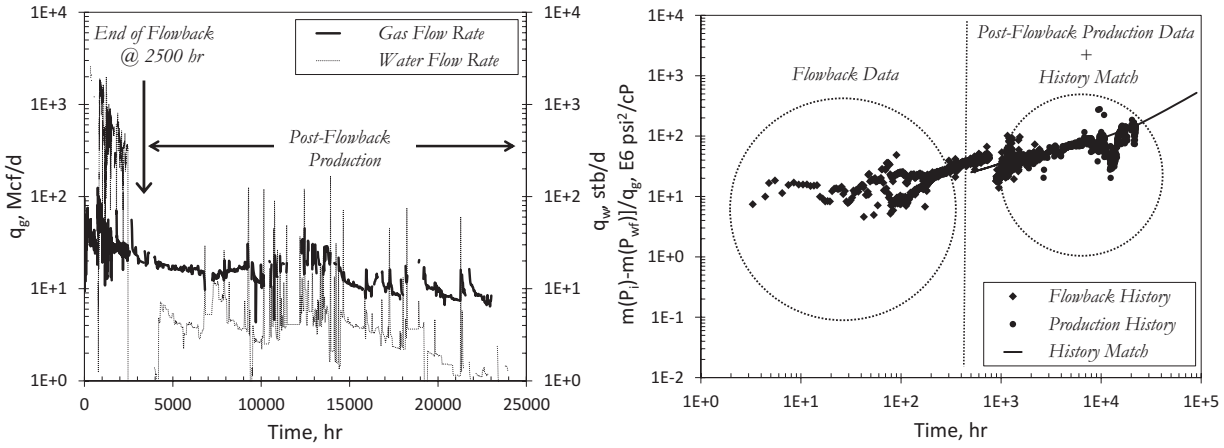

(a) (b)

Fig. 4.1: Field data plots showing flowback and post-flowback production data from a multi-fractured horizontal well. (a) Transient two-phase gas and water flow rate. (b) Rate normalized pressure (vertical axis is in per unit rate). The production data is history-matched with a type-curve from the single phase linear dual porosity model (Bello, 2009). It is done independent of flowback data from the same well.

One key challenge facing conventional PDA is non-uniqueness of solution. This causes uncertainty in reservoir parameter estimates and hydrocarbon forecasts. Also, the fact that post-flowback production data is still multiphase (Alkouh et al., 2013; Alkouh and

Wattenbarger, 2013) violates the key assumption of single phase (Fig. 4.1a) in many PDA models. Hence, there is a need for an alternative approach to PDA.

This chapter proposes an integrated approach to reduce the uncertainty in reservoir parameter estimates and hydrocarbon forecasts. This approach uses flowback data analysis (FDA) as a constraint to guide the conventional psot-flowback PDA. This chapter has three main parts — independent flowback data analysis, independent post-flowback data analysis, complementary flowback and post-flowback data analysis.

4.2 Methodology

The models used to investigate the benefits of analyzing flowback and post-flowback data together are the linear dual-porosity model [DPM, Bello (2009)] and the flowback analysis model [FAM, Ezulike and Dehghanpour (2014c)]. These models use the dual-porosity static framework shown in Fig. 4.2. DPM is a single phase model which accounts for reservoir depletion from both matrix and hydraulic fractures, under the assumption of negligible secondary fracture effects. FAM is a multiphase model which extends DPM by incorporating a dynamic-relative-permeability function (an explicit relationship between relative permeability and time to capture the rapidly changing fluid saturations in hydraulic fractures) into its static framework. Details of the implementation of DPM and FAM are provided in the results section of this chapter.

The dimensionless wellbore pressure equation for FAM in Laplace space under variable rate inner boundary conditions is given in Eq. 4.1 (Ezulike and Dehghanpour, 2014c). Eq. 4.1 simplifies to the dimensionless wellbore pressure equation for DPM when $\beta_2 = 1$ and $\beta_3 = 0$ for $0 \leq t_{_{D_{AC}}} \leq t_{_{D_{AC\,inf}}}$, and $\beta_1 = 1$ and $\beta_2 = 0$ for $t_{_{D_{AC}}} > t_{_{D_{AC\,inf}}}$ respectively.

$$\overline{P}_{_{wDL}} = \frac{f^*(s)}{\sqrt{f(s)}} \left\{ \coth\left(\sqrt{f(s)} y_{_{De}}\right) + I_{_D} \sqrt{f(s)} \right\} \tag{4.1}$$

$$\text{where } I_{_D} = \frac{r_w}{\sqrt{A_{cw}}} I \tag{4.2}$$

$$\text{and } f(s) = \begin{cases} \dfrac{1}{\beta_2}\left[\omega_{_F}(s+\beta_3^*) + \dfrac{\lambda_{_{AC,Fm}}}{3}\sqrt{f_m(s+\beta_3^*)}\tanh\left(\sqrt{f_m(s+\beta_3^*)}\right)\right] & 0 \le t_{_{D_{AC}}} \le t_{_{D_{AC}inf}} \\ \dfrac{1}{\beta_1}\left(\omega_{_F}\left[s+\beta_2(s+\beta_3^{**})\right] + \dfrac{\lambda_{_{AC,Fm}}}{3}\left[\sqrt{f_m(s)}\tanh\left(\sqrt{f_m(s)}\right) + \right.\right. & \\ \left.\left.\beta_2\sqrt{f_m(s+\beta_3^{**})}\tanh\left(\sqrt{f_m(s+\beta_3^{**})}\right)\right]\right) & t_{_{D_{AC}}} > t_{_{D_{AC}inf}} \end{cases} \tag{4.3}$$

$$\text{and } f^*(s) = \begin{cases} \dfrac{1}{\beta_2}\left[\dfrac{1}{(s+\beta_3^*)}\right] & 0 \le t_{_{D_{AC}}} \le t_{_{D_{AC}inf}} \\ \dfrac{1}{\beta_1}\left[\dfrac{1}{s} + \dfrac{\beta_2}{(s+\beta_3^{**})}\right] & t_{_{D_{AC}}} > t_{_{D_{AC}inf}} \end{cases} \tag{4.4}$$

$$\text{and } f_m(s) = \frac{3s\omega_m}{\lambda_{_{AC,Fm}}} \tag{4.5}$$

This study is done under three key steps (Fig. 4.3). Step 1 handles data processing, Step 2 involves independent flowback and post-flowback data analyses and Step 3 deals with constrained post-flowback data analysis.

Step 1 entails gathering and preparing quality controlled, flowback and post-flowback production data from the same wells. This is achieved by ensuring that there are no spurious discontinuities between the trends of flow rate and cumulative production data recorded during flowback and post-flowback production periods.

Step 2 starts with an independent flowback data analysis using FAM (Ezulike and Dehghanpour, 2014c) to history-match flowback data from Step 1, estimate key fracture parameters (e.g. effective half-length and pore-volume of interconnected fracture networks) and forecast post-flowback hydrocarbon production. It continues with an independent production data analysis using DPM (Bello, 2009) to history-match post-flowback data from Step 1. Finally, it ends with a comparison of the results from independent flowback and post-flowback data analyses.

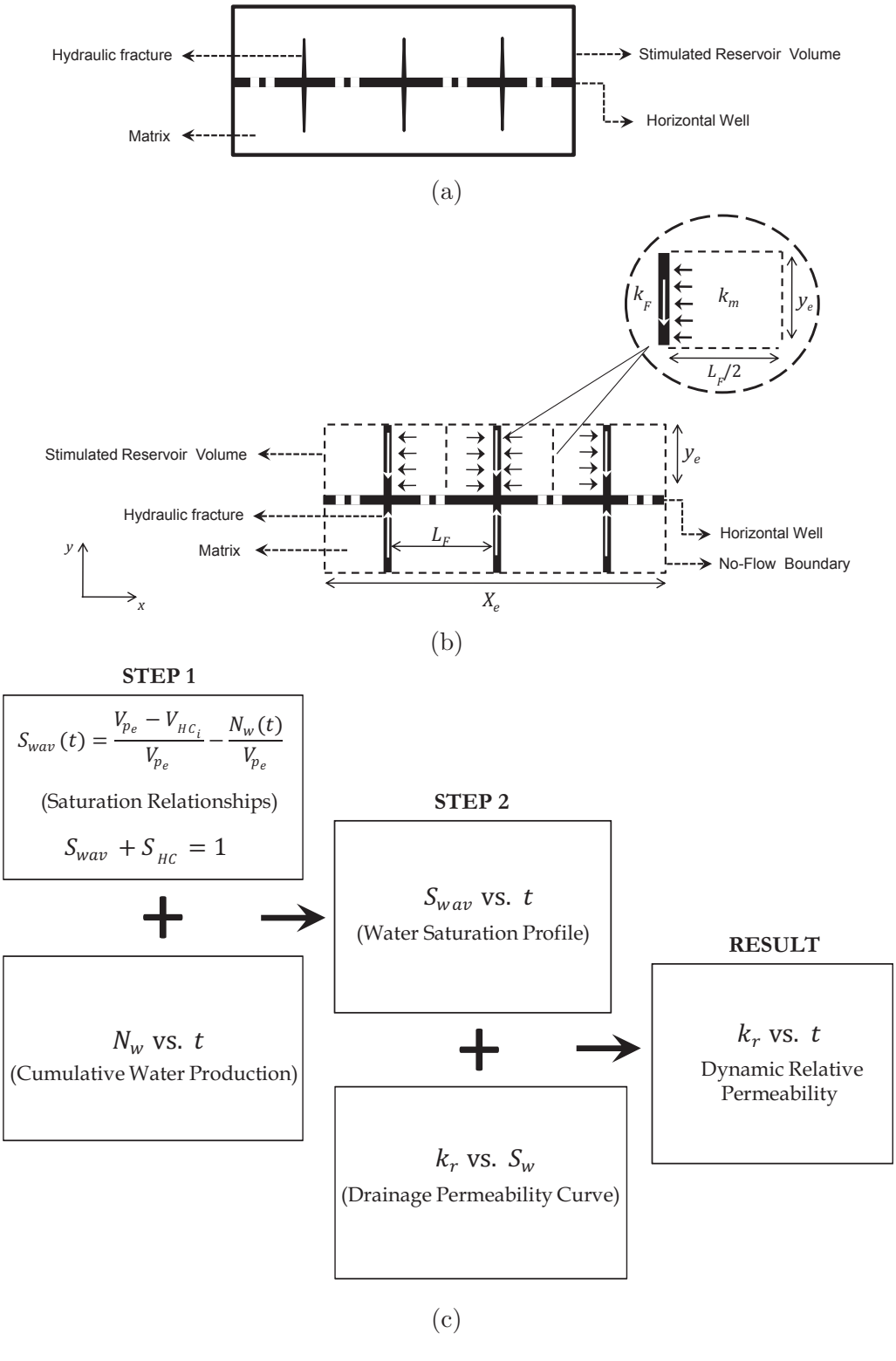

Fig. 4.2: Horizontal cross-section of idealized dual-porosity framework after multi-stage hydraulic fracturing in tight reservoirs. (a) static reservoir framework (b) single-phase dynamic framework with arrows showing fluid flow directions (c) dynamic relative permeability function that incorporates multiphase effects to the static reservoir framework. Adapted from Ezulike and Dehghanpour (2014c).

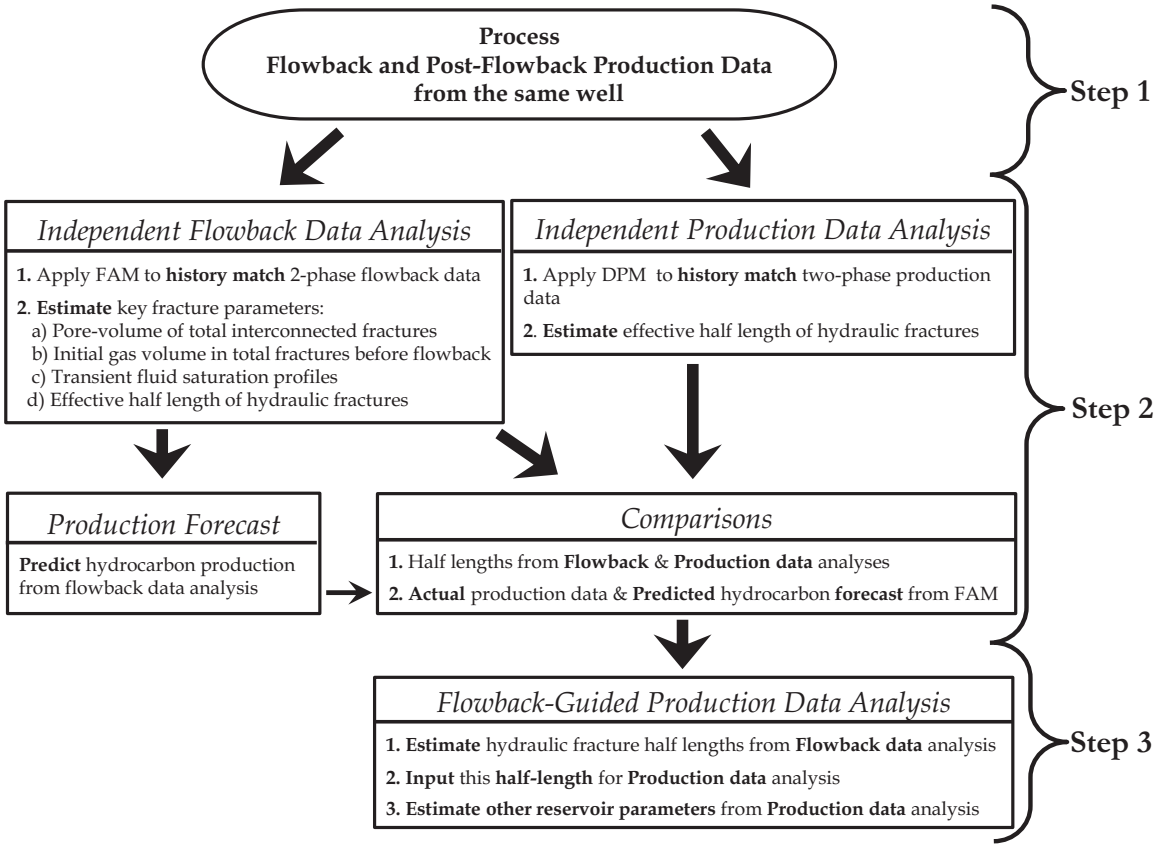

Fig. 4.3: Three-step procedure for complementary flowback and production data analysis.

Step 3 involves a flowback-guided, production data analysis. It tests the accuracy of FAM to predict gas production in the field during post-flowback periods. This is achieved by comparing the hydrocarbon forecast from FDA in step 2 against actual field production. The results of this accuracy test would make a case for combining both flowback and post-flowback data analyses to minimize the uncertainty associated with fracture and reservoir parameter estimates from conventional production data analysis.

The history-match cases in this chapter are automated using the non-linear regression (*nlinfit*) module in Matlab 2012a and a module for residual sum of squares in Microsoft Excel. The "*nlinfit*" module captures the degree of certainty (confidence interval) with which a range of output parameters represent the model physics under investigation. This confidence interval is then be subsequently used to generate probabilistic distributions for the output parameters.

4.3 Results

This starts with a brief description of well pattern and geology considered in the chapter. Next is a qualitative analysis based on volumetric balance calculations. Finally, it ends with quantitative analyses involving independent flowback data analysis, independent post-flowback production data analysis, and flowback-guided production data analysis. One key goal is to evaluate the benefits of complementary flowback and post-flowback data analysis over conventional production data analysis.

4.3.1 Well Pattern and Geology

This chapter considers eight multi-fractured (Fig. 4.4) Shale gas wells. They are drilled from a single well pad (Pad X) and completed in the Muskwa and Otter Park members of the Horn River Shale group.

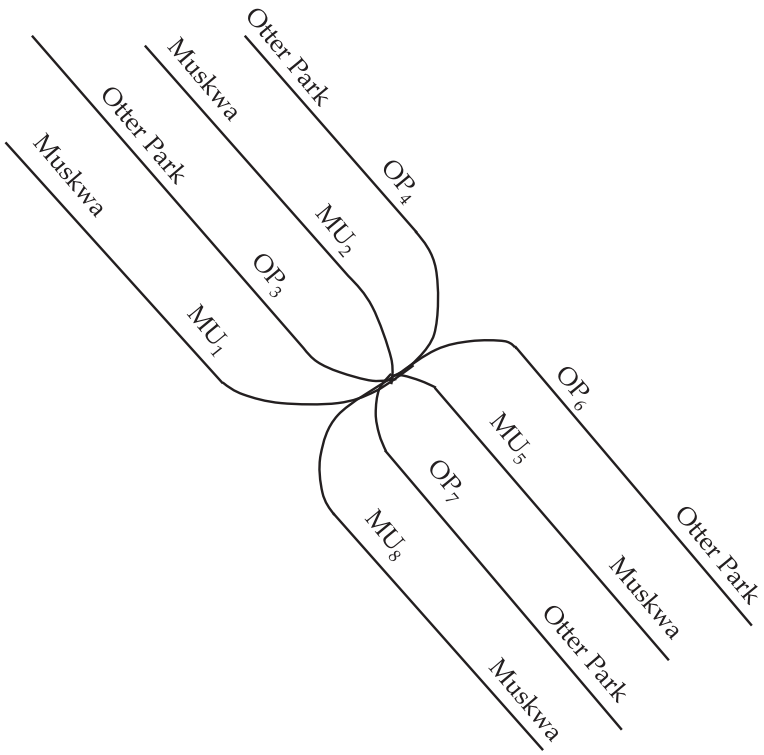

Fig. 4.4: Pictorial representation of Pad X. Wells are drawn according to length, named according to completion formation and numbered according to flowback sequence.

Each bank of Pad X has four wells with two drilled into each of the Muskwa and Otter park formations respectively. Wells in the left bank (MU_1, MU_2, OP_3 and OP_4) are completed and put on production between day 1 and 7. After producing for about a

month, wells in the left bank are shut-in for approximately 29 days. Wells in the right bank (MU_5, OP_6, OP_7 and MU_8) are then brought on between day 40 and 46, and shut-in until day 75 when all eight wells are opened in Pad X.

The Horn River Shales have an approximate total organic content of 4% by weight, with an average composition of 60% quartz, 20% clay, 10% carbonates and 10% of other minerals (Virués et al., 2013). Due to high quartz content and complex basin history, the Horn River Shales have abundant natural fractures which are optimally oriented to the in-situ stress field (Virués et al., 2013). This makes the natural fractures prone to reactivation during hydraulic fracturing.

The Shale reservoir under consideration is over-pressured with gas (predominantly methane) of 0.66 specific gravity. The reservoir has an initial pressure, temperature, gas viscosity and gas saturation of 4900 psi, 279 ^oF, 0.02 cP and 90% respectively. Also, it has an average reservoir thickness (h), matrix porosity (ϕ_m) and compressibility $(c_t)_m$ of 390 ft, 5%, and 6.5×10^{-6} psi^{-1} respectively. On the basis of field experience and existing Shale literature (Gale et al., 2014), the average hydraulic fracture aperture ($a_{_F}$), porosity ($\phi_{_F}$) and compressibility $(c_t)_{_F}$ are assumed to be $1mm$, 50%, and 6.482×10^{-4} psi^{-1} respectively. The hydraulic fracture permeabilities are estimates from production data analysis done by the operator using a commercial numerical simulator. Other properties for Pad X are given in Table 4.1.

Table 4.1: Reservoir and well parameters for Pad X. MU = Muskwa and OP = Otter Park. t_{sh} = shut in time after MU_1 was first opened for flowback. X_e = horizontal well. $n_{_F}$ = fracture stages, $n_{_{CL}}$ = cluster per fracture stage, $L_{_F}$ = fracture spacing. TIV = Total Injected Volume. rm^3 = reservoir cubic meters.

Well	t_{sh} **(days)**	k_m **(mD)**	$k_{_F}$ **(mD)**	X_e **(m)**	$n_{_F}$	$n_{_{CL}}$	$L_{_F}$ **(m)**	**TIV** (rm^3)
MU_1	2	4.47×10^{-4}	70000	1400	15	1	88	69373
MU_2	3	3.79×10^{-4}	28000	1700	17	4	94	66246
MU_5	40	2.66×10^{-4}	31000	1500	15	4	94	53927
MU_8	46	3.44×10^{-4}	31000	1600	17	1	89	54217
OP_3	4	4.42×10^{-4}	200000	1900	20	1	90	75504
OP_4	6	3.43×10^{-4}	28000	1500	15	4	94	60590
OP_6	42	2.06×10^{-4}	16000	1970	20	4	94	54217
OP_7	43	4.47×10^{-4}	90000	1900	20	1	90	58678

4.3.2 Qualitative Analysis

This part presents a qualitative analysis on volumetric flowback data recorded at surface conditions from wells in Pad X. Fig. 4.5 shows the multiphase correlation plots used to convert the two-phase flowback and post-flowback data to bottom-hole conditions. These correlations are modules from the IHS[21] Harmony software.

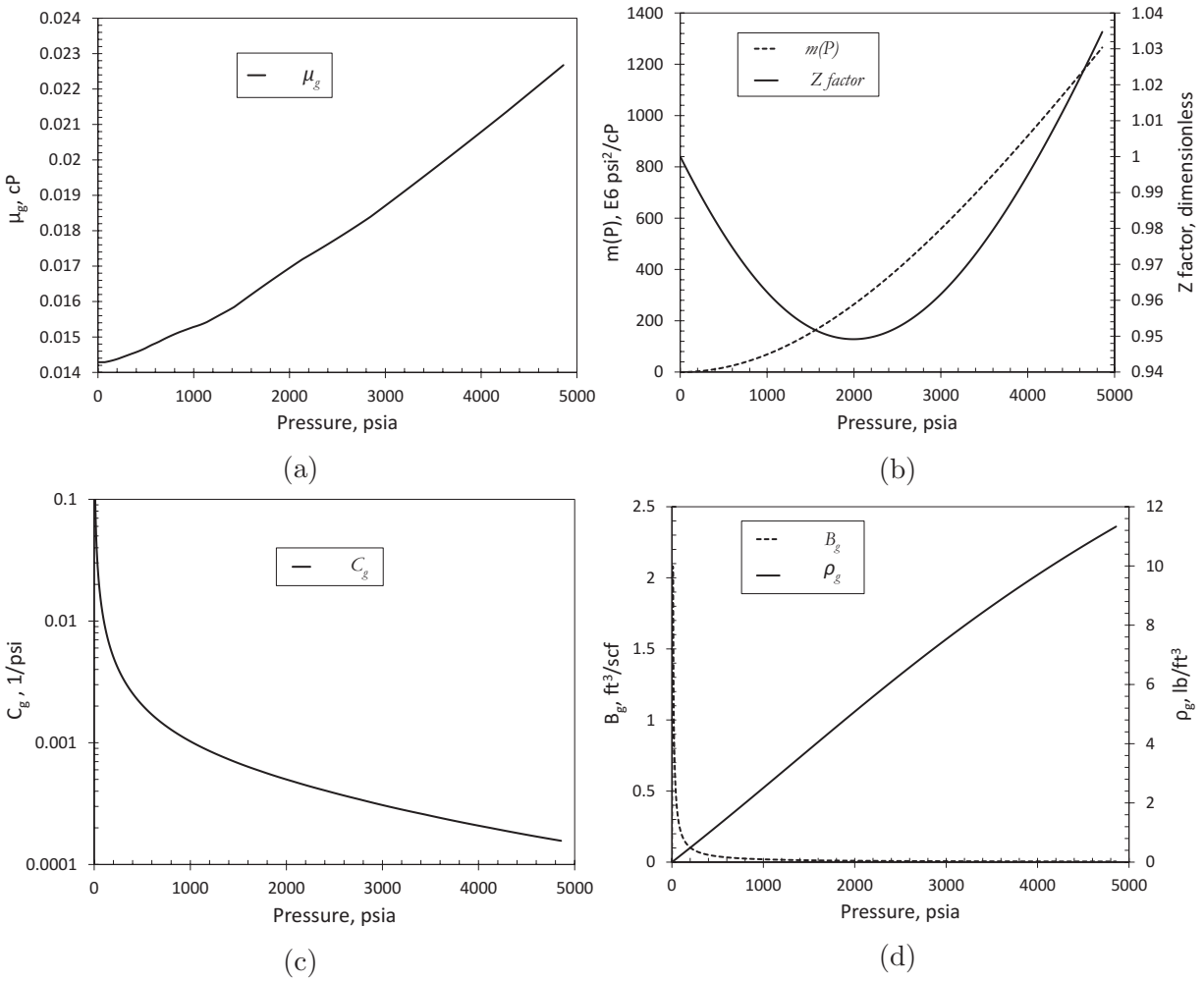

Fig. 4.5: Transient multiphase correlation models for converting Well MU_1 flowback data from surface to bottom-hole conditions. (a) Viscosity (b) Pseudo-pressure and Z factor (c) Compressibility and (d) Formation volume factor and density.

Fig. 4.6 shows the gas and water flow rates for two choice wells from Pad X. It covers both the flowback and post-flowback production time periods. Fig. 4.6 reveals that the two-phase flow during flowback continues in the post-flowback production period. Also, it shows that post-flowback production only becomes single phase after long times (ap-

[21] https://www.ihs.com/products/harmony-oil-well-performance-software.html (last accessed 31-01-2017).

proximately 25000 hours in this case) when water rate gets close to zero values. Table 4.2 summarizes the volumetric analysis of well data from Pad X after flowback.

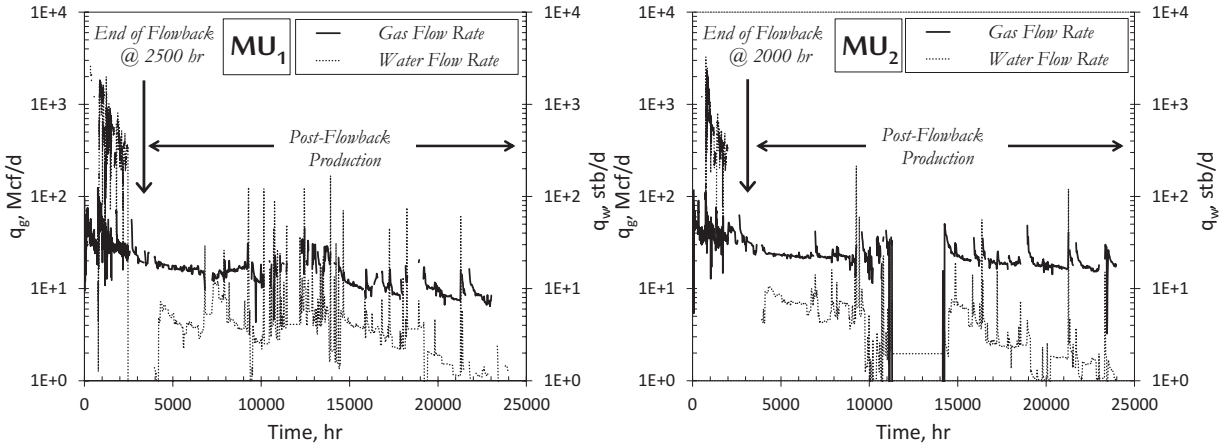

(a) (b)

Fig. 4.6: Gas and water flow rate plots for Pad X. (a) MU_1 (b) MU_2.

Table 4.2: Parameter estimates from volumetric analysis of well data from pad X. t_{sh} = shut in time after MU_1 was first opened for flowback, t_{fl} = duration of flowback, N_w and N_p = cumulative water and gas production at the end of flowback respectively, $LR = N_w$ / TIV = current load recovery, and $PR = N_p$ / TIV = current pay recovery. All data are taken at the end of flowback and have been converted to initial reservoir conditions. rm^3 = reservoir cubic meters.

Well	t_{sh} **(days)**	t_{fl} **(days)**	**TIV** (rm^3)	N_w (rm^3)	N_p (rm^3)	LR (%)	PR (%)
MU_1	2	102	69373	12186	100638	18	145
MU_2	3	83	66246	9148	99303	14	150
MU_5	40	57	53927	6915	74661	13	138
MU_8	45	33	54217	4453	34733	8	64
OP_3	4	79	75504	7882	70264	10	93
OP_4	6	102	60590	12186	100638	20	166
OP_6	42	84	54217	5030	131383	9	242
OP_7	43	40	58678	5020	44646	9	76

4.3.3 Quantitative Analysis

This part deals with independent flowback data analysis, independent post-flowback production data analysis, and flowback-guided production data analysis. The independent flowback data analysis estimates reservoir parameters and forecasts gas production during post-flowback periods. The independent post-flowback production data analysis investigates the effects of applying a single phase model (which ignores secondary fracture effects) on the rate and pressure data from wells completed in reservoirs with abundant secondary fractures and two-phase fluid flow. The flowback-guided production data analysis investigates an appropriate way to combine both flowback and post-flowback data as a single complementary analysis. One important point of note is that all the relevant input parameters are assumed to hold true for all analyses.

4.3.3.1 Independent Flowback Data Analysis

Independent FDA is achieved in two linked steps — relative permeability history-match using residual sum of square method and rate-normalized-pressure (RNP) history-match using non-linear regression method. Fig. 4.7 summarizes the tightly coupled procedure for the relative permeability and RNP history-matches. Details of this procedure are provided in Ezulike and Dehghanpour (2014c).

Here, FAM is applied to history-match the flowback data for seven of the eight multi-fractured wells from Pad X. The last well (MU_8) is left out because the later part of its rate-normalized pressure plot (RNP against time) was difficult to history-match with FAM. The match also provides an average saturation and relative permeability history in the fracture stages of these wells.

The relative permeability history-match is done by tuning the initial gas volume (V_{gi}) in, and effective pore-volume (V_{p_e}) of, the active fracture network. This is done until there is at least a 90% match between the gas relative permeability profile [$k_{rg}(t)$] from field cumulative water and gas flowback data and the two-phase drainage relative permeability curve used for FAM. Fig. 4.8 shows the history match of $k_{rg}(t)$ in the fracture network (during flowback) of seven wells from Pad X history and the two-phase drainage relative permeability curve used for FAM. This match yields β parameters (Ezulike and Dehghanpour, 2014b). These parameters describe how fast the fractures are cleaned during the flowback process. The $k_{rg}(t)$ history-match is coupled with the RNP history-match in Fig. 4.8 using the β parameters (determined by the shape of the RNP curve). Table 4.3 shows the parameter estimates from tuning the $k_{rg}(t)$ history-match. Also, Table 4.3 provides estimates of the leak-off volume ($V_{lf} = TIV - V_{p_e}$) lost from the active fracture

network and the volume of water left in the fracture network ($V_w = V_{p_e} - N_w(t)$). N_w is the cumulative water production at the end of flowback. All these parameters have been converted to initial reservoir conditions. It is surprising to see zero V_{gi} values for most wells in Fig. 4.3, since immediate gas production is recorded in most of these wells at the onset of flowback. One reason for this could be the coupling of relative permeability (which assumes a volumetric total fracture network) history-match and RNP (which assumes a planar bi-wing hydraulic fracture of fixed length and height) history-match. This coupling appears to reduce FAM's sensitivity to identify lower V_{gi} values.

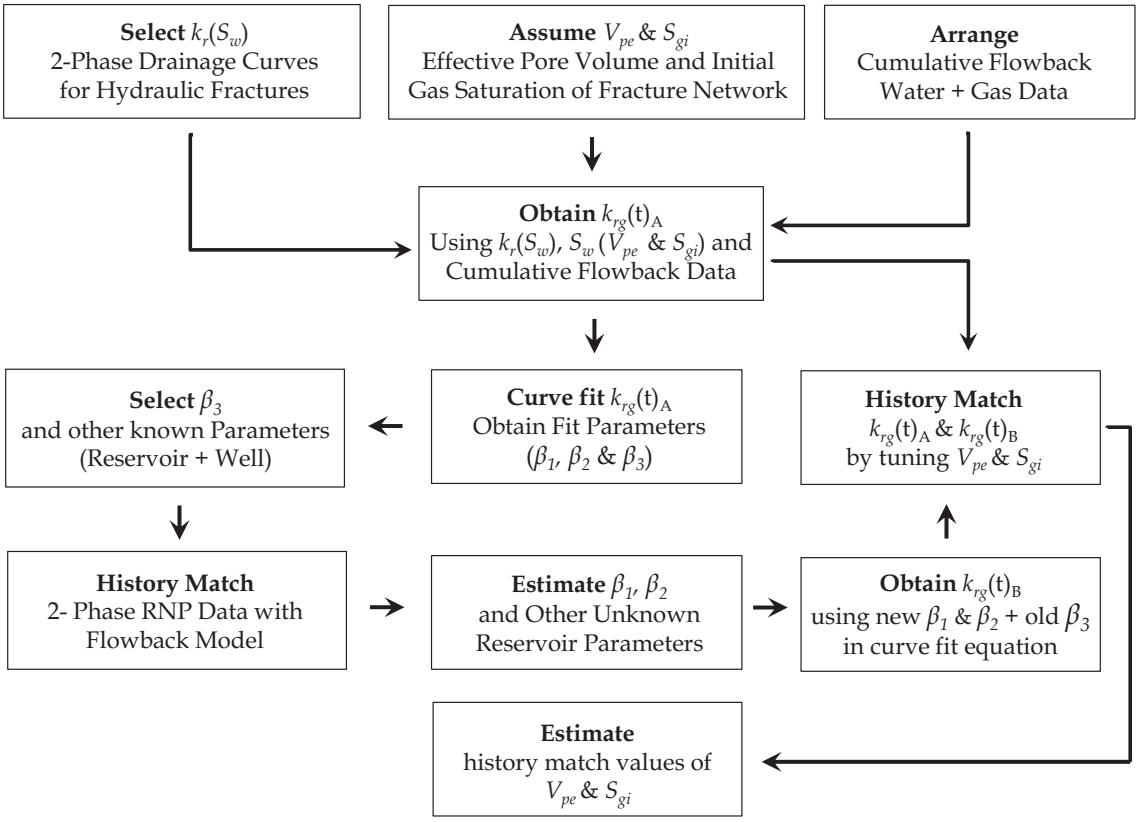

Fig. 4.7: Flowchart for independent flowback data analysis.

Fig. 4.9 shows the RNP history-match between the flowback data of seven wells from Pad X and FAM. The match is coupled with and constrained by the β parameter outputs from the $k_{rg}(t)$ history-match in Fig. 4.8. Tables 4.1 and 4.4 show the input data and hydraulic fracture half-length estimates from the history-match respectively. The low signal to noise ratio in the early 60 – 100 hours plots in Fig. 4.9 could be a result of storage (wellbore + fracture) effects due to shut-in after fracturing and before flowback. This is deduced from the clear unit slope (Abbasi et al., 2014) in Fig. 4.9. However, this chapter focuses on the possible representative flow regimes obtainable in the absence of

storage effects. This explains the match discrepancy in the early hours of Fig. 4.9. The interpretation procedure assumes continuous operations (ignoring the shut-in that occurs between 700 – 1000 hours during flowback) on most plots in Fig. 4.9. The choice of initial guess might introduce bias to the history-match shown in Fig. 4.9. However, other input half-length guesses between 100 and 1000 m gave results similar to those in Table 4.4.

Table 4.3: Parameter estimates from the relative permeability history-match of well data from pad X. All data are calculated under initial reservoir conditions after flowback.

Well	V_{p_e} (rm^3)	V_{gi} (rm^3)	V_{lf} (rm^3)	V_w (rm^3)
MU_1	31441	92	37934	19253
MU_2	27301	0	38947	18152
MU_5	14640	0	39288	7725
OP_3	22107	0	53399	14223
OP_4	24948	0	35644	12760
OP_6	12089	1580	42129	7059
OP_7	8847	0	49832	3827

Table 4.4: Hydraulic fracture half-length estimates for wells from Pad X after flowback data analysis.

Well	**Initial Guess**	**95% Confidence Interval**		
		Lower Bound	**Optimal Estimate**	**Upper Bound**
MU_1	150 m	117.9 m	118.2 m	118.5 m
MU_2	150 m	132.1 m	133.0 m	133.5 m
MU_5	150 m	105.6 m	107.0 m	107.6 m
OP_3	150 m	72.8 m	73.0 m	73.8 m
OP_4	150 m	97.6 m	98.0 m	98.2 m
OP_6	150 m	153.8 m	155.0 m	155.7 m
OP_7	150 m	52.2 m	52.0 m	52.3 m

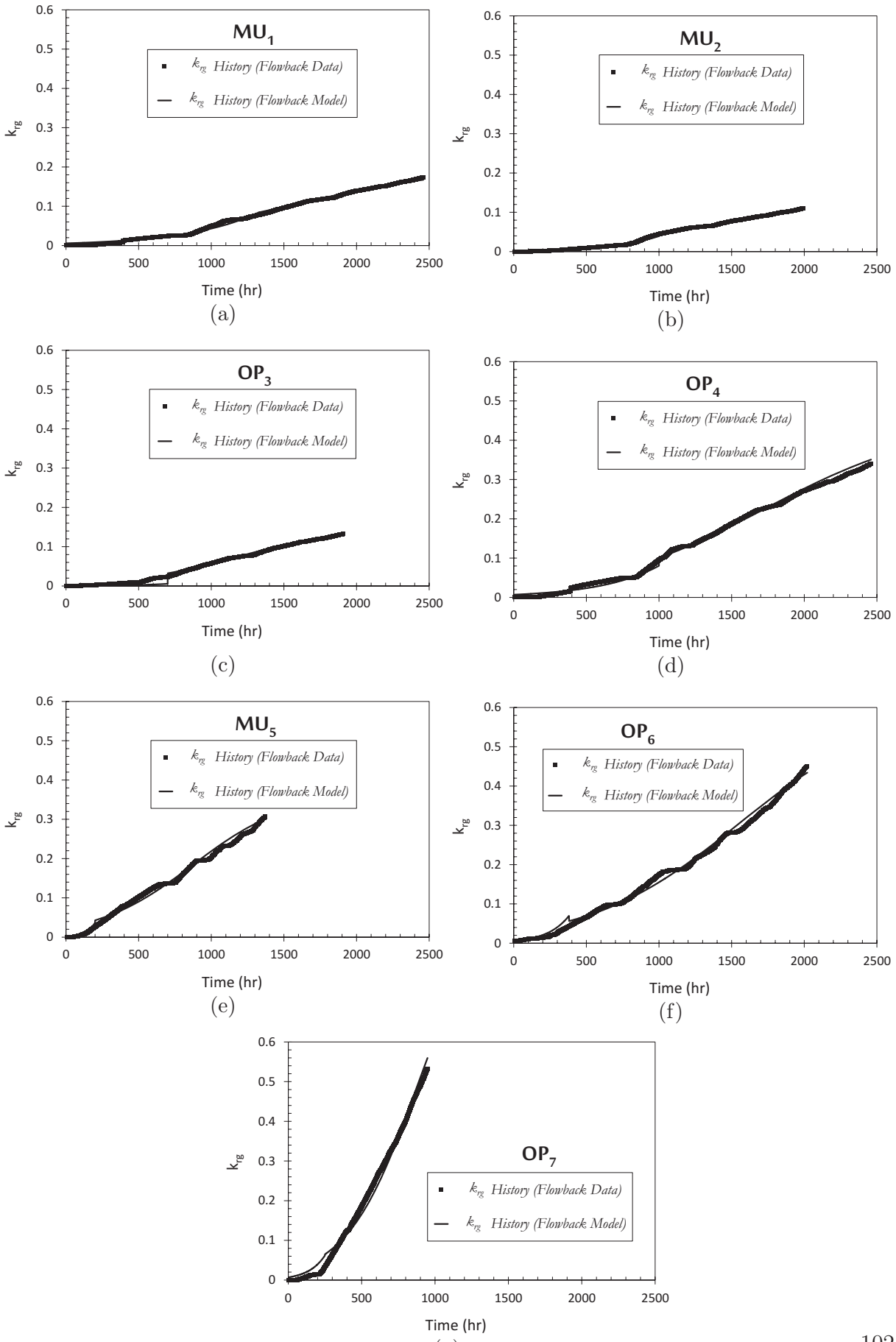

Fig. 4.8: History-match of relative permeability in the hydraulic fractures of seven wells from Pad X. The plots are labeled according to flowback sequence.

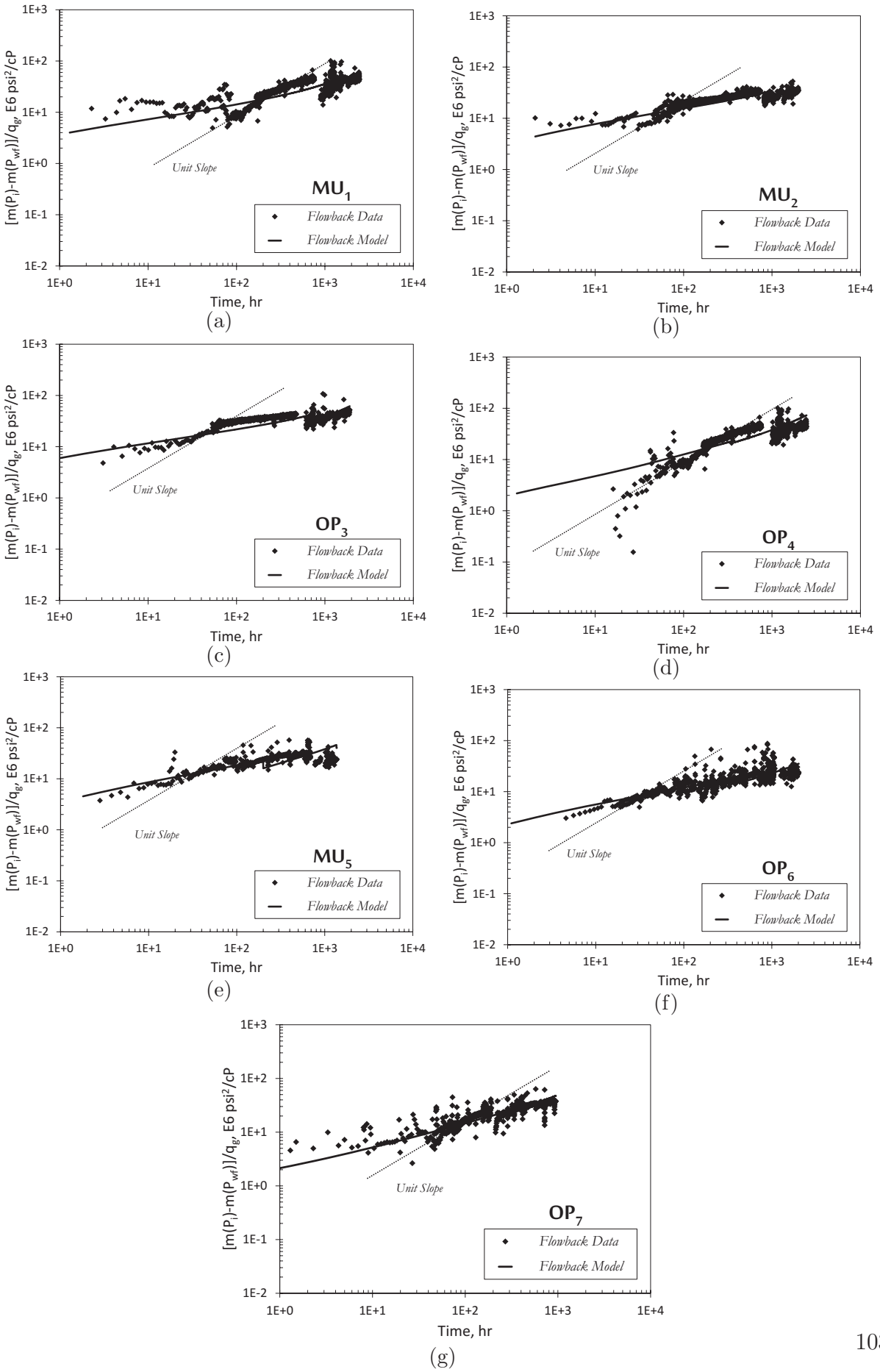

Fig. 4.9: Rate normalized plot for the history-match of flowback data of seven wells from Pad X. The unit of the vertical axis is per unit rate and the dotted unit slope line represents storage (wellbore + fracture) effects. The plots are labeled according to flowback sequence

4.3.3.2 Independent Post-Flowback Production Data Analysis

This part presents a history-match of two-phase post-flowback production data from Pad X using type-curves from the single phase dual-porosity model, DPM (Bello, 2009). It investigates the impact of ignoring multiphase effects on post-flowback, production data analysis. The focus will be on wells MU_1 and MU_2.

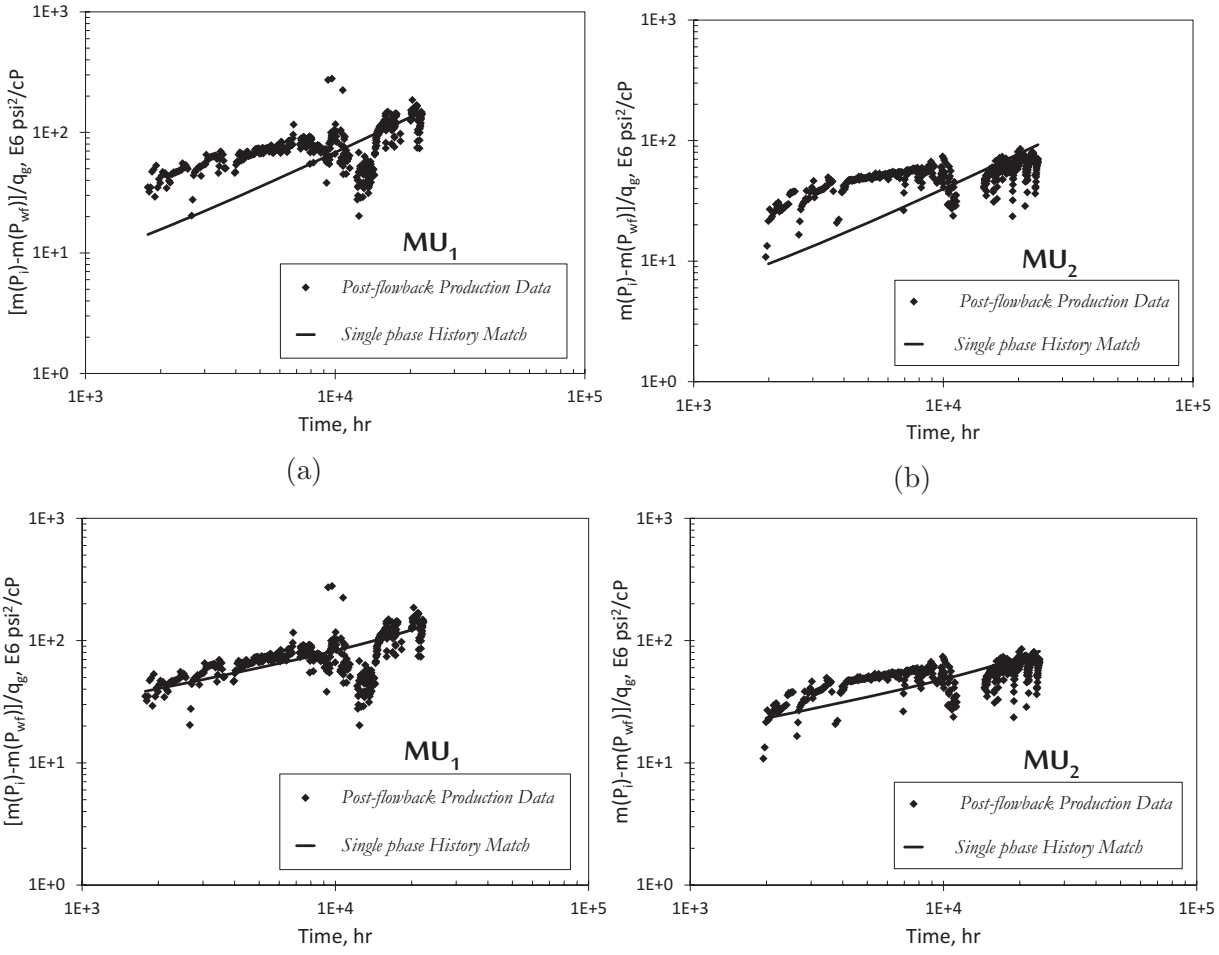

Fig. 4.10: Rate normalized plot for the DPM history-match of post-flowback production data from wells MU_1 and MU_2 (the vertical axis is in per unit rate). Case 1 (a & b) is done with hydraulic fracture half-length as output parameter. Case 2 (b & c) is done with hydraulic fracture half-length and permeability as output parameters.

Since this post-flowback data comes from the same well which has just undergone flowback, the same input parameters from flowback data analysis (FDA) are used for post-flowback, production data analysis (PDA). This provides reasonable ground for comparing the results from FDA and post-flowback PDA. DPM assumes that multiphase, secondary fractures and gas desorption effects are negligible. Therefore, there will be two

cases for DPM history-match. Case 1 is run to test if multiphase, secondary fractures and gas desorption effects can be ignored for these wells, Case 2 is run to test how multiphase, secondary fractures and gas desorption effects influence the post-flowback history-match in these wells. Case 1 tunes the hydraulic fracture half-length as the only unknown parameter, while Case 2 tunes hydraulic fracture half-length and effective gas permeability with the aim to obtain the best match. Fig. 4.10 shows the post-flowback history-matches of wells MU_1 and MU_2 with DPM (ignoring flowback data). Table 4.5 gives the resulting parameter estimates. Although, the choice of initial parameter guess might bias the history-match, input half-length guesses as low as 50 m gave results similar to those in Table 4.5.

Table 4.5: Hydraulic fracture half-length and effective gas permeability estimates for Wells MU_1 and MU_2 after independent post-flowback production data analysis.

Parameter	**Well**	**Guess**	**95% Confidence Interval**		
			Lower Bound	**Optimal Estimate**	**Upper Bound**
			Case 1 (Figs. 4.10a and 4.10b)		
y_e	MU_1	150 m	391.4 m	396.1 m	400.8 m
	MU_2	150 m	549.3 m	550.2 m	555.2 m
			Case 2 (Figs. 4.10c and 4.10d)		
y_e	MU_1	150 m	748.5 m	750.4 m	751.5 m
	MU_2	150 m	995.9 m	998.6 m	1000.1 m
k_{Fe}	MU_1	70000 mD	2872450 mD	2872518 mD	2872550 mD
	MU_2	28000 mD	873325 mD	873338 mD	873342 mD

Fig. 4.10 shows that independent single phase post-flowback PDA could yield poor history-matches. Table 4.5 shows that it could overestimate the values of reservoir parameters (compared with independent FDA results, see Table 4.4). The overestimation of hydraulic fracture half-lengths and poor history-matches in Case 1 show that multiphase, secondary fractures and gas desorption effects play important roles in post-flowback PDA. Despite the overestimation of hydraulic fracture half-lengths and effective gas permeability in Case 2 (compared with independent FDA results, see Tables 4.1 and 4.4), the improved

history-matches further confirms the importance of multiphase, secondary fractures and gas desorption effects in post-flowback PDA.

Apart from half-length, the inclusion of fracture permeability to gas (to account for two-phase effects since single-phase flow is assumed for DPM) as unknown tuning parameters improved the history-matches (Case 2). The three possible explanations for the observations are the neglect of multiphase effects during the single-phase DPM history-match (see Fig. 4.6), neglect of secondary fracture effects on a dual-porosity model and neglect of gas desorption effects from the reservoir matrix. The choice of initial guess might introduce bias in the history-match shown in Fig. 4.10. However, other input guesses as low as 50 m gave similar results as those in Table 4.5. In summary, accounting for multiphase, secondary fracture and gas desorption effects in post-flowback PDA might improve history-match results.

4.3.3.3 Flowback-Guided Production Data Analysis

In this part, gas production forecasts from the flowback data analysis of wells MU_1 and MU_2 using the two-phase FAM is matched against actual post-flowback gas data. This is simply a constrained post-flowback PDA where the forecast from an independent flowback. One goal is to investigate if the same input parameters which gave good flowback history-match results will also give similar results for post-flowback periods. Another goal is to investigate if accounting for multiphase, secondary fracture and gas desorption effects will improve the poor history-match observed during independent post-flowback PDA (Fig. 4.10). These goals are achieved in progressive steps – by accounting for only multiphase, combined multiphase + secondary fracture effects, and combined multiphase + secondary fracture + gas desorption effects (see Fig. 4.11).

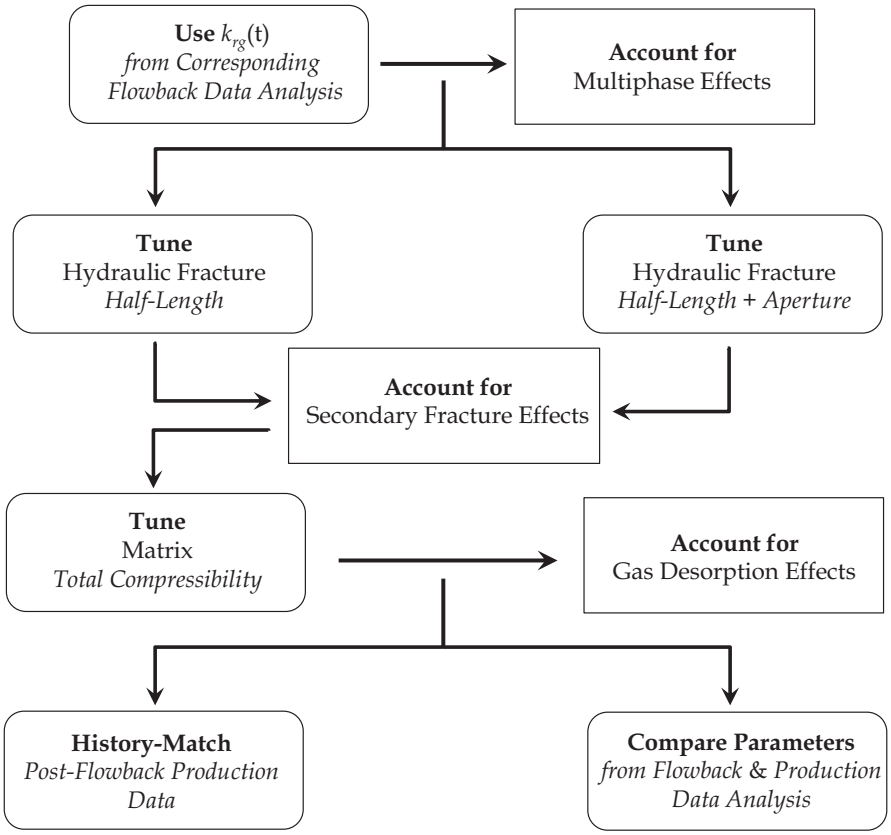

Fig. 4.11: Flowchart for flowback-guided production data analysis.

4.3.3.3.1 Multiphase Effects This part uses FAM to account for multiphase effects during post-flowback periods. This is based on the understanding that the same two-phase fluid flow physics during flowback continues into post-flowback (see Fig. 4.6).

Table 4.6: Hydraulic fracture half-length estimates of Wells MU_1 and MU_2 after accounting for multiphase effects during flowback-guided production data analysis.

Parameter	Well	Guess	95% Confidence Interval		
			Lower Bound	Optimal Estimate	Upper Bound
y_e	MU_1	150 m	117.9 m	118.2 m	118.5 m
	MU_2	150 m	132.1 m	133.0 m	133.5 m

At this point, FAM is primarily a dual-porosity based model which accounts for multiphase effects during flowback. FAM uses the same input parameters from flowback data analysis in wells MU_1 and MU_2 to forecast gas production. In turn, this forecast is used

to history-match post-flowback data from the same wells. The goal is to see if accounting for multiphase effects is sufficient to explain the poor history-match results observed in Fig. 4.10.

Fig. 4.12 shows the history-match results of post-flowback data. Table 4.6 shows the hydraulic-fracture half-lengths for wells MU_1 and MU_2 after accounting for multiphase effects. Despite the reasonable hydraulic fracture half-lengths, Fig.

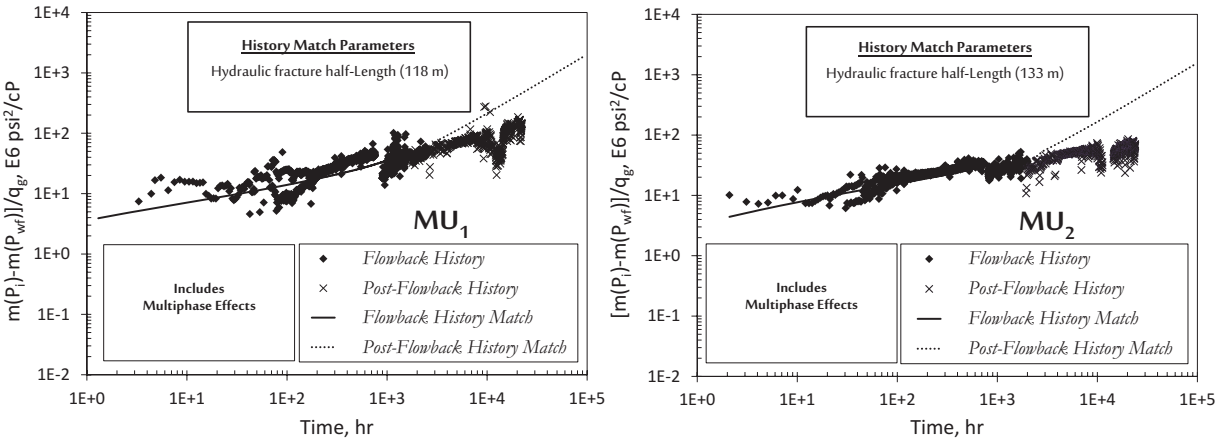

(a) (b)

Fig. 4.12: Rate normalized plots for wells (a) MU_1 and (b) MU_2 after accounting for multiphase effects during flowback-guided production data analysis (vertical axis is in per unit rate).

4.3.3.3.2 Combined Multiphase and Secondary Fracture Effects This part accounts for both multiphase and secondary fracture effects during post-flowback periods by lumping both secondary and hydraulic fractures into an equivalent fracture system in FAM. This adapts the actual field situation to the multiphase, dual-porosity based (only matrix and hydraulic fracture porous units) FAM. This adaptation is done without an explicit extension of FAM's static framework to triple-porosity (the extension is the subject of a future study). Here, the equivalent fracture half-length (y_{eq}) and aperture ($a_{_{Fq}}$) are the possible history-match parameters to account for the extra gas production observed in Fig. 4.12. The history-match is done in incremental steps to investigate the best way to account for secondary fracture effects using a dual-porosity based model like FAM. Case 1 tunes the fracture half-length during history-match. Case 2 tunes both fracture half-length and aperture during history-match.

Fig. 4.13 and Table 4.7 show the flowback-guided production data history-matches and equivalent fracture half-lengths and apertures for wells MU_1 and MU_2 after accounting for both multiphase and secondary fracture effects. The results show that adjusting both

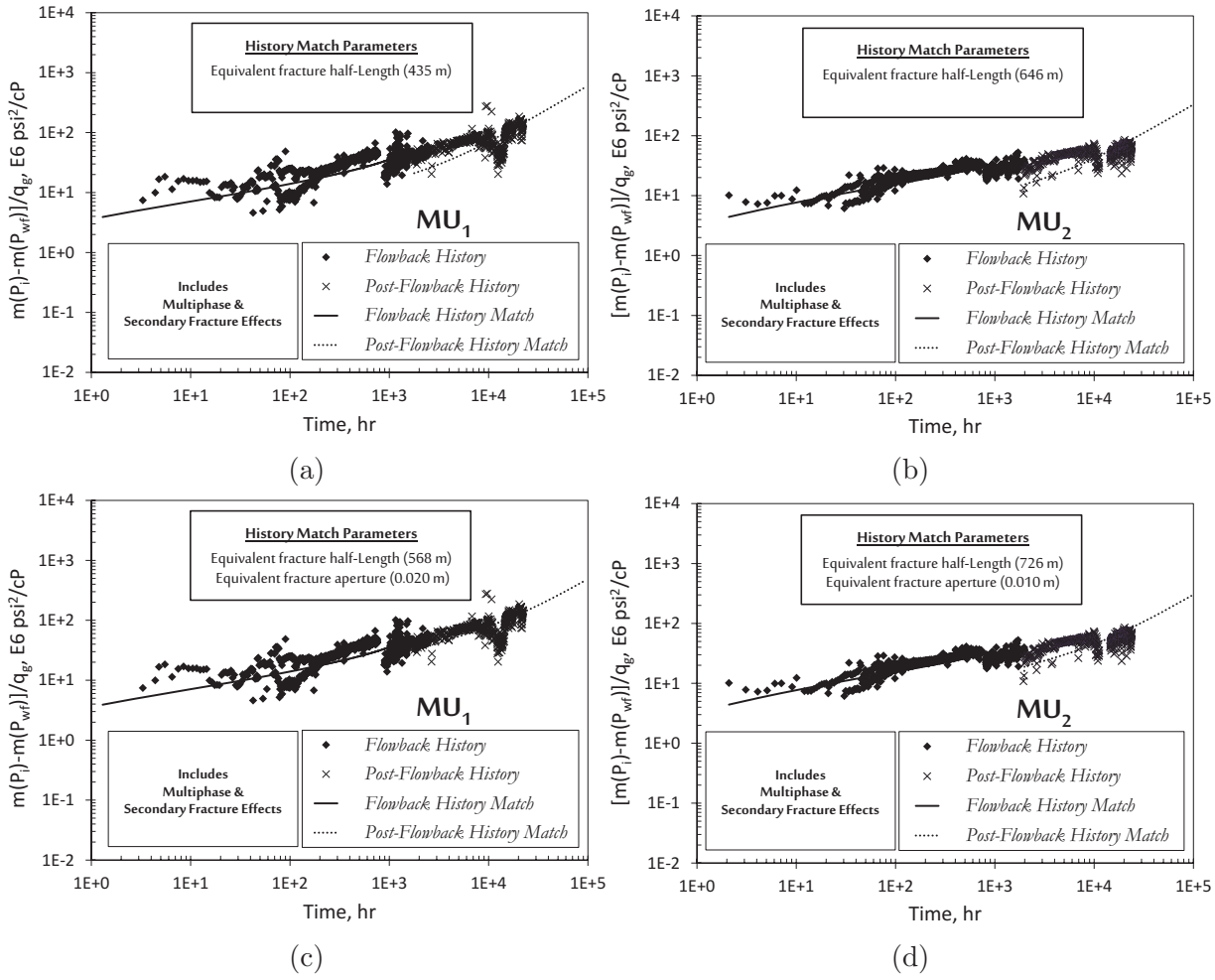

Fig. 4.13: Rate normalized plots for wells MU_1 and MU_2 after accounting for secondary fracture effects during flowback-guided production data analysis (vertical axis is in per unit rate). Case 1 – (a) & (b) tunes fracture half-length as history-match parameter. Case 2 – (c) & (d) tunes both fracture half-length and aperture as history-match parameters.

fracture half-lengths and apertures (instead of only half-length) gives higher gas production and a better history-match. Therefore, this should be a good way to account for the extra gas volume due to secondary fracture effects in a dual-porosity model during post-flowback periods. Despite the good history-match in Fig. 4.13, very high equivalent fracture half-lengths and fracture apertures are observed in Table 4.7. One possible explanation is that the equivalent fracture parameters do not just reflect hydraulic fracture properties but a combination of secondary and hydraulic fracture properties. Therefore, the equivalent fracture is a "fracture" which models the same reservoir response obtained from an actual secondary and hydraulic fracture combination existing in the field.

Table 4.7: Equivalent fracture half-length and aperture estimates of Wells MU_1 and MU_2 after accounting for multiphase and secondary fracture effects during flowback-guided production data analysis.

Parameter	Well	Guess	95% Confidence Interval		
			Lower Bound	Optimal Estimate	Upper Bound
			Case 1 (Figs. 4.13a and 4.13b)		
y_{eq}	MU_1	118 m	429.7 m	434.6 m	439.4 m
	MU_2	133 m	631.9 m	645.8 m	659.7 m
			Case 2 (Figs. 4.13c and 4.13d)		
y_{eq}	MU_1	118 m	567.7 m	570.3 m	572.8 m
	MU_2	133 m	713.4 m	726.1 m	738.8 m
$a_{_{Fq}}$	MU_1	0.001 m	0.0200 m	0.0203 m	0.0204 m
	MU_2	0.001 m	0.0094 m	0.0097 m	0.0099 m

4.3.3.3.3 Combined Multiphase, Secondary Fracture and Desorption Effects

This part accounts for multiphase, secondary fracture and gas desorption effects during post-flowback periods by lumping both secondary and hydraulic fractures into an equivalent fracture system (secondary fracture effects) and increasing total matrix compressibility (gas desorption effects) in FAM. Although FAM assumes negligible gas desorption from the matrix during flowback periods, this is not the case for high matrix pressure drops during post-flowback periods. From existing literature (Bumb and McKee, 1988; Clarkson et al., 2008), the net effect of gas desorption on fluid depletion in a reservoir is to create desorption compressibility (in addition to the gas compressibility). Therefore, the net effect of gas desorption on production data analysis is to increase the equivalent matrix compressibility $(c_t)_{mq}$ (Bumb and McKee, 1988; Clarkson et al., 2008). Numerical values of this desorption compressibility can be estimated from isotherm models. However, for the purpose of this chapter, the matrix compressibility will be tuned as history-match parameter to investigate desorption effects during post-flowback production.

The history-match parameters are the equivalent fracture half-length, equivalent fracture aperture and equivalent matrix compressibility. Fig. 4.14 shows the flowback-guided

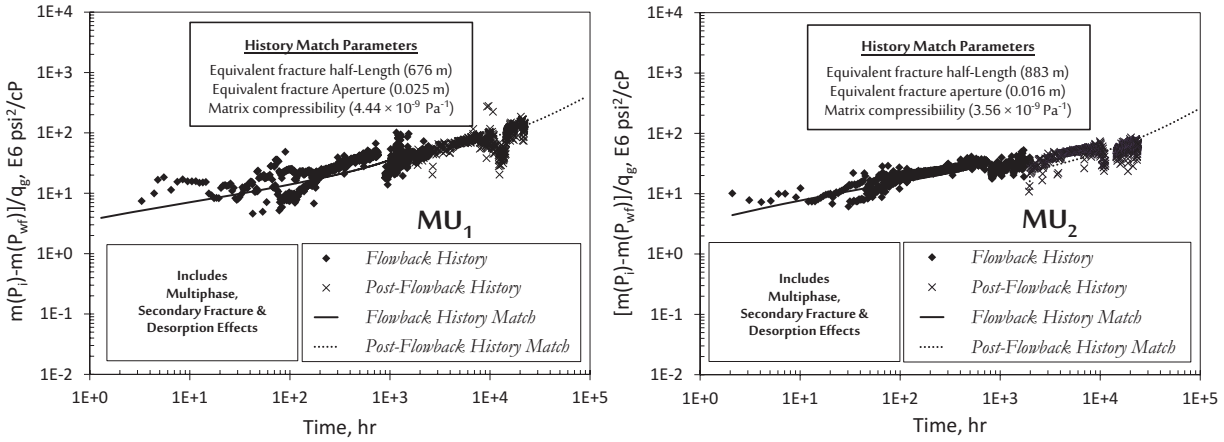

(a) (b)

Fig. 4.14: Rate normalized plots for wells MU_1 and MU_2 after accounting for gas desorption effects during flowback-guided production data analysis. Fracture half-length, fracture aperture and matrix compressibility are history-match parameters.

post-flowback history-matches and and Table 4.8 shows the equivalent fracture half-lengths, fracture apertures and matrix compressibilities for wells MU_1 and MU_2 after accounting for gas desorption effects. These values are higher than the corresponding values in Table 4.7. Also, Fig. 4.14 shows a higher gas production and better history-match in comparison to Fig. 4.13. This means that desorption physics plays an important role during post-flowback periods. This extra gas requires more secondary fractures for depletion (compared to the case neglecting desorption effects). These observations show that multiphase, secondary fracture and gas desorption effects need to be accounted for where necessary during post-fowback data analysis. This is supported by the multiphase observation in the flow rate plots of wells MU_1 and MU_2 (see Fig 4.6), high degree of natural fracturing in the reservoir (Virués et al., 2013) and huge drop in the reservoir pressure (from 4900 psia to about 1600 psia).

Table 4.8: Equivalent fracture half-length, fracture aperture and matrix compressibility estimates of Wells MU_1 and MU_2 after accounting for multiphase, secondary fracture and gas desorption effects during flowback-guided production data analysis.

Parameter	Well	Guess	95% Confidence Interval		
			Lower Bound	Optimal Estimate	Upper Bound
y_{eq}	MU_1	118 m	674.7 m	675.9 m	677.1 m
	MU_2	133 m	870.6 m	882.6 m	894.7 m
$a_{_{Fq}}$	MU_1	0.001 m	0.0246 m	0.0247 m	0.0248 m
	MU_2	0.001 m	0.0153 m	0.0157 m	0.0161 m
$(c_t)_{mq}$	MU_1	$9.4 \times 10^{-10}\ Pa^{-1}$	$4.4 \times 10^{-9}\ Pa^{-1}$	$4.4 \times 10^{-9}\ Pa^{-1}$	$4.5 \times 10^{-9}\ Pa^{-1}$
	MU_2	$9.4 \times 10^{-10}\ Pa^{-1}$	$3.5 \times 10^{-9}\ Pa^{-1}$	$3.6 \times 10^{-9}\ Pa^{-1}$	$3.7 \times 10^{-9}\ Pa^{-1}$

4.4 Comparisons

This part compares the reservoir parameter estimates and observations from i) qualitative flowback data analysis, and ii) quantitative flowback and post-flowback analyses.

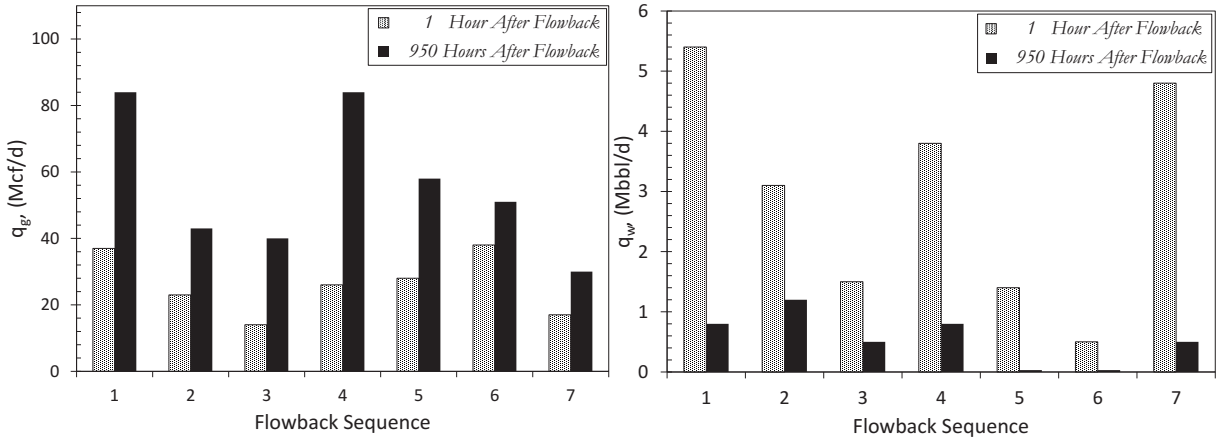

(a) (b)

Fig. 4.15: Flow rate comparison for wells MU_1, MU_2, OP_3, OP_4, MU_5, OP_6 and OP_7 at specific flowback times. (a) Gas rate and (b) Water rate.

Fig 4.15a shows that the low gas rates at the start of flowback (after 1 hour) quickly increase to high values at the end of flowback (after 950 hours). Fig 4.15b shows the reverse

trend for the case of water rate. These observations form the basis for comparing the wells from Pad X in this section. This is because all wells have low water rate (compared to gas rate which is now almost constant, see Fig. 4.6) at the end of flowback compared to the values at the start of flowback (despite different flowback durations for each well).

4.4.1 Qualitative Analysis

This part compares the general observations from key performance indicators of the seven wells from Pad X at the end of flowback operations. These indicators (see Table 4.2) are current pay recovery ($PR = N_p$ / TIV) and current load recovery ($LR = N_w$ / TIV). Fig. 4.16 shows poor trends for both pay and load recoveries in Pad X.

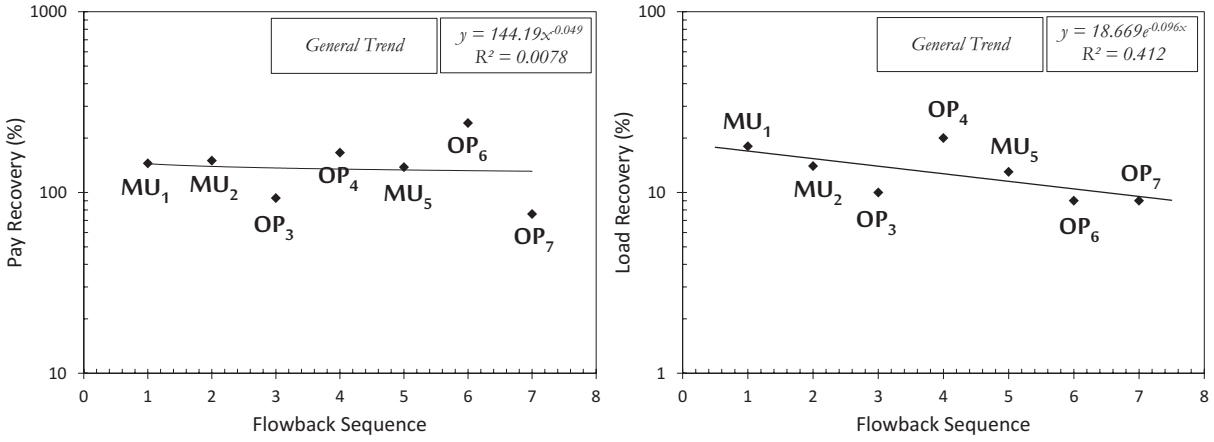

(a) (b)

Fig. 4.16: Key qualitative flowback performance indicator plots for Pad X. (a) Pay recovery and (b) Load recovery.

The large pay recovery ($PR \gg 100$ %) in almost all the wells shows that for every 1 m^3 of water injected, there is at least an average equivalent of 2 m^3 of gas (at reservoir conditions) recovered from Pad X after flowback operations. The general low load recovery ($LR \leq 20$ %) after flowback shows that the remaining TIV is still left in the matrix or hydraulic fractures. However if most of this remaining TIV is considered to be in the hydraulic fractures, gas flow should appreciably slow down (after accounting for gravity effects). This is not the case as the gas rates in these wells are almost steady and not decreasing (see Fig. 4.6). Also, it is very unlikely that majority of this remaining TIV would have been lost to the matrix within 110 – 160 days (of shut-in after fracturing + flowback duration in Table 4.2 and Fig. 4.6) due to imbibition. This is because the characteristic rates observed during imbibition (Dehghanpour et al., 2012, 2013) are not high enough to transfer this high water volume (remaining TIV) within the given time. One possible

explanation is the presence of active secondary fractures (Virués et al., 2013), having some of its pore network filled with water. Fig. 4.16b shows a general weak correlation ($R^2 \ll 0.5$) between load recovery and flowback sequence in wells from Pad X. In the general sense, this means that these wells might not have similar physics governing their load recovery during flowback.

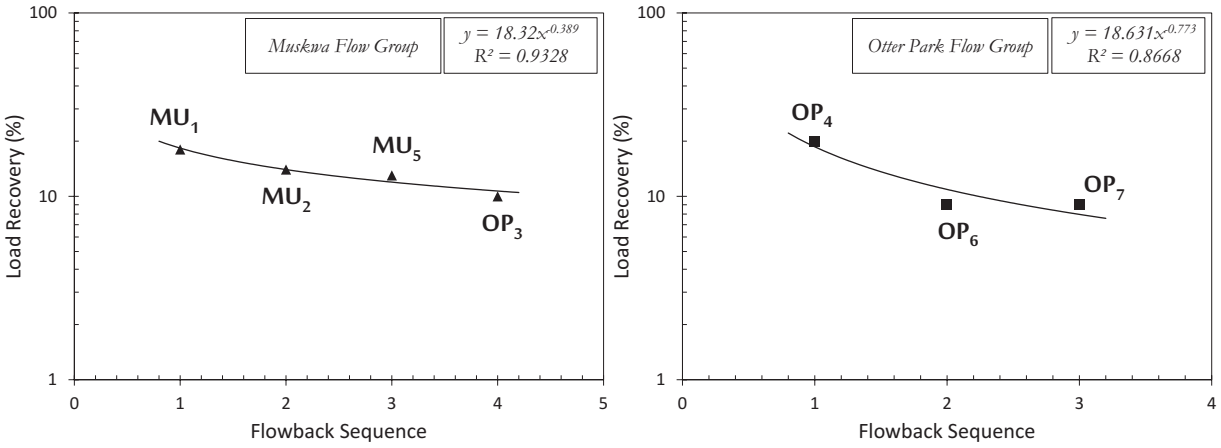

Fig. 4.17: Load recovery correlation plots for Pad X according to formation geology. (a) Muskwa trend and (b) Otter Park trend.

However, separating the load recovery of these wells into groups according to Formation geology reveals an interesting trend. Fig. 4.17 reveals a strong correlation ($R^2 \gg 0.5$) between load recovery and flowback sequence, when wells are grouped according to Formation. Generally, Fig. 4.17 shows that more water volume is recovered from wells which are opened for flow earlier in the flowback sequence. This could suggest that wells completed in the same formation have some kind of communication. This communication is such that the first well to be put on flowback gets to produce the greatest volume of water and vice versa for the last well. Well OP_3 correlates better in the Muskwa Flow Group rather than the Otter Park Group. This is an anomaly, which suggests that there are certain geologic or/and operating factors that differentiates well OP_3 from the others completed in the Otter-Park Formation. Further studies is required to investigate what these factors are. In summary, the results suggest that comparative load recovery analysis should be restricted to wells completed in the same geologic formation. One possible reason for this is that the brittleness (natural and secondary fracture tendency) and water retention property of the Muskwa and Otter Park formations are different. Hence, they affect the water recovery physics (provided that the well completion strategy remains the same across the wells).

4.4.2 Quantitative Analysis

This part compares parameter estimates and general observations from history-matches of both flowback and post-flowback data from Pad X.

4.4.2.1 Effective Fracture Pore-Volume and Total Injected Volume

The effective fracture pore-volume (V_{p_e}) calculated from history-match of flowback data includes both hydraulic fractures and active secondary fracture network. Flowback sequence is the same as completion sequence, and TIV is approximately the same for most wells in this pad (Fig. 4.18a).

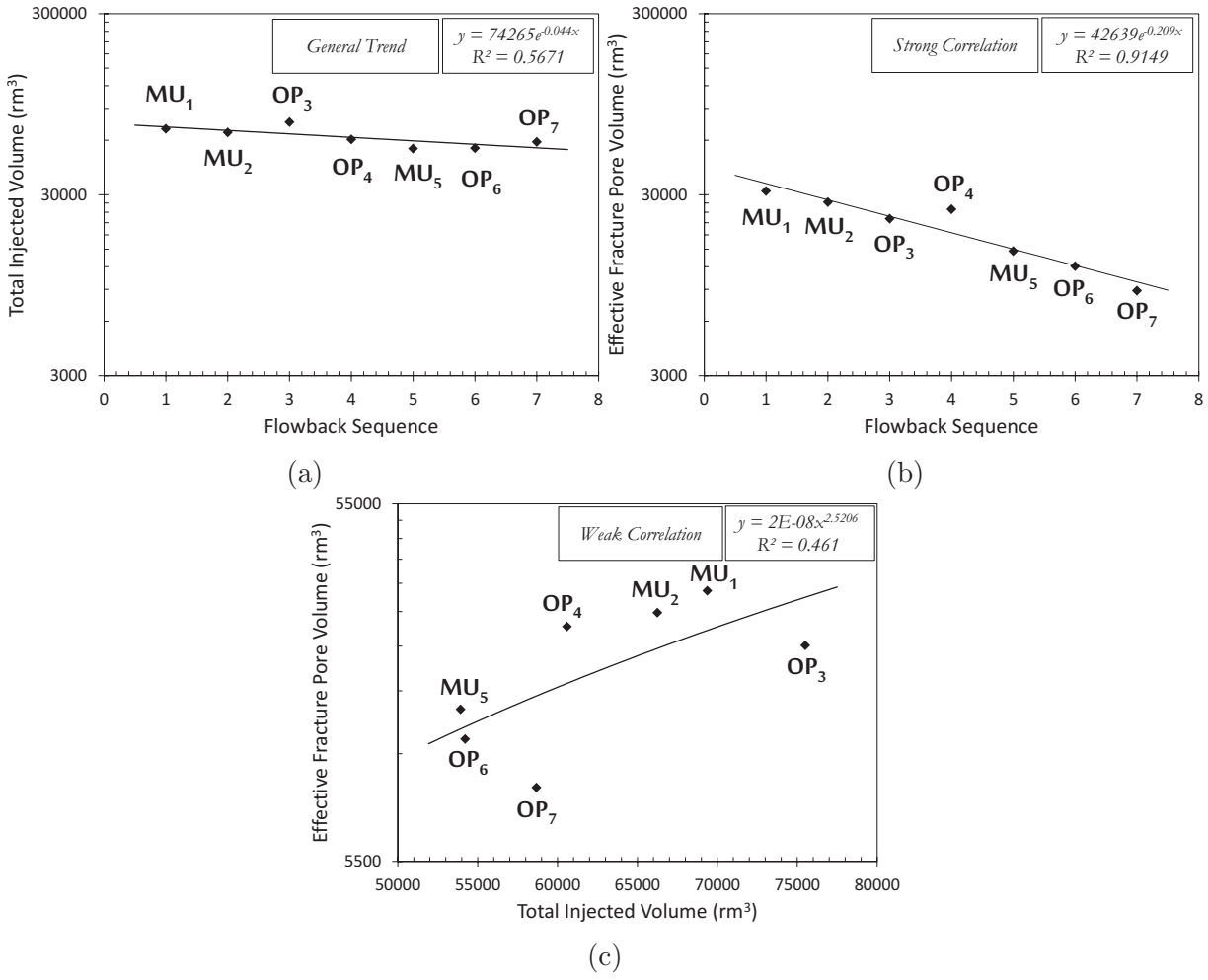

Fig. 4.18: Correlation plots for Pad X according to flowback sequence. (a) Total injected volume, (b) Effective fracture pore-volume and (c) Cross-plot.

Fig. 4.18b shows that V_{p_e} has a strong correlation ($R^2 \gg 0.5$) with flowback sequence in Pad X. This correlation shows a decreasing trend irrespective of TIV (approximately

the same water volume was used to fracture each well). This suggests that the fracturing process done on earlier wells reduces the effectiveness of that for subsequent wells in the pad. However, this trend could also be influenced by the history-match method used for calculating V_{p_e}.

Fig. 4.18c shows that V_{p_e} generally has a weak correlation ($R^2 < 0.5$) with TIV for wells in Pad X. This suggests that high amount of TIV does not necessarily result in high volume of active fractures. One reason is that fracture creation (Yoon et al., 2014) is primarily a function of formation geology (brittleness, clay content, stress orientations etc.). Since V_{p_e} is generally less than TIV, the difference could provide estimates of leak-off volume (V_{lf} = TIV – V_{p_e}). Here, V_{lf} is the percentage of TIV residing outside the hydraulic fractures and active secondary fracture network (i.e. in matrix, isolated hydraulic fractures and inactive secondary fractures).

4.4.2.2 Effective Fracture Pore-Volume and Cumulative Water Production

The cumulative water production here is the total recovered volume from Pad X wells at the end of flowback. Fig. 4.19 shows that the cumulative water produced (N_w) in Pad X wells generally decreases with flowback sequence. Also, the effective fracture pore-volume connected to wells in Pad X shows a strong correlation ($R^2 \gg 0.5$) with the cumulative water produced from the same wells during flowback.

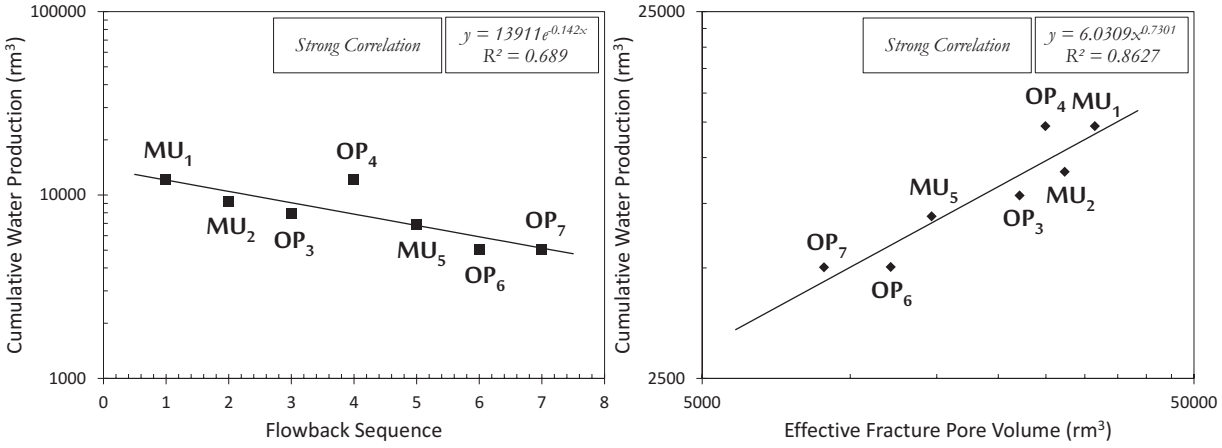

(a) (b)

Fig. 4.19: Correlation plots for Pad X (a) Cumulative water production with flowback sequence and (b) Cross-plot of cumulative water production and fracture pore-volume.

4.4.2.3 Initial Volume of Gas in Active Fracture Network

The flowback history-match shows that most wells in Pad X have little or no initial gas (V_{gi}) in their hydraulic fracture networks before flowback (Table 4.3). However, this is contrary to the observation of immediate gas production in most of these wells at the onset of flowback. Therefore, the zero V_{gi} values estimated from the flowback history-match could be as a result of the history-match procedure. This is because the current procedure couples relative permeability (which does not require fracture geometry and uses the total volume of hydraulic-fracture and possible active secondary fractures) history-match and RNP (which requires fracture geometry and assumes a planar bi-wing hydraulic fracture of fixed length and height) history-match.

4.4.3 Complementary Flowback and Post-Flowback Analysis

This part compares the history-match results from independent two-phase FDA, independent single-phase post-flowback PDA and flowback-guided PDA for Wells MU_1 and MU_2. also, it compares the performance of using a single model for combined flowback + production data analysis against an independent post-flowback data analysis which ignores flowback data.

The results show that integrating flowback data analysis and properly accounting for the combined effects of multiphase, secondary fracture and gas desorption during multiphase post-flowback well data yields better history-match and parameter estimates.

Flowback data analysis offers the earliest opportunity to characterize the fracture after a multi-fractured horizontal well is opened for fluid flow. Although the proposed FAM accounts for multiphase effects during flowback and yields good results, its application for long-term post-flowback production forecasts should be done with caution and sound engineering judgment. This is because it does not account for secondary fracture and gas desorption effects. Most secondary fractures (when present) which might appear inactive due to water plugging during flowback might become active during post-flowback production and increase hydrocarbon recovery. In addition, gas desorption effects which are negligible during flowback due to the small pressure drop in the matrix becomes significant during post-flowback due to high reservoir pressure drop in matrix (as a result of fluid depletion). Nevertheless, an engineer could still use the results from a dual-porosity based flowback model for reasonable post-flowback production analysis using a complementary approach. The first step is to obtain half-length and permeability of the hydraulic fracture from an independent flowback data analysis. Next, these properties of the hydraulic fractures could then be used as an input to constrain post-flowback production data anal-

ysis. This complementary approach reduces the uncertainty in the remaining reservoir parameter estimates.

The appropriate post-flowback model required for this complementary analysis should account for both multiphase (almost all post-flowback production data are two-phase), secondary fracture (some reservoirs have large secondary fracture networks) and gas desorption effects (when reservoir pressure drops below critical desorption pressure). In summary, FAM's dual-porosity framework could be mathematically extended to account for both secondary fracture and gas desorption effects. This should result in a single model capable of interpreting both flowback and post-flowback data from the same well.

4.5 Summary

The results of this chapter can be summarized under five points namely: i) qualitative volumetric data analysis to estimate key indicators such as load recovery; ii) history-match of transient two-phase flowback rate + pressure data to estimate key reservoir parameters such as effective fracture pore-volume; iii) comparing production forecast from flowback data analysis against actual post-flowback production data; iv) complementary two-phase flowback and post-flowback analysis; and iv) comparative study of well performance in a Pad.

The volumetric results show that there is a general correlation between load recovery and flowback sequence, effective fracture pore-volume and flowback sequence, cumulative water production and effective fracture pore-volume. It shows that comparative load recovery analysis should be restricted to wells completed in the same formation for improved results. Also, this chapter provides a way to estimate the percentages of the total injected volume left inside and outside the active fracture network respectively.

The history-match results provide estimates of the pore-volume of active fracture networks, effective half-length and initial gas volume in hydraulic fractures during flowback. The history-match forecast yields lower gas rates compared to actual post-flowback production data. This is due to neglecting the secondary fracture and gas desorption effects on the dual-porosity based flowback model used in this study. The communication interface between secondary fractures and hydraulic fractures significantly increases during post-flowback periods (when most of the water in the active secondary fractures have been displaced by gas influx from the matrix and reservoir pressure drops below the critical desorption pressure). Therefore, post-flowback analysis should properly account for secondary fracture and gas desorption effects to yield reasonable results. The results show that although a multiphase dual-porosity framework is sufficient for flowback data analy-

sis, proper post-flowback analysis should account for both secondary fracture effects (using a triple-porosity framework) and gas desorption effects.

Key parameters like permeability and effective pore-volume of fractures should be estimated using an appropriate flowback model once high quality flowback data is available. In turn, these parameters should be used as input parameters in post-flowback production data analysis to minimize uncertainty in reservoir parameter estimates. Alternatively, the results from flowback data analysis could be used as as inputs for production data analysis to obtain better hydrocarbon forecasts, when low-quality flowback data is available. Future studies will focus on the i) extension of FAM to account for the presence of reactivated natural fractures, ii) reduction of uncertainty in parameter estimates from flowback data analysis by developing analysis equations

Nomenclature

Symbols

a	Fracture aperture/width, L, m, $[ft]$.
c	Compressibility, Lt^2M^{-1}, atm^{-1}, $[Pa^{-1}$, $psi^{-1}]$.
h	Reservoir thickness, L, m, $[ft]$.
k	Bulk permeability of hydrocarbon phase, L^2, m^2 $[D]$.
n	Number, L, m, $[ft]$.
q	Rate, L^3t^{-1}, $m^3.s^{-1}$, $[rb.day^{-1}]$.
r	Wellbore radius, L, m, $[ft]$.
s	Laplace variable, t^{-1}, s^{-1}, $[hr^{-1}$, $day^{-1}]$.
t	Time, t, s, $[hr$, $day]$.
z	Gas compressibility factor, dimensionless.
A	Area, L^2, m^2, $[ft^2]$.
B	Formation volume factor, L^3L^{-3}, ft^3scf^{-1}, $[bblstb^{-1}]$.
L	Distance or length, L, m, $[ft]$.
N	Cumulative Production, L^3, m^3, $[ft^3]$.
P	Pressure of hydrocarbon phase, $ML^{-1}t^{-2}$, Pa, $[psi]$.
S	Saturation, dimensionless.
V	Volume, L^3, m^3, $[ft^3]$.
X	Horizontal well length, L, m, $[ft]$.
TIV	Total Injected Volume, L^3, m^3, $[ft^3]$.
β	Clean-up parameter, dimensionless.
ϕ	Bulk porosity, dimensionless.

μ	Viscosity of hydrocarbon phase, $ML^{-1}t^{-1}$, $Pa.s$, $[cP]$.
Δ	Change.

Superscripts

$\bar{}$	Laplace transform.
^{o}	End-Point.
^{r}	Residual.

Subscripts

$_c$	cross-section.
$_e$	equivalent or effective.
$_g$	Gas.
$_i$	Initial.
$_m$	Matrix.
$_n$	Normalized.
$_o$	Oil.
$_p$	Pore.
$_q$	Equivalent.
$_r$	Relative.
$_t$	Total.
$_w$	Well.
$_D$	Dimensionless.
$_F$	Hydraulic fracture.
$_L$	Reference length.
$_{wf}$	Bottom-hole flowing.
$_{CL}$	Fracture clusters per stage.
$_{HC}$	Hydrocarbon.
$_{inf}$	Inflexion point on relative-permeability curve.
$_{wav}$	Average water.

Chapter 5

Simultaneous Matrix Depletion into Natural and Hydraulic Fracture Networks

5.1 Introduction

Unconventional reservoirs (very-low permeability reservoirs) have emerged as a significant supply of hydrocarbon in North America (Clarkson and Pederson, 2010). Although horizontal drilling combined with hydraulic-fracturing techniques have enabled commercial hydrocarbon production from unconventional reservoirs, modeling fluid flow in such complex reservoirs remains challenging.

The number of distinct porous regions in a reservoir determines the appropriate conceptual model for simulating fluid flow through it. An example of such conceptual model is the dual-porosity model which comprises a single fracture network and matrix blocks. Communication between fracture network and matrix blocks can be transient or pseudo-steady. Warren and Root (1963) proposed an ideal sugar-cube model of a naturally fractured reservoir which consists of uniformly distributed fractures and matrix blocks. The sugar-cube model assumes a pseudo-steady matrix–fracture communication and negligible matrix flow capacity. Warren and Root (1963) concluded that two parameters (ω — storativity ratio and λ — interporosity coefficient) are sufficient to characterize the deviation of a dual-porosity medium from that of a homogeneous porous medium. Kazemi (1969) extended Warren and Root (1963)'s model by replacing the pseudo-steady matrix–fracture communication with transient communication. Kazemi (1969) concluded that Warren and Root (1963)'s model is applicable only when there is uniform fracture distribution and large contrast between fracture and matrix flow capacities. Carlson and Mercer (1991) extended the dual-porosity model for application in Shale reservoirs and observed that portions of the tight rock matrix remain at initial pressure, unaffected by depletion in the adjacent fracture network.

All dual-porosity models discussed so far assume radial flow towards the well. However,

production data from fractured horizontal wells completed in tight formations shows long periods of transient linear behavior (El-Banbi, 1998). This linear behavior is observed as half-slope line on a log-log plot of pressure or inverse-rate against time (El-Banbi, 1998). The dominance of linear flow regime observed in field data could result from: production from fractures whose lengths extend to reservoir boundaries (Wattenbarger et al., 1996); transient drainage of low permeability matrix blocks into adjoining fractures; and linear shape of certain reservoirs (Stright Jr. and Gordon, 1983). Since the existing radial dual-porosity models could not explain this extended linear flow regime, it became necessary to develop a suitable model for analyzing production data from fractured horizontal wells completed in tight formations.

El-Banbi (1998) extended previous dual-porosity models (Warren and Root, 1963; Kazemi, 1969) to produce a list of dual-porosity solutions for linear reservoirs. Bello (2009) extended El-Banbi (1998)'s linear dual-porosity model for application in rate transient analysis of fractured Shale reservoirs. His model is a bounded rectangular fractured reservoir with slab matrix blocks. The matrix drains into adjoining fractures and the fractures subsequently drain into a horizontal well at the center of the reservoir. By assuming a transient matrix–fracture fluid transfer, Bello (2009) developed asymptotic analysis equations and specialized plots to describe observable flow regimes. The application of these plots and analysis equations on production data yielded acceptable results.

Dual-porosity models assume uniform matrix and fractures properties throughout the reservoir which may not be true in reality. Recent petrographic studies in Western Canadian Sedimentary Basin (Castillo et al., 2011) show that tight rocks may contain different pore-types: inter-granular; slot + micro-fractures; and isolated non-effective porosities. Therefore, hydraulic fracturing could reactivate some of these non-effective porosities, transforming the dual-porosity reservoir into a triple porosity system (Gale et al., 2007; Dahi, 2009). Additionally, studies in the Horn River Basin (Rogers et al., 2010) show that the connection between hydraulic fracture (HF) and the natural fracture network enhances the reservoir volume drained by a well. These observations among others, raised the need for triple porosity models that could interpret production data from reservoirs with non-uniform fracture or matrix properties.

Triple-porosity models can comprise two fracture networks and one matrix type or one fracture network and two matrix types. Triple-porosity models can be further classified into pseudo-steady and transient state models, depending on the nature of matrix–fracture interactions. Abdassah and Ershaghi (1986) proposed a transient triple porosity model where fractures have homogeneous properties and interact with two distinct groups of matrix blocks (different permeabilities and porosities). Liu et al. (2003) developed a

pseudo-steady triple porosity model to analyze the pressure behavior of fractured lithophysal reservoirs comprising fractures, rock matrices, and cavities. Wu et al. (2004) used the same mathematical model to simulate the flow and transport processes in fractured reservoirs comprising matrices, large fractures, and small fractures. Dehghanpour and Shirdel (2011) extended Ozkan et al. (2010)'s transient dual-porosity model and Warren and Root (1963)'s pseudo-steady model to obtain two triple porosity models comprising sub-matrices (nano-Darcy permeabilities) and micro-fractures (milli- to micro-Darcy permeabilities). The resulting models can be used to explain the unexpected high gas production in some Shale gas reservoirs which cannot be justified by conventional dual-porosity models.

Al-Ahmadi (2010) extended the linear dual-porosity model of Bello (2009) to account for linear fluid depletion through hydraulic fracture and micro-fractures (MF) in fractured horizontal wells. Assuming different modes of communication between HF and MF, Al-Ahmadi (2010) proposed four dual-fracture, triple porosity models for linear reservoirs — fully transient (Model 1), two mixed transient and pseudo-steady (Models 2 and 3) and fully pseudo-steady (Model 4).

Furthermore, Brown et al. (2011) presented a general analytical trilinear model (a combination of dual-porosity model and linear flow models) coupling flow in three contiguous regions of a fractured horizontal well. These regions are: outer reservoir beyond the tips of the hydraulic-fracture; inner dual-porosity reservoir between hydraulic-fractures; and hydraulic fractures. This trilinear model was used to simulate pressure transient and production behavior of fractured horizontal wells in Shale reservoirs. Brown et al. (2011) concluded that the trilinear flow model should be sufficient to study the key characteristics of flow convergence toward a fractured horizontal well within the stimulated reservoir volume, despite the complex interplay of flow among matrix, natural fractures and hydraulic fractures. This conclusion is based on the assumption that the inner dual-porosity reservoir may be homogeneous or naturally fractured.

All existing triple porosity models and trilinear flow model assume sequential depletion (negligible matrix–HF communication). This assumption holds only if the matrix–MF communication is far greater than the matrix–HF communication. In situations where there is significant matrix–HF communication or negligible bulk matrix–MF contact area compared to bulk matrix–HF contact area, the sequential assumption can result in unreasonable estimates of MF and/or HF properties. Also existing linear sequential triple porosity models do not converge to dual-porosity solutions in the absence of micro-fractures. The outlined deficiencies of the existing linear triple porosity models will be addressed in this study.

This study proposes a quadrilinear flow model (QFM) that relaxes the sequential depletion assumption in existing triple porosity models. QFM is achieved in the following three steps — model development, verification and application respectively. Model development involves: deriving flow equations which govern simultaneous transient matrix-depletion to micro-fractures and hydraulic-fractures; solving these equations with Laplace transforms under constant bottom-hole pressure and rate inner boundary conditions respectively; and generating type-curves by numerically inverting the Laplace-space solutions to real time using Gaver-Stefhest algorithm. Model verification involves: testing QFM's convergence to the existing linear sequential triple porosity model and linear dual-porosity model using type-curves, and its match with synthetic data from a commercial reservoir simulator; and analyzing QFM's sensitivity to reservoir parameters using type-curves. Model application involves: matching QFM type-curves with the production history of two fractured horizontal wells completed in the Bakken and Cardium formations; and estimating reservoir parameters from type-curve match.

5.2 Methodology

This part describes the conceptual QFM, its governing flow equations under the constant rate inner boundary condition, and the procedure for solving QFM flow equations.

5.2.1 Conceptual Model

Fig. 5.1a shows reactivated natural fractures (NF), micro-fractures (MF) and hydraulic fractures (HF) in a given stimulated reservoir volume (SRV). Fig. 5.1b is an idealized representation of the proposed QFM used to develop the governing equations for fluid flow. Irrespective of differences in properties and orientations in the field, the induced MF and reactivated NF shown in the Fig. 5.1a are lumped as one representative, porous unit (MF) in Fig. 5.1b. The inset in Fig. 5.1b shows the simultaneous matrix-depletion into HF and MF.

The proposed model assumes that the SRV after multi-stage hydraulic fracturing can be approximated as a continuum of three representative media (see Fig. 5.1):

1. Hydraulic fractures denoted by F and usually of maximum permeability.
2. Micro-fractures denoted by f and usually of intermediate permeability.
3. Matrix blocks denoted by m and usually of minimum permeability.

In Fig. 5.1, y_e is the half-length of HF and L_F is the spacing between consecutive HF. L_f is the spacing between consecutive MF and X_e is the horizontal well length.

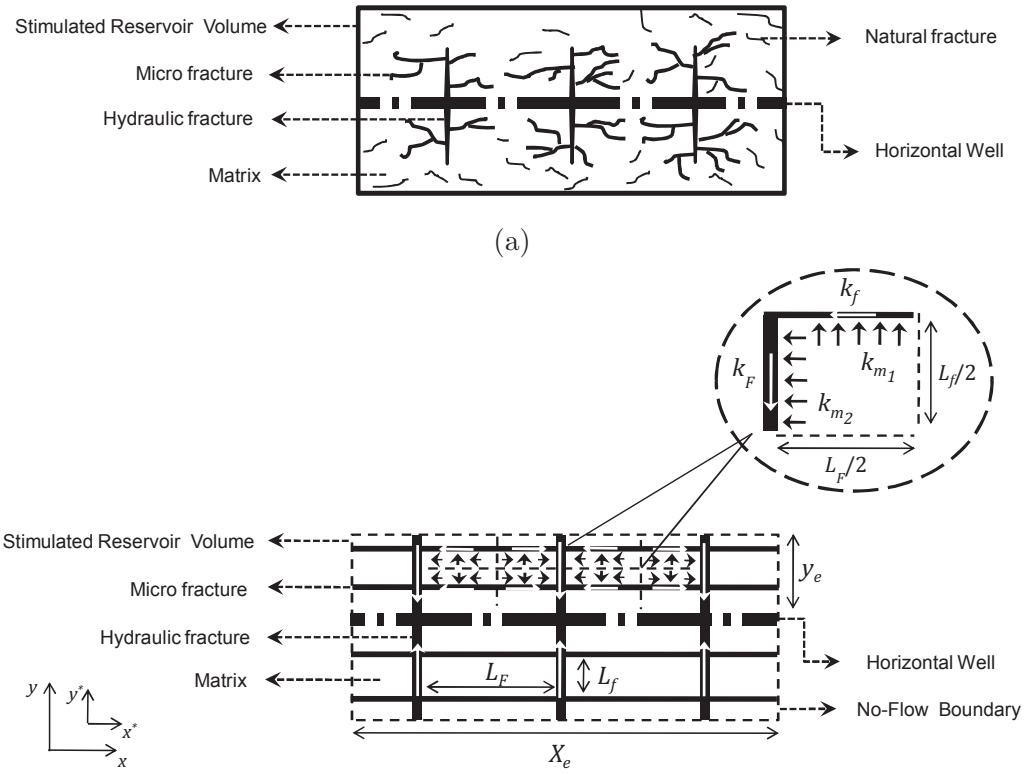

Fig. 5.1: Horizontal cross-section of idealized QFM after multi-stage hydraulic fracturing in tight reservoirs. Solid arrows in the matrix, micro-fracture and hydraulic fracture show show fluid flow directions.

Bulk/effective/macroscopic values of matrix, MF and HF permeabilities and porosities are used in this study (Warren and Root, 1963; Bello, 2009; Al-Ahmadi, 2010; Tivayanonda, 2012). The bulk porosity of each medium can be defined the total pore volume of that medium per reservoir bulk volume. The following equations define bulk porosities and bulk permeabilities as proposed in this study.

$$\phi_m \approx \frac{L_f/2 \times L_F/2}{(L_f/2 + a_f)\,(L_F/2 + a_F)} \times \phi_m^t \approx \phi_m^t \tag{5.1}$$

$$\phi_f \approx \frac{a_f \times L_F/2}{(L_f/2 + a_f)\,(L_F/2 + a_F)} \times \phi_f^t \tag{5.2}$$

$$\phi_F \approx \frac{a_F \times L_f/2}{(L_f/2 + a_f)\,(L_F/2 + a_F)} \times \phi_F^t \tag{5.3}$$

Where a_f and $a_{_F}$ are widths/apertures of MF and HF respectively; ϕ_m^t, ϕ_f^t and $\phi_{_F}^t$ are the true/actual/intrinsic (Warren and Root, 1963; Bello, 2009; Al-Ahmadi, 2010; Tivayanonda, 2012) porosities of matrix, MF and HF respectively. In Eq. 5.2, ϕ_f^t is assumed to be unity due to the un-propped nature of MF.

In Eqs. 5.4, 5.5 and 5.6, k_m^t, k_f^t and $k_{_F}^t$ are true permeability of matrix, MF and HF respectively. V represents bulk volume.

$$k_m \approx \frac{L_f/2 \times L_{_F}/2}{(L_f/2 + a_f)\,(L_{_F}/2 + a_{_F})} \times k_m^t \tag{5.4}$$

$$k_f \approx \frac{a_f \times L_{_F}/2}{(L_f/2 + a_f)\,(L_{_F}/2 + a_{_F})} \times k_f^t \tag{5.5}$$

$$k_{_F} \approx \frac{a_{_F} \times L_f/2}{(L_f/2 + a_f)\,(L_{_F}/2 + a_{_F})} \times k_{_F}^t \tag{5.6}$$

Furthermore, the number of MF (n_f) within a given HF spacing is estimated using the relationship given in the equation below:

$$n_f = \frac{y_e}{L_f} - 1 \tag{5.7}$$

5.2.2 Mathematical Formulation

This chapter makes the following assumptions to derive QFM fluid flow equations:

- Reservoir fluid is slightly compressible, single phase with constant viscosity
- Fully penetrating horizontal well is located at the center of a closed rectangular SRV.
- MF are interconnected within HF spacing. MF and HF are perpendicular.
- Matrix supplies fluid simultaneously to MF and HF. Only HF directly communicates with the horizontal well.
- Fluid influx from the SRV boundaries beyond the tips of HF and MF is negligible. Fluid flow from matrix to horizontal well is negligible.
- Stress and temperature effects on reservoir parameters are negligible.

QFM relaxes the assumption of sequential depletion in existing linear triple porosity models to achieve simultaneous depletion by dividing the matrix into two virtual parts:

- Sub-matrix m_1 feeding the MF; and

- Sub-matrix m_2 feeding the HF

This matrix division breaks a single 2-D matrix flow equation into two 1-D flow equations:

$$\frac{\partial^2 \Delta P_{m_1}}{\partial y^{*2}} = \frac{\mu(\phi c_t)_{m_1}}{k_{m_1}} \frac{\partial \Delta P_{m_1}}{\partial t} \tag{5.8}$$

$$\frac{\partial^2 \Delta P_{m_2}}{\partial x^{*2}} = \frac{\mu(\phi c_t)_{m_2}}{k_{m_2}} \frac{\partial \Delta P_{m_2}}{\partial t} \tag{5.9}$$

To conserve fluid mass, fluid masses of the sub-matrices (m_1 and m_2) add up to the total matrix fluid mass present:

$$(\phi c_t)_{m_1} + (\phi c_t)_{m_2} = (\phi c_t)_m \tag{5.10}$$

The following equations show the governing single-phase flow equations through matrix, HF and MF for QFM.

Diffusivity equation, initial condition and boundary conditions that control fluid flow within sub-matrix 1 are:

$$\frac{\partial^2 \Delta P_{m_1}}{\partial y^{*2}} = \frac{\mu(\phi c_t)_{m_1}}{k_{m_1}} \frac{\partial \Delta P_{m_1}}{\partial t} \tag{5.11}$$

$$\Delta P_{m_1}(y^*,\ 0) = 0 \tag{5.12}$$

$$\Delta P_{m_1}\Big|_{y^*=\frac{L_f}{2}} = \Delta P_f\Big|_{y^*=\frac{L_f}{2}} \tag{5.13}$$

$$\left.\frac{\partial \Delta P_{m_1}}{\partial y^*}\right|_{y^*=0} = 0 \tag{5.14}$$

Diffusivity equation, initial condition and boundary conditions that control within sub-matrix 2 are:

$$\frac{\partial^2 \Delta P_{m_2}}{\partial x^{*2}} = \frac{\mu(\phi c_t)_{m_2}}{k_{m_2}} \frac{\partial \Delta P_{m_2}}{\partial t} \tag{5.15}$$

$$\Delta P_{m_2}(x^*,\ 0) = 0 \tag{5.16}$$

$$\Delta P_{m_2}\Big|_{x^*=\frac{L_F}{2}} = \Delta P_{_F}\Big|_{x^*=\frac{L_F}{2}} \tag{5.17}$$

$$\frac{\partial \Delta P_{m_2}}{\partial x^*}\bigg|_{x^*=0} = 0 \tag{5.18}$$

Diffusivity equation, initial condition and boundary conditions that control fluid flow within MF and matrix–MF communication are:

$$\frac{\partial^2 \Delta P_f}{\partial x^2} = \frac{\mu(\phi c_t)_f}{k_f}\frac{\partial \Delta P_f}{\partial t} + \frac{1}{L_f/2}\frac{k_{m_1}}{k_f}\frac{\partial \Delta P_{m_1}}{\partial y^*}\bigg|_{y^*=\frac{L_f}{2}} \tag{5.19}$$

$$\Delta P_f(x,\ 0) = 0 \tag{5.20}$$

$$\Delta P_f\Big|_{x=\frac{L_F}{2}} = \Delta P_{_F}\Big|_{x=\frac{L_F}{2}} \tag{5.21}$$

$$\frac{\partial \Delta P_f}{\partial x}\bigg|_{x=0} = 0 \tag{5.22}$$

Diffusivity equation, initial condition and boundary conditions that control fluid flow within HF; matrix–HF, MF–HF, and HF–well communication respectively are:

$$\frac{\partial^2 \Delta P_{_F}}{\partial y^2} = \frac{\mu(\phi c_t)_{_F}}{k_{_F}}\frac{\partial \Delta P_{_F}}{\partial t} + \frac{1}{L_{_F}/2}\frac{k_{m_2}}{k_{_F}}\frac{\partial \Delta P_{m_2}}{\partial x^*}\bigg|_{x^*=\frac{L_F}{2}} + \frac{1}{L_{_F}/2}\frac{k_f}{k_{_F}}\frac{\partial \Delta P_f}{\partial x}\bigg|_{x=\frac{L_F}{2}} \tag{5.23}$$

$$\Delta P_{_F}(y,\ 0) = 0 \tag{5.24}$$

$$q = -\frac{k_{_F} A_{cw}}{\mu}\frac{\partial \Delta P_{_F}}{\partial y}\bigg|_{y=0} \tag{5.25}$$

$$\frac{\partial \Delta P_{_F}}{\partial y}\bigg|_{y=y_e} = 0 \tag{5.26}$$

The equations above govern fluid flow in QFM under constant rate inner boundary conditions and no-flow outer boundary conditions. Eq. 5.11 models fluid flow in m_1 while Eq. 5.15 models fluid flow in m_2. The left hand side (LHS) and first term on the right

hand side (RHS) of Eq. 5.19 model fluid flow in MF. The second term on the RHS of Eq. 5.19 models matrix–MF linear fluid transfer.

The LHS and first term on the RHS of Eq. 5.23 model fluid flow in HF. The second term on the RHS of Eq. 5.23 models matrix-HF linear fluid transfer. The third term on the RHS of Eq. 5.23 models MF–HF linear fluid transfer.

Eqs. 5.12, 5.16, 5.20 and 5.24 indicate that the sub-matrices (m_1 and m_2), MF and HF are at initial reservoir pressure before reservoir depletion (t=0). Eqs. 5.13, 5.17 and 5.21 represent pressure continuity boundary conditions. Eq. 5.25 includes the inner boundary condition of constant terminal flow-rate toward the horizontal well.

Eq. 5.26 denotes negligible fluid flow to the HF tips beyond the SRV. The no-flow boundary conditions represented by Eqs. 5.14, 5.18 and 5.22 denote the line of symmetry for transient simultaneous matrix depletion into HF and MF. This line of symmetry is at the center of two consecutive fractures (HF or MF).

Darcy units are used throughout this chapter except when indicated otherwise. E as used in figures represents a power of 10. Also, the notations used are described in the Nomenclature section.

5.2.3 Solution Methodology

This chapter considers two inner boundary conditions – constant flowing bottom-hole pressure and constant flowing bottom-hole rate. The flow equations for single phase depletion under both boundary conditions are given in Appendices B and C respectively. The equations are then solved separately under both boundary conditions.

First, the flow equations are made dimensionless using parameters similar to those used in previous works (Bello, 2009; Al-Ahmadi, 2010). This enables comparison of the resulting dimensionless solutions to the existing solutions. Second, Laplace transform is applied on the resulting dimensionless fluid flow equations under both inner boundary conditions to obtain QFM solutions. New transfer functions are obtained from the resulting solutions in Laplace space. Third, type-curves are generated by numerically inverting the QFM solutions using the Gaver-Stefhest algorithm (Stehfest, 1970) implemented in MATLAB 2007b.

5.3 Results

Detailed solution of the QFM equations under constant terminal rate and bottom-hole pressure inner boundary conditions are given in Appendices B and C respectively. This part summarizes the solution of the QFM equations, their validation, and the sensitivity of QFM flow regimes to reservoir parameters using the similarities between dimensionless rate (q_D) and dimensionless logarithmic pressure derivative [$\partial P_D/\partial ln(t_D)$] type-curves (Eq. 5.32). This sensitivity analysis uses dimensionless rate (q_D) type-curves because of their ability to detect subtle flow regime transitions and reduce non-uniqueness associated with type-curves (Stanislav et al., 1987).

5.3.1 QFM Solutions

The solution of Eqs. 5.11, 5.15, 5.19 and 5.23 using Laplace transforms yields the dimensionless wellbore pressure equation in Laplace space under constant rate inner boundary conditions:

$$\overline{P}_{wDL} = \frac{\coth\left(\sqrt{sf(s)}y_{De}\right)}{s\sqrt{sf(s)}} \tag{5.27}$$

A similar solution process yields the dimensionless wellbore rate equation under constant bottom-hole pressure inner boundary conditions:

$$\overline{q}_D = \frac{\sqrt{sf(s)}}{s\coth\left(\sqrt{sf(s)}y_{De}\right)} \tag{5.28}$$

$$\text{where } f(s) = \omega_F + \frac{\lambda_{AC,Ff}}{3s}\sqrt{sf_f(s)}\tanh\left(\sqrt{sf_f(s)}\right) + \frac{\lambda_{AC,Fm}}{3s}\sqrt{f_m(s)}\tanh\left(\sqrt{f_m(s)}\right) \tag{5.29}$$

$$\text{and } f_m(s) = \frac{3s\omega_2\omega_m}{\lambda_{AC,Fm}} \tag{5.30}$$

$$\text{and } f_f(s) = \left\{\frac{3\omega_f}{\lambda_{AC,Ff}} + \frac{\lambda_{AC,fm}}{s\lambda_{AC,Ff}}\sqrt{\frac{3s\omega_1\omega_m}{\lambda_{AC,fm}}}\tanh\left(\sqrt{\frac{3s\omega_1\omega_m}{\lambda_{AC,fm}}}\right)\right\} \tag{5.31}$$

Here, $f_m(s)$ is the transfer function controlling fluid flow from sub-matrix 2 to HF; $f_f(s)$ is the transfer function controlling fluid flow from sub-matrix 1 to MF and from MF to HF; while $f(s)$ is the transfer function controlling fluid transfer from sub-matrix 1, sub-matrix 2 and MF into HF. ω_1 and ω_2 are heuristic, weighting parameters. They control the fraction of fluid volume in the matrix which flows into MF and HF respectively during production.

5.3.2 Model Verification

This part of the chapter validates QFM by: testing the conformance of QFM solutions under constant bottom-hole pressure and constant rate inner boundary conditions to the relationship proposed by Van Everdingen and Hurst (1949); testing the convergence of QFM to the linear sequential triple porosity model (STPM) in the absence of matrix–HF communication and to the linear dual-porosity model (DPM) in the absence of MF; and history-matching synthetic data from IMEX CMG [22] software using QFM's Eq. 5.28.

5.3.2.1 Verification against Van Everdingen and Hurst (1949)'s Relation

Eqs. 5.27 and 5.28 obey the relation proposed by Van Everdingen and Hurst (1949) for fluid flow under constant terminal rate and constant terminal pressure inner boundary conditions:

$$\overline{P}_{wDL} \times \overline{q}_D = \frac{1}{s^2} \tag{5.32}$$

5.3.2.2 Verification against Existing Models

QFM should converge to the dual-porosity model in the absence of MF, and to the sequential triple porosity model in the absence of matrix–HF flow communication. This convergence is achieved using q_D type-curves generated by numerically inverting Eq. 5.28 from Laplace space to time space using the Stefhest algorithm (Stehfest, 1970). Two datasets representing possible field operating conditions are substituted into Eq. 5.28.

Fig. 5.2 demonstrates QFM's behavior at limits where it converges to the existing DPM or STPM. Setting $\omega_1 = 0$ and $\omega_f = 0$ in Eq. 5.29 simplifies QFM to the DPM proposed by Bello (2009). Setting $\omega_1 = 1$ or $\omega_2 = 0$ in Eq. 5.29 simplifies QFM to the STPM proposed by Al-Ahmadi (2010). The data match in Fig. 5.2 proves that QFM converges to existing linear dual and triple porosity models in the absence of MF and matrix–HF fluid influx respectively.

[22] Computer Modeling Group (http://www.cmgl.ca, last accessed 18-11-2016)

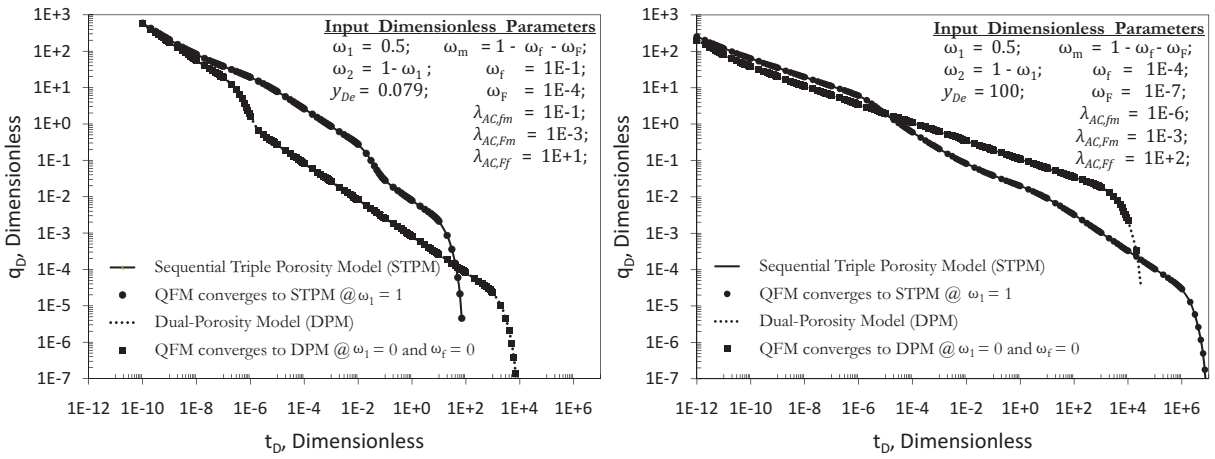

(a) (b)

Fig. 5.2: QFM converges to linear dual-porosity model (Bello, 2009) and linear sequential triple porosity model (Al-Ahmadi, 2010). (a) first dataset (b) second dataset

5.3.2.3 Verification against Synthetic Data from IMEX CMG

IMEX CMG is used to simulate an undersaturated oil reservoir comprising matrix, micro-fracture and hydraulic as its fracture porous media. Fig. 5.3 shows the top view for one stage of hydraulic fracture in the reservoir.

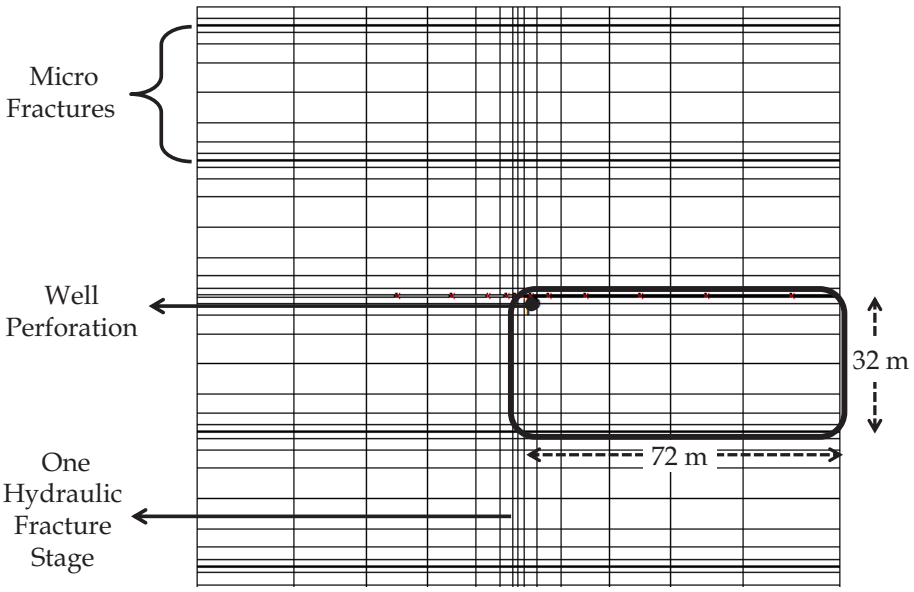

Fig. 5.3: Top view of static framework used for flow simulation in IMEX CMG.

The boxed part is the representative volume that was flow simulated to obtain synthetic data for this verification. Table 5.1 shows the fluid, rock and well properties which are

typical of Cardium Formation. These were inputted as reservoir parameters for the flow simulation. To ensure single phase, oil production, the simulation was carried out at a constant bottom-hole pressure which is above the oil bubble point in the reservoir.

Table 5.1: Input Dataset for IMEX CMG Simulation.

Reservoir Parameter	**Value**	**Units**
h	2.5	m
X_e	576	m
y_e	124	m
$n_{_F}$	7	—
L_f	32	m
$L_{_F}$	72	m
a_f	1×10^{-4}	m
$a_{_F}$	1×10^{-3}	m
k_m^t	0.035	mD
k_f^t	100	mD
$k_{_F}^t$	10000	mD
ϕ_m^t	0.012	—
ϕ_f^t	0.9	—
ϕ_F^t	0.48	—
$(c_t)_m$	2.51×10^{-6}	kPa^{-1}
$(c_t)_f$	2.51×10^{-6}	kPa^{-1}
$(c_t)_{_F}$	2.51×10^{-6}	kPa^{-1}
P_i	46896	kPa
P_{wf}	35100	kPa
P_b	35000	kPa

Fig. 5.4 shows the history match ($R^2 = 0.98$) between Eq. 5.28 and the synthetic data obtained from IMEX CMG. This was done using the non-linear regression (*nlinfit*) module in the Matlab 2012a software. Table. 5.2 shows the corresponding bulk porosity and permeability values used for this history match.

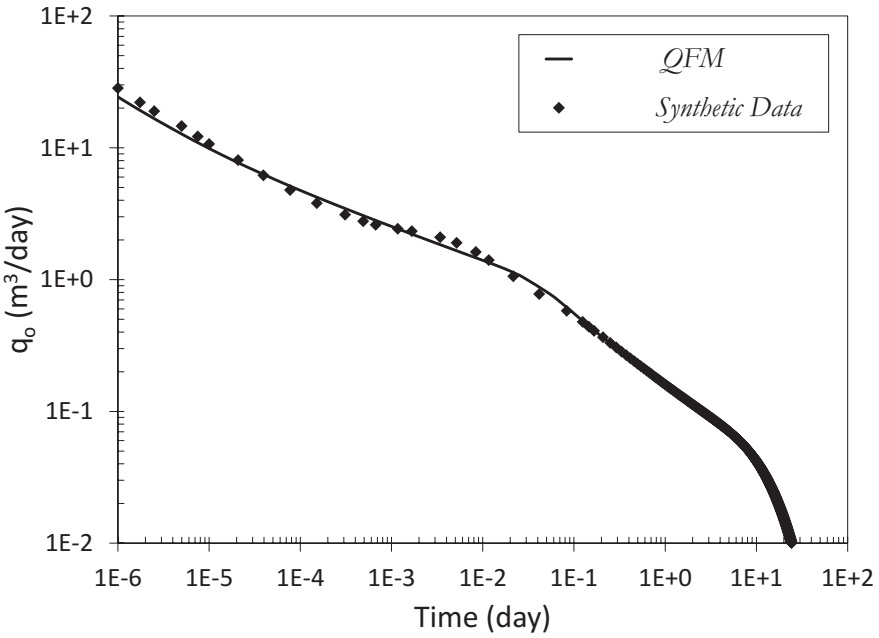

Fig. 5.4: History-match of gas flow rate from QFM and synthetic data from IMEX CMG.

Table 5.2: Bulk porosity and permeability values used to history-match the synthetic data from IMEX CMG ($R^2 = 0.98$). The initial guess values were obtained by converting the true porosity and permeability input values from Table refchap-5:table:2 to bulk porosity and permeability values us9ing the equations proposed in Subsection 5.2.1. The confidence interval is the degree of certainty with which the range of history-match parameters represent the model physics under investigation.

Parameter	**Guess**	**95% Confidence Interval**		
		Lower Bound	**Optimal Estimate**	**Upper Bound**
k_m	3.5×10^{-2} mD	2.86×10^{-2} mD	3.68×10^{-2} mD	4.49×10^{-2} mD
k_f	3.12×10^{-4} mD	3.06×10^{-9} mD	5.35×10^{-9} mD	7.63×10^{-9} mD
k_F	1.3×10^{-1} mD	1.16×10^{-3} mD	1.37×10^{-3} mD	1.57×10^{-3} mD
ϕ_m	1.2×10^{-2}	6.2×10^{-4}	7.79×10^{-4}	9.38×10^{-4}
ϕ_f	2.81×10^{-6}	5.48×10^{-7}	7.64×10^{-7}	9.81×10^{-7}
ϕ_F	6.67×10^{-6}	1.8×10^{-6}	2.17×10^{-6}	2.54×10^{-6}

5.3.3 Flow Regimes

Although detailed equation analysis (Ezulike and Dehghanpour, 2016a) is required for proper flow regime interpretation, Table 5.3 provides a qualitative description of the physics behind the typical QFM flow regimes shown in Fig. 5.5.

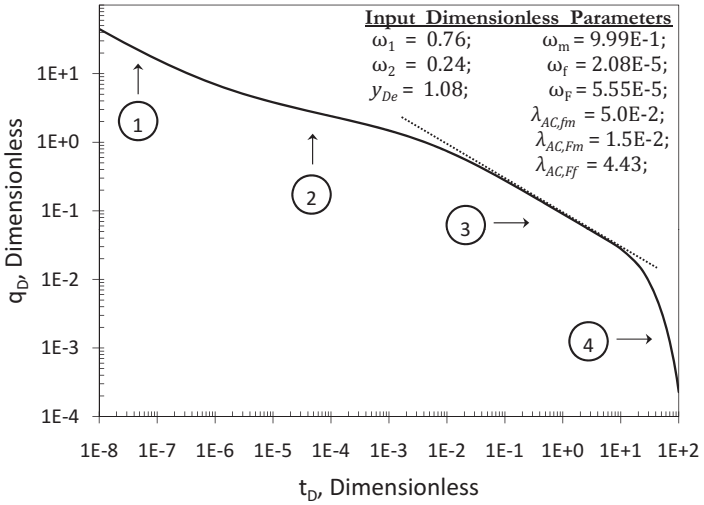

Fig. 5.5: Typical QFM flow regimes (1 to 4). The dotted line has a slope of −0.5.

Table 5.3: Qualitative description of typical QFM flow regimes.

Flow Regime	Slope	Flow regime physics
1	−0.5	Early transient linear flow in HF (Bello, 2009).
2	−0.25	Bilinear flow due to simultaneous linear flow in HF and MF (Al-Ahmadi and Wattenbarger, 2011).
3	−0.5	Transient linear flow from matrix to surrounding MF (Al-Ahmadi, 2010).
4	*exp*	Exponential flow decline (Bello, 2009; Al-Ahmadi and Wattenbarger, 2011) as depletion reaches all no-flow boundaries (boundary dominated flow).

It is important to note that other sequences and types of flow regimes apart from

those in Fig. 5.5 are possible. The type, number, progression and time of occurrence of these flow regimes depend on the relative magnitude of the reservoir properties to one another (Ezulike and Dehghanpour, 2016a).

5.3.4 Sensitivity Analysis

QFM's sensitivity analysis focuses on two reservoir parameters — spacing aspect ratio (i.e. MF spacing divided by HF spacing) and bulk MF permeability. Table 5.4 shows the base case dataset for QFM sensitivity analysis. This dataset is substituted into Eq. 5.28 to obtain dimensionless q_D type-curves.

Table 5.4: Base case dataset for QFM sensitivity analysis.

Reservoir Parameter	Value	Units
h	7	m
X_e	1370	m
y_e	150	m
n_F	18	—
L_f	40	m
L_F	72	m
a_f	1×10^{-5}	m
a_F	1×10^{-3}	m
k_m	0.035	mD
k_f	1	mD
k_F	1000	mD
ϕ_m^t	0.12	—
ϕ_f^t	1	—
ϕ_F^t	0.48	—
$(c_t)_m$	2.209×10^{-6}	kPa^{-1}
$(c_t)_f$	2.209×10^{-6}	kPa^{-1}
$(c_t)_F$	2.209×10^{-6}	kPa^{-1}

5.3.4.1 Spacing Aspect Ratio

Fig. 5.6a shows the effect of spacing aspect ratio (R_{sp}) on the intermediate and late time QFM flow regimes. R_{sp} is the MF spacing divided by HF spacing (details about R_{sp} is in Appendix D). High MF concentration within a given HF spacing results in low R_{sp}. However, ineffective (e.g. water-plugged) MF can result in high spacing aspect ratios

despite a high MF concentration. The early time flow regimes are not sensitive to changes in R_{sp}. The reservoir behaves as a dual-porosity system (DPM) at very high R_{sp} and as a sequential triple porosity system (STPM) at very low R_{sp}. High R_{sp} results in: weak MF–HF support (short bilinear slope); weak transient MF flow (could be absent); and late occurrence of boundary effects (slow reservoir depletion).

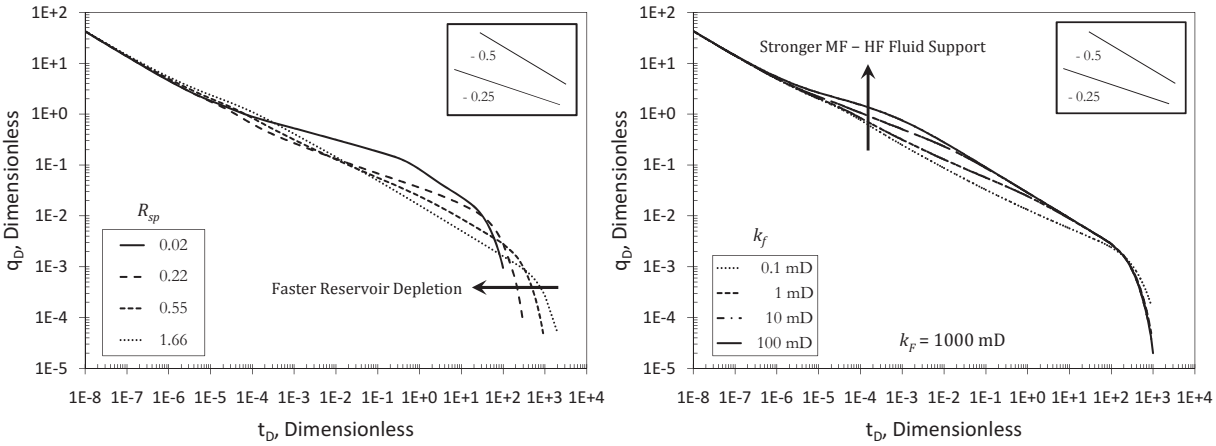

(a) (b)

Fig. 5.6: QFM's sensitivity to key reservoir parameters. The lines at the top right hand corner of each plot have -0.5 and -0.25 slopes (from top to bottom). (a) Sensitivity to spacing aspect ratio (R_{sp}). (b) Sensitivity to bulk MF permeability (k_f) when bulk HF permeability (k_F) is 1000 mD.

5.3.4.2 Bulk MF Permeability

Fig. 5.6b shows the effect of bulk MF permeability (k_f) on the intermediate and late time QFM flow regimes. The reservoir behaves as a dual-porosity system (DPM) at low bulk MF permeability (see $k_f = 0.1mD$). High k_f results in: strong MF–HF support (bilinear slope of -0.25); early occurrence of MF–HF support; weak MF linear flow (can be absent); and strong matrix–MF support (elongated linear slope) support. This also results in a rise in flow rate during intermediate times, and a drop in flow rate during late times.

5.4 Application

This part presents the application of QFM dimensionless type-curves to match production history of fractured horizontal oil wells A and B, and estimate unknown reservoir parameters. Wells A and B are completed in the Cardium (Justen, 1957; MacKenzie, 1975; Purvis and Bober, 1979; Krasey and Fawcett, 1998; Clarkson and Pederson, 2011)

and Bakken (Hlidek and Rieb, 2011; Clarkson and Pederson, 2011; Alcoser et al., 2012) Formations respectively. Fig. 5.7 highlights the region of interest during the history-match of production rate and pressure from the target wells.

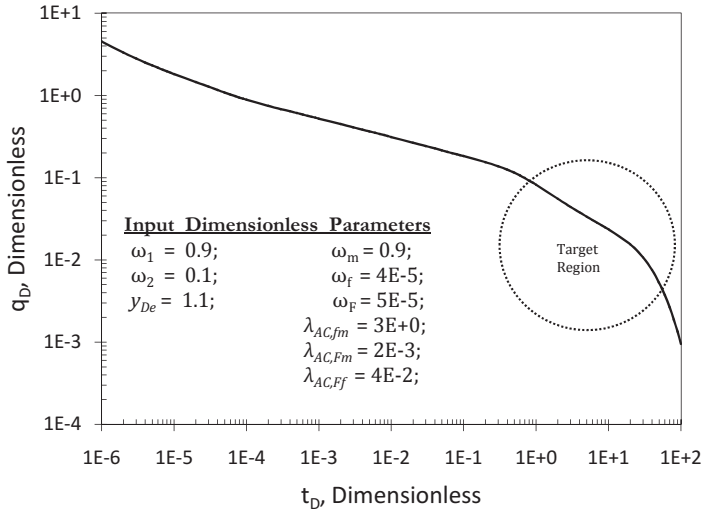

Fig. 5.7: Typical inverse QFM dimensionless rate type-curve. The circled portion shows flow regimes used for matching field production data.

5.4.1 QFM Type-Curve Match

Table 5.5 summarizes the known reservoir parameters (from field reports) for Wells A and B. The application of QFM type-curves on production data from Wells A and B yields the history-matches shown in Fig. 5.8.

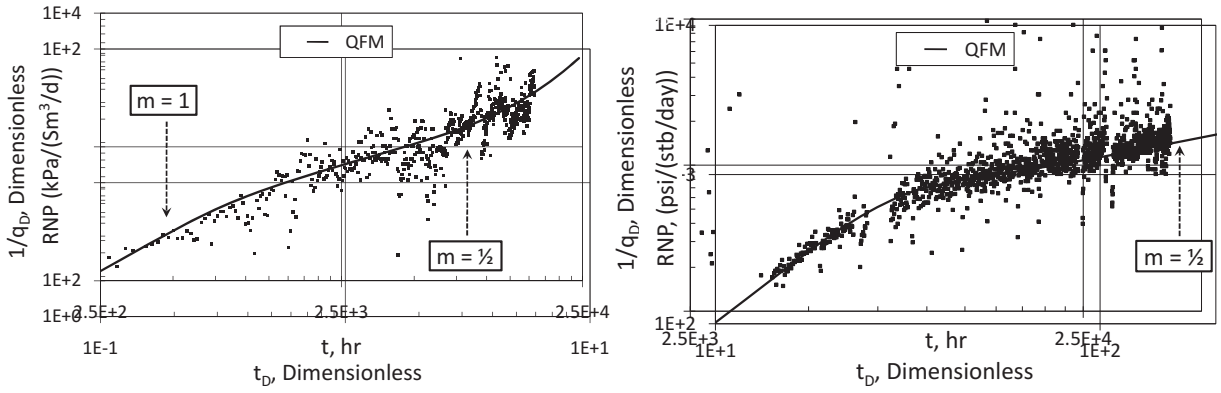

Fig. 5.8: QFM type-curve match with production data from (a) Well A and (b) Well B. m shows slope.

Table 5.5: Data for Wells A and B completed in the Cardium and Bakken Formations respectively.

Parameter	Well A	Well B	Units
B_o	1.221	1.329	rm^3/m^3
μ	1.13	0.5643	cP
P_i	15575	46884	kPa
P_{wf}	7413	4826	kPa
c_t	2.209×10^{-6}	2.51×10^{-6}	kPa^{-1}
k_m	1.34	0.026	mD
ϕ_m	0.108	0.09	-
X_e	1370	1707	m
h	7	5.8	m
$L_{_F}$	72	100	m
$n_{_F}$	18	16	-

Table 5.6: Initial and final (before and after uncertainty analysis) values of input dimensionless parameters for QFM type-curves used to match production data from Wells A and B respectively.

Parameter	Well A		Well B	
	Initial	Final	Initial	Final
ω_1	0.4	0.3 – 0.5	0.3	0.28 – 0.52
ω_2	0.6	0.5 – 0.7	0.7	0.48 – 0.72
ω_m	0.89	≥ 0.89	0.89	0.89
ω_f	0.1	0.1	0.1	0.1
$\omega_{_F}$	0.001	≤ 0.001	0.001	0.001
$\lambda_{_{AC,fm}}$	0.1	0.1	0.1	0.07 – 0.2
$\lambda_{_{AC,Fm}}$	0.001	0.001	0.001	0.0005 – 0.0025
$\lambda_{_{AC,Ff}}$	10	10	10	10
$y_{_{De}}$	1	0.7 – 1.2	1	1

The dots and solid lines in this figure are field data points and inverse dimensionless rate type-curves respectively. Table 5.6 summarizes the dimensionless reservoir parameters obtained before and after performing uncertainty analysis on the QFM type-curve match.

5.4.2 QFM Parameter Estimation

Table 5.8 summarizes the unknown reservoir parameters estimated from a combination of known reservoir parameters (from Table 5.5), assumed reservoir parameters (from Table 5.7) and QFM dimensionless parameters (from Fig. 5.8).

Table 5.7: Assumed data for Wells A and B completed in the Cardium and Bakken Formations respectively.

Parameter	Well A	Well B	Units
$(\phi c_t)_f$	$(\phi c_t)_m \times 10^{-1}$	$(\phi c_t)_m \times 10^{-1}$	kPa^{-1}
$(\phi c_t)_F$	$(\phi c_t)_m \times 10^{-2}$	$(\phi c_t)_m \times 10^{-2}$	kPa^{-1}

Table 5.8: Initial and final (before and after uncertainty analysis) values of unknown reservoir parameters estimated from matching QFM type-curves and production data of Wells A and B respectively. The low end values of micro-fracture spacing corresponds to the low end values of hydraulic fracture half-length and high end values of the number of micro-fractures.

Parameter	Well A		Well B		Units
	Initial	Final	Initial	Final	
k_f	350	350	260	104 – 520	mD
k_F	1549	1549	612	245 – 1224	mD
L_f	8	7 – 13	13	7 – 19	m
y_e	138	97 – 166	141	141	m
n_f	16	6 – 22	9	6 – 19	—

QFM type-curve matches for Wells A and B yield y_e values (Table 5.8) which fall within the general range documented in literature. Duhault (2012) observed from micro-seismic studies in the Cardium Formation that HF created using slickwater have complex pattern and variable y_e. Quirk et al. (2012) and Duhault (2012) observed that the y_e values in the Cardium Formation could range from 60m to 300m. A similar micro-seismic study by O'Brien et al. (2012) shows that the average y_e values in the Bakken Formation could range from 137m to 274m.

The position where the unit slope occurs in Fig. 5.8 does not follow the typical sequence observed in Fig. 5.5. However the type and number of flow regimes observed in a field data plot depends on the relative magnitude of the well and reservoir properties. Hence, the range of well and reservoir property combination responsible for this unit slope will be investigated in a subsequent study on flow-regime analysis equations (Ezulike and Dehghanpour, 2016a).

It is important to note that the matrix permeability of well A and B from well test reports might have lumped fractures as part of matrix. Also, the possibility of fluid contribution beyond the SRV is ignored in this chapter. This is because the observed flow-regimes indicate that the total SRV has not been contacted. Incorporating flow contribution of the area beyond SRV in QFM would be the subject of a future study.

5.5 Discussions

The results of this chapter can be summarized under four points namely: development of a mathematical model (QFM) which relaxes the sequential depletion assumption of previous models; validation of QFM against the existing STPM and DPM, and synthetic data from CMG IMEX simulator; analysis of QFM's sensitivity to reservoir parameters; and application of QFM on field production data to estimate reservoir parameters.

Result 1 is significant for the evaluation of the communication between hydraulically created fractures (HF) and reactivated natural fractures (or MF), and the amount of matrix–HF and matrix–MF communication present in a reservoir. This evaluation is based on the assumption that active MF contributes to reservoir fluid depletion. However, this assumption has to be confirmed from other studies (e.g. outcrop and micro-seismic studies) before applying QFM on production data. This is because QFM cannot diagnose the presence or absence of MF. Result 1 is also significant for its application to production data obtained under constant bottom-hole pressure and constant bottom-hole rate conditions. Although result 1 was developed for oil wells, it could be extended to gas wells by replacing pressure with the appropriate pseudo-pressure function $[m(P)]$. An example of such pseudo-pressure function (Al-Hussainy and Ramey Jr., 1966) is:

$$m(P) = 2\int_{P_i}^{P} \frac{P}{\mu(P)z(P)}\,\mathrm{d}P$$

Result 2 shows that QFM does not violate the physics of fluid flow when compared to simpler models at key limiting conditions. QFM converges to the existing STPM and DPM at the limits of negligible matrix–HF communication and negligible effective

micro-fractures respectively. The discrepancies between some of the bulk porosity and permeability values obtained from history-matching synthetic data with QFM and those calculated from the relationships proposed in this study require further investigation.

Result 3 indicates that prior knowledge of reservoir spacing aspect ratio (R_{sp}) can simplify the process of reservoir characterization at certain limits: high R_{sp} (> 1.5) and low R_{sp} (< 0.2). Reservoirs with high R_{sp} or low R_{sp} can be characterized using DPM or STPM respectively. However, reservoirs with intermediate R_{sp} (between 0.2 and 1.5) should be characterized using QFM. The impact of R_{sp} and k_f on QFM flow regimes observed in this study will be exploited to develop QFM flow regime analysis equations in a subsequent study (Ezulike and Dehghanpour, 2016a). These analysis equations will be developed using techniques similar to those in Bello (2009) and Ezulike and Igbokoyi (2012). The impact of R_{sp} and k_f on QFM flow regimes will also be relevant in the development of a flowback analysis model in subsequent studies because R_{sp} and k_f both affect the early-time flow regimes (Ezulike and Dehghanpour, 2014c).

Result 4 proposes a procedure to evaluate the uncertainty (non-uniqueness) associated with reservoir parameters estimated from matching QFM type-curve and hydrocarbon production data. This procedure indicates that the uncertainty associated with a target reservoir parameter (keeping other reservoir parameters constant) causes this parameter to be estimated as a range of values (instead of a single value) from the type-curve match. The low and high limits of the estimated parameter range (Williams-Kovacs and Clarkson, 2013b) could be taken as the expected realistic end-point P_{10} and P_{90} parameter values respectively. Generally, reservoir parameters with higher degrees of uncertainty are estimated as wider ranges of values and vice versa. This uncertainty increases as the number of flow regimes observed on RNP versus time plot decreases (typical gas production data show less than three flow regimes). However, this uncertainty could be minimized by estimating some of these reservoir parameters from complementary tests (e.g L_f from micro-seismic or image logs) and QFM flow regime analysis equations (e.g. y_e) proposed in the previous paragraph. Additionally, the application of de-noising techniques like wavelet transform (Soliman et al., 2001) could enhance the signal in the production data.

The non-uniqueness associated with QFM should be carefully considered during field analysis with a numerical simulator. This is because (provided that the instantaneous flux transferred from matrix to both MF and HF, and from MF to HF; and the matrix–MF, matrix–HF and MF–HF interfaces remain constant) different combination of reservoir parameters can produce a similar history match. One such combination is either longer y_e and smaller n_f or shorter y_e and larger n_f respectively.

5.6 Summary

A mathematical model (QFM) has been developed which handles simultaneous fluid depletion from the matrix into MF and HF networks under two well constraints (constant terminal bottom-hole rate and constant terminal bottom-hole pressure). QFM converges to the linear sequential triple porosity model in the absence of matrix–HF communication; and converges to the linear dual-porosity model in the absence of micro-fractures.

This chapter provides guidelines on selecting the appropriate model for interpreting production data from multi-fractured horizontal wells in formations with or without secondary (natural or micro) fracture reactivation. Also, the results from this chapter could be extended to gas wells by replacing pressure with the appropriate pseudo-pressure function.

Future studies will focus on: investigating the accuracy of the proposed bulk porosity and permeability relationships; further testing of QFM on datasets from other plays e.g. eagle ford; and extension of QFM for complementary flowback and post-flowback data analysis.

Nomenclature

Symbols

a	Fracture width, L, m, $[ft]$.
c	Compressibility, Lt^2M^{-1}, atm^{-1}, $[Pa^{-1}$, $psi^{-1}]$.
h	Reservoir thickness, L, m, $[ft]$.
k	Bulk permeability, L^2, m^2 $[D]$.
l	Characteristic length, L, m, $[ft]$.
n	Number, L, m, $[ft]$.
q	Rate, L^3t^{-1}, $m^3.s^{-1}$, $[rb.day^{-1}]$.
s	Laplace variable, t^{-1}, s^{-1}, $[hr^{-1}$, $day^{-1}]$.
t	Time, t, s, $[hr$, $day]$.
x, y	Principal reference SRV co-ordinates , L, m, $[ft]$.
z	Gas compressibility factor, dimensionless.
A	Area, L^2, m^2, $[ft^2]$.
L	Distance or length, L, m, $[ft]$.
P	Pressure, $ML^{-1}t^{-2}$, Pa, $[psi]$.
R	Aspect Ratio, dimensionless.

S	Connection area per unit volume of rock, L^{-1}, m^{-1}, $[ft^{-1}]$.
V	Volume, L^3, m^3, $[ft^3]$.
X	Horizontal well length, L, m, $[ft]$.
α	Interporosity shape factor, L^{-2}, m^{-2}, $[ft^{-2}]$.
ϕ	Bulk porosity, dimensionless.
λ	Interporosity transmissivity ratio.
μ	Viscosity, $ML^{-1}t^{-1}$, $Pa.s$, $[cP]$.
ω	Storativity ratio, dimensionless.
Δ	Change.

Superscripts

*	Secondary axis parallel to principal axis.
$^-$	Laplace transform.
^{t}	true.

Subscripts

$_b$	bubble point.
$_c$	cross-section.
$_e$	equivalent.
$_f$	Micro-fracture.
$_i$	Initial.
$_m$	Matrix.
$_p$	Production.
$_t$	Total.
$_w$	Well.
$_D$	Dimensionless.
$_F$	Hydraulic fracture.
$_L$	Reference length.
$_{sp}$	Spacing.
$_{wf}$	Bottom-hole flowing.

Chapter 6

Capturing the Effects of Secondary Fractures on Production Data Using Flow Regime Analysis

6.1 Introduction

Although low permeability reservoirs are now significant sources of hydrocarbon worldwide (King, 2012), modeling fluid flow in such complex reservoirs is still challenging due to the complex structure of the porous media.

The number of distinct porous regions in a reservoir determines the appropriate conceptual fluid flow model for analyzing its production data. An example is the dual-porosity model which comprises two porous regions: fracture network and matrix blocks. Communication between both regions can be transient or pseudo-steady state. Warren and Root (1963) proposed an idealized, sugar-cube, dual-porosity model consisting of uniformly distributed fractures and matrix blocks. Kazemi (1969) extended Warren and Root (1963)'s model by replacing the pseudo-steady state matrix-fracture communication with transient communication. Carlson and Mercer (1991) were one of the first to extend the existing dual-porosity model for application in Shale reservoirs.

All dual-porosity models discussed so far assume radial flow towards the well. However, long transient linear behavior (half-slope line) has been observed on log-log plots (El-Banbi, 1998) of production rate against time. This phenomenon could be as a result of: production from fractures whose lengths extend to reservoir boundaries (Wattenbarger et al., 1996); transient drainage of low permeability matrix blocks into adjoining fractures; and linear shape of certain reservoirs (Stright Jr. and Gordon, 1983). Since the existing radial dual-porosity models could not explain this extended linear flow regime, it became necessary to develop a suitable model for analyzing production data from fractured reservoirs.

El-Banbi (1998) extended the previous dual-porosity models (Warren and Root, 1963; Kazemi, 1969) to produce a list of dual-porosity solutions for linear reservoirs. Bello (2009) extended El-Banbi (1998)'s linear dual-porosity model for rate transient analysis of frac-

tured Shale reservoirs by assuming dual linear depletion (Fig. 6.1) from: matrix into adjoining fractures and fractures into the horizontal well. He developed asymptotic analysis equations and specialized plots to describe observable flow regimes.

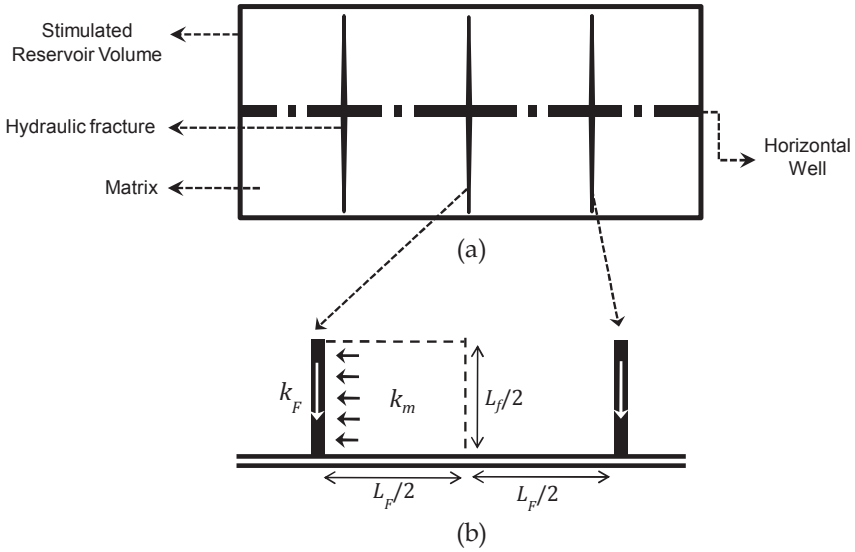

Fig. 6.1: Linear Dual Porosity Model (DPM). (a) Horizontal cross-section of hydraulically fractured horizontal well in tight reservoirs. (b) Conceptual flow physics.

Dual-porosity models assume uniform matrix and fracture properties throughout the reservoir, which may not be true in reality. Studies in the Western Canadian Sedimentary Basin (Castillo et al., 2011; Rogers et al., 2010) show that the connection between effective hydraulic fracture (HF) and the existing system of natural fractures enhances the reservoir volume drained by a well. This HF connection transforms the dual-porosity reservoir into a triple porosity system (Gale et al., 2007; Dahi, 2009). These observations, among others, raised the need for triple porosity models that could interpret production data from reservoirs with non-uniform matrix or fracture properties.

Triple-porosity models can comprise: two fracture networks and one matrix type or one fracture network and two matrix types. Triple-porosity models can be classified further into pseudo-steady state and transient models depending on the matrix–fracture communication. Abdassah and Ershaghi (1986) proposed a transient triple porosity model where fractures with homogeneous properties interact with two distinct groups of matrix blocks (different permeabilities and porosities). Liu et al. (2003) developed a pseudo-steady state triple porosity model to analyze the transient, pressure behavior of fractured lithophysal reservoirs comprising fractures, rock matrices, and cavities. Wu et al. (2004) used the same mathematical model to simulate the flow and transport processes in fractured reservoirs comprising matrices, large fractures, and small fractures. Dehghanpour and Shirdel (2011) extended Ozkan et al. (2010)'s transient dual-porosity model and Warren and

Root (1963)'s pseudo-steady state model to obtain two triple porosity models comprising sub-matrices (nano-Darcy permeabilities) and micro-fractures (milli- to micro-Darcy permeabilities). The resulting models can be used to explain the unexpected high gas production in some Shale gas reservoirs which cannot be justified by conventional dual-porosity models.

Al-Ahmadi (2010) proposed a linear sequential triple porosity model (STPM) by extending the linear dual-porosity model (DPM) of Bello (2009) to account for linear fluid depletion from: matrix to secondary- or micro-fractures (MF); MF to HF; and HF to horizontal well.

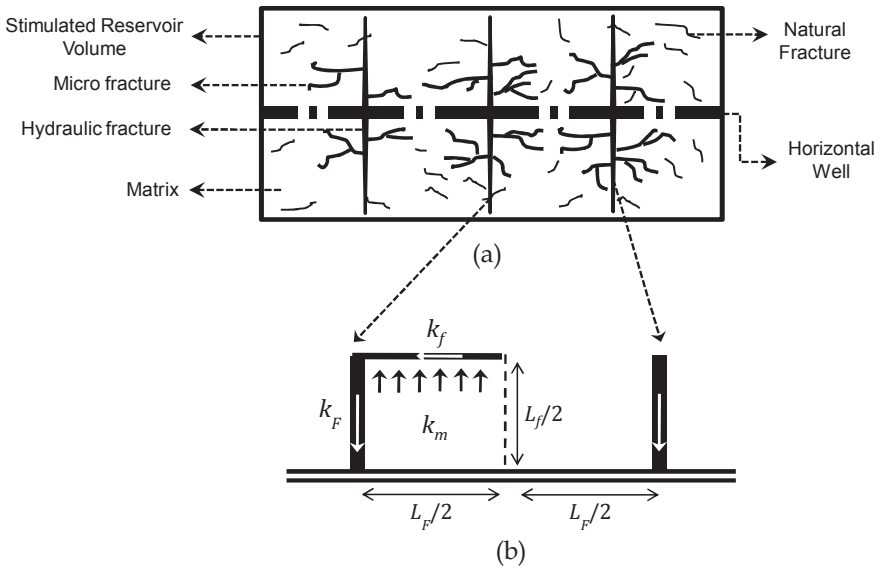

Fig. 6.2: Linear sequential triple porosity model (STPM). (a) Horizontal cross-section of hydraulically fractured horizontal well in tight reservoirs. (b) Conceptual flow physics.

Siddiqui et al. (2012) and Ali et al. (2013) simplified Al-Ahmadi (2010)'s model (Fig. 6.2) to obtain STPM analysis equations for interpreting flow-regimes from production data. Similarly, Tivayanonda et al. (2012) presented a simplified case of Al-Ahmadi (2010)'s model by treating the hydraulic fractures as constant-pressure boundaries. They further proposed analysis equations and interpretation guidelines for five possible production scenarios. Tivayanonda (2012) and Ezulike and Dehghanpour (2014a, 2016b) are among the first to do a comparative study of the existing dual and triple porosity models. Tivayanonda (2012) studied and compared the: homogeneous linear flow model (Wattenbarger et al., 1998); transient linear dual porosity model (Bello, 2009); and fully transient linear triple porosity model (Al-Ahmadi, 2010). The application of these models on the same production data was done with the assumption of infinite HF conductivity ($k_F = \infty$). Tivayanonda (2012) proposed guidelines and flow-regime analysis equations for

applying these models on production data and Ezulike et al. (2013) proposed application guidelines for selecting the appropriate model to apply on a given production data set.

Brown et al. (2011) presented a general analytical trilinear model (a combination of dual-porosity model and linear flow model) to simulate pressure transient and production behavior of fractured horizontal wells in Shale reservoirs. They concluded that the trilinear flow model should be sufficient to analyze production data from tight reservoirs despite the complex interplay of flow among matrix, natural fractures and hydraulic-fractures.

However, all existing triple porosity and triple-linear flow models assume sequential depletion (negligible matrix–HF communication). This assumption holds only if the matrix–MF communication is far greater than the matrix–HF communication (e.g. high MF density or concentration with a given HF spacing). In situations where there is significant matrix–HF communication or negligible bulk matrix–MF contact area compared to bulk matrix–HF contact area, the sequential assumption can result in unreasonable estimates of MF and/or HF properties.

Hence, Ezulike and Dehghanpour (2014a) proposed a quadrilinear flow model (QFM) which relaxes the sequential depletion assumption by conceptually dividing the matrix volume into two sub-domains: one feeds HF and the other feeds MF (Fig. 6.3). QFM also converges to the STPM in the absence of matrix-HF communication; and converges to the DPM in the absence of MF.

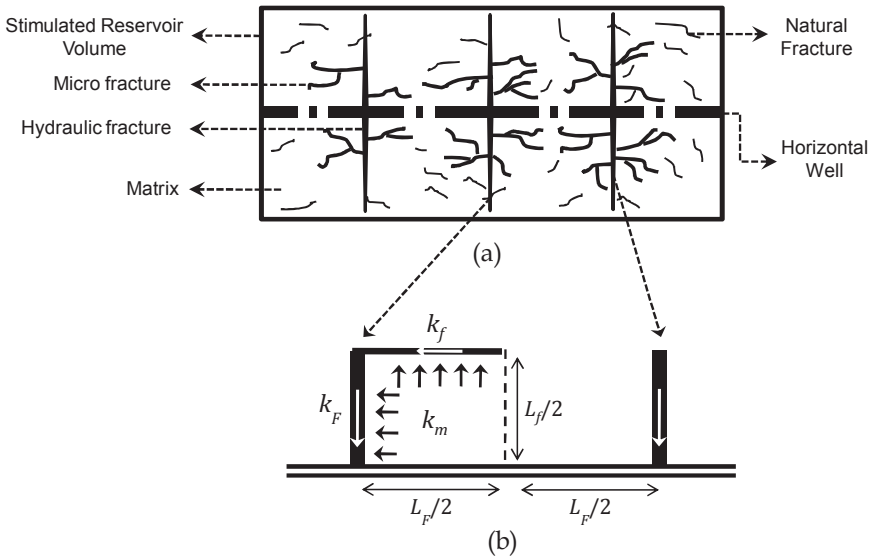

Fig. 6.3: Quadrilinear flow model (QFM). (a) Horizontal cross-section of hydraulically fractured horizontal well in tight reservoirs. (b) Conceptual flow physics.

However, there is considerable non-uniqueness and uncertainty associated with the parameter estimates from QFM type-curves. This chapter intends to minimize this uncer-

tainty and non-uniqueness by simplifying the QFM solution (Ezulike and Dehghanpour, 2014a). The simplification should yield analysis equations for interpreting production data from tight reservoirs with active secondary fracture networks. This is achieved in three steps: derivation, application and discussion. Step 1 carefully splits the resulting Laplace-space QFM solution into analysis equations based on flow regimes observed from type-curves representing typical field scenarios. Step 2 applies the simplified analyses equations on field production data plots. Step 3 considers the implications of non-uniqueness in flow regimes on production data analysis.

6.2 Methodology

The study approach used in this chapter comprises following the seven steps:

- Select different sets of reservoir and well parameters typical of field production.
- Put these parameters into the general QFM solution.
- Generate dimensionless type-curves and observe the progression of flow regions or regimes.
- Determine the parameters which control the duration and strength of each flow region.
- Investigate the physics behind each flow region.
- Split the QFM solution to analysis equations based on the physics of flow region.
- Apply the simplified analysis equations on field production data.

6.3 Results

A detailed derivation of the analysis equations from the general QFM solution is given in Appendix E. Here, the resulting analysis equations are used to: explain the physics behind the possible flow regions observable on field data; and propose specialized field data plots for production data analysis. Also, it exploits the ability of dimensionless logarithmic pressure derivative ($\partial P_{_D}/\partial lnt_{_D}$) and dimensionless rate ($q_{_D}$) type-curves to detect subtle flow region transitions in reducing the non-uniqueness associated with type-curves (Stanislav et al., 1987).

6.3.1 QFM Solution

The general, dimensionless, Laplace space, QFM solution (Ezulike and Dehghanpour, 2014a) under variable bottom-hole rate and pressure well conditions are given below as:

$$\overline{P}_{wDL} = \frac{coth\left(\sqrt{sf(s)}y_{De}\right)}{s\sqrt{sf(s)}} \text{ and} \tag{6.1}$$

$$\overline{q}_{wDL} = \frac{\sqrt{sf(s)}}{s\ coth\left(\sqrt{sf(s)}y_{De}\right)} \tag{6.2}$$

$$\text{where } f_m(s) = \frac{3s\omega_2\omega_m}{\lambda_{AC,Fm}} \tag{6.3}$$

$$f_f(s) = \left\{\frac{3\omega_f}{\lambda_{AC,Ff}} + \frac{\lambda_{AC,fm}}{s\lambda_{AC,Ff}}\sqrt{\frac{3s\omega_1\omega_m}{\lambda_{AC,fm}}}\ tanh\left(\sqrt{\frac{3s\omega_1\omega_m}{\lambda_{AC,fm}}}\right)\right\} \tag{6.4}$$

$$\text{and } f(s) = \omega_F + \frac{\lambda_{AC,Ff}}{3s}\sqrt{sf_f(s)}\ tanh\left(\sqrt{sf_f(s)}\right) + \frac{\lambda_{AC,Fm}}{3s}\sqrt{f_m(s)}\ tanh\left(\sqrt{f_m(s)}\right) \tag{6.5}$$

In this model, $f_m(s)$ represents the transfer function for fluid flow from sub-matrix 2 to HF; $f_f(s)$ represents the transfer function for fluid flow from sub-matrix 1 to MF, and from MF to HF respectively; while $f(s)$ represents the transfer function for fluid flow from sub-matrices 1 and 2, and micro-fractures into hydraulic fractures. ω_1 and ω_2 are heuristic, weighting parameters that control the fraction of fluid volume in the matrix which goes into micro-fractures and hydraulic fractures respectively during production.

6.3.2 Type Curves

Table 6.1 shows a sample dataset which is substituted into Eqs. 6.1 and 6.2 to obtain dimensionless, logarithmic pressure derivative ($\partial P_D/\partial lnt_D$) and rate ($q_D$) type-curves respectively. The bulk permeability and porosity values are calculated using the relationships proposed in Ezulike and Dehghanpour (2014a). Fig. 6.4 shows the subtle changes in typical QFM flow regions on dimensionless QFM type-curves. Table 6.2 shows the slopes of these flow regions.

Table 6.1: Sample dataset for QFM type-curves.

Reservoir Parameter	**Value**	**Units**
h	7	m
X_e	1370	m
y_e	150	m
$n_{_F}$	18	—
L_f	32	m
$L_{_F}$	72.1	m
a_f	1×10^{-4}	m
$a_{_F}$	1×10^{-3}	m
k_m	0.035	mD
k_m (bulk)	0.035	mD
k_f	100	mD
k_f (bulk)	3×10^{-4}	mD
$k_{_F}$	10000	mD
$k_{_F}$ (bulk)	0.14	mD
ϕ_m	0.012	—
ϕ_m (bulk)	0.012	—
ϕ_f	0.9	—
ϕ_f (bulk)	3×10^{-6}	—
ϕ_F	0.48	—
ϕ_F (bulk)	7×10^{-6}	—
$(c_t)_m$	2.209×10^{-6}	kPa^{-1}
$(c_t)_f$	2.209×10^{-3}	kPa^{-1}
$(c_t)_{_F}$	2.209×10^{-5}	kPa^{-1}

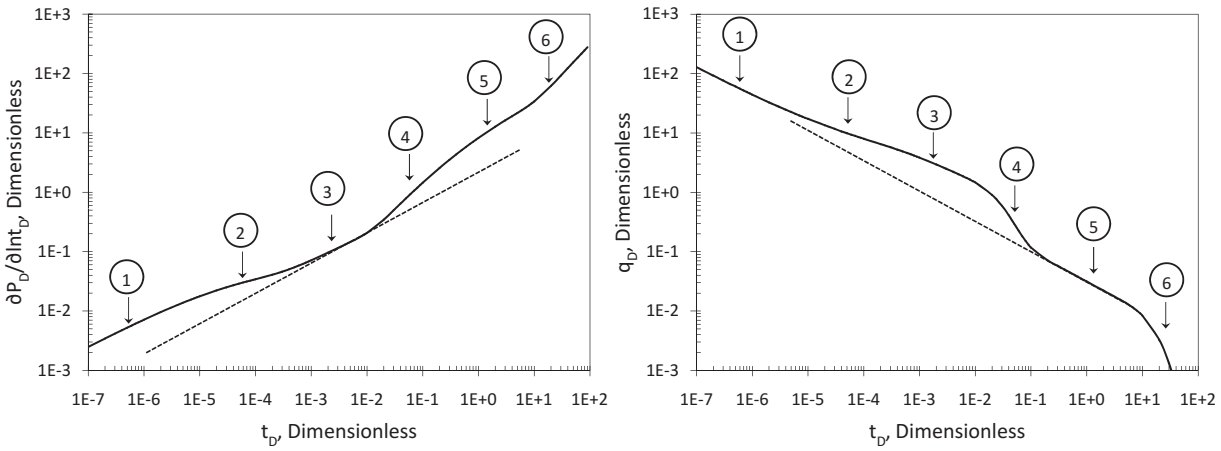

(a) (b)

Fig. 6.4: Typical QFM flow regions (from 1 to 6). (a) Dimensionless logarithmic pressure derivative ($\partial P_D/\partial lnt_D$) plot. (b) Dimensionless rate (q_D) plot. The dotted lines have +0.5 and -0.5 slopes (from left to right) respectively.

Table 6.2: Typical QFM flow regions.

Flow region	**Slope**	
	$\partial P_D/\partial lnt_D$	q_D
1	0.5	-0.5
2	0.25	-0.25
3	0.5	-0.5
4	1	$-exp$ trend
5	0.5	-0.5
6	1	$-exp$ trend

6.3.3 Analysis Equations

This part discusses the physics of some observable flow regions in QFM. It also provides specialized plots for production data analysis. The development of possible analysis equations for constant rate and constant pressure conditions are provided here. For example, the flow region sequence for the data set in Table 6.1 is 1, 2A, 3A, 4A, 5A and 6 (see Table 6.3). Different flow regions could occur within a similar time interval due to the differences in relative magnitude of reservoir parameters for that specific reservoir case. Here, the permeability and porosity values are bulk values calculated from the relationships proposed in Ezulike and Dehghanpour (2014a). Bulk values are used instead of actual values to account for each distinct porous region (matrix, micro-fracture, hydraulic fracture) as part of the whole reservoir system and not in isolation (Warren and Root, 1963).

Flow Region 1

There is generally one possible transient response during this flow region.

Linear Transient Depletion in Hydraulic Fractures ($\frac{1}{2}$ slope)

This flow region is the same as Region 1 in DPM (Bello, 2009) and STPM (Ali et al., 2013) respectively. It occurs at very early times $\left[t \leq \frac{\mu y_e^2 (\phi c_t)_F}{9 k_F}\right]$ when there is negligible fluid influx from matrix and micro-fractures into the hydraulic fractures. It is not seen on most post-flowback, production data plots since it might have occurred during well clean-up, i.e. flowback (Abbasi et al., 2014; Ezulike and Dehghanpour, 2014b,c). The duration and strength of this flow region depend on the half-length (y_e), permeability (k_F) and storage capacity $(\phi c_t)_F$ of the hydraulic fractures. Applying dimensional transformations (Ezulike and Dehghanpour, 2014a), Eq. F.1 for rate-constrained wells and Eq. F.14 for pressure-constrained wells become:

$$\sqrt{k_F (\phi c_t)_F} = \frac{1}{m_{11}} \times \frac{1}{A_{cw}} \sqrt{\frac{\mu}{\pi}} \tag{6.6}$$

$$\sqrt{k_F (\phi c_t)_F} = \frac{1}{m_{12}} \times \frac{1}{A_{cw}} \sqrt{\pi \mu} \tag{6.7}$$

where m_{11} and m_{12} are slopes from the specialized rate-normalized-pressure derivative [$\frac{\partial \mathsf{RNP}}{\partial (lnt)}$ against $\sqrt{t}$] and rate-normalized-pressure [RNP against $\sqrt{t}$] plots. RNP represents $\frac{\Delta P_{wL}}{q}$ and $\frac{\Delta P_{wL}}{q(t)}$ for the specialized rate-normalized-pressure derivative and rate-normalized-pressure plots respectively. A_{cw} is the cross-sectional area at the face of the

horizontal well. Eqs. 6.6 and 6.7 show that production pressure and rate during this period depend on — hydraulic fracture permeability and its storage capacity. This means that all fluid depletion takes place in the hydraulic fractures during this period. Therefore, Eqs. 6.6 and 6.7 provide estimates of hydraulic fracture permeability if the storage capacity of the hydraulic fractures is known; and vice versa.

Flow Region 2

Of the possible responses during this flow period, three of them observed in this study include — Region 2A (when fluid support from matrix kicks in to supplement transient depletion in hydraulic fractures), Region 2B (when fluid support from the micro-fractures kicks in to supplement transient depletion in hydraulic fractures), and Region 2C (when no fluid support from either matrix or micro-fracture kicks in to supplement transient depletion in hydraulic fractures).

Case A: Bilinear Flow due to Transient Depletion in Matrix and Hydraulic Fractures ($\frac{1}{4}$ slope after $\frac{1}{2}$ slope)

The transient depletion of hydraulic fractures from Region 1 becomes weak and requires fluid support from the surrounding matrix or micro-fractures for production to continue. This case describes the situation when the communication strength between matrix and hydraulic fractures overshadows that between micro-fractures and hydraulic fractures. Hence, transient linear depletion in the matrix towards the depleted hydraulic fractures becomes the primary mechanism for production during this time period $\left[t \leq \frac{\mu L_F^2 \omega_2 (\phi c_t)_m}{36 k_m}\right]$, where $\omega_2 = \frac{R_{sp}^2}{1+R_{sp}^2}$. The duration and strength of this region depend on matrix permeability (k_m), micro-fracture intensity (as seen from the spacing aspect ratio, R_{sp}) and matrix storage capacity $(\phi c_t)_m$. ω_2 represents the conceptual fraction of fluid volume in the matrix which feeds the hydraulic fractures. R_{sp} is the ratio between micro-fracture spacing (L_f) and hydraulic fracture spacing (L_F). Therefore, micro-fracture intensity is inversely proportional to both R_{sp} and ω_2 respectively. It means that this flow region lasts longer when there is low micro-fracture intensity. This flow region could be observed in DPM in the absence of micro-fractures ($\omega_2 \longrightarrow 1$) but not in STPM due to the assumption of negligible matrix and hydraulic fracture communication ($\omega_2 \longrightarrow 0$). Applying dimensional transformations, Eq. F.2 for rate-constrained wells and Eq. F.15 for pressure-constrained

wells become:

$$\sqrt[4]{k_m\omega_2(\phi c_t)_m}\sqrt{k_{_F}} = \frac{1}{m_{21}} \times \frac{0.195\mu}{A_{cw}}\sqrt[4]{\frac{L_{_F}^2}{\mu}} \tag{6.8}$$

$$\sqrt[4]{k_m\omega_2(\phi c_t)_m}\sqrt{k_{_F}} = \frac{1}{m_{22}} \times \frac{0.867\mu}{A_{cw}}\sqrt[4]{\frac{L_{_F}^2}{\mu}} \tag{6.9}$$

where m_{21} and m_{22} are slopes from the specialized rate-normalized-pressure derivative [$\frac{\partial \mathsf{RNP}}{\partial(lnt)}$ against $\sqrt[4]{t}$] and rate-normalized-pressure [RNP against $\sqrt[4]{t}$] plots. Eqs. 6.8 and 6.9 show that production pressure and rate during this period depend on — matrix permeability and its storage capacity, hydraulic fracture permeability, and micro-fracture intensity (R_{sp} in ω_2). Therefore, Eqs. 6.8 and 6.9 provide estimates of micro-fracture intensity if matrix permeability and storage capacity (e.g. from core analysis),and hydraulic fracture permeability (e.g. from flow region 1A analysis) are known, and vice versa.

Case B: Bilinear Flow due to Transient Depletion in Micro-Fractures and Hydraulic Fractures ($\frac{1}{4}$ slope after $\frac{1}{2}$ slope)

This happens after the transient depletion from Region 1 becomes weak and requires fluid support from the surrounding matrix or micro-fractures for production to continue. This case describes the situation when the communication strength between micro-fractures and hydraulic fractures overshadows that between matrix and hydraulic fractures. Hence, transient linear depletion in the micro-fractures towards the depleted hydraulic fractures becomes the primary mechanism for production during this time period $\left[t \leq \frac{\mu L_{_F}^2(\phi c_t)_f}{36k_f}\right]$. The duration and strength of this region depend on micro-fracture permeability (k_f) and its storage capacity $(\phi c_t)_f$. $(\phi c_t)_f$ is directly proportional to micro-fracture intensity but inversely proportional to spacing aspect ratio (R_{sp}). This flow region is the same as Region 2 in STPM. However, it is not seen in DPM due to the absence of micro-fractures ($k_f \longrightarrow 0$). Applying dimensional transformations, Eq. F.3 for rate-constrained wells and Eq. F.16 for pressure-constrained wells become:

$$\sqrt[4]{k_f(\phi c_t)_f}\sqrt{k_{_F}} = \frac{1}{m_{21}} \times \frac{0.195\mu}{A_{cw}}\sqrt[4]{\frac{L_{_F}^2}{\mu}} \tag{6.10}$$

$$\sqrt[4]{k_f(\phi c_t)_f}\sqrt{k_{_F}} = \frac{1}{m_{22}} \times \frac{0.867\mu}{A_{cw}}\sqrt[4]{\frac{L_{_F}^2}{\mu}} \tag{6.11}$$

where m_{21} and m_{22} are slopes from the specialized rate-normalized-pressure derivative

[$\frac{\partial \text{RNP}}{\partial(lnt)}$ against $\sqrt[4]{t}$] and rate-normalized-pressure [RNP against $\sqrt[4]{t}$] plots. Eqs. 6.10 and 6.11 show that production pressure and rate during this period depend on — micro-fracture permeability and its storage capacity, and hydraulic fracture permeability. Therefore, Eqs. 6.10 and 6.11 provide estimates of micro-fracture permeability if hydraulic fracture permeability (e.g. from flow region 1A analysis) and micro-fracture storage capacity (e.g. from micro-seismic) are known, and vice versa.

Case C: Pseudo-steady State Depletion of Hydraulic Fractures due to Insufficient Fluid Support from Matrix and Micro-Fractures (unit slope after $\frac{1}{2}$ slope)

After the transient depletion of hydraulic fractures from Region 1 ends, fluid support from the surrounding matrix or micro-fractures is required for production to continue. In this case, there is negligible communication between matrix and micro-fractures, and the hydraulic fractures. This could be a result of damage to the interface of hydraulic fractures. This is a special case which happens when $t \geq \frac{\mu y_e^2 (\phi c_t)_F}{k_F}$. The duration and strength of this region depend on the half-length (y_e), permeability (k_F) and storage capacity $(\phi c_t)_F$ of the hydraulic fractures. Applying dimensional transformations, Eq. F.4 for rate-constrained wells becomes

$$y_e (\phi c_t)_F = \frac{1}{m_{21}} \times \frac{1}{A_{cw}} \tag{6.12}$$

where m_{21} is the slope from the specialized rate-normalized-pressure derivative [$\frac{\partial \text{RNP}}{\partial(lnt)}$ against t] plot. Eq. 6.12 shows that production pressure and rate during this period depends on two key parameters — the half-length and storage capacity of hydraulic fractures. This means that all fluid depletion takes place in the hydraulic fractures during this period, as it behaves like an isolated tank. Therefore, Eq. 6.12 provides estimates of hydraulic fracture half-length if its storage capacity is known, and vice versa. Pressure-constrained wells require a combination of the productivity index (J in Eq. 6.13) and a material balance equation for a closed hydraulic fracture system (Bello, 2009).

$$q_g = J \left[m(\overline{P}) - m(P_{wf}) \right] \tag{6.13}$$

where $m(P)$ in Eq. 6.13 is the gas pseudo-pressure.

Flow Region 3

Of the possible responses during this flow period, three of them observed in this study include — Region 3A (when the primary depletion is transient linear as a result of the micro-fractures and matrix acting as a single, porous medium), Region 3B (when the primary depletion is transient linear in micro-fractures alone) and Region 3C (when the primary depletion is transient linear in the matrix alone).

Case A: Linear Flow due to Simultaneous Transient Depletion in Matrix and Micro-Fractures ($\frac{1}{2}$ slope after $\frac{1}{4}$ slope)

This happens after Region 2A when the existing, transient, linear depletion in the hydraulic fracture dies out. Now, the micro-fractures join the existing matrix support, and both matrix and micro-fractures behave as a single porous unit. This happens when $t \geq \frac{\pi\mu y_e^4\left(\sqrt{k_f(\phi c_t)_f}+\sqrt{k_m\omega_2(\phi c_t)_m}\right)}{k_F^2 L_F^2}$. This flow region is not seen in DPM and STPM due to the absence of micro-fractures ($k_f \longrightarrow 0$) and the assumption of negligible matrix and hydraulic fracture communication ($\omega_2 \longrightarrow 0$) respectively. The duration and strength of this region depend on hydraulic fracture half-length and its permeability (y_e and $k_{_F}$), micro-fracture permeability and its storage capacity (k_f and $(\phi c_t)_f$), and matrix permeability and its storage capacity (k_m and $(\phi c_t)_m$). Also, they depend on micro-fracture intensity (R_{sp} in ω_2). Applying dimensional transformations, Eq. F.6 for rate-constrained wells and Eq. F.17 for pressure-constrained wells become:

$$y_e\left[\sqrt{k_f(\phi c_t)_f}+\sqrt{k_m\omega_2(\phi c_t)_m}\right]=\frac{1}{m_{31}}\times\frac{L_{_F}}{2A_{cw}}\sqrt{\frac{\mu}{\pi}} \tag{6.14}$$

$$y_e\left[\sqrt{k_f(\phi c_t)_f}+\sqrt{k_m\omega_2(\phi c_t)_m}\right]=\frac{1}{m_{32}}\times\frac{L_{_F}}{2A_{cw}}\sqrt{\pi\mu} \tag{6.15}$$

where m_{31} and m_{32} are slopes from the specialized rate-normalized-pressure derivative [$\frac{\partial \mathsf{RNP}}{\partial(lnt)}$ against $\sqrt{t}$] and rate-normalized-pressure [RNP against $\sqrt{t}$] plots. Eqs. 6.14 and 6.15 show that production pressure and rate during this period depend on several key parameters — hydraulic fracture half-length, micro-fracture permeability and its storage capacity, matrix permeability and its storage capacity, and micro-fracture intensity. In fact, the micro-fracture intensity determines the amount of matrix contribution (see ω_2 in the second term of the left hand side of Eqs. 6.14 and 6.15). Therefore, this flow region provides micro-fracture intensity estimates if hydraulic fracture half-length (e.g. from micro-seismic), micro-fracture permeability and its storage capacity (e.g. from micro-seismic), matrix permeability and its storage capacity (e.g. both from core experiments)

are known, and vice versa.

Case B: Linear Flow due to Transient Depletion in Micro-Fractures ($\frac{1}{2}$ slope after $\frac{1}{4}$ slope)

This happens after Region 2B, when the transient depletion of hydraulic fractures dies out and while transient, linear depletion in the surrounding micro-fractures continues. This occurs when $t \geq \frac{\pi\mu y_e^4 k_f (\phi c_t)_f}{k_F^2 L_F^2}$. This flow region is the same as Region 3 in STPM. However, it is not seen in DPM due to the absence of micro-fractures ($k_f \longrightarrow 0$). The duration and strength of this region depend on hydraulic fracture half-length (y_e), micro-fracture permeability and its storage capacity [k_f and $(\phi c_t)_f$]. $(\phi c_t)_f$ is directly proportional to micro-fracture intensity but inversely proportional to spacing aspect ratio (R_{sp}). Applying dimensional transformations, Eq. F.7 for rate-constrained wells and Eq. F.18 for pressure-constrained wells become:

$$y_e \sqrt{k_f (\phi c_t)_f} = \frac{1}{m_{31}} \times \frac{L_F}{2A_{cw}} \sqrt{\frac{\mu}{\pi}} \tag{6.16}$$

$$y_e \sqrt{k_f (\phi c_t)_f} = \frac{1}{m_{32}} \times \frac{L_F}{2A_{cw}} \sqrt{\pi\mu} \tag{6.17}$$

where m_{31} and m_{32} are slopes from the specialized rate-normalized-pressure derivative [$\frac{\partial \mathsf{RNP}}{\partial (lnt)}$ against $\sqrt{t}$] and rate-normalized-pressure [RNP against $\sqrt{t}$] plots. Eqs. 6.16 and 6.17 show that production pressure and rate during this period depend on three key parameters — hydraulic fracture half-length, micro-fracture permeability and its storage capacity. Therefore, Eqs. 6.16 and 6.17 provide estimates of hydraulic fracture half-length if micro-fracture permeability and its storage capacity (e.g. from flow region 2B analysis) are known, and vice versa.

Case C: Linear Transient Depletion in the Matrix ($\frac{1}{2}$ slope after $\frac{1}{4}$ slope)

This happens after Region 2A, as the transient depletion from in the hydrualic fracture finally dies out leaving just the matrix support to continue. It occurs when $t \geq \frac{\pi\mu y_e^4 k_m \omega_2 (\phi c_t)_m}{k_F^2 L_F^2}$. This flow region can be seen in DPM ($\omega_2 \longrightarrow 1$) but not in STPM due to the assumption of negligible matrix and hydraulic fracture communication ($\omega_2 \longrightarrow 0$). The duration and strength of this region depend on hydraulic fracture half-length (y_e), micro-fracture intensity (R_{sp} in ω_2), matrix permeability and its storage capacity [k_m and $(\phi c_t)_m$]. Applying dimensional transformations, Eq. F.8 for rate-constrained wells and

Eq. F.19 for pressure-constrained wells become:

$$y_e\sqrt{k_m\omega_2(\phi c_t)_m} = \frac{1}{m_{31}} \times \frac{L_{_F}}{2A_{cw}}\sqrt{\frac{\mu}{\pi}} \tag{6.18}$$

$$y_e\sqrt{k_m\omega_2(\phi c_t)_m} = \frac{1}{m_{32}} \times \frac{L_{_F}}{2A_{cw}}\sqrt{\pi\mu} \tag{6.19}$$

where m_{31} and m_{32} are slopes from the specialized rate-normalized-pressure derivative [$\frac{\partial \mathsf{RNP}}{\partial(lnt)}$ against $\sqrt{t}$] and rate-normalized-pressure [RNP against $\sqrt{t}$] plots. Eqs. 6.18 and 6.19 show that production pressure and rate during this period depend on four key parameters — hydraulic fracture half-length, micro-fracture intensity, matrix permeability and its storage capacity. Therefore, Eqs. 6.18 and 6.19 provide estimates of hydraulic fracture half-length if micro-fracture intensity (e.g. from flow region 2A analysis or micro-seismic), matrix permeability and its storage capacity (e.g. from flow region 2A analysis and core experiments) are known, and vice versa.

Flow Region 4

Of the possible responses during this flow period, two of them observed in this study include — Region 4A (when the matrix support becomes weak, leaving only micro-fractures as the primary source for fluid depletion) and Region 4B (when the matrix is the primary source of fluid supply to both micro-fractures and hydraulic fractures).

Case A: Pseudo-steady State Depletion in Micro-Fractures due to Insufficient Fluid Support from Matrix (unit slope after $\frac{1}{2}$ slope)

This is a short flow region which happens after Region 3A. The matrix to hydraulic fracture fluid support which started in Region 2A becomes weak, leaving the micro-fractures as the primary source of pressure support to the hydraulic fractures. With negligible fluid influx from the matrix, the micro-fractures behave as a tank whose depletion is the driving mechanism for production during this time period $\left[t \geq \frac{25\mu L_{_F}^2(\phi c_t)_f}{k_f}\right]$. This flow region can be seen in STPM but not in DPM due to the absence of micro-fractures [$(\phi c_t)_f \longrightarrow 0$]. The duration and strength of this region depend on micro-fracture storage capacity and its permeability [$(\phi c_t)_f$ and k_f] and. $(\phi c_t)_f$ is directly proportional to micro-fracture intensity but inversely proportional to spacing aspect ratio (R_{sp}). Applying dimensional transformations, Eq. F.9 for rate-constrained wells becomes:

$$y_e(\phi c_t)_f = \frac{1}{m_{41}} \times \frac{1}{A_{cw}} \tag{6.20}$$

where m_{41} is the slope from the specialized pressure derivative [$\frac{\partial \mathsf{RNP}}{\partial(lnt)}$ against t] plot. Eq. 6.20 shows that production pressure and rate during this period depends on two key parameters — the hydraulic fracture half-length and micro-fracture storage capacity. Therefore, Eq. 6.20 provides micro-fracture storage capacity estimates if hydraulic fracture half-length (e.g. from micro-seismic) is known, and vice versa. Pressure-constrained wells require a combination of the productivity index and a material balance equation for a closed micro-fracture system (see Eq. 6.13).

Case B: Bilinear Flow due to Transient Depletion from Matrix towards both Micro-Fractures and Hydraulic Fractures ($\frac{1}{4}$ slope after $\frac{1}{2}$ slope)

This is a long flow region which can happen after Regions 3B or 3C. Here, fluid support from matrix to both micro- and hydraulic fractures becomes the primary production mechanism. This occurs when $t \geq \frac{2500\mu L_F^4 \omega_1 (\phi c_t)_m k_m}{k_f^2 L_f^2}$. This flow region is seen in DPM ($\omega_1 \longrightarrow 0$ and $\omega_2 \longrightarrow 1$) but not in STPM due to the assumption of negligible matrix and hydraulic fracture communication ($\omega_1 \longrightarrow 1$ and $\omega_2 \longrightarrow 0$) respectively. The duration and strength of this region depend on micro-fracture intensity (R_{sp} in ω_1) and its permeability (k_f), matrix permeability and its storage capacity [k_m and $(\phi c_t)_m$]. Applying dimensional transformations, Eq. F.10 for rate-constrained wells and Eq. F.20 for pressure-constrained wells become:

$$\sqrt{k_F}\sqrt{\sqrt{\frac{k_m\omega_1(\phi c_t)_m}{L_f^2}}+\sqrt{\frac{k_m\omega_2(\phi c_t)_m}{L_F^2}}} = \frac{1}{m_{41}} \times \frac{0.195\mu}{A_{cw}} \sqrt[4]{\frac{1}{\mu}} \tag{6.21}$$

$$\sqrt{k_F}\sqrt{\sqrt{\frac{k_m\omega_1(\phi c_t)_m}{L_f^2}}+\sqrt{\frac{k_m\omega_2(\phi c_t)_m}{L_F^2}}} = \frac{1}{m_{42}} \times \frac{0.867\mu}{A_{cw}} \sqrt[4]{\frac{1}{\mu}} \tag{6.22}$$

where m_{41} and m_{42} are slopes from the specialized rate-normalized-pressure derivative [$\frac{\partial \mathsf{RNP}}{\partial(lnt)}$ against $\sqrt[4]{t}$] and rate-normalized-pressure [RNP against $\sqrt[4]{t}$] plots. Eqs. 6.21 and 6.22 show that production pressure and rate during this period depend on — hydraulic fracture permeability, micro-fracture intensity, matrix permeability and its storage capacity. Therefore, Eqs. 6.21 and 6.22 provide estimates of micro-fracture intensity if hydraulic fracture permeability (e.g. from the analysis of flow region 2B), matrix permeability and its storage capacity (e.g. from the analysis of flow region 3C and core experiments) are known, and vice versa.

Flow Region 5

Of the possible responses during this flow period, two of them observed in this study include — Region 5A (when there is negligible fluid transfer from matrix to hydraulic fracture) and Region 5B (when there is negligible fluid transfer from micro-fracture to hydraulic fracture).

Case A: Linear Flow due to Transient Depletion in Matrix with Negligible Matrix to Hydraulic Fractures Fluid Transfer ($\frac{1}{2}$ slope after unit slope)

This flow region happesn after Region 4A when $t \leq \frac{\mu L_F^2 \omega_1 (\phi c_t)_m}{36 k_f}$. Here, the transient depletion in both micro- and hydraulic fractures becomes weak and insufficient to sustain production. Hence, production is a result of fluid supply from the matrix closely surrounding the micro- and hydraulic fracture (while depletion has not yet reached the matrix outer edges). At this point, the surrounding matrix, micro-fracture and hydraulic fracture behave as a single porous unit undergoing transient sequential fluid depletion. The matrix serves as the fluid tank that supplies fluid only through the micro-fracture to the hydraulic fracture. This flow region is seen in STPM due to negligible matrix and hydraulic fracture communication ($\omega_1 \longrightarrow 1$) but not in DPM due to the assumption of negligible micro-fractures ($\omega_1 \longrightarrow 0$). The duration and strength of this region depend on micro-fracture intensity (R_{sp} in ω_1) and its permeability (k_f), and matrix storage capacity $(\phi c_t)_m$. Applying dimensional transformations, Eq. F.11 for rate-constrained wells and Eq. F.21 for pressure-constrained wells become:

$$y_e \sqrt{\frac{k_f \omega_1 (\phi c_t)_m}{L_F^2}} = \frac{1}{m_{51}} \times \frac{1}{2A_{cw}} \sqrt{\frac{\mu}{\pi}} \tag{6.23}$$

$$y_e \sqrt{\frac{k_f \omega_1 (\phi c_t)_m}{L_F^2}} = \frac{1}{m_{52}} \times \frac{1}{2A_{cw}} \sqrt{\mu \pi} \tag{6.24}$$

where m_{51} and m_{52} are slopes from the specialized rate-normalized-pressure derivative [$\frac{\partial \mathsf{RNP}}{\partial (lnt)}$ against $\sqrt{t}$] and rate-normalized-pressure [RNP against $\sqrt{t}$] plots. Eqs. 6.23 and 6.24 show that production pressure and rate during this period depend on four key parameters — micro-fracture intensity and its permeability, matrix storage capacity and hydraulic fracture half-length. Therefore, Eqs. 6.23 and 6.24 provide estimates of micro-fracture intensity if micro-fracture permeability (e.g. from micro-seismic), hydraulic fracture half-length (e.g. from flow region 3A or 4A analysis) and matrix storage capacity (e.g. from core experiments) are known, and vice versa.

Case B: Linear Flow due to Transient Depletion from Outer Edges of Matrix Blocks with Negligible Micro-fracture to Hydraulic Fractures Fluid Transfer ($\frac{1}{2}$ slope after unit slope)

This flow region happens after Region 4B when $t \geq \frac{2500\mu L_F^4 \omega_1 (\phi c_t)_m k_m}{k_f^2 L_f^2}$. The transient matrix depletion that started in Region 4B reaches the outer edges of the matrix blocks. This flow region is the same as Region 4 in DPM due to the absence of micro-fractures ($\omega_1 \longrightarrow 0$ and $\omega_2 \longrightarrow 1$) and as Region 5 in STPM due to the assumption of negligible matrix and hydraulic fracture communication ($\omega_1 \longrightarrow 1$ and $\omega_2 \longrightarrow 0$). The duration and strength of this region depend on micro-fracture intensity (R_{sp} in ω_1) and its permeability (k_f), matrix permeability and its storage capacity (k_m and $(\phi c_t)_m$). Applying dimensional transformations, Eq. F.12 for rate-constrained wells and Eq. F.22 for pressure-constrained wells become:

$$y_e \left[\sqrt{\frac{k_m \omega_1 (\phi c_t)_m}{L_f^2}} + \sqrt{\frac{k_m \omega_2 (\phi c_t)_m}{L_F^2}} \right] = \frac{1}{m_{51}} \times \frac{1}{2A_{cw}} \sqrt{\frac{\mu}{\pi}} \tag{6.25}$$

$$y_e \left[\sqrt{\frac{k_m \omega_1 (\phi c_t)_m}{L_f^2}} + \sqrt{\frac{k_m \omega_2 (\phi c_t)_m}{L_F^2}} \right] = \frac{1}{m_{52}} \times \frac{1}{2A_{cw}} \sqrt{\pi \mu} \tag{6.26}$$

where m_{51} and m_{52} are slopes from the specialized rate-normalized-pressure derivative [$\frac{\partial \mathsf{RNP}}{\partial (lnt)}$ against $\sqrt{t}$] and rate-normalized-pressure [RNP against $\sqrt{t}$] plots. Eqs. 6.25 and 6.26 show that production pressure and rate during this period depend on — hydraulic fracture half-length, micro-fracture intensity, matrix permeability and its storage capacity. Therefore, Eqs. 6.25 and 6.26 provide estimates of micro-fracture intensity if hydraulic fracture half-length (e.g. from the analysis of flow region 2B), matrix permeability and its storage capacity (e.g. from the analysis of flow region 3C and core experiments) are known, and vice versa.

Flow Region 6

There is generally one possible transient response during this flow region.

Pseudo-steady State Depletion in Matrix, Micro- and Hydraulic Fractures (unit slope after $\frac{1}{2}$ slope)

This happens once depletion has reached all no-flow boundaries in the reservoir. Also the matrix, micro- and hydraulic fractures behave as a single flow unit. This occurs when $t \geq \frac{\mu y_e^2 (\phi c_t)_t}{k_F}$ and it is the last flow region in both DPM (where $(\phi c_t)_f \longrightarrow 0$) and in STPM.

The duration and strength of this region depend on hydraulic fracture half-length and storage capacity of the reservoir system. Applying dimensional transformations, Eq. F.13 for rate-constrained wells becomes

$$y_e \left[(\phi c_t)_m + (\phi c_t)_f + (\phi c_t)_F\right] = \frac{1}{m_{61}} \times \frac{1}{A_{cw}} \tag{6.27}$$

where m_{61} is the slope from the specialized pressure derivative $[\frac{\partial \mathsf{RNP}}{\partial(lnt)}$ against $t]$ plot. Eq. 6.27 shows that production pressure and rate during this period depends on two key parameters — the hydraulic fracture half-length and reservoir (matrix, micro-fracture and hydraulic fracture) storage capacity. Therefore, Eq. 6.27 provides reservoir storage capacity estimates if hydraulic fracture half-length (e.g. from micro-seismic) is known, and vice versa. Pressure-constrained wells require a combination of the productivity index and a material balance equation for a closed hydraulic fracture system (see Eq. 6.13).

6.3.4 Specialized Plots

This part summarizes the QFM analysis equations for specialized production data analysis in Table 6.3 — where *, $^\circ$, $^\diamond$ show that m_{x1} and m_{x2} are slopes from the $\frac{\partial \mathsf{RNP}}{\partial(lnt)}$ and RNP against $\sqrt[4]{t}$, $\sqrt{t}$ and t plots respectively. The subscript, x, is a number from 1 to 6.

Table 6.3: QFM analysis equations.

Region	Case	Parameters	Analysis Equations	
			Constant Rate	Constant Pressure
1	—	$\sqrt{k_{_F}(\phi c_t)_{_F}}$	$\frac{1}{\circ m_{11}} \times \frac{1}{A_{cw}}\sqrt{\frac{\mu}{\pi}}$	$\frac{1}{\circ m_{12}} \times \frac{1}{A_{cw}}\sqrt{\mu\pi}$
2	A	$\sqrt[4]{k_m\omega_2(\phi c_t)_m}\sqrt{k_{_F}}$	$\frac{1}{\star m_{21}} \times \frac{0.195\mu}{A_{cw}}\sqrt[4]{\frac{L_{_F}^2}{\mu}}$	$\frac{1}{\star m_{22}} \times \frac{0.867\mu}{A_{cw}}\sqrt[4]{\frac{L_{_F}^2}{\mu}}$
	B	$\sqrt[4]{k_f(\phi c_t)_f}\sqrt{k_{_F}}$	$\frac{1}{\star m_{21}} \times \frac{0.195\mu}{A_{cw}}\sqrt[4]{\frac{L_{_F}^2}{\mu}}$	$\frac{1}{\star m_{22}} \times \frac{0.867\mu}{A_{cw}}\sqrt[4]{\frac{L_{_F}^2}{\mu}}$
	C	$y_e(\phi c_t)_{_F}$	$\frac{1}{\diamond m_{21}} \times \frac{1}{A_{cw}}$	—
3	A	$y_e\left[\sqrt{k_f(\phi c_t)_f} + \sqrt{k_m\omega_2(\phi c_t)_m}\right]$	$\frac{1}{\circ m_{31}} \times \frac{L_{_F}}{2A_{cw}}\sqrt{\frac{\mu}{\pi}}$	$\frac{1}{\circ m_{32}} \times \frac{L_{_F}}{2A_{cw}}\sqrt{\mu\pi}$
	B	$y_e\sqrt{k_f(\phi c_t)_f}$	$\frac{1}{\circ m_{31}} \times \frac{L_{_F}}{2A_{cw}}\sqrt{\frac{\mu}{\pi}}$	$\frac{1}{\circ m_{32}} \times \frac{L_{_F}}{2A_{cw}}\sqrt{\mu\pi}$
	C	$y_e\sqrt{k_m\omega_2(\phi c_t)_m}$	$\frac{1}{\circ m_{31}} \times \frac{L_{_F}}{2A_{cw}}\sqrt{\frac{\mu}{\pi}}$	$\frac{1}{\circ m_{32}} \times \frac{L_{_F}}{2A_{cw}}\sqrt{\mu\pi}$
4	A	$y_e(\phi c_t)_f$	$\frac{1}{\diamond m_{41}} \times \frac{1}{A_{cw}}$	—
	B	$\sqrt{k_{_F}}\sqrt{\sqrt{\frac{k_m\omega_1(\phi c_t)_m}{L_f^2}} + \sqrt{\frac{k_m\omega_2(\phi c_t)_m}{L_{_F}^2}}}$	$\frac{1}{\star m_{41}} \times \frac{0.195\mu}{A_{cw}}\sqrt[4]{\frac{1}{\mu}}$	$\frac{1}{\star m_{42}} \times \frac{0.867\mu}{A_{cw}}\sqrt[4]{\frac{1}{\mu}}$
5	A	$y_e\sqrt{\frac{k_f\omega_1(\phi c_t)_m}{L_{_F}^2}}$	$\frac{1}{\circ m_{51}} \times \frac{1}{2A_{cw}}\sqrt{\frac{\mu}{\pi}}$	$\frac{1}{\circ m_{52}} \times \frac{1}{2A_{cw}}\sqrt{\mu\pi}$
	B	$y_e\left[\sqrt{\frac{k_m\omega_1(\phi c_t)_m}{L_f^2}} + \sqrt{\frac{k_m\omega_2(\phi c_t)_m}{L_{_F}^2}}\right]$	$\frac{1}{\circ m_{51}} \times \frac{1}{2A_{cw}}\sqrt{\frac{\mu}{\pi}}$	$\frac{1}{\circ m_{52}} \times \frac{1}{2A_{cw}}\sqrt{\mu\pi}$
6	—	$y_e\left[(\phi c_t)_m + (\phi c_t)_f + (\phi c_t)_{_F}\right]$	$\frac{1}{\diamond m_{61}} \times \frac{1}{A_{cw}}$	—

6.3.5 Verification against Synthetic Data from IMEX CMG

This part presents the application of QFM analysis equations (see Table 6.3) on a synthetic data from IMEX CMG [23] software. The goal is to see how the reservoir parameters estimated from this application compare with the actual inputs used in the simulation run. This simulation case is for an undersaturated oil reservoir. Details about it can be found in Subsection 5.3.2.3.

Fig. 6.5 shows the sequence of flow regions (1 to 4) observed on the inverse RNP versus time plot from the synthetic data. From Table 6.3, the observed flow regions 1 to 4 in Fig. 6.5 could be regions 1, 2A, 3A/5A and 6. Since region 6 is exponential (pseudo-steady state depletion, see Subsection 6.3.3), the focus will be on the previous three regions.

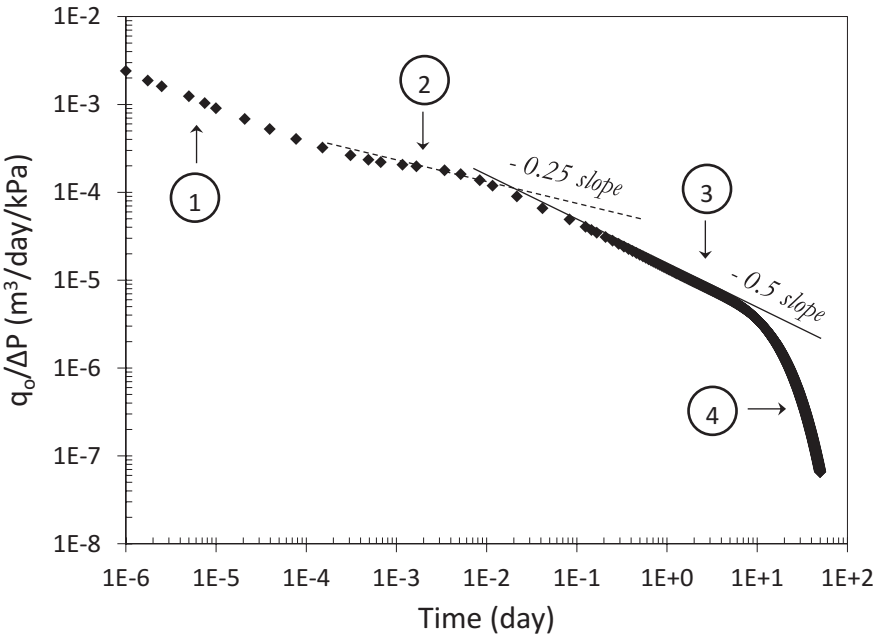

Fig. 6.5: Inverse RNP versus time plot from IMEX CMG's synthetic dataset showing sequence of flow regions.

Fig. 6.6 shows the specialized plots for analyzing regions 1, 2A and 3A/5A. The slopes from the corresponding plots are 362432.96 $kPa/m^3/\sqrt{day}$, 28367.37 $kPa/m^3/\sqrt{day}$ and 73823.08 $kPa/m^3/day^{0.75}$ respectively. Table 6.4 shows the resulting output parameters after applying the appropriate conversion factors to these slopes and substituting it to the relevant equations from Table 6.3.

[23] Computer Modeling Group (http://www.cmgl.ca, last accessed 18-11-2016)

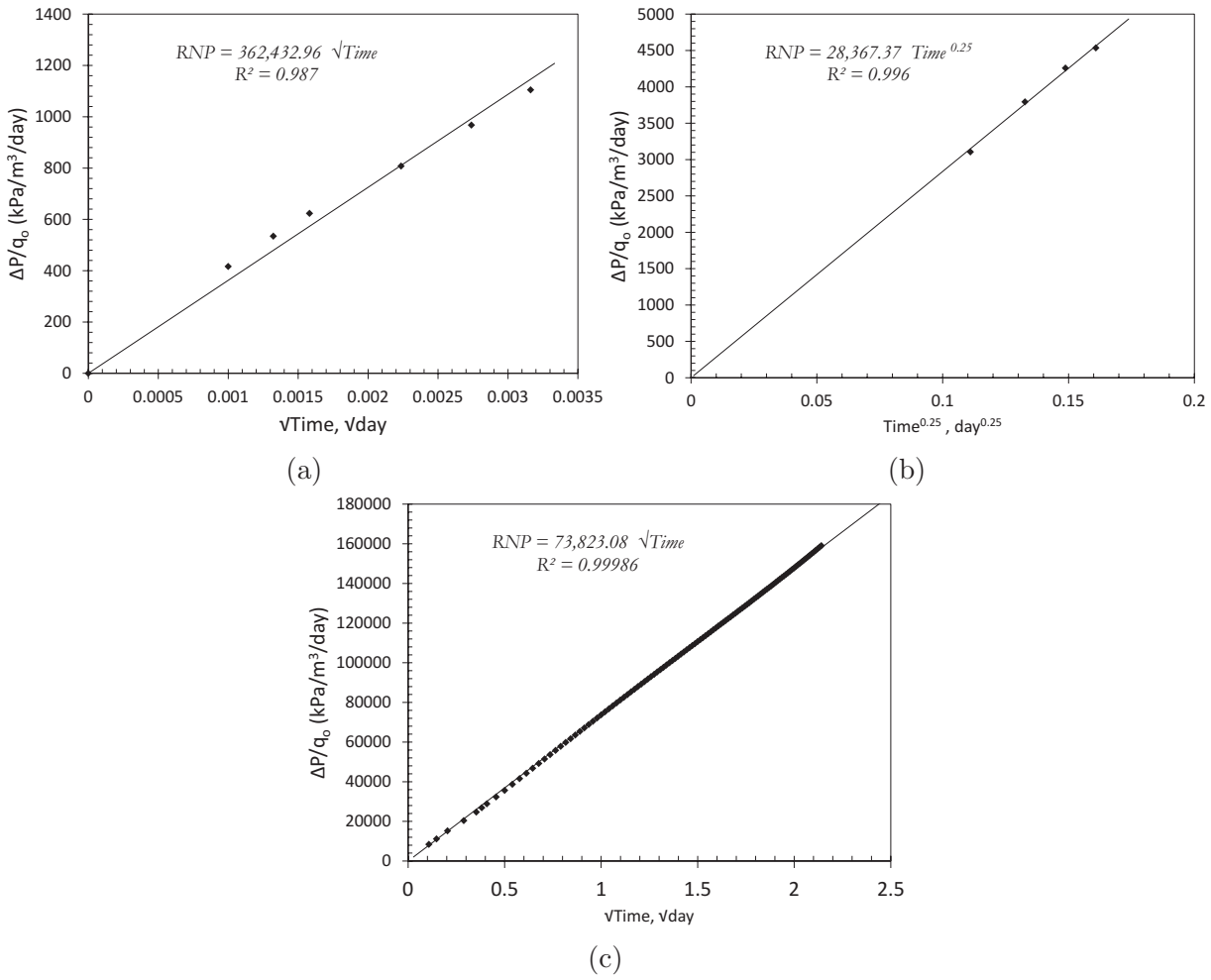

Fig. 6.6: Specialized RNP plots for synthetic dataset from IMEX CMG.

Table 6.4: Input values used to generate synthetic data and output values from applying QFM analysis equations on the synthetic data.

Region	Parameter	Input Value	Output Value
1	k_F	1.37×10^{-3} mD	3.43×10^{-3} mD
2A	L_f	32 m	28 m
3A 5A	y_e	124 m	7 m 8000 m

6.4 Application

This part estimates unknown reservoir parameters by applying QFM analysis equations on production data from multi-fractured horizontal Oil Wells A and B. Wells A and B are completed in the Cardium (Justen, 1957; MacKenzie, 1975; Purvis and Bober, 1979; Krasey and Fawcett, 1998; Clarkson and Pederson, 2011) and Bakken (Hlidek and Rieb, 2011; Clarkson and Pederson, 2011; Alcoser et al., 2012) Formations respectively.

6.4.1 Field Data

Field reports show that Well A was produced under fairly constant bottom-hole rates while Well B was produced under constant bottom-hole pressure constraints. Well A was drilled open hole as a 22 proppant tonne per stage frac job, using the StackFRAC technology in the Cardium Pembina Oil field. Well B was drilled cased hole in the Bakken Formation. Table 6.5 summarizes the known reservoir parameters (from field reports) for Wells A and B.

Table 6.5: Data for Wells A and B completed in the Cardium and Bakken Formations respectively.

Parameter	Well A	Well B	Unit
B_o	1.221	1.329	rm^3/m^3
μ	1.13	1.5643	cP
P_i	15575	46884	kPa
P_{wf}	7413	4826	kPa
$(c_t)_m$	2.209×10^{-6}	2.51×10^{-6}	kPa^{-1}
ϕ_m	0.01	0.09	—
X_e	1370	1707	m
h	7	5.8	m
L_F	72	100	m
n_F	18	16	—

The procedure for applying QFM analysis equations on field production data can be summarized under the following steps:

- Obtain down-hole flow rate and pressure data from field production.
- Make a log-log plot of $\frac{\partial \mathsf{RNP}}{\partial(lnt)}$ against t for constant bottom-hole rate case or log-log plot of RNP against t for constant bottom-hole pressure case.

- Identify the various linear, bilinear and pseudo-steady state flow regions.
- Make specialized plots (based on the identified flow regions) on arithmetic scale (see Subsection 6.3.3).
- Draw a straight line passing through the origin on these specialized plots.
- Determine the slope of this line.
- Estimate unknown reservoir parameters by inputting this slope and other known parameters into the corresponding analysis equations from Table 6.3.

For the rest of this chapter, $\frac{\partial \mathsf{RNP}}{\partial(lnt)}$ will be subsequently denoted as RNP log derivative.

6.4.1.1 Well A

Fig. 6.7 shows the field plots for analyzing production rate and pressure data from Well A. Reservoir depletion through Well A creates a flow region sequence that moves from linear to pseudo-steady state (Fig. 6.7a). Fig. 6.7b shows the rate-normalized-pressure derivative plot. Specialized plots in Figs. 6.7c and 6.7d are made based on the flow regions observed in Fig. 6.7b.

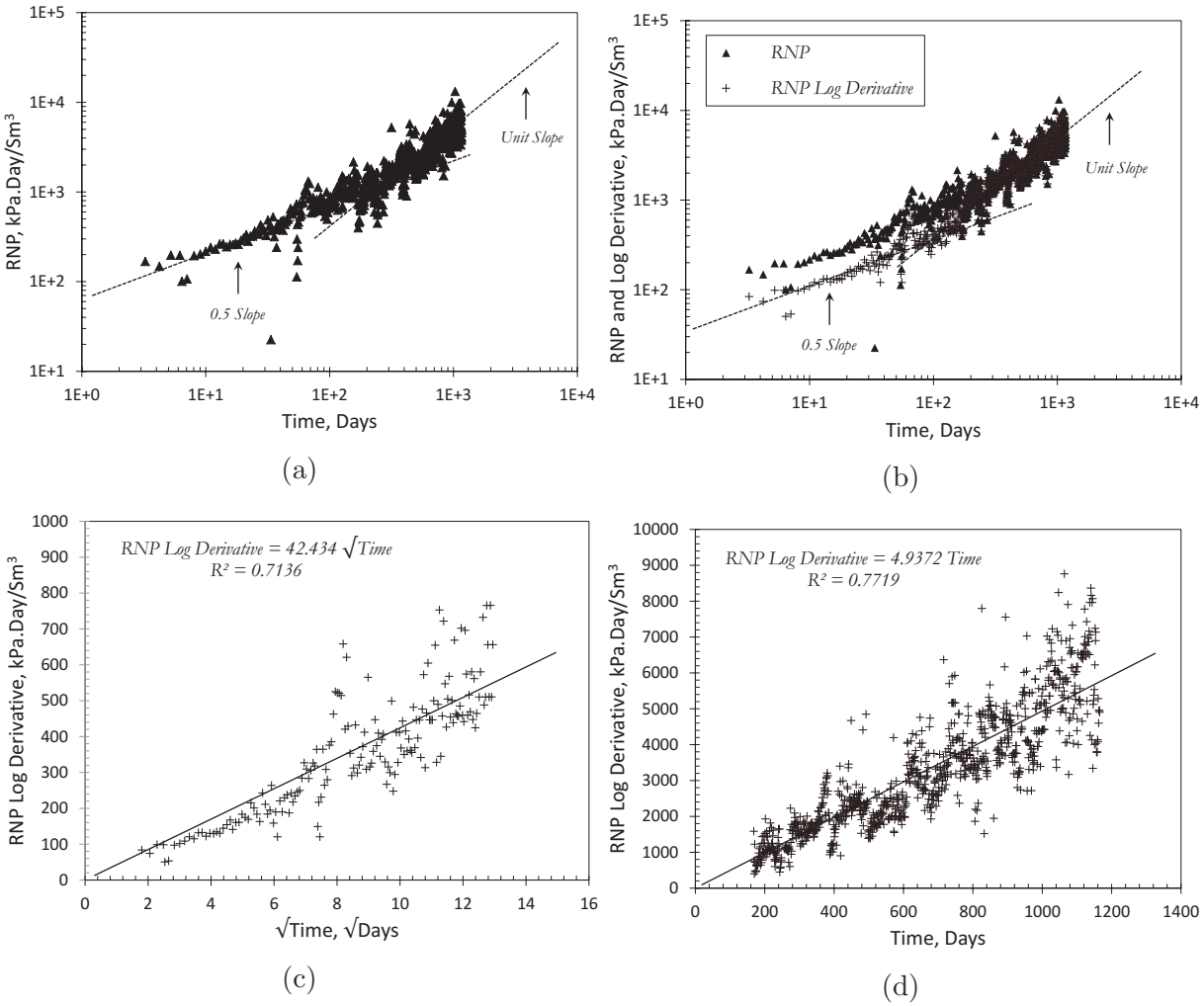

Fig. 6.7: Production data plots for Well A. (a) RNP against t log-log plot (b) RNP log derivative against t log-log plot (c) Specialized RNP against $\sqrt{t}$ plot and (d) Specialized RNP against t plot.

6.4.1.2 Well B

Fig. 6.8 shows the field plots for analyzing production rate and pressure data from Well B. Reservoir depletion in Well B results in a flow region sequence from pseudo-steady state flow to linear (Fig. 6.8a). Fig. 6.8b shows the specialized rate-normalized-pressure plot based on the late linear flow region observed in Fig. 6.8a.

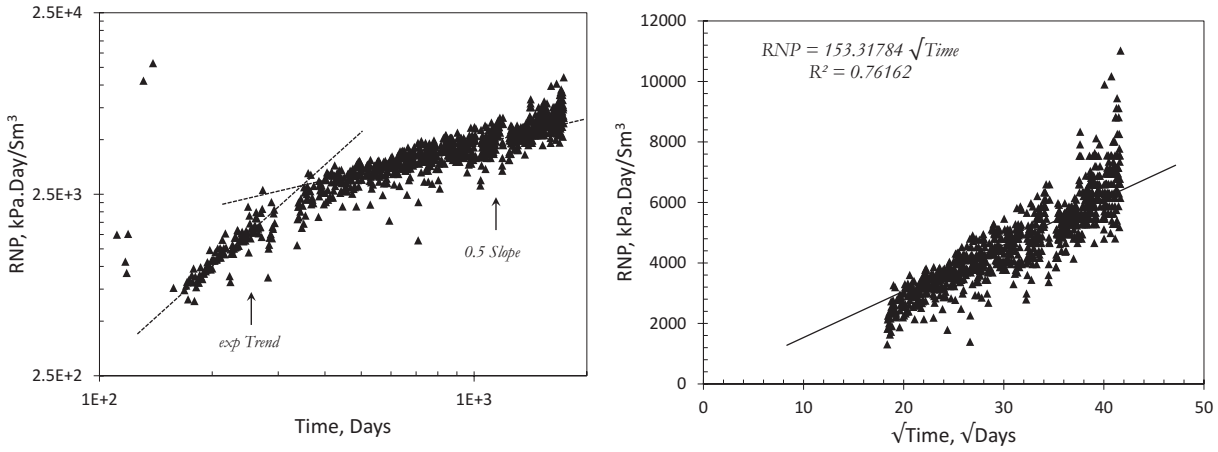

Fig. 6.8: Production data plots for Well B. (a) RNP against t log-log plot and (b) Specialized RNP against $\sqrt{t}$ plot.

6.4.2 Uncertainty Analysis

This part deals with the uncertainty in determining the correct flow region sequence on production data plots and the corresponding reservoir parameter estimates.

6.4.2.1 Well A

The flow region sequence (Fig. 6.7a) for Well A could be regions 3 and 4 or 5 and 6 (see Fig. 6.4a). Hence, the linear (0.5 slope) flow region could be Case 3A, 3B, 3C, 5A or 5B (Table 6.3). Also, the pseudo-steady state (unit slope) flow region could be Case 4A or 6. The slopes (m) from the specialized plots in Figs. 6.7c and 6.7d are $1.231 \times 10^{-4}\ atm\sqrt{sec}/Scm^3$ ($42.434\ kPa\sqrt{day}/Sm^3$) and $4.873 \times 10^{-8}\ atm/Scm^3$ ($4.937\ kPa/Sm^3$) respectively. Table 6.6 shows the lumped reservoir parameter values resulting from substituting these slopes into the corresponding analysis equations from Table 6.3.

Considering the long production time (about 1200 days) for Well A, the linear (0.5 slope) flow region should possibly be Case 5A or 5B (Table 6.3) while the pseudo-steady state (unit slope) flow region should possibly be Case 6. For the purpose of this study, Case 5A would be selected for the linear flow region analysis. Also, engineering judgment from existing literature (Justen, 1957; MacKenzie, 1975; Purvis and Bober, 1979; Krasey and Fawcett, 1998; Clarkson and Pederson, 2011) is applied to provide reasonable guesses (Table 6.7) of some unknown data that are hard to measure.

Table 6.6: QFM analysis equations for constant bottom-hole rate constraints.

Region	Case	Parameters	Value	Unit
3	A	$y_e\left[\sqrt{k_f(\phi c_t)_f}+\sqrt{\omega_2 k_m(\phi c_t)_m}\right]$	9.15×10^{-2}	$cm\sqrt{D/atm}$
	B	$y_e\sqrt{k_f(\phi c_t)_f}$	9.15×10^{-2}	
	C	$y_e\sqrt{k_m\omega_2(\phi c_t)_m}$	9.15×10^{-2}	
4	A	$y_e(\phi c_t)_f$	1.07×10^{-1}	cm/atm
5	A	$y_e\sqrt{\omega_1 k_f(\phi c_t)_f}$	9.15×10^{-2}	$cm\sqrt{D/atm}$
	B	$y_e\left[\sqrt{\frac{k_m\omega_1(\phi c_t)_m}{L_f^2}}+\sqrt{\frac{k_m\omega_2(\phi c_t)_m}{L_{_F}^2}}\right]$	1.27×10^{-7}	$\sqrt{D/atm}$
6	—	$y_e\left[(\phi c_t)_m+(\phi c_t)_f+(\phi c_t)_{_F}\right]$	1.07×10^{-1}	cm/atm

Table 6.7: Assumed Data for Well A. These are actual values of porosity and permeability. They are converted to bulk values during calculations.

Parameter	Value	Unit
a_f	1×10^{-4}	m
$a_{_F}$	1×10^{-3}	m
ϕ_f	0.68	—
$\phi_{_F}$	0.58	—
k_m	1×10^{-4}	mD
$(c_t)_f$	$1000\times(c_t)_m$	kPa^{-1}
$(c_t)_{_F}$	$100\times(c_t)_m$	kPa^{-1}

The next step involves estimating some individual values of the unknown reservoir parameters. This is achieved by combining the lumped reservoir parameter values from

various depletion scenarios from Table 6.6. The procedure for calculating the reservoir parameter estimates in Table 6.8 is given in the following steps:

- Estimate half-length (y_e) value by substituting the assumed parameters from Table 6.7 into flow region 6 analysis equation.
- Estimate micro-fracture permeability (k_f), micro-fracture spacing (L_f) and micro-fracture intensity [$n_f = (y_e/L_f) - 1$] by substituting y_e from previous step into flow region 5A analysis equation.
- Conduct a sensitivity analysis on the micro-fracture parameter estimates from the previous step.

Table 6.8: Possible reservoir parameter estimates from analyzing data from Well A. These are actual values of porosity and permeability.

Parameter	Low Range	Mid Range	High Range	Unit
ϕ_f	0.27	0.68	0.9	—
k_f	210	520	690	mD
L_f	1	3	4	m
y_e	134	134	134	m
n_f	111	44	33	—

6.4.2.2 Well B

The flow region sequence (Fig. 6.8a) for Well B should be regions 4 and 5 (see Fig. 6.4a). The first one is a pseudo-steady state flow region (*exp* trend) which requires a special analysis that is beyond the scope of this study (see Subsection 6.3.3).

However, the late linear flow region (0.5 slope) could be Case 5A and 5B (Table 6.3). The focus of this analysis would be on Case 5A. The slope (m) from the specialized plot in Fig. 6.8b is 4.45×10^{-4} $atm\sqrt{sec}/Scm^3$ (153.31784 $kPa\sqrt{day}/Sm^3$). Table 6.9 shows the lumped reservoir parameter values resulting from substituting these slopes into the corresponding analysis equations from Table 6.3. Engineering judgment from existing literature (Hlidek and Rieb, 2011; Clarkson and Pederson, 2011; Alcoser et al., 2012) is applied to provide reasonable guesses (Table 6.10) of some unknown data that are hard to measure.

Table 6.9: QFM analysis equations for constant bottom-hole pressure constraints.

Region	Case	Parameters	Value	Unit
5	A	$y_e\sqrt{\omega_1 k_f(\phi c_t)_f}$	2.41×10^{-2}	$cm\sqrt{D/atm}$
	B	$y_e\left[\sqrt{\frac{k_m\omega_1(\phi c_t)_m}{L_f^2}} + \sqrt{\frac{k_m\omega_2(\phi c_t)_m}{L_{_F}^2}}\right]$	2.41×10^{-6}	$\sqrt{D/atm}$

Table 6.10: Assumed Data for Well B. These are actual values of porosity and permeability. They are converted to bulk values during calculations.

Parameter	Value	Unit
a_f	1×10^{-4}	m
$a_{_F}$	1×10^{-3}	m
ϕ_f	0.60	—
L_f	2	m
k_m	1×10^{-4}	mD
$(c_t)_f$	$1000 \times (c_t)_m$	kPa^{-1}
$(c_t)_{_F}$	$100 \times (c_t)_m$	kPa^{-1}

The next step involves estimating some individual values of the unknown reservoir parameters. This is achieved by combining the lumped reservoir parameter values from various depletion scenarios from Table 6.9. The procedure for calculating the reservoir parameter estimates in Table 6.11 is given in the following steps:

- Estimate half-length y_e and micro-fracture permeability (k_f) values by substituting the assumed parameters from Table 6.10 into flow region 5A analysis equation.
- Conduct sensitivity analysis on the various y_e and k_f combinations which give similar results as that from step 1.
- Estimate micro-fracture intensity (n_f) in a given hydraulic-fracture spacing ($L_{_F}$) as $(y_e/L_f) - 1$.

Table 6.11: Possible reservoir parameter estimates from analyzing data from Well B. These are actual values of porosity and permeability. They are converted to bulk values during calculations.

Parameter	Low Range	Mid Range	High Range	Unit
y_e	220	280	299	m
n_f	110	140	150	—
k_f	3000	1900	1700	mD

6.5 Discussions

The results of this chapter can be summarized under three points namely: development of simplified analysis equations for the quadrilinear flow model; application of these equations on specialized field production data plots; and estimating reservoir parameters by accounting for uncertainty in unique flow regime identification.

Result 1 is significant when analyzing production data from multi-fractured horizontal wells completed in reservoirs with active secondary fractures (e.g. reactivated natural fractures) interconnected with the hydraulic fractures. This result is applicable to gas wells by replacing pressure with the appropriate pseudo-pressure function $[m(P)]$. An example of such function (Al-Hussainy and Ramey Jr., 1966) as used in this paper is:

$$m(P) = 2\int_{P_i}^{P} \frac{P}{\mu(P)z(P)}\,\mathrm{d}P$$

Result 2 shows how QFM analysis equations apply to field production data using specialized plots. The choice of the appropriate specialized plot depends on the approximate operating bottom-hole constraints in the well — constant rate or constant pressure. Noise poses a challenge to reliable production data analysis. However, noise reduction in production data plots to enhance interpretation should be guided by engineering judgment. This ensures that the data still represents the fracture/reservoir. The discrepancy in half-lengths from the verification section shows the possibility that other flow regions might exist. Therefore, further investigation is required in this regard.

Result 3 provides a method for estimating individual reservoir parameters by combining the lumped parameters from various possible reservoir depletion scenarios. However, some unknown reservoir parameters (e.g. total fracture compressibility, fracture width, fracture porosity) are difficult to measure in the field or laboratory. For practical purposes, engineering judgment is applied to select "reasonable guesses" of these reservoir

parameters. This might introduce analysis bias because the guessed parameter values determine the remaining unknown parameter estimates. Hence, the estimated reservoir parameter values should not be considered individually, but as meaningful groups e.g. fracture length/spacing × fracture permeability, ratio of micro–fracture to hydraulic–fracture permeability or matrix to fracture permeability. In subsequent studies, new analysis equations will be developed based on the intersection point of flow regions. This should further reduce the uncertainty in reservoir parameter estimation.

One key observation from the production data analysis of both Wells A and B is the huge number of secondary fracture (≈ 120) within a given hydraulic-fracture spacing of about 100 m. This is supported by the high degree of active secondary fractures observed by several authors in the Western Canadian Sedimentary Basin (Castillo et al., 2011; Rogers et al., 2010).

6.6 Summary

This chapter presents analysis equations (based on the quadrilinear flow model) for interpreting different flow regions of production data from tight reservoirs with active secondary fracture networks. Also, it proposes a procedure for estimating reservoir parameters by applying these analysis equations on specialized production data plots. The application of this procedure on two production data sets yields reasonable estimates of fracture half-length, spacing and permeabilities. More importantly, the results reveal the high intensity of active secondary fractures in the reservoir. This shows that a properly connected network of hydraulic fractures with short lengths might be an optimal choice for depleting this reservoir. Future studies will focus on further reduction in the uncertainty related to parameter estimation and automating the application procedure. This enhanced reduction in uncertainty will be achieved by developing new analysis equations based on the flow region intersection points and integrating the analysis equation results with type-curve matching procedure.

Nomenclature

Symbols

a	Fracture width, L, m, $[ft]$.
c	Compressibility, Lt^2M^{-1}, atm^{-1}, $[Pa^{-1}, psi^{-1}]$.
h	Reservoir thickness, L, m, $[ft]$.

k	Bulk permeability, L^2, m^2 $[D]$.
l	Characteristic length, L, m, $[ft]$.
n	Number, L, m, $[ft]$.
q	Rate, L^3t^{-1}, $m^3.s^{-1}$, $[rb.day^{-1}]$.
s	Laplace variable, t^{-1}, s^{-1}, $[hr^{-1}$, $day^{-1}]$.
t	Time, t, s, $[hr$, $day]$.
x, y	Principal reference SRV co-ordinates , L, m, $[ft]$.
z	Gas compressibility factor, dimensionless.
A	Area, L^2, m^2, $[ft^2]$.
L	Distance or length, L, m, $[ft]$.
P	Pressure, $ML^{-1}t^{-2}$, Pa, $[psi]$.
R	Aspect Ratio, dimensionless.
S	Connection area per unit volume of rock, L^{-1}, m^{-1}, $[ft^{-1}]$.
V	Volume, L^3, m^3, $[ft^3]$.
X	Horizontal well length, L, m, $[ft]$.
α	Interporosity shape factor, L^{-2}, m^{-2}, $[ft^{-2}]$.
ϕ	Bulk porosity, dimensionless.
λ	Interporosity transmissivity ratio.
μ	Viscosity, $ML^{-1}t^{-1}$, $Pa.s$, $[cP]$.
ω	Storativity ratio, dimensionless.
Δ	Change.

Superscripts

$\bar{}$	Laplace transform.

Subscripts

$_e$	Equivalent or effective.
$_c$	Cross-section.
$_f$	Micro-fracture.
$_i$	Initial.
$_m$	Matrix.
$_F$	Hydraulic fracture.

$_L$	Reference length.
$_t$	Total.
$_w$	Well.
$_D$	Dimensionless.
$_{sp}$	Spacing.
$_{wf}$	Bottom-hole flowing.

Chapter 7

Implications of Characterizing Tight Reservoirs with Dual-porosity and Triple-porosity Models

7.1 Introduction

Although unconventional or tight reservoirs are now significant sources of hydrocarbon in North America (Clarkson and Pederson, 2010) and beyond, modeling fluid flow in such complex reservoirs remains challenging.

The number of distinct porous regions present in a reservoir determines the appropriate conceptual fluid flow model. An example is the dual-porosity model (Kucuk et al., 1981; Stopa and Nawrat, 2012) which comprises two porous regions: fracture network and matrix blocks. Communication between both regions can be transient or pseudo-steady. Warren and Root (1963) proposed an ideal sugar-cube dual-porosity model which consists of uniformly distributed fractures and matrix blocks. Kazemi (1969) extended Warren and Root's Warren and Root (1963) model by replacing the pseudo-steady matrix-fracture communication with transient communication. Carlson and Mercer (1991) were one of the first authors who extended the existing dual-porosity model for application in Shale reservoirs.

All the dual-porosity models discussed so far assume radial flow towards the well. However, long transient linear behavior (half-slope line) has been observed on log-log plots (El-Banbi, 1998) of production pressure/inverse-rate against time. This could result from: fluid production from fractures whose lengths extend to reservoir boundaries (Wattenbarger et al., 1996); transient drainage of low permeability matrix blocks into adjoining fractures; and linear shape of certain reservoirs (Stright Jr. and Gordon, 1983). Since the existing radial dual-porosity models could not explain this extended linear flow, it became necessary to develop a suitable model for analyzing production data from such fractured reservoirs.

El-Banbi (1998) extended previous dual-porosity models (Warren and Root, 1963;

Kazemi, 1969) to produce a list of dual-porosity solutions for linear reservoirs. Bello (2009) extended El-Banbi (1998)'s linear dual-porosity model for rate transient application on data recorded in fractured Shale reservoirs. This model extension assumes dual, linear depletion (Fig. 7.1) — from matrix into adjoining fractures and from fractures into the horizontal well. He developed asymptotic analysis equations and specialized plots to describe observable flow regimes.

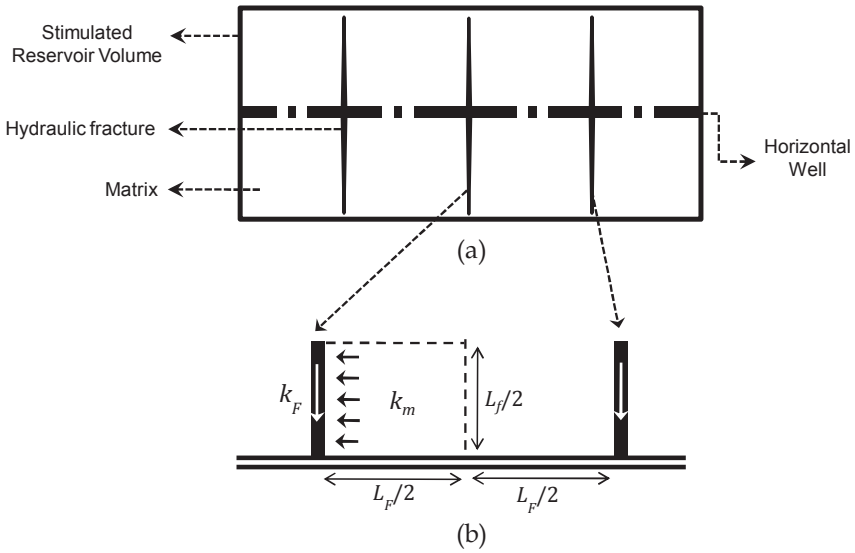

Fig. 7.1: Linear dual-porosity model (DPM). (a) Horizontal cross-section of hydraulically fractured horizontal well in tight reservoirs. (b) Conceptual flow physics.

Dual-porosity models assume uniform matrix and fractures properties throughout the reservoir, which may not be true in reality. Studies in Western Canadian Sedimentary Basin (Castillo et al., 2011; Rogers et al., 2010) show that an effective connection of hydraulic fracture (HF) with the existing natural fractures enhances the reservoir volume drained by a well. This HF connection transforms the dual-porosity reservoir into a triple porosity system (Gale et al., 2007; Dahi, 2009). These observations among others, raised the need for triple porosity models that could interpret production data from reservoirs with non-uniform fracture/matrix properties.

Triple porosity models can comprise: two fracture networks and one type of matrix or one fracture network and two types of matrix. Triple-porosity models can be further classified into pseudo-steady and transient state models, depending on the matrix–fracture interaction. Abdassah and Ershaghi (1986) proposed a transient, triple porosity model where fractures have homogeneous properties and interact with two distinct groups of matrix blocks (different permeabilities and porosities). Liu et al. (2003) developed a pseudo-steady state, triple porosity model to analyze the transient pressure behavior of fractured lithophysal reservoirs comprising fractures, rock matrices, and cavities. Wu et al. (2004)

used the same mathematical model to simulate the flow and transport processes in fractured reservoirs comprising matrices, large fractures, and small fractures. Dehghanpour and Shirdel (2011) extended Ozkan et al. (2010) transient dual-porosity model and Warren and Root (1963) pseudo-steady model to obtain two triple porosity models comprising sub-matrices (nano-Darcy permeabilities) and micro-fractures (milli- to micro-Darcy permeabilities). The resulting models can be used to explain the unexpected high gas production in some Shale gas reservoirs which cannot be justified by conventional dual-porosity models.

Al-Ahmadi (2010) proposed a linear sequential triple porosity model (STPM) by extending the linear dual-porosity model (DPM) of Bello (2009) to account for linear fluid depletion from: matrix to micro-fractures (MF); MF to HF; and HF to horizontal well.

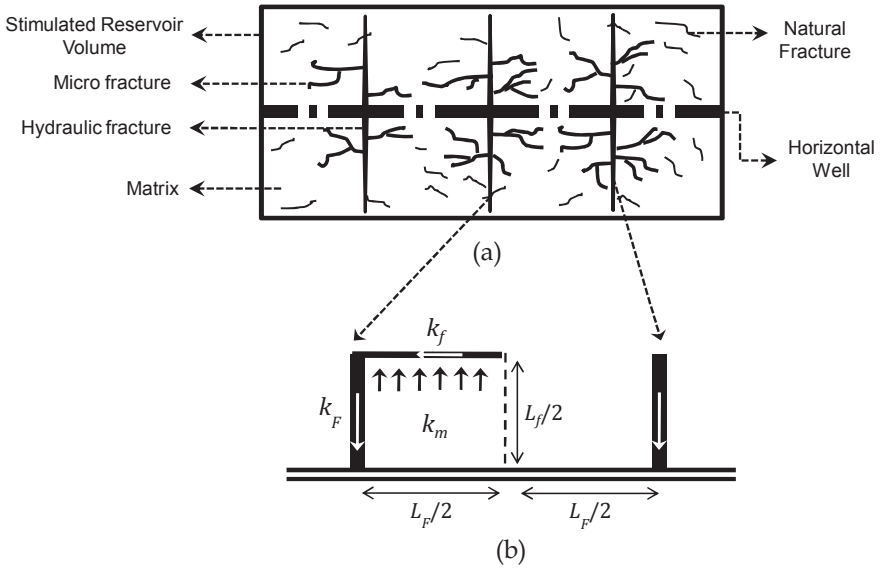

Fig. 7.2: Linear sequential triple porosity model (STPM). (a) Horizontal cross-section of hydraulically fractured horizontal well in tight reservoirs. (b) Conceptual flow physics.

Siddiqui et al. (2012) and Ali et al. (2013) simplified Al-Ahmadi (2010)'s model (Fig. 7.2) to obtain STPM analysis equations for interpreting flow regimes from production data. Similarly, Tivayanonda et al. (2012) presented a simplified case of Al-Ahmadi (2010)'s model by treating the hydraulic fractures as constant-pressure boundaries. They further proposed analysis equations and interpretation guidelines for five possible production scenarios. Tivayanonda (2012) studied and compared the homogeneous linear flow model (Wattenbarger et al., 1998), transient linear dual-porosity model (Bello, 2009), and fully transient linear triple porosity model (Al-Ahmadi, 2010). The application of these models on the same production data was done with the assumption of infinite HF conductivity ($k_F = \infty$). Tivayanonda (2012) proposed guidelines and flow regime analysis

equations for applying these models on production data.

Brown et al. (2011) presented a general analytical trilinear model (a combination of dual-porosity model and linear flow model) to simulate pressure transient and production behavior of fractured horizontal wells in Shale reservoirs. They concluded that the trilinear flow model should be sufficient to analyze production data from tight reservoirs despite the complex interplay of flow among matrix, natural fractures and hydraulic-fractures.

However, all existing triple porosity and triple-linear flow models assume sequential depletion (negligible matrix–HF communication). This assumption holds only if the matrix–MF communication is far greater than the matrix–HF communication (e.g. high MF density/concentration with a given HF spacing). In situations where there is significant matrix–HF communication or negligible bulk matrix–MF contact area compared to bulk matrix–HF contact area, the sequential assumption can result in unreasonable estimates of MF and/or HF properties.

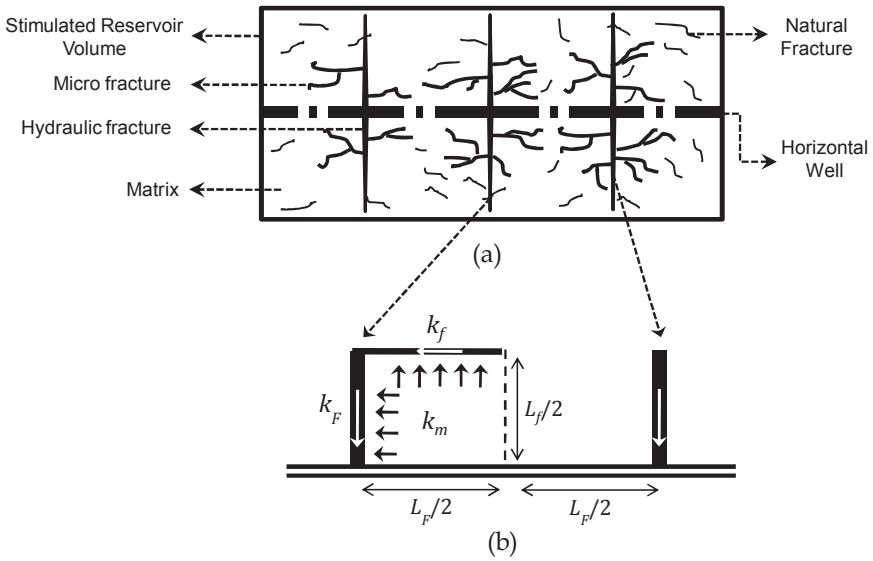

Fig. 7.3: Quadrilinear flow model (QFM). (a) Horizontal cross-section of hydraulically fractured horizontal well in tight reservoirs. (b) Conceptual flow physics.

Hence, Ezulike and Dehghanpour (2014a) proposed a quadrilinear flow model (QFM) which relaxes the sequential depletion assumption in STPM (Al-Ahmadi, 2010) by conceptually dividing the matrix volume into two sub-domains: one feeding HF and the other feeding MF (Fig. 7.3). QFM converges to the STPM in the absence of matrix–HF communication; and converges to the DPM in the absence of MF. These characteristics of QFM were also observed in the simulation studies done by Yue et al. (2013). Their results reveal the necessity of reducing uncertainty by estimating some unknown reservoir parameters from complementary studies (e.g. outcrop, micro-seismic and image log analyses) when

possible.

Although all the existing models considered so far can be generally classified into dual-porosity and triple porosity, each of them have unique sets of simplifying assumptions. These assumptions will cause each of them to produce different results when used for production data analysis. Therefore, this chapter considers the implications of applying the QFM, STPM and DPM on the same production data set. The study is done in three steps – application, comparison, and discussion. Step 1 analyzes different flow regions of the same field data using different models to estimate key reservoir parameters (e.g. HF half-length and MF spacing). Step 2 carefully evaluates the possible causes for the differences observed in the comparative (not absolute) values of key reservoir parameters estimated from these models. Step 3 considers the implications of applying these models on production data.

7.2 Methodology

This study is done in three steps: application, comparison and discussion. Micro-fracture and hydraulic fracture parameters are usually hard to measure for each well drilled in a reservoir. Therefore, this chapter uses the fracture parameters reported in existing literature for the corresponding formations as inputs to estimate HF half-length (y_e) and average MF spacing (L_f). The estimated y_e and L_f values are combined to get the average number ($n_f = \frac{y_e}{L_f} - 1$) of MF within a given HF spacing. Parameter estimation is achieved by analyzing various flow regimes in the same production data using type-curves and analysis equations from linear dual-porosity and triple porosity models (Figs. 7.4 and 7.5).

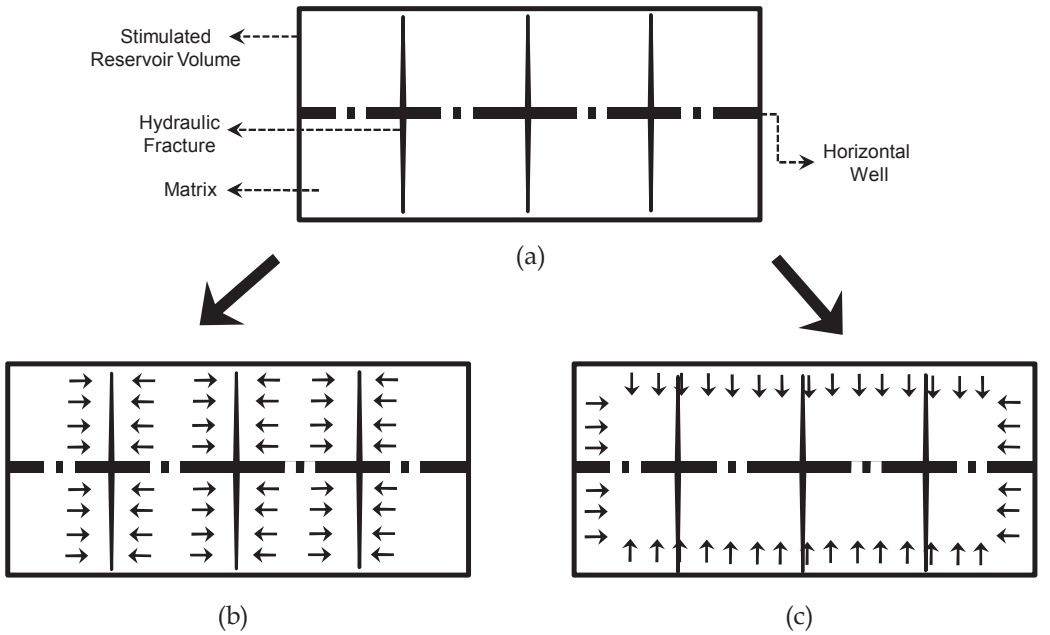

Fig. 7.4: Dual-porosity model with negligible micro-fractures. (a) Horizontal cross-section of reservoir model (b) Linear transient flow regime – LT (c) Pseudo-steady state flow regime – PSS.

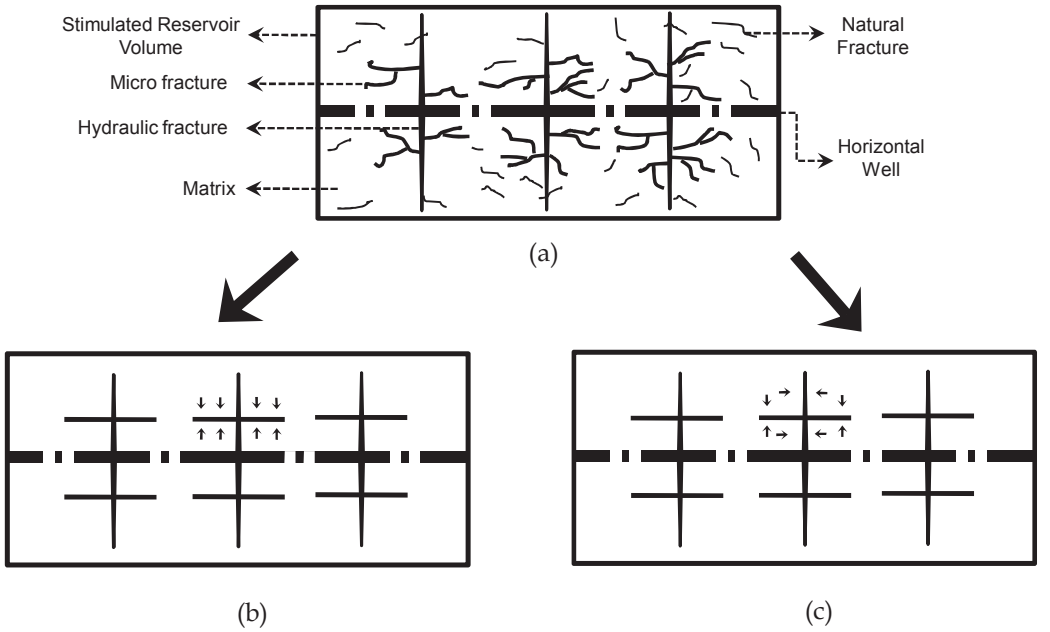

Fig. 7.5: Linear triple porosity model with micro-fractures. (a) Horizontal cross-section of reservoir model. (b) Sequential matrix depletion (STPM). (c) Simultaneous matrix depletion (QFM).

Step 1 starts from simple dual-porosity models and ends in complex triple porosity models. The application outline for this step is provided below as:

- Analysis Equations
  - Dual-porosity based Linear Transient (Bello, 2009) — (LT)
    1. Production Time Plots (PTP)
    2. Material Balance Time Plots (MBT-P)
  - Dual-porosity based Pseudo-Steady State (Ezulike et al., 2015) — (PSS)
- Type-Curves
  - Linear Dual-porosity Model (Bello, 2009) — (DPM)
  - Linear Sequential Triple-porosity Model (Al-Ahmadi, 2010) — (STPM)
  - Quadrilinear Flow Model (Ezulike and Dehghanpour, 2014a) — (QFM)

Step 2 compares reservoir parameters estimated from the application methods outline from step 1 in five stages (from simple to complex) namely:

- Analysis Equations
  - LT (PTP versus MBT-P)
  - LT versus PSS
- Analysis Equations versus DPM
- DPM versus STPM
- DPM versus QFM
- STPM versus QFM

Step 3 discusses the similarities and differences among reservoir parameters estimated from various application methods in step 2. The abbreviations presented here would be used for the rest of this chapter.

The absolute values of reservoir parameters compared in this study should be taken with a grain of salt. Rather, the key point is the how the parameter values estimated from various models compare to one another. The permeability and porosity values used in this study are bulk values as defined in Ezulike and Dehghanpour (2014a).

7.3 Application

This part presents the application of two dual-porosity analysis equations (for linear and pseudo-steady state flow regimes), and three dimensionless type-curves (one dual-porosity and two triple porosity models) to match the production history of multi-fractured horizontal oil Wells A and B. These wells are completed in the Cardium (Justen, 1957; MacKenzie, 1975; Purvis and Bober, 1979; Krasey and Fawcett, 1998; Clarkson and Pederson, 2011) and Bakken (Hlidek and Rieb, 2011; Clarkson and Pederson, 2011; Alcoser et al., 2012) Formations respectively. Here, it is assumed that boundary-dominated flow regime occurs immediately after late transient linear flow regime (Clarkson and Pederson, 2010; Song et al., 2011). These models are applied on the same production data to estimate unknown reservoir parameters. The dots and solid lines in the figures are field and model data respectively.

7.3.1 Input Data

Table 7.1 summarizes the known reservoir parameters (from field reports) for Wells A and B. Some unknown reservoir parameters are assigned assumed values based on field, laboratory studies and previous studies (Ezulike and Dehghanpour, 2014a) in the Cardium and Bakken Formations.

Table 7.1: Known data for Wells A and B.

Parameter	Well A	Well B	Unit
B_o	1.221	1.329	rm^3/m^3
μ	1.13	0.5643	cP
P_i	15575	46884	kPa
P_{wf}	7413	4826	kPa
c_t	3.91×10^{-5}	4.02×10^{-5}	kPa^{-1}
k_m	1.34	0.026	mD
ϕ_m	0.108	0.09	–
X_e	1370	1707	m
h	7	5.8	m
$L_{_F}$	72	100	m
$n_{_F}$	18	16	–

This allows the study to focus on key parameters (e.g. HF half-length and MF spacing) which control fluid flow behavior as we move from dual to triple porosity models. Table 7.2

summarizes the assumed unknown reservoir parameters for Wells A and B considered for the comparative analysis. Tables 7.1 and 7.2 will be subsequently used in estimating values of hydraulic fracture half-length and micro-fracture spacing for different models. In this study, RNP ($\frac{P_i - P_{wf}}{q}$) is the rate-normalized-pressure.

Table 7.2: Assumed data for Wells A and B

Parameter	Well A	Well B	Unit
k_f	350	250	mD
$k_{_F}$	1500	600	mD
$(\phi c_t)_f$	3.91×10^{-7}	4.02×10^{-7}	kPa^{-1}
$(\phi c_t)_{_F}$	3.91×10^{-9}	4.02×10^{-9}	kPa^{-1}
$(\phi c_t)_{_t}$	3.91×10^{-6}	4.02×10^{-6}	kPa^{-1}

7.3.2 Analysis Equations

This part applies the linear transient [LT, Bello (2009)] and the pseudo-steady state [PSS, Ezulike et al. (2015)] equations (derived from DPM) on production data from Wells A and B respectively. The LT analysis is done using plots with two different types of time axis — production time and material-balance time. This is to compare the effect of using material-balance time for analyzing production data during transient flow regimes.

7.3.2.1 Linear Transient Equation (LT)

Here, the half-lengths of hydraulic fracture are estimated from equations governing matrix transient linear depletion in a dual-porosity system. Also, this is done using both production time and material-balance time (Palacio and Blasingame, 1993) plots respectively. Production time plot (RNP against $\sqrt{t}$) and material-balance time plot (RNP against $\sqrt{MBT}$) yield straight line slopes (m — $\frac{psi \times \sqrt{day}}{stb}$) which are substituted into Bello (2009)'s region 4 analysis equation:

$$y_e\,(m) = m \times \frac{5.8 B_o L_{_F}}{A_{cw}} \sqrt{\frac{\mu}{k_m (\phi c_t)_m}} \tag{7.1}$$

The units of μ, L_f, A_{cw}, k_m and c_t in Eq. 7.1 are cP, ft, ft^2, mD and psi^{-1} respectively. Table 7.3 summarizes the half-length estimates obtained from the application of Eq. 7.1 on the slopes from Fig. 7.6. The appropriate conversion factors have been applied on the slopes used in this calculation.

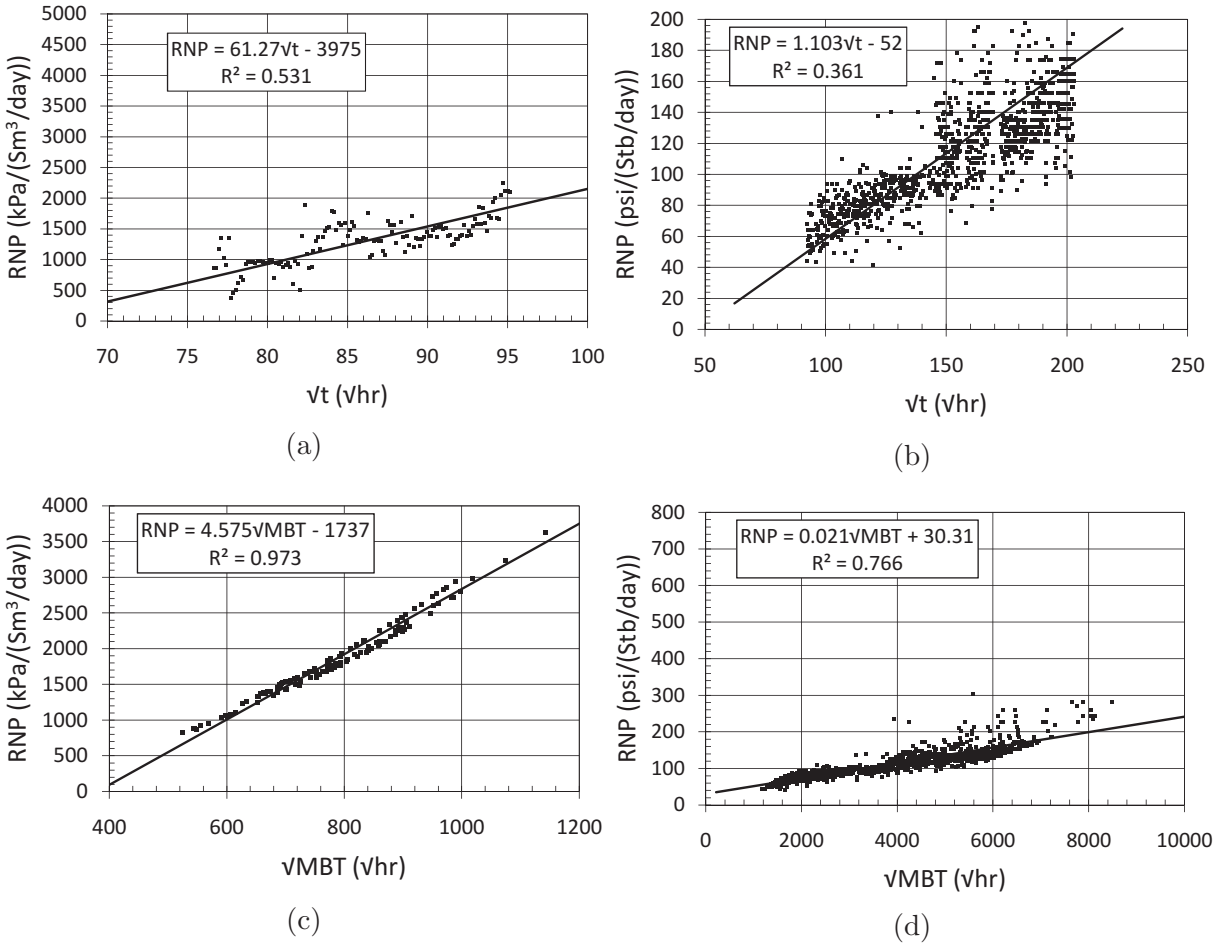

Fig. 7.6: RNP against $\sqrt{t}$ plot (a and b) and RNP against $\sqrt{MBT}$ plot (c and d) of production data from Wells A and B respectively.

Table 7.3: HF half-lengths estimated by applying production time plots (PTP) and material-balance time plots (MBT-P) on production data from Wells A and B.

Parameter	**PTP** (Eq. 7.1)	**MBT-P** (Eq. 7.1)	**Unit**
y_e (Well A)	168	12	m
y_e (Well B)	177	3	m

7.3.2.2 Pseudo-Steady State Equation (PSS)

Here, hydraulic fracture half-lengths are estimated from equations derived during linear pseudo-steady state depletion in a dual-porosity system. A plot of RNP against MBT yields a straight line slope (m — $\frac{atm}{scm^3}$) and intercept (b — $\frac{atm \times s}{scm^3}$) which are substituted into the modified relationships proposed by Ezulike et al. (2015). Half-length and average

matrix permeability estimates can be obtained using both m and b as shown in Eqs. 7.2 and 7.3:

$$y_e\,(cm) = \frac{1}{m} \times \frac{B_o}{2(\phi c_t)_m h n_{_F} L_{_F}} \tag{7.2}$$

$$k_m\,(D) = \frac{1}{b} \times \frac{\mu B_o L_{_F}}{24 y_e h n_{_F}} \tag{7.3}$$

The units of μ, h, L_f and c_t in Eqs. 7.2 and 7.3 are cP, cm, cm and atm^{-1} respectively. Eqs. 7.2 and 7.3 apply only to Well A's data because there is no clear evidence (exponential trend) of pseudo-steady (or boundary-dominated) flow regime in Well B's data (Fig. 7.8b). The values of 243 m and 173.7 mD for the hydraulic fracture half-length and average matrix permeability are estimated by applying Eqs. 7.2 and 7.3 on production data (Fig. 7.7) from Well A.

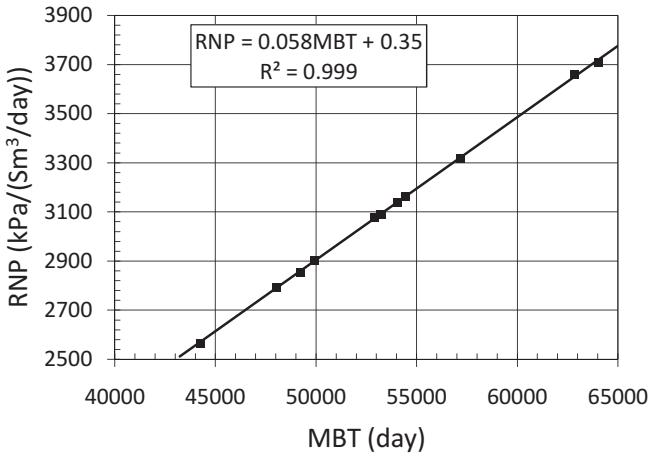

Fig. 7.7: RNP against MBT plot of production data from Well A.

7.3.3 Type Curves

This part of the chapter estimates reservoir parameters by applying three type-curves to the same field data. In order of increasing model complexity, DPM (Bello, 2009), STPM (Al-Ahmadi and Wattenbarger, 2011) and QFM (Ezulike and Dehghanpour, 2014a) type-curves is applied on production data from Wells A and B respectively.

7.3.3.1 DPM Type-Curve Match

Here, the half-length of hydraulic fracture is estimated from type-curves of the dual-porosity model using all available flow regimes (including linear transient and pseudo-

steady state regimes) in the production data.

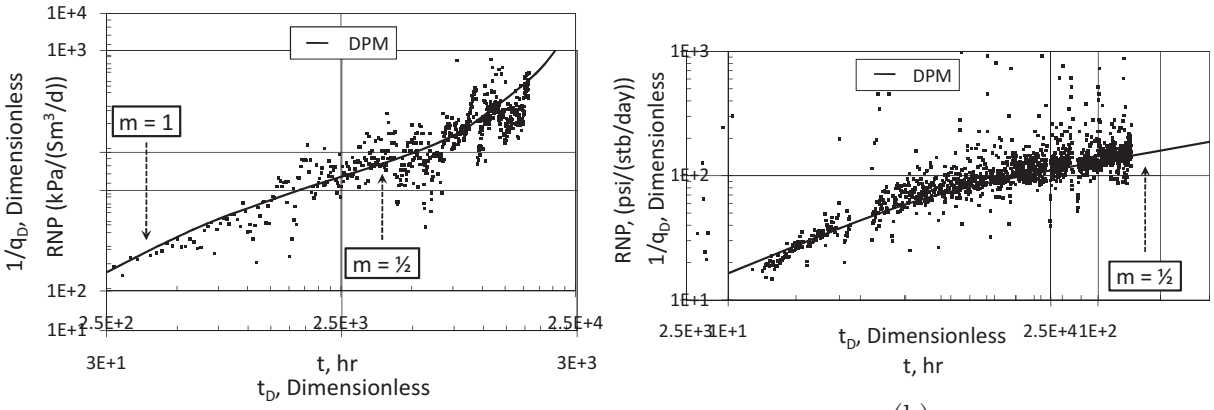

Fig. 7.8: DPM type-curve match with production data from (a) Well A and (b) Well B. m is slope.

Fig. 7.8 shows the match between DPM type-curves and production data from Wells A and B respectively. Table 7.4 summarizes the half-lengths estimates from this type-curve match.

Table 7.4: Initial and final (before and after uncertainty analysis) hydraulic fracture half-length estimated by matching DPM type-curves and production data from Wells A and B respectively.

Parameter	**Well A**		**Well B**		**Unit**
	Initial	**Final**	**Initial**	**Final**	
y_e	225	220 – 240	190	177 – 212	m

7.3.3.2 STPM Type-Curve Match

Assuming there is negligible matrix to hydraulic fracture fluid communication in the triple porosity system, increasing or decreasing the half-length of hydraulic fractures should have negligible effect on fluid depletion in STPM. Therefore, micro-fracture properties should primarily control the depletion behavior as we move from DPM to STPM. Here, average spacing and intensity of micro-fractures are estimated from STPM type-curves using all available flow regimes (including linear transient and pseudo-steady state regimes) in the production data.

Fig. 7.9 shows the match between STPM type-curves and production data from Wells A and B respectively. Table 7.5 summarizes the average micro-fracture spacing and intensity estimates from this type-curve match.

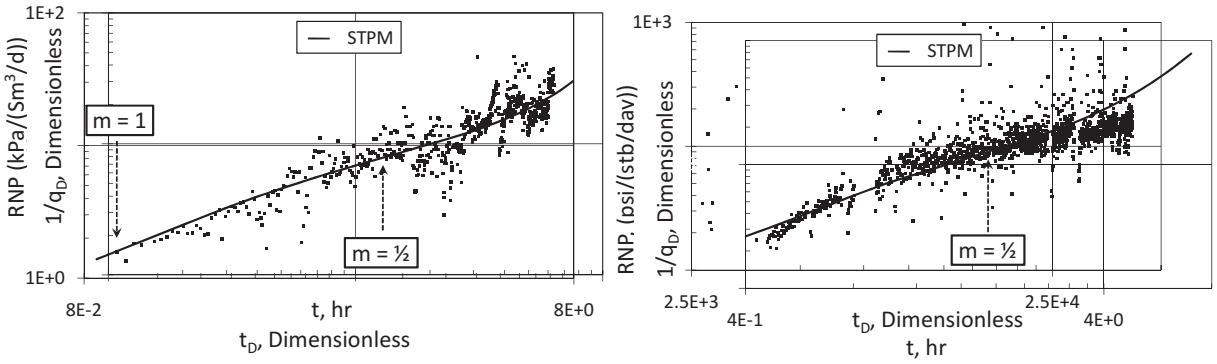

Fig. 7.9: STPM type-curve match with production data from (a) Well A and (b) Well B. m is slope.

Table 7.5: Initial and final (before and after uncertainty analysis) estimates of average micro-fracture spacing and intensity obtained from matching STPM type-curves with production data from Wells A and B respectively. The low end values of micro-fracture spacing corresponds to the low end values of hydraulic fracture half-length and high end values of the number of micro-fractures.

Parameter	Well A		Well B		Unit
	Initial	Final	Initial	Final	
y_e	32	21 – 45	33	≈ 33	m
L_f	1.5	1 – 1.2	1.5	1.5	m
n_f	20	20 – 36	18	21	—

7.3.3.3 QFM Type-Curve Match

Assuming there is matrix to hydraulic fracture fluid communication in the triple porosity system, both the hydraulic fracture half-length and average micro-fracture spacing should affect fluid depletion in QFM (compared to STPM). Therefore, the parameters are estimated from QFM type-curves using all available flow regimes (including linear transient and pseudo-steady state regimes) in the production data.

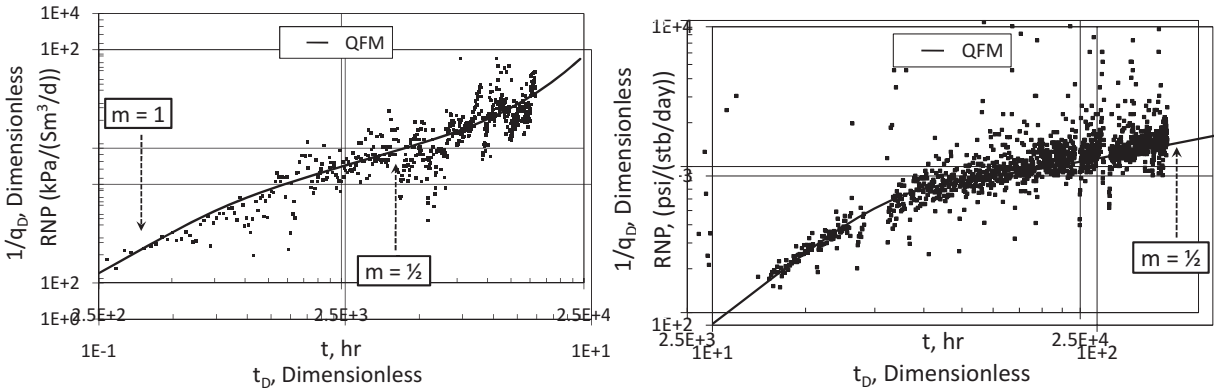

(a) (b)

Fig. 7.10: QFM type-curve match with production data from (a) Well A and (b) Well B. m is slope.

Fig. 7.10 shows the match between QFM type-curves and production data from Wells A and B respectively. Table 7.6 summarizes the hydrualic fracture and micro-fracture parameters estimated from this type-cure match.

Table 7.6: Initial and final (before and after uncertainty analysis) estimates of unknown reservoir parameters obtained from matching QFM type-curves and production data from Wells A and B respectively. The low end values of micro-fracture spacing corresponds to the low end values of hydraulic fracture half-length and high end values of the number of micro-fractures.

Parameter	**Well A**		**Well B**		**Unit**
	Initial	**Final**	**Initial**	**Final**	
y_e	33	23 – 40	35	≈ 35	m
L_f	2	1.5 – 1.8	3	2	m
n_f	16	14 – 21	11	17	—

7.4 Comparisons

This part investigates the effects of various physics on parameter estimates from production data analysis. First is the effect of production time and material-balance time on the half-length estimates from LT and PSS analysis equations. Second is the effect of active micro-fracture on the half-length estimates from DPM and QFM type-curve matches. Third

is the effect of simultaneous fluid depletion (from matrix to both micro- and hydraulic fractures) on micro-fracture parameter estimates from STPM and QFM.

7.4.1 Comparison of Analysis Equation Results

This compares the half-length estimates from analysis equations — LT and PSS.

7.4.1.1 Production Time versus Material-Balance Time

There is a significant difference between the half-length estimates from production time plots and material-balance time plots. The material-balance time plots underestimates half-length compared to the corresponding production time plots (Table 7.3). This is due to the misapplication of material-balance time to Bello (2009)'s transient flow equation. Eq. 7.1 is meant for transient flow analysis (production time) while material-balance time is meant for pseudo-steady state reservoir fluid depletion analysis (Palacio and Blasingame, 1993; Camacho-V. and Raghavan, 1979). Although material-balance time plots reduce the scatter in production data compared to production time plots (see Fig. 7.6), its use in production data analysis should be restricted to the pseudo-steady state (boundary-dominated) flow regimes.

7.4.1.2 Linear Transient versus Pseudo-Steady State

The LT and PSS analysis equations assume that micro-fractures have negligible effect on reservoir depletion. The goal of this comparison is to investigate the discrepancy of the estimates of hydraulic fracture half-length (y_e) and average matrix permeability (k_m) obtained from analyzing different flow regimes. PSS yields larger half-length values compared to LT (Table 7.7) due to neglect of micro-fractures in the reservoir model. This effect is more pronounced in PSS than LT because it is the total tank/reservoir volume (matrix, hydraulic fractures and possible micro-fractures) that controls flow behavior in the reservoir during PSS. Another possible reason is the use of non-representative k_m values. The interface or communication area available between porous regions (primarily matrix and micro-fracture to hydraulic fracture in this case) contributing to fluid depletion controls flow behavior in the reservoir during LT. Therefore, the presence of neglected micro-fractures would affect the resulting k_m. Since y_e estimates from LT depend on k_m (which is not the case for PSS; compare Eqs. 7.1 and 7.2), its accuracy depends on k_m's accuracy. For these wells, the input value of k_m for LT analysis was estimated from core laboratory measurements. This value appears to be significantly lower than the average value estimated from PSS analysis (Eq. 7.3; compare 1.34 mD and 173.7 mD). This is

because the larger k_m from PSS is an average matrix permeability estimate which accounts for possible micro-fractures in the reservoir. Hence, careful measurement is needed in the laboratory to obtain more representative k_m values and ensure better y_e estimates from LT analysis (especially in reservoirs with significant MF intensity).

7.4.2 Comparison of Analysis Equation and Type-Curve Results

This compares the half-length values estimated from analysis equations, DPM type-curves, and QFM type-curves. Also, it compares the micro-fracture spacing estimated from STPM and QFM type-curves. Finally, it investigates the effects of the presence micro-fractures on both DPM and STPM results.

7.4.2.1 Analysis Equations versus DPM Type-Curve

This part compares the results from analysis equations (LT and PSS) and DPM type-curve match. Although these results are similar, PSS yields the largest half-length (y_e) values followed by DPM type-curves then LT (PSS > DPM > LT — see Table 7.7). This is because the y_e values from PSS are calculated independent of average matrix permeability while those from LT and DPM type-curve match require average matrix permeability as an input. Also, LT is simply Bello (2009)'s Region 4 transient flow regime analysis equation of the complete DPM type-curve. Hence, the smaller y_e values estimated from LT compared to DPM is because the former uses only one flow regime while the later uses all available flow regions.

Table 7.7: HF half-lengths estimated from the application of analysis equations (LT and PSS) and DPM type-curves on production data from Wells A and B respectively.

Parameter	LT	DPM	PSS
y_e (Well A)	168 m	220 – 240 m	243 m
y_e (Well B)	177 m	177 – 212 m	—

7.4.2.2 DPM Type-Curve versus STPM Type-Curve

There is little basis for comparing DPM and STPM. This is because the matrix to hydraulic fracture communication present in DPM is now absent and replaced by matrix to micro-

fracture communication path in STPM (compare Figs. 7.1 and 7.2). Also, the STPM solution does not analytically converge to the DPM solution (Ezulike and Dehghanpour, 2014a).

7.4.2.3 DPM Type-Curve versus QFM Type-Curve

This part compares the results from DPM and QFM type-curve matches. DPM type-curve match yields larger half-lengths of hydraulic fracture (Table 7.8) compared to QFM type-curve match.

Table 7.8: HF half-lengths estimated from the application of DPM and QFM Type-Curves on production data from Wells A and B respectively.

Parameter	DPM	QFM
y_e (Well A)	220 – 240 m	23 – 40 m
y_e (Well B)	177 – 212 m	$\approx$ 35 m

This could be due to the differences in model assumptions. QFM accounts for the presence of MF and simultaneous fluid depletion from matrix to both MF and HF. DPM assumes that MF (when present) has negligible effects on fluid production. Hence, DPM compensates for the absence of approximately 18 MF for Wells A and B respectively (Table 7.6) by increasing the output value of effective y_e. This increase in y_e could be explained in two ways: dimensionless fracture conductivity ($F_{cD} = \frac{a_F k_F}{y_e(k_f+k_m)}$; adapted from Agarwal et al. (1979)) and equivalent HF length. In terms of dimensionless fracture conductivity, the absence of MF ($k_f = 0$) in DPM requires a corresponding great increase in y_e (since $k_f \gg k_m$) to maintain the same F_{cD} (a_F, k_F and k_m are kept constant) value obtained from QFM type-curve matching. In terms of equivalent HF length, DPM requires an additional length of about ($\frac{n_f a_f L_F}{a_F}$; where $a_F \approx 10 \times a_f$) to compensate for the absence of MF. This results in an increase of y_e in the order of 130 and 180 m for Wells A and B respectively. Therefore, the application of DPM on production data analysis (from reservoirs with evidence of reactivated natural fractures) could result in misleading y_e estimates.

7.4.2.4 STPM Type-Curve versus QFM Type-Curve

This part compares the output parameters from STPM and QFM type-curve matches. Although both type-curves produce similar half-length values, STPM type-curve match

yields smaller micro-fracture spacing (L_f) and higher micro-fracture intensity (n_f) values (see Table 7.9) compared to corresponding outputs from QFM type-curve match. An explanation for this is the difference in simultaneous and sequential reservoir depletion physics. QFM accounts for simultaneous fluid depletion from matrix to both micro- and hydraulic fractures. STPM assumes sequential fluid depletion from matrix to micro-fracture, then from micro-fracture to hydraulic fracture (negligible matrix to hydraulic fracture communication). Hence when compared to QFM, STPM compensates for the absence of matrix to hydraulic fracture communication by decreasing L_f (see Table 7.9).

Table 7.9: Micro-fracture spacing and number estimated from the application of STPM and QFM Type-Curves on production data from Wells A and B respectively. The low end values of micro-fracture spacing corresponds to the low end values of hydraulic fracture half-length and high end values of the number of micro-fractures.

Parameter	**STPM**	**QFM**
y_e (Well A)	21 – 45 m	23 – 40 m
y_e (Well B)	$\approx$ 33 m	$\approx$ 35 m
L_f (Well A)	1 – 1.2 m	1.5 – 1.8 m
L_f (Well B)	1.5 m	2 m
n_f (Well A)	20 – 36	14 – 21
n_f (Well B)	21	17

This decrease in L_f increases the n_f within the same hydraulic fracture spacing. This results in a larger matrix to micro-fracture communication area in STPM compared to QFM. Therefore, the application of STPM on production data analysis (from reservoirs with active matrix–HF communication) could result in misleading L_f or n_f estimates.

7.5 Summary

The results of this chapter can be summarized under five points as the comparison of the output parameters from: production time against material-balance time plots in terms of LT analysis equation; LT and PSS analysis equations respectively; analysis equations

against DPM type-curves; QFM type-curves against DPM type-curves; and QFM type-curves against STPM type-curves.

Result 1 is significant because it shows that the application of material-balance time plots on transient flow regimes of production data could result is unreasonable estimates of reservoir parameters. Therefore material-balance time analysis should be restricted to the boundary-dominated flow regimes of production data.

Result 2 reveals that half-lengths estimated from PSS analysis equations can be larger than those from LT analysis equations. This is because the PSS estimates are independent of matrix permeability while the LT estimates require it as an input. Therefore, the use of non-representative matrix permeability values for LT can result in underestimation of hydraulic fracture half-lengths.

Result 3 shows that although single flow regime (transient linear for LT and boundary-dominated for PSS) analysis is a quick and simple means of estimating reservoir parameters, it can result in erroneous estimates of reservoir parameters when compared to results from multiple flow regime analysis (e.g. type-curve matching). This happens because using more flow regimes (when available) captures more of the fluid flow physics and imposes a better constraint on the estimated reservoir parameter value.

Result 4 shows that applying DPM on production data from a reservoir with low to intermediate fracture spacing aspect ratios (Ezulike and Dehghanpour, 2014a) can result in overestimation of hydraulic fracture half-length. Fracture spacing aspect ratio is micro-fracture spacing divided by hydraulic fracture spacing.

Result 5 shows that applying STPM on production data from a reservoir with intermediate to high spacing-aspect ratios can result in underestimation of micro-fracture spacing present within a given hydraulic fracture spacing.

Nomenclature

Symbols

c	Compressibility, Lt^2M^{-1}, atm^{-1}, $[Pa^{-1}$, $psi^{-1}]$.
h	Reservoir thickness, L, m, $[ft]$.
k	Bulk permeability, L^2, m^2 $[D]$.
n	Number, L, m, $[ft]$.
q	Rate, L^3t^{-1}, $m^3.s^{-1}$, $[rb.day^{-1}]$.
s	Laplace variable, t^{-1}, s^{-1}, $[hr^{-1}$, $day^{-1}]$.
t	Time, t, s, $[hr$, $day]$.

A	Area, L^2, m^2, $[ft^2]$.
L	Spacing or distance, L, m, $[ft]$.
N	Cumulative, L^3, m^3, $[ft^3]$.
P	Pressure, $ML^{-1}t^{-2}$, Pa, $[psi]$.
X	Horizontal well length, L, m, $[ft]$.
ϕ	Bulk porosity, dimensionless.
μ	Viscosity, $ML^{-1}t^{-1}$, $Pa.s$, $[cP]$.

Subscripts

$_c$	cross-section.
$_e$	equivalent.
$_f$	Micro-fracture.
$_i$	Initial.
$_m$	Matrix.
$_p$	Production.
$_t$	Total.
$_w$	Well.
$_D$	Dimensionless.
$_F$	Hydraulic fracture.
$_L$	Reference length.
$_{sp}$	Spacing.
$_{wf}$	Bottom-hole flowing.

Chapter 8

Conclusions and Recommendations

This study presents complementary workflows for the qualitative and quantitative analysis of flowback and post-flowback production data. These data are obtained from multi-fractured horizontal wells completed in low permeability reservoirs with a significant amount of reactivated natural fractures.

8.1 Conclusions

The key conclusions from this study can be summarized under the following points, namely:

- Physics of fluid flow in the reservoir changes as depletion transitions from flowback periods to post-flowback periods.
- Flowback physics differs in tight oil, tight gas and Shale gas wells respectively.
- The occurrence of pseudo-steady state flow regime during intermediate flowback periods suggests a "*pressure supercharge*" effect in the fracture network. Rate and pressure data from this flow regime can be analyzed to estimate key fracture properties (e.g. effective pore-volume and initial average gas saturation in the active fracture network) and drive mechanisms (i.e. fracture closure, gas expansion and water depletion).
- Fracture closure effects play a significant role in the physics of fluid flow during early flowback periods. However, fluid expansion becomes the dominant drive mechanism towards the end of flowback in gas wells.
- Flowback data from tight oil wells are dominated by single phase, water depletion during early time periods (about 100 hours). This is unlike many Shale gas wells, which show immediate gas and water production.
- The concept of dynamic-relative-permeability was proposed to capture the transient, multiphase, fluid saturations in the effective fracture network during flowback. The

resulting model enables complementary, 2-phase flowback and post-flowback production data analysis.

- Qualitative production data analysis show that there is a general correlation between: load recovery and flowback sequence; effective fracture pore volume and flowback sequence; and cumulative water production and effective fracture pore volume. The restriction of comparative load recovery analysis to wells completed in the same formation produces better correlations. Also, this qualitative analysis provides a way to estimate the percentage of the total injected volume left inside and outside the active fracture network respectively.

- Quantitative production data analysis provides estimates of the pore-volume of active fracture networks, effective half-length and initial gas volume in hydraulic fractures during flowback. This analysis shows that the gas desorption effects from the matrix and the communication interface between secondary fractures and hydraulic fractures, significantly increases as production progresses from flowback to post-flowback periods. However, fracture closure as a result of geomechanical effects is expected to be a counter-agent to this increased effective fracture volume (due to the increasing communication interface).

- A comparison of transient load recovery and ultimate load recovery should show if mobile water in matrix is contributing to flowback.

- Production data from tight reservoirs with significant reactivated natural fractures can be appropriately analyzed using the proposed quadrilinear flow model. This is achieved by providing type-curves and analysis equations (from flow regimes).

- The application of a wrong model for production data analysis could result in the overestimation or underestimation of reservoir parameters (e.g. half-lengths of hydraulic fractures and intensity of secondary fractures). This study proposes a criterion (based on spacing aspect ratio) for selecting the appropriate model when interpreting production data from multi-fractured horizontal wells in tight reservoirs.

- Lumping secondary fracture and hydraulic fracture properties together can result in unreliable parameter estimates and production forecasts.

- Use of actual values of matrix/fracture porosity and permeability results will not properly capture the physics of fluid flow. Use bulk values instead.

- Although material balance time can smoothen noisy data, it should not be used to analyze data from transient flow regions. Its use should be restricted to analyzing pseudo-steady state flow regions.

- Use of non-representative values of matrix permeability (e.g. from laboratory core experiments) can result in underestimation of fracture half length .

- Uncertainty in parameters estimated from production data analysis can be reduced by using the results from flowback data analysis as inputs (or initial guesses) for post-flowback production data analysis. Also, this can be achieved by comparing the parameters independently estimated using analysis equations from individual flow regimes.

8.2 Recommendations

Several simplifying assumptions were made in this study such as: splitting the dynamic-relative-permeability function into pre-inflexion and post-inflexion parts to allow semi-analytic solution of the diffusivity equations; neglecting any water influx from matrix to fractures; ignoring geomechanical effects (e.g. using constant fracture compressibility, porosity and permeability).

To address these limitations, the following points are recommended as possible directions for further studies.

- Numerical solution of flow equations from the flowback analysis model using the complete dynamic-relative-permeability function (without splitting it into two).

- Inclusion of both water influx from matrix to the fractures for reservoirs with mobile formation brine.

- Extension of the static framework for the flowback analysis model from dual-porosity to triple-porosity using the quadrilinear flow model proposed in this study. The purpose is to explicitly account for the presence of reactivated natural fractures.

- Accounting for geomechanical effects (e.g. accounting for pore-volume change as a function of time or pressure) in the proposed flowback models. If possible, accounting for the differences in properties of unpropped natural fractures, propped hydraulic fractures and other micro-fractures.

- Further reduction of uncertainty in the estimates of reservoir parameters by developing additional analysis equations. Some of these equations would be based on the intersection among flow regimes.

- Improvement in the proposed equations for converting true/intrinsic/microscopic values of porosity and permeability to their corresponding bulk/effective/macroscopic values. Various simulation cases could be used as a starting point for this improvement.

References

Abbasi, M. A., 2013. A Comparative Study of Flowback Rate and Pressure Transient Behaviour in Multifractured Horizontal Wells. Master's thesis, University of Alberta, Edmonton, Alberta, Canada, (September 2013).

Abbasi, M. A., Ezulike, D. O., Dehghanpour, H., et al., (March) 2014. A Comparative Study of Flowback Rate and Pressure Transient Behavior in Multifractured Horizontal Wells Completed in Tight Gas and Oil Reservoirs. Journal of Natural Gas Science and Engineering 17, 82–93, http://dx.doi.org/10.1016/j.jngse.2013.12.007.

Abdassah, D., Ershaghi, I., (April) 1986. Triple-Porosity Systems for Representing Naturally Fractured Reservoirs. SPE Formation Evaluation 1 (2), 113–127. SPE–13409–PA, http://dx.doi.org/10.2118/13409-PA.

Abdelaziz, K., Hani, Q., Naiem, B., (31 January–2 February) 2011. Tight Gas Sands Development is Critical to Future World Energy Resources. Paper SPE-42049-MS presented at the SPE Middle East Unconventional Gas Conference and Exhibition, Muscat, Oman. http://dx.doi.org/10.2118/42049-MS.

Adefidipe, O. A., Dehghanpour, H., Virues, C. J., (19–21 October) 2014. Immediate Gas Production from Shale Gas Wells: A Two-Phase Flowback Model. Paper SPE-168982-MS presented at the SPE Unconventional Resources Conference, The Woodlands, Texas, USA. http://dx.doi.org/10.2118/168982-MS.

Agarwal, R. G., Carter, R. D., Pollock, C. B., (March) 1979. Evaluation and Performance Prediction of Low–Permeability Gas Wells Stimulated by Massive Hydraulic Fracturing. J. Pet. Technol. 31 (3), 362–372. SPE–6838–PA, http://dx.doi.org/10.2118/6838-PA.

Aguilera, R., (December) 2006. Effect of Fracture Compressibility on Oil Recovery From Stress-Sensitive Naturally Fractured Reservoirs. Journal of Canadian Petroleum Technology 45 (12), 49–59. PETSOC–06–12–01, http://dx.doi.org/10.2118/06-12-01.

Al-Ahmadi, A. H., 2010. A Triple-Porosity Model for Fractured Horizontal Wells. Master's thesis, Texas A & M University, College Station, Texas, USA, (August 2010).

Al-Ahmadi, A. H., Wattenbarger, R. A., (15–18 May) 2011. Triple-porosity Models: One Further Step Towards Capturing Fractured Reservoirs Heterogeneity. Paper SPE-149054-MS presented at the SPE/DGS Saudi Arabia Section Technical Symposium and Exhibition, Al-Khobar, Saudi Arabia. http://dx.doi.org/10.2118/149054-MS.

Al-Hussainy, R., Ramey Jr., H. J., (May) 1966. Application of Real Gas Flow Theory to Well Testing and Deliverability Forecasting. Journal of Petroleum Technology 18 (5), 637–642. SPE–1243–B–PA, http://dx.doi.org/10.2118/1243-B-PA.

Al-Khalifa, A. J., Aziz, K., Horne, R. N., (27–30 September) 1987. A New Approach to Multiphase Well Test Analysis. Paper SPE-16743-MS presented at the SPE Annual Technical Conference and Exhibition, Dallas, Texas, USA. http://dx.doi.org/10.2118/16743-MS.

Al-Khalifa, A. J., Horne, R. N., Aziz, K., (5–7 April) 1989. Multiphase Well Test Analysis: Pressure and Pressure-Squared Methods. Paper SPE-18803-MS presented at the SPE California Regional Meeting, Bakersfield, California, USA. http://dx.doi.org/10.2118/18803-MS.

Alcoser, L., Ovalle, A., Parsons, M., (24–25 Septemeber) 2012. The Bakken: Utilizing a Petroleum System Based Analysis to Optimally Exploit One of the World's Largest Oil Deposit. Paper SPE-158918-MS presented at the Hydrocarbon Economics and Evaluation Symposium, Calgary, Alberta, Canada. http://dx.doi.org/10.2118/158918-MS.

Ali, J. A., Siddiqui, S., Dehghanpour, H., (November) 2013. Analyzing the Production Data of Fractured Horizontal Wells by a Linear Triple Porosity Model: Development of Analysis Equations. Journal of Petroleum Science and Engineering (In Press)http://dx.doi.org/10.1016/j.petrol.2013.10.016.

Alkouh, A., McKetta, S., Wattenbarger, R. A., (September) 2014. Estimation of Effective-Fracture Volume Using Water-Flowback and Production Data for Shale-Gas Wells. Journal of Canadian Petroleum Technology 53 (5), 290–303. SPE–166279–PA, http://dx.doi.org/10.2118/166279-PA.

Alkouh, A., Schechter, D., Wattenbarger, R. A., et al., (30 October–1 November) 2012. Practical Use of Simulators for Characterization of Shale Reservoirs. Paper SPE-162645-MS presented at the SPE Canadian Unconventional Resources Conference, Calgary, Alberta, Canada. http://dx.doi.org/10.2118/162645-MS.

Alkouh, A. B., Mcketta, S. F., Wattenbarger, R. A., (30 September–2 October) 2013. Estimation of Fracture Volume Using Water Flowback and Production Data for Shale Gas Wells. Paper SPE-166279-MS presented at the SPE Annual Technical Conference & Exhibition, New Orleans, Louisiana, USA. http://dx.doi.org/10.2118/166279-MS.

Alkouh, A. B., Wattenbarger, R. A., (20–22 August) 2013. New Advances in Shale Reservoir Analysis Using Flowback Data. Paper SPE-165721-MS presented at the SPE Eastern Regional Meeting, Pittsburgh, Pennsylvania, USA. http://dx.doi.org/10.2118/165721-MS.

Almulhim, A., Alharthy, N., Tutuncu, A. N., et al., (10–13 November) 2014. Impact of Imbibition Mechanism on Flowback Behavior: A Numerical Study. Paper SPE-171799-MS presented at the Abu Dhabi International Petroleum Exhibition and Conference, Abu Dhabi, UAE. http://dx.doi.org/10.2118/171799-MS.

Asadi, M., Woodroof, R. A., Himes, R. E., (May) 2008. Comparative Study of Flowback Analysis Using Polymer Concentrations and Fracturing-Fluid Tracer Methods: A Field Study. SPE Production & Operations 3 (3), 147–157. SPE–101614–PA, http://dx.doi.org/10.2118/101614-PA.

Bello, R., Wattenbarger, R. A., (14–17 February) 2010a. Multi-stage Hydraulically Fractured Horizontal Shale Gas Well Rate Transient Analysis. Paper SPE-126754-MS presented at the SPE North Africa Technical Conference and Exhibition, Cairo, Egypt. http://dx.doi.org/10.2118/126754-MS.

Bello, R. O., 2009. Rate Transient Analysis in Shale Gas Reservoirs with Transient Linear Behavior. Ph.D. thesis, Texas A & M University, College Station, Texas, USA, (May 2009).

Bello, R. O., Wattenbarger, R. A., (14–17 February) 2010b. Multi-stage Hydraulically Fractured Horizontal Shale Gas Well Rate Transient Analysis. Paper SPE-126754-MS presented at the SPE North Africa Technical Conference and Exhibition, Cairo, Egypt. http://dx.doi.org/10.2118/126754-MS.

Birch, C. P. D., (March) 1999. A New Generalized Logistic Sigmoid Growth Equation Compared with the Richards Growth Equation. Annals of Botany 83 (6), 713–723, http://dx.doi.org/10.1006/anbo.1999.0877.

Brown, M., Ozkan, E., Raghavan, R., et al., (December) 2011. Practical Solutions for Pressure Transient Responses of Fractured Horizontal Wells in Unconventional Reser-

voirs. SPE Reservoir Evaluation & Engineering 14 (6), 663–676. SPE–125043–PA, http://dx.doi.org/10.2118/125043-PA.

Bumb, A. C., McKee, C. R., (March) 1988. Gas–Well Testing in the Presence of Desorption for Coalbed Methane and Devonian Shale. SPE Form. Eval. 3 (1), 179–185., http://dx.doi.org/10.2118/15227-PA.

Buscaglia, R., Miller, M. C., L., D. W., et al., (June) 2013. Polyethylene Glycol Binding alters Human Telomere G-Quadruplex Structure by Conformational Selection. Nucleic Acids Research, 1–13,http://dx.doi.org/10.1093/nar/gkt440.

Camacho-V., R. G., Raghavan, R., (June) 1979. Some Theoretical Results Useful in Analyzing Well Performance Under Solution-Gas Drive. SPE Formation Evaluation 6 (2), 190–198. SPE–16580–PA, http://dx.doi.org/10.2118/16580-PA.

Carlson, E. S., Mercer, J. C., (April) 1991. Devonian Shale Gas Production: Mechanisms and Simple Models. J. Cdn. Pet. Tech. 43 (4), 476–482. SPE–19311–PA, http://dx.doi.org/10.2118/19311-PA.

Castillo, F., Aguilera, F., Lawton, D., (15–17 November) 2011. Integration of Seismic Data and a Triple Porosity Model for Interpretation of Tight Gas Formations in Western Canada Sedimentary Basin. Paper SPE-149496-MS presented at the Canadian Unconventional Resources Conference, Calgary, Alberta, Canada. http://dx.doi.org/10.2118/149496-MS.

Chacon, A., Djebbar, T., (15–18 April) 2007. Effects of Stress on Fracture Properties of Naturally Fractured Reservoirs. Paper SPE-107418-MS presented at the SPE Latin American & Caribbean Petroleum Engineering Conference, Buenos Aires, Argentina. http://dx.doi.org/10.2118/107418-MS.

Cheng, Y., (October) 2012. Impact of Water Dynamics in Fractures on the Performance of Hydraulically Fractured Wells in Gas-Shale Reservoirs. Journal of Canadian Petroleum Technology 51 (2), 143–151. SPE–127863–PA, http://dx.doi.org/10.2118/127863-PA.

Chin, L. Y., Raghavan, R., Thomas, L. K., (October) 2000. Pressure-Dependent Natural-Fracture Permeability in Shale and Its Effect on Shale-Gas Well Production. SPE Reservoir Evaluation & Engineering 3 (5), 435–443. SPE–66222–PA, http://dx.doi.org/10.2118/66222-PA.

Cho, Y., Apaydin, O. G., Ozkan, E., (May) 2013. Pressure-Dependent Natural-Fracture Permeability in Shale and Its Effect on Shale-Gas Well Production. SPE Reservoir Evaluation & Engineering 16 (2), 216–228. SPE–159801–PA, http://dx.doi.org/10.2118/159801-PA.

Cholet, H., 2008. Well Production Practical Handbook, 3rd Edition. Éditions Technip, Paris, France, http://app.knovel.com/hotlink/toc/id:kpWPPHNEE4/well-production-practical.

Chu, W., Little, T. M., Robinson, J. C., (4–7 October) 1992. Transient Test Analysis: Solution-Gas-Drive Reservoir Examples. Paper SPE-24721-MS presented at the SPE Annual Technical Conference and Exhibition, Washington, D.C., USA. http://dx.doi.org/10.2118/24721-MS.

Clarkson, C. R., (30 October–1 November) 2012. Modeling 2-Phase Flowback of Multi-Fractured Horizontal Wells Completed in Shale. Paper SPE-162593-MS presented at the SPE Canadian Unconventional Resources Conference, Calgary, Alberta, Canada. http://dx.doi.org/10.2118/162593-MS.

Clarkson, C. R., Jordan, C. L., Gierhart, R. R., et al., (16–18 April) 2007. Production Data Analysis of CBM Wells. Paper SPE-107705-MS presented at the SPE Rocky Mountain Oil & Gas Technology Symposium held in Denver, Colorado, USA. http://dx.doi.org/10.2118/107705-MS.

Clarkson, C. R., Jordan, C. L., Gierhart, R. R., et al., (April) 2008. Production Data Analysis of Coalbed–Methane Wells. SPE Res. Eval. & Eng. 11 (2), 311–325., http://dx.doi.org/10.2118/107705-PA.

Clarkson, C. R., McGovern, J. M., (December) 2005. Optimization of Coalbed-Methane-Reservoir Exploration and Development Strategies Through Integration of Simulation and Economics. SPE Reservoir Evaluation & Engineering 8 (6), 502–519. SPE–88843–PA, http://dx.doi.org/10.2118/88843-PA.

Clarkson, C. R., Pederson, P. K., (19–21 October) 2010. Tight Oil Production Analysis: Adaptation of Existing Rate-Transient Analysis Techniques. Paper SPE-137352-MS presented at the Canadian Unconventional Resources & International Petroleum Conference, Calgary, Alberta, Canada. http://dx.doi.org/10.2118/137352-MS.

Clarkson, C. R., Pederson, P. K., (15–17 November) 2011. Production Analysis of Western Canadian Unconventional Light Oil Plays. Paper SPE-149005-MS presented

at the Canadian Unconventional Resources Conference, Calgary, Alberta, Canada. http://dx.doi.org/10.2118/149005-MS.

Clarkson, C. R., Williams-Kovacs, J., (July) 2013. Two-Phase Flowback of Multifractured Horizontal Wells Completed in Shale. SPE Journal 18 (4), 795–812. SPE–162593–PA, http://dx.doi.org/10.2118/162593-PA.

Crafton, J. W., (9–11 March) 1997. Oil and Gas Well Evaluation Using the Reciprocal Productivity Index Method. Paper SPE-37409-MS presented at the SPE Production Operations Symposium, Oklahoma City, Oklahoma, USA. http://dx.doi.org/10.2118/37409-MS.

Crafton, J. W., (27–30 September) 1998. Well Evaluation Using Early Time Post-Stimulation Flowback Data. Paper SPE-49223-MS presented at the SPE Annual Technical Conference and Exhibition, New Orleans, Louisiana, USA. http://dx.doi.org/10.2118/49223-MS.

Crafton, J. W., (16–18 November) 2008. Modeling Flowback Behavior or Flowback Equals "Slowback". Paper SPE-119894-MS presented at the SPE Shale Gas Production Conference, Fort Worth, Texas, USA. http://dx.doi.org/10.2118/119894-MS.

Crafton, J. W., (23–25 February) 2010. Flowback Performance in Intensely Naturally Fractured Shale Gas Reservoirs. Paper SPE-131785-MS presented at the SPE SUnconventional Gas Conference, Pittsburgh, Pennsylvania, USA. http://dx.doi.org/10.2118/131785-MS.

Crafton, J. W., Gunderson, D., (24–27 September) 2006. Use of Extremely High Time-Resolution Production Data To Characterize Hydraulic Fracture Properties. Paper SPE-103591-MS presented at the SPE Annual Technical Conference and Exhibition, San Antonio, Texas, USA. http://dx.doi.org/10.2118/103591-MS.

Crafton, J. W., Gunderson, D., (11–14 November) 2007. Stimulation Flowback Management–Keeping a Good Completion Good. Paper SPE-110851-MS presented at the SPE Annual Technical Conference and Exhibition, Anaheim, California, USA. http://dx.doi.org/10.2118/110851-MS.

Dahi, T. A., 2009. Analysis of Hydraulic Fracture Propagation in Fractured Reservoirs: an Improved Model for the Interaction between Induced and Natural fractures. Ph.D. thesis, Texas A & M University, College Station, Texas, USA, (May 2009).

Davies, B., 2001. Integral Transforms and their Applications, 3rd Edition. Springer-Verlag New York Inc., New York.

Dehghanpour, H., Lan, Q., Saeed, Y., et al., (May) 2013. Spontaneous Imbibition of Brine and Oil in Gas Shales: Effect of Water Adsorption and Resulting Microfractures. Energy Fuels 27 (6), 3039–3049, http://dx.doi.org/10.1021/ef4002814.

Dehghanpour, H., Shirdel, M., (15–17 November) 2011. A Triple Porosity Model for Shale Gas Reservoirs. Paper SPE-149501-MS presented at the Canadian Unconventional Resources Conference, Calgary, Alberta, Canada. http://dx.doi.org/10.2118/149501-MS.

Dehghanpour, H., Zubair, H. A., Chhabra, A., et al., (August) 2012. Liquid Intake of Organic Shales. Energy Fuels 26 (9), 5750–5758, http://dx.doi.org/10.1021/ef3009794.

Duhault, J. L. J., 2012. Cardium Formation Hydraulic "Frac" Microseismic: Observations and Conclusions. Canadian Society of Exploration Geophysicists GeoConvention 2012: Vision. http://cseg.ca/assets/files/resources/abstracts/2012/302_GC2012_Cardium_Formation_Hydraulic_Frac_Microseismic.pdf (last accessed 13-05-2013).

El-Banbi, A. H., 1998. Analysis of Tight Gas Well Performance. Ph.D. thesis, Texas A & M University, College Station, Texas, USA, (May 1998).

Ezulike, D. O., (30 Septemeber–2 October) 2013. A Simultaneous Matrix-Depletion Model for Characterizing Fractured Reservoirs. SPE Student Paper presented at the International Student Paper Contest at the SPE Annual Technical Conference and Exhibition, New Orleans, Louisiana, USA.

Ezulike, D. O., Dehghanpour, H., (January) 2014a. A Model for Simultaneous Matrix Depletion into Natural and Hydraulic Fracture Networks. Journal of Natural Gas Science and Engineering 16, 57–69., http://dx.doi.org/10.1016/j.jngse.2013.11.004.

Ezulike, D. O., Dehghanpour, H., (25–27 August) 2014b. A Workflow for Flowback Data Analysis – Creating Value out of Chaos. Paper SPE-2014-1922047-MS presented at the SPE/AAPG/SEG Unconventional Resources Technology Conference held in Denver, Colorado, USA. http://dx.doi.org/10.15530/urtec-2014-1922047.

Ezulike, D. O., Dehghanpour, H., (June) 2014c. Modelling Flowback as a Transient Two-Phase Depletion Process. Journal of Natural Gas Science and Engineering 19, 258–278., http://dx.doi.org/10.1016/j.jngse.2014.05.004.

Ezulike, D. O., Dehghanpour, H., (November) 2015. A Complementary Approach for Uncertainty Reduction in Post-flowback Production Data Analysis. Journal of Natural Gas Science and Engineering 27, 1074–1091., http://dx.doi.org/10.1016/j.jngse.2015.09.059.

Ezulike, D. O., Dehghanpour, H., Hawkes, R. V., (5–7 November) 2013. Understanding Flowback as a Transient 2 Phase Displacement Process: An extension of the Linear Dual Porosity Model. Paper SPE-167164-MS presented at the SPE Canadian Unconventional Resources Conference, Calgary, Alberta, Canada. http://dx.doi.org/10.2118/167164-MS.

Ezulike, D. O., Ghanbari, E., Siddiqui, S., et al., (May) 2015. Pseudo-steady State Analysis in Linear Tight Oil Reservoirs. Journal of Petroleum Science and Engineering 129, 40–47, http://dx.doi.org/10.1016/j.petrol.2015.01.009.

Ezulike, D. O., Igbokoyi, A. O., (December) 2012. Horizontal Well Pressure Transient Analysis in Anisotropic Composite Reservoirs – A Three Dimensional Semi-analytical Approach. Journal of Petroleum Science and Engineering 96–97, 120–139, http://dx.doi.org/10.1016/j.petrol.2012.09.002.

Ezulike, O., Dehghanpour, H., (February) 2016a. Capturing the Effects of Secondary Fractures on Production Data Using Flow Regime Equations and Specialised Plots: An Uncertainty Analysis Approach. Journal of Petroleum Science and Engineering 138, 201–217, http://dx.doi.org/10.1016/j.petrol.2015.11.016.

Ezulike, O., Dehghanpour, H., (May) 2016b. Characterizing Tight Oil Reservoirs with Dual- and Triple-Porosity Models. Journal of Energy Resources Technology 138 (3), 032801–1—032801–10., http://dx.doi.org/10.1115/1.4032520.

Fekete, 2014. How to Define Compositions in IHS Piper. http://fekete.com/SAN/WebHelp/Piper/WebHelp/c-gs-EOS.htm (last accessed 10-11-2016).

Fisher, M. K., Wright, C. A., Davidson, B. M., et al., (29 September–2 October) 2002. Integrating Fracture Mapping Technologies to Optimize Stimulations in the Barnett Shale. Paper SPE-77441-MS presented at the SPE Annual Technical Conference and Exhibition, San Antonio, Texas, USA. http://dx.doi.org/10.2118/77441-MS.

Gale, J. F. W., Laubach, S. E., Olson, J. E., et al., 2014. Natural Fractures in Shale: A Review and New Observations. AAPG Bulletin 98 (11), 2165–2216., http://aapgbull.geoscienceworld.org/content/98/11/2165.full.pdf+html.

Gale, J. F. W., Reed, R. M., Holder, J., (April) 2007. Natural Fractures in the Barnett Shale and their importance for Hydraulic Fracture Treatments. AAPG Bulletin 91 (4), 603–622.

Gdanski, R., Weaver, J., Slabaugh, B., (29–31 January) 2007. A New Model for Matching Fracturing Fluid Flowback Composition. Paper SPE-106040-MS presented at the SPE Hydraulic Fracturing Technology Conference, College Station, Texas, USA. http://dx.doi.org/10.2118/106040-MS.

Ghanbari, E., Abbasi, M. A., Dehghanpour, H., et al., (5–7 November) 2013. Flowback Volumetric and Chemical Analysis for Evaluating Load Recovery and Its Impact on Early-Time Production. Paper SPE-167165-MS presented at the Canadian Unconventional Resources Conference, Calgary, Alberta, Canada. http://dx.doi.org/10.2118/167165-MS.

Ghanbari, E., Dehghanpour, H., (January) 2016. The Fate of Fracturing Water: A Field and Simulation Study. Fuel 163, 282–294., http://dx.doi.org/10.1016/j.fuel.2015.09.040.

Harris, D., (March) 1989. Comparison of 1-, 2-, and 3-Parameter IRT Models. Educational Measurement: Issues and Practice 8 (1), 35–41, http://dx.doi.org/10.1111/j.1745-3992.1989.tb00313.x.

Hazewinkel, M. (Ed.), 2002. Encyclopedia of Mathematics. Springer Publishers.

Hlidek, B., Rieb, B., (24–26 January) 2011. Fracture Stimulation Treatment Best Practices in the Bakken Oil Shale. Paper SPE-140252-MS presented at the SPE Hydraulic Fracturing Technology Conference, The Woodlands, Texas, USA. http://dx.doi.org/10.2118/140252-MS.

Holditch, S. A., (November) 2003. The Increasing Role of Unconventional Reservoirs in the Future of the Oil and Gas Business. Journal of Petroleum Technology 55 (11), 34–79. SPE–1103–0034–JPT, http://dx.doi.org/10.2118/1103-0034-JPT.

Honarpour, M., Koederitz, L., Harvey, H., January 1986. Relative Permeability of Petroleum Reservoirs. CRC Press Inc., Boca Raton, Florida.

Ilk, D., Currie, S. M., Symmons, D., et al., (19–22 September) 2010. A Comprehensive Workflow for Early Analysis and Interpretation of Flowback Data from wells in Tight Gas/Shale Reservoir Systems. Paper SPE-135607-MS presented at the SPE Annual Technical Conference and Exhibition, Florence, Italy. http://dx.doi.org/10.2118/135607-MS.

Jones Jr., R. S., Pownall, B., Franke, J., (25–27 August) 2014. Estimating Reservoir Pressure from Early Flowback Data. Paper URTeC 1934785 presented at the Unconventional Resources Technology Conference held in Denver, Colorado, USA. http://dx.doi.org/10.15530/urtec-2014-1934785.

Justen, J. J., (September) 1957. Canadas Pembina Field. J. Pet. Technol. 9 (9), 21–26. SPE–856–G, http://dx.doi.org/10.2118/856-G.

Kamal, M. M., Pan, Y., (April) 2010. Use of Transient Data To Calculate Absolute Permeability and Average Fluid Saturations. SPE Reservoir Evaluation & Engineering 13 (2), 306–312, http://dx.doi.org/10.2118/113903-PA.

Kazemi, H., (December) 1969. Pressure Transient Analysis of Naturally Fractured Reservoirs with Uniform Fracture Distribution. SPE Journal 9 (4), 451–462. SPE–2156–A, http://dx.doi.org/10.2118/2156-A.

King, G. E., (6–8 February) 2012. Hydraulic Fracturing 101: What Every Representative, Environmentalist, Regulator, Reporter, Investor, University Researcher, Neighbor and Engineer Should Know About Estimating Frac Risk and Improving Frac Performance in Unconventional Gas and Oil Wells. Paper SPE-152596-MS presented at the SPE Hydraulic Fracturing Technology Conference, The Woodlands, Texas, USA. http://dx.doi.org/10.2118/152596-MS.

Krasey, R., Fawcett, R., (8-10 June) 1998. New Life From an Old Field – PKCU#2 Waterflood. Paper SPE-98-31 presented at the Annual Technical Meeting, Calgary, Alberta, Canada. http://dx.doi.org/10.2118/98-31.

Kucuk, F., Sawyer, W. K., Alam, J., (December) 1981. Modeling Capabilities for the Devonian Gas Shales. J. Energy Resour. Technol 103 (4), 270–276, http://dx.doi.org/10.1115/1.3230851.

Leibowitz, N., Baum, B., Enden, G., et al., (June) 2010. The Exponential Learning Equation as a Function of Successful Trials Results in Sigmoid Performance. J. Math. Psychol. 54 (3), 338–340, http://dx.doi.org/10.1016/j.jmp.2010.01.006.

Li, C., Lafollette, R., Sookprasong, A., , et al., (26–28 March) 2013. Characterization of Hydraulic Fracture Geometry in Shale Gas Reservoirs Using Early Production Data. Paper IPTC-16896-MS presented at the SPE International Petroleum Technology Conference, Beijing, China. http://dx.doi.org/10.2118/16896-MS.

Liang, F., Sayed, M., Al-Muntasheri, G. A., et al., (March) 2016. A Comprehensive Review on Proppant Technologies. Journal of Petroleum 2 (1), 26–39, http://dx.doi.org/10.1016/j.petlm.2015.11.001.

Liu, J. C., Bodvarsson, G. S., Wu, Y. S., (April–May) 2003. Analysis of Flow Behavior in Fractured Lithophysal Reservoirs. Journal of Contaminant Hydrology 62–63, 189–211, http://dx.doi.org/10.1016/S0169-7722(02)00169-9.

Lorenz, J. C., Warpinski, N. R., (September) 1992. Natural Fracture Systems Studies. SAND–92-1648C; DOE/DP/00789–92/C0045; CONF-920584–26 ON: DE92019426http://www.osti.gov/scitech/servlets/purl/10174107 (last accessed 12-01-2017).

Lorenz, J. C., Warpinski, N. R., Teufel, L. W., (August) 1996. Natural Fracture Characteristics and Effects. The Leading Edge 15 (8), 909–911., http://dx.doi.org/10.1190/1.1437388.

MacKenzie, W. T., (28 September–1 October) 1975. Petrophysical Study of the Cardium Sand in the Pembina Field. Paper SPE-5541-MS presented at the Fall Meeting of the Society of Petroleum Engineers of AIME, Dallas, Texas, USA. http://dx.doi.org/10.2118/5541-MS.

Makhanov, K., Habibi, A., Dehghanpour, H., et al., 2014. Liquid Uptake of Gas Shales: A Workflow to Estimate Water Loss During Shut-in Periods after fracturing Operations. Journal of Unconventional Oil and Gas Resources 7, 22–32., http://dx.doi.org/10.1016/j.juogr.2014.04.001.

Martin, J. C., 1959. Simplified Equations of Flow in Gas Drive Reservoirs and the Theoretical Foundation of Multiphase Pressure Buildup Analyses. Petroleum Transactions, AIME. 216, 321–323, http://dx.doi.org/10.2118/1235-G.

Moradian, Z., Fathi, A., Evans, B., (26–29 June) 2016. Shear Reactivation of Natural Fractures in Hydraulic Fracturing. Paper ARMA-2016-829 presented at the 50th US Rock Mechanics/Geomechanics Symposium, Houston, Texas, USA.

Narusawa, U., (July) 2001. General Characteristics of the Sigmoidal Model Equation Representing Quasi-static Pulmonary P-V Curves. J. Appl. Physiol. 91 (1), 201–210.

Nelson, R. A., 2001. Geologic Analysis of Naturally Fractured Reservoirs, 3rd Edition. Gulf Professional, Boston, USA.

Newman, G. H., (February) 1973. Pore-Volume Compressibility of Consolidated, Friable, and Unconsolidated Reservoir Rocks under Hydrostatic Loading. Journal of Petroleum Technology 25 (2), 129–134. SPE–3835–PA, http://dx.doi.org/10.2118/3835-PA.

O'Brien, D. G., Larson Jr., R. T., Parham, R. C., et al., (February) 2012. Using Real-Time Downhole Microseismic To Evaluate Fracture Geometry for Horizontal Packer-Sleeve Completions in the Bakken Formation, Elm Coulee Field, Montana. SPE Production & Operations 27 (1), 27–43. SPE–139774–PA, http://dx.doi.org/10.2118/139774-PA.

Ozkan, E., Raghavan, R., Apaydin, O., (19–22 September) 2010. Modeling of Fluid Transfer from Shale Matrix to Fracture Network. Paper SPE-134830-MS presented at the presented at the SPE Annual Technical Conference and Exhibition, Florence, Italy. http://dx.doi.org/10.2118/134830-MS.

Palacio, J., Blasingame, T., (12–14 April) 1993. Decline-Curve Analysis With Type Curves – Analysis of Gas Well Production Data. Paper SPE-25909-MS presented at the SPE Joint Rocky Mountain Regional and Low Permeability Reservoirs Symposium, Denver, Colorado, USA. http://dx.doi.org/10.2118/25909-MS.

Parmar, J., Dehghanpour, H., Kuru, E., (30 October–1 November) 2012. Unstable Displacement: A Missing Factor in Fracturing Fluid Recovery. Paper SPE-162649-MS presented at the SPE Canadian Unconventional Resources Conference, Calgary, Alberta, Canada. http://dx.doi.org/10.2118/162649-MS.

Parmar, J., Dehghanpour, H., Kuru, E., (March) 2014. Displacement of Water by Gas in Propped Fractures: Combined effects of Gravity, Surface Tension, and Wettability. Journal of Unconventional Oil and Gas Resources 5, 10–21., http://dx.doi.org/10.1016/j.juogr.2013.11.005.

Purvis, R. A., Bober, W. G., (July–September) 1979. A Reserves Review of the Pembina Cardium Oil Pool. J. Can. Pet. Technol. 18 (3), 20–34. SPE–79–03–02, http://dx.doi.org/10.2118/79-03-02.

Quirk, D., Ziarani, A. S., Mills, S., et al., (8–10 October) 2012. Integration of Microseismic Data, Fracture and Reservoir Simulation into the Development of Fractured Horizontal

Wells in the Cardium Formation – A Tight Oil Case Study. Paper SPE-160002-MS presented at the SPE Annual Technical Conference and Exhibition, San Antonio, Texas, USA. http://dx.doi.org/10.2118/160002-MS.

Raghavan, R., (August) 1976. Well Test Analysis: Wells Producing by Solution Gas Drive. SPE Journal 16 (4), 196–208, http://dx.doi.org/10.2118/5588-PA.

Roberts, J., (October) 2009. Gas Fuels Proppant Prospects. Industrial Minerals, 37–43.http://victorynickel.ca/_resources/SF_Proppants_1109.pdf (last accessed 10-01-2017).

Rogers, S., Elmo, D., Dunphy, R., et al., (19–21 October) 2010. Understanding Hydraulic Fracture Geometry and Interactions in the Horn River Basin Through DFN and Numerical Modeling. Paper SPE-137488-MS presented at the SPE Canadian Unconventional Resources and International Petroleum Conference, Calgary, Alberta, Canada. http://dx.doi.org/10.2118/137488-MS.

Sawabini, C. T., Chilingar, G. V., Allen, D. R., (April) 1973. Compressibility of Unconsolidated, Arkosic Oil Sands. SPE Journal 14 (2), 132–138. SPE–4058–PA, http://dx.doi.org/10.2118/4058-PA.

Siddiqui, S., Ali, A., Dehghanpour, H., (30 October–1 November) 2012. New Advances in Production Data Analysis of Hydraulically Fractured Tight Reservoirs. Paper SPE-162830-MS presented at the SPE Canadian Unconventional Resources Conference, Calgary, Alberta, Canada. http://dx.doi.org/10.2118/162830-MS.

Soliman, Y. M., Anash, J., Stephenson, S., et al., (30 September–3 October) 2001. Application of Wavelet Transform to Analysis of Pressure Transient Data. Paper SPE-71571-MS presented at the SPE Annual Technical Conference and Exhibition, New Orleans, Louisiana, USA. http://dx.doi.org/10.2118/71571-MS.

Song, B., Economides, M. J., Ehlig-Economides, C., (24–26 January) 2011. Design of Multiple Transverse Fracture Horizontal Wells in Shale Gas Reservoirs. Paper SPE-140555-MS presented at the SPE Hydraulic Fracturing Technology Conference held in The Woodlands, Texas, USA. http://dx.doi.org/10.2118/140555-MS.

Stanislav, J., Easwaran, G., Kokal, S., (September – October) 1987. Analytical Solutions for Vertical Fractures in a Composite System. J. Cdn. Pet. Tech. 26 (5), 51–56. PET–SOC–87–05–04–P, http://dx.doi.org/10.2118/87-05-04.

Stehfest, H., (January) 1970. Algorithm 358 – Numerical Inversion of Laplace Transforms. Comm. ACM 13 (1), 47–49.

Stopa, J., Nawrat, S., (August) 2012. Computer Modeling of Coal Bed Methane Recovery in Coal Mines. J. Energy Resour. Technol 134 (3), 03280401–03280411, http://dx.doi.org/10.1115/1.4007003.

Stright Jr., D. H., Gordon, J. I., (14–16 March) 1983. Decline Curve Analysis in Fractured Low Permeability Gas Wells in the Piceance Basin. Paper SPE-11640-MS presented at the SPE/DOE Low Permeability Gas Reservoirs Symposium, Denver, Colorado. http://dx.doi.org/10.2118/11640-MS.

Sullivan, R., Woodroof, R., Steinberger-Glaser, A., et al., (26–29 September) 2004. Optimizing Fracturing Fluid Cleanup in the Bossier Sand Using Chemical Frac Tracers and Aggressive Gel Breaker Deployment. Paper SPE-90030-MS presented at the SPE Annual Technical Conference and Exhibition, Houston, Texas, USA. http://dx.doi.org/10.2118/90030-MS.

Taal-van Koppen, J. K. J., 2008. A Multi-Scale Case Study of Natural Fracture Systems in Outcrops and Boreholes with Applications to Reservoir Modelling. Ph.D. thesis, Delft University of Technology, Delft, The Netherlands, (September 2008).

Tivayanonda, V., 2012. A Triple-Porosity Model for Fractured Horizontal Wells. Master's thesis, Texas A & M University, College Station, Texas, USA, (August 2012).

Tivayanonda, V., Apiwathanasorn, S., Ehlig-Economides, C., et al., (8–10 October) 2012. Alternative Interpretations of Shale Gas/Oil Rate Behaviour Using Triple Porosity Model. Paper SPE-159703-MS presented at the SPE Annual Technical Conference and Exhibition held in San Antonio, Texas, USA. http://dx.doi.org/10.2118/159703-MS.

Tranter, C. J., 1966. Integral Transforms in Mathematical Physics. Methuen & Co. Ltd., London.

Van Everdingen, A. F., Hurst, W., (December) 1949. The Application of the Laplace Transformation to Flow Problems in Reservoirs. J. Pet. Tech. 1 (12), 305–324. SPE–949305–G, http://dx.doi.org/10.2118/949305-G.

Virués, C., Chin, A., Anderson, D., (11–13 November) 2013. Application of Rate Transient Analysis Workflow in Unconventional Reservoirs: Horn River Shale Gas Case Study.

Paper SPE-167042-MS presented at the SPE Unconventional Resources Conference & Exhibition - Asia Pacific held in Brisbane, Australia. http://dx.doi.org/10.2118/167042-MS.

Warren, J. E., Root, P. J., (September) 1963. The Behavior of Naturally Fractured Reservoirs. SPE Journal 3 (3), 245–255. SPE–426–PA, http://dx.doi.org/10.2118/426-PA.

Wattenbarger, R. A., El-Banbi, A. H., Villegas, M., et al., (5–8 April) 1998. Production Analysis of Linear Flow into Fractured Tight Gas Wells. Paper SPE-39931-MS presented at the SPE Rocky Mountain Regional/Low-Permeability Reservoirs Symposium, Denver, Colorado, USA. http://dx.doi.org/10.2118/39931-MS.

Wattenbarger, R. A., Maggard, J. B., El-Banbi, A. H., (May) 1996. Quarterly Reports for Reservoir Modelling Consortium. Texas A & M University, College Station.

Weiss, J. N., (September) 1997. The Hill Equation Revisited: Uses and Misuses. FASEB J. 11 (11), 835–841.

Willberg, D. M., Steinsberger, N., Hoover, R., et al., (5–8 April) 1998. Optimization of Fracture Cleanup Using Flowback Analysis. Paper SPE-39920-MS presented at the SPE Rocky Mountain Regional Low Permeability Reservoirs Symposium & Exhibition, Denver, Colorado, USA. http://dx.doi.org/10.2118/39920-MS.

Williams-Kovacs, J. D., Clarkson, C. R., (5–7 November) 2013a. Stochastic Modeling of Multi-Phase Flowback from Multi-Fractured Horizontal Tight Oil Wells. Paper SPE-167232-MS presented at the SPE Canadian Unconventional Resources Conference, Calgary, Alberta, Canada. http://dx.doi.org/10.2118/167232-MS.

Williams-Kovacs, J. D., Clarkson, C. R., (10–12 April) 2013b. Stochastic Modeling of Two-Phase Flowback of Multi-Fractured Horizontal Wells to Estimate Hydraulic Fracture Properties and Forecast Production. Paper SPE-164550-MS presented at the SPE Unconventional Resources Conference, The Woodlands, Texas, USA. http://dx.doi.org/10.2118/164550-MS.

Woodroof, R. A. J., Asadi, M., Warren, M. N., (13–14 May) 2003. Monitoring Fracturing Fluid Flowback and Optimizing Fracturing Fluid Cleanup Using Chemical Frac Tracers. Paper SPE-82221-MS presented at the SPE European Formation Damage Conference, The Hague, Netherlands. http://dx.doi.org/10.2118/82221-MS.

Wu, Y. S., Liu, H. H., Bodvarsson, G. S., (September) 2004. A Triple-Continuum Approach for Modeling Flow and Transport Processes in Fractured Rock. Journal of Contaminant Hydrology 73 (1–4), 145–179, http://dx.doi.org/10.1016/j.jconhyd.2004.01.002.

Xu, Y., Adefidipe, O. A., Dehghanpour, H., (July) 2015. Estimating Fracture Volume Using Flowback Data from the Horn River Basin: A Material Balance Approach. Journal of Natural Gas Science and Engineering 25, 253–270, http://dx.doi.org/10.1016/j.jngse.2015.04.036.

Yoon, J. S., Zimmermann, G., Zang, A., (December) 2014. Numerical Investigation on Stress Shadowing in Fluid Injection–Induced Fracture Propagation in Naturally Fractured Geothermal Reservoirs. Rock Mechanics and Rock Engineering, 1–16.http://dx.doi.org/10.1007/s00603-014-0695-5.

Yue, M., Leung, J., Dehghanpour, H., (5–7 November) 2013. Integration of Numerical Simulations for Uncertainty Analysis of Transient Flow Responses in Heterogeneous Tight Reservoirs . Paper SPE-167174-MS presented at the Canadian Unconventional Resources & International Petroleum Conference, Calgary, Alberta, Canada. http://dx.doi.org/10.2118/167174-MS.

Zahid, S., Bhatti, A. A., Khan, H. A., et al., (31 March–3 April) 2007. Development of Unconventional Gas Resources: Stimulation Perspective. Paper SPE-107053-MS presented at the SPE Production & Operations Symposium, Oklahoma City, Oklahoma, USA. http://dx.doi.org/10.2118/107053-MS.

Zhou, Q., Dilmore, R., Kleit, A., et al., (May) 2016. Evaluating Fracture-Fluid Flowback in Marcellus Using Data-Mining Technologies. SPE Production & Operations 31 (2), 132–138. SPE–173364–PA, http://dx.doi.org/10.2118/173364-PA.

Zolfaghari, A., Dehghanpour, H., Ghanbari, E., et al., (February) 2016. Fracture Characterization Using Flowback Salt-Concentration Transient. SPE Journal 21 (1), 233–244. SPE–168598–PA, http://dx.doi.org/10.2118/168598-PA.

Appendix A

Flowback Analysis Model: Variable Terminal Flowing Rate

A.1 Fluid Flow Equations

Matrix

$$\frac{\partial^2 \Delta P_m}{\partial x^2} = \frac{\mu(\phi c_t)_m}{k_m} \frac{\partial \Delta P_m}{\partial t} \tag{A.1}$$

$$\Delta P_m(x,\ 0) = 0 \tag{A.2}$$

$$\Delta P_m\Big|_{x=\frac{L_F}{2}} = \Delta P_{_F}\Big|_{x=\frac{L_F}{2}} \tag{A.3}$$

$$\left.\frac{\partial \Delta P_m}{\partial x}\right|_{x=0} = 0 \tag{A.4}$$

Hydraulic-Fracture

$$k_{_F} k_{r_{HC}}(t) \frac{\partial^2 \Delta P_{_F}}{\partial y^2} = \mu(\phi c_t)_{_F} \frac{\partial \Delta P_{_F}}{\partial t} + \frac{k_m}{L_{_F}/2} \left.\frac{\partial \Delta P_m}{\partial x}\right|_{x=\frac{L_F}{2}} \tag{A.5}$$

$$\text{where } k_{r_{HC}}(t) = \begin{cases} \beta_2 \exp(\beta_3 t) & 0 \le t \le t_{inf} \\ \dfrac{\beta_1}{1+\beta_2 \exp(-\beta_3 t)} & t > t_{inf} \end{cases} \tag{A.6}$$

$$\Delta P_{_F}(y,\ 0) = 0 \tag{A.7}$$

$$q(t) = -\frac{k_{_F} k_{r_{HC}}(t) A_{cw}}{\mu} \left.\frac{\partial \Delta P_{_F}}{\partial y}\right|_{y=0} \tag{A.8}$$

$$\left.\frac{\partial \Delta P_{_F}}{\partial y}\right|_{y=y_e} = 0 \tag{A.9}$$

It is important to note that $k_{r_{HC}}(t)$ is a piecewise continuous function. The shifting technique is required to appropriately represent it in the most suitable form for Laplace transform. However, the application of this technique will make the equations near impossible to solve analytically. One reason for this is that there is no explicit relationship of Pressure as a function of time. Hence, these equations are solved independently for the pre-inflexion and post-inflexion parts. This is done in such a way that they are linked with t_{inf} which serves as a switch. This is just an approximate solution. One way to ensure that this solution does not violate the physics of fluid flow during flowback is to test its convergence to existing single-phase models (see Subsection 3.3.4).

A.2 Dimensionless Transformations

$$x_{_D} = \frac{x}{L_{_F}/2} \tag{A.10}$$

$$y_{_D} = \frac{y}{\sqrt{A_{cw}}} \tag{A.11}$$

$$A_{cw} = 2 \times X_e \times h \tag{A.12}$$

$$X_e \approx L_w \tag{A.13}$$

$$y_{_{De}} = \frac{y_e}{\sqrt{A_{cw}}} \tag{A.14}$$

$$t_{_{D_{AC}}} = \frac{k_{_F} t}{(\phi c_t)_t \mu A_{cw}} \tag{A.15}$$

$$P_{_{DL}} = \frac{k_{_F}\sqrt{A_{cw}}\Delta P_\tau}{q(t)\mu} \tag{A.16}$$

$$\Delta P_\tau = P_i - P_\tau;\ _{\forall \tau = m,\, F} \tag{A.17}$$

$$\omega_{_F} = \frac{(\phi c_t)_{_F}}{(\phi c_t)_t} \tag{A.18}$$

$$\omega_m = \frac{(\phi c_t)_m}{(\phi c_t)_t} \tag{A.19}$$

$$\omega_m + \omega_{_F} = 1 \tag{A.20}$$

$$\alpha_{_{Fm}} = \frac{T_{_{Fm}}}{l_{_{Fm}}} \tag{A.21}$$

$$\lambda_{_{AC,Fm}} = \frac{\alpha_{_{Fm}} k_m}{k_{_F}} A_{cw} = \frac{12}{L_{_F}^2} \frac{k_m}{k_{_F}} A_{cw} \tag{A.22}$$

A.3 Dimensionless Procedure

This section offers an explanation for the dimensionless approximation applied to obtain subsequent dimensionless equations. It is a fact that from Eq. A.16,

$$\frac{\partial P_{_{DL}}}{\partial t} = \frac{k_{_F}\sqrt{A_{cw}}}{q(t)\mu} \frac{\partial \Delta P_\tau}{\partial t} - \frac{k_{_F}\sqrt{A_{cw}} \Delta P_\tau}{q(t)^2 \mu} \frac{\partial q(t)}{\partial t} \tag{A.23}$$

From field data, hydrocarbon flow rate, q(t) can be approximated by

$$q(t) \approx q_o exp^{-bt} \tag{A.24}$$

$$\text{where } \; q_o \gg b \; \text{ and } \; b \ll t$$

Substituting for Eq. A.24, the second term on the right hand side (RHS) of Eq. A.23 becomes negligible compared to the first term on the RHS (see Eq. A.24).

$$-\frac{1}{q(t)^2} \frac{\partial \Delta q(t)}{\partial t} = \frac{b}{q_o} exp^{-bt} \tag{A.25}$$

$$\text{where } \; exp^{-bt} \longrightarrow 1 \; \text{ and } \; \frac{b}{q_o} \ll 0.0001$$

Applying the understanding from Eq. A.24, Eq. A.23 can be approximated as

$$\frac{\partial P_{_{DL}}}{\partial t} \approx \frac{k_{_F}\sqrt{A_{cw}}}{q(t)\mu} \frac{\partial \Delta P_\tau}{\partial t} \tag{A.26}$$

A.4 Dimensionless Flow Equations

Matrix

$$\frac{\partial^2 P_{_{DLm}}}{\partial {x_{_D}}^2} = \frac{3\omega_m}{\lambda_{_{AC,Fm}}} \frac{\partial P_{_{DLm}}}{\partial t_{_{D_{AC}}}} \tag{A.27}$$

$$P_{_{DLm}}(x_{_D},\ 0) = 0 \tag{A.28}$$

$$P_{_{DLm}}\Big|_{x_{_D}=1} = P_{_{DLF}}\Big|_{x_{_D}=1} \tag{A.29}$$

$$\frac{\partial P_{_{DLm}}}{\partial x_{_D}}\bigg|_{x_{_D}=0} = 0 \tag{A.30}$$

Taking Laplace Transforms of Matrix Equations

$$\frac{\partial^2 \overline{P}_{_{DLm}}}{\partial {x_{_D}}^2} - \frac{3s\omega_m}{\lambda_{_{AC,Fm}}} \overline{P}_{_{DLm}} = 0 \tag{A.31}$$

$$\overline{P}_{_{DLm}} = A\cosh\left(\sqrt{\frac{3s\omega_m}{\lambda_{_{AC,Fm}}}}x_{_D}\right) + B\sinh\left(\sqrt{\frac{3s\omega_m}{\lambda_{_{AC,Fm}}}}x_{_D}\right) \tag{A.32}$$

Applying Eq. A.29 and Eq. A.30 to Eq. A.32 results in

$$\overline{P}_{_{DLm}} = \overline{P}_{_{DLF}}\Big|_{x_{_D}=1} \times \frac{\cosh\left(\sqrt{f_m(s)}x_{_D}\right)}{\cosh\left(\sqrt{f_m(s)}\right)} \tag{A.33}$$

$$\text{Where } f_m(s) = \frac{3s\omega_m}{\lambda_{_{AC,Fm}}} \tag{A.34}$$

Hydraulic-Fracture

$$\frac{\partial^2 P_{_{DLF}}}{\partial {y_{_D}}^2} = \begin{cases} \dfrac{\exp(-\beta_3^* t_{_{D_{AC}}})}{\beta_2}\left(\omega_{_F}\dfrac{\partial P_{_{DLF}}}{\partial t_{_{D_{AC}}}} + \dfrac{\lambda_{_{AC,Fm}}}{3}\dfrac{\partial P_{_{DLm}}}{\partial x_{_D}}\bigg|_{x_{_D}=1}\right) & 0 \le t_{_{D_{AC}}} \le t_{_{D_{AC}inf}} \\ \dfrac{1+\beta_2\exp(-\beta_3^{**} t_{_{D_{AC}}})}{\beta_1}\left(\omega_{_F}\dfrac{\partial P_{_{DLF}}}{\partial t_{_{D_{AC}}}} + \dfrac{\lambda_{_{AC,Fm}}}{3}\dfrac{\partial P_{_{DLm}}}{\partial x_{_D}}\bigg|_{x_{_D}=1}\right) & t_{_{D_{AC}}} > t_{_{D_{AC}inf}} \end{cases} \tag{A.35}$$

$$\text{For pre-inflexion, } \beta_3^* = \beta_3 \times \frac{(\phi c_t)_t \mu A_{cw}}{k_{_F}} \tag{A.36}$$

$$\text{For post-inflexion, } \beta_3^{**} = \beta_3 \times \frac{(\phi c_t)_t \mu A_{cw}}{k_{_F}} \tag{A.37}$$

$$P_{_{DLF}}(y_{_D},\ 0) = 0 \tag{A.38}$$

$$\left.\frac{\partial P_{_{DLF}}}{\partial y_{_D}}\right|_{y_D=0} = \begin{cases} -\dfrac{\exp(-\beta_3^* t_{_{D_{AC}}})}{\beta_2} & 0 \le t_{_{D_{AC}}} \le t_{_{D_{AC}inf}} \\ -\dfrac{1+\beta_2\exp(-\beta_3^{**} t_{_{D_{AC}}})}{\beta_1} & t_{_{D_{AC}}} > t_{_{D_{AC}inf}} \end{cases} \tag{A.39}$$

$$\left.\frac{\partial P_{_{DLF}}}{\partial y_{_D}}\right|_{y_D=y_{De}} = 0 \tag{A.40}$$

Taking Laplace Transforms of Hydraulic-Fracture Equations

$$\frac{\partial^2 \overline{P}_{_{DLF}}(s)}{\partial {y_{_D}}^2} = \begin{cases} \dfrac{1}{\beta_2}\left[\omega_{_F}(s+\beta_3^*)\overline{P}_{_{DLF}}(s+\beta_3^*) + \dfrac{\lambda_{_{AC,Fm}}}{3}\left.\dfrac{\partial \overline{P}_{_{DLm}}(s+\beta_3^*)}{\partial x_{_D}}\right|_{x_D=1}\right] & 0 \le t_{_{D_{AC}}} \le t_{_{D_{AC}inf}} \\ \dfrac{1}{\beta_1}\left(\omega_{_F}\left[s\overline{P}_{_{DLF}}(s) + \beta_2(s+\beta_3^{**})\overline{P}_{_{DLF}}(s+\beta_3^{**})\right] + \dfrac{\lambda_{_{AC,Fm}}}{3}\right. & \\ \left.\left[\left.\dfrac{\partial \overline{P}_{_{DLm}}(s)}{\partial x_{_D}}\right|_{x_D=1} + \beta_2\left.\dfrac{\partial \overline{P}_{_{DLm}}(s+\beta_3^{**})}{\partial x_{_D}}\right|_{x_D=1}\right]\right) & t_{_{D_{AC}}} > t_{_{D_{AC}inf}} \end{cases} \tag{A.41}$$

$$\left.\frac{\partial \overline{P}_{_{DLF}}}{\partial y_{_D}}\right|_{y_D=0} = -f^*(s) \tag{A.42}$$

$$\text{where } f^*(s) = \begin{cases} \dfrac{1}{\beta_2}\left[\dfrac{1}{(s+\beta_3^*)}\right] & 0 \le t_{_{D_{AC}}} \le t_{_{D_{AC}inf}} \\ \dfrac{1}{\beta_1}\left[\dfrac{1}{s} + \dfrac{\beta_2}{(s+\beta_3^{**})}\right] & t_{_{D_{AC}}} > t_{_{D_{AC}inf}} \end{cases} \tag{A.43}$$

$$\left.\frac{\partial \overline{P}_{DLF}}{\partial y_D}\right|_{y_D=y_{De}} = 0 \tag{A.44}$$

Differentiating Eq. A.33 results in

$$\left.\frac{\partial \overline{P}_{DLm}}{\partial x_D}\right|_{x_D=1} = \overline{P}_{DLF} \times \sqrt{f_m(s)} \times \tanh\left(\sqrt{f_m(s)}\right) \tag{A.45}$$

Provided $\overline{P}_{DLF}(s) \approx \overline{P}_{DLF}(s+\beta_3^*)$ or $\overline{P}_{DLF}(s+\beta_3^{**})$

Eq. A.41 becomes

$$\frac{\partial^2 \overline{P}_{DLF}}{\partial y_D^{\,2}} - f(s)\overline{P}_{DLF} = 0 \tag{A.46}$$

$$\text{where } f(s) = \begin{cases} \dfrac{1}{\beta_2}\left[\omega_F(s+\beta_3^*) + \dfrac{\lambda_{AC,Fm}}{3}\sqrt{f_m(s+\beta_3^*)}\tanh\left(\sqrt{f_m(s+\beta_3^*)}\right)\right] & 0 \le t_{D_{AC}} \le t_{D_{AC\,inf}} \\ \dfrac{1}{\beta_1}\left(\omega_F\left[s+\beta_2(s+\beta_3^{**})\right] + \dfrac{\lambda_{AC,Fm}}{3}\left[\sqrt{f_m(s)}\tanh\left(\sqrt{f_m(s)}\right) + \right.\right. & \\ \left.\left.\beta_2\sqrt{f_m(s+\beta_3^{**})}\tanh\left(\sqrt{f_m(s+\beta_3^{**})}\right)\right]\right) & t_{D_{AC}} > t_{D_{AC\,inf}} \end{cases} \tag{A.47}$$

Solving Eq. A.46 results in

$$\overline{P}_{DLF} = A\,\exp\left(\sqrt{f(s)}y_D\right) + B\,\exp\left(-\sqrt{f(s)}y_D\right) \tag{A.48}$$

Differentiating Eq. A.48 results in

$$\frac{\partial \overline{P}_{DLF}}{\partial y_D} = \sqrt{f(s)}\left[A\,\exp\left(\sqrt{f(s)}y_D\right) - B\,\exp\left(-\sqrt{f(s)}y_D\right)\right] \tag{A.49}$$

Applying Eq. A.42 and Eq. A.44 to Eq. A.49 results in

$$-\frac{f^*(s)}{\sqrt{f(s)}} = A - B \tag{A.50}$$

and

$$A = B\ \exp\left(-2\sqrt{f(s)}y_{_{De}}\right) \tag{A.51}$$

Putting Eq. A.51 into Eq. A.50 results in

$$B = \frac{f^*(s)}{\sqrt{f(s)}}\left\{\frac{1}{\left[1 -\ \exp\left(-2\sqrt{f(s)}y_{_{De}}\right)\right]}\right\} \tag{A.52}$$

Putting Eq. A.52 into Eq. A.51 results in

$$A = \frac{f^*(s)}{\sqrt{f(s)}}\left\{\frac{\exp\left(-2\sqrt{f(s)}y_{_{De}}\right)}{\left[1 -\ \exp\left(-2\sqrt{f(s)}y_{_{De}}\right)\right]}\right\} \tag{A.53}$$

Substituting Eq. A.52 and Eq. A.53 into Eq. A.48 and incorporating convergence skin (Bello, 2009; Ezulike and Igbokoyi, 2012) results in

$$\overline{P}_{_{wDL}} = \overline{P}_{_{DLF}}\Big|_{y_{_D}=0} = \frac{f^*(s)}{\sqrt{f(s)}}\left\{\left[\frac{1 +\ \exp\left(-2\sqrt{f(s)}y_{_{De}}\right)}{1 -\ \exp\left(-2\sqrt{f(s)}y_{_{De}}\right)}\right] + I_{_D}\sqrt{f(s)}\right\} \tag{A.54}$$

$$I_{_D} = \frac{r_w}{\sqrt{A_{cw}}}I \tag{A.55}$$

$$\overline{P}_{_{wDL}} = \frac{f^*(s)}{\sqrt{f(s)}}\left\{\coth\left(\sqrt{f(s)}y_{_{De}}\right) + I_{_D}\sqrt{f(s)}\right\} \tag{A.56}$$

Appendix B

Quadrilinear Flow Model: Constant Terminal Flowing Rate Case

B.1 Dimensionless Transformations

$$x_{_D} = \frac{x}{L_{_F}/2} \tag{B.1}$$

$$x^*_{_D} = \frac{x^*}{L_{_F}/2} \tag{B.2}$$

$$y_{_D} = \frac{y}{\sqrt{A_{cw}}} \tag{B.3}$$

$$y^*_{_D} = \frac{y^*}{L_f/2} \tag{B.4}$$

$$A_{cw} = 2 \times X_e \times h \tag{B.5}$$

$$X_e \approx L_w \tag{B.6}$$

$$y_{_{De}} = \frac{y_e}{\sqrt{A_{cw}}} \tag{B.7}$$

$$t_{_{D_{AC}}} = \frac{k_{_F} t}{(\phi c_t)_t \mu A_{cw}} \tag{B.8}$$

$$P_{_{DL}} = \frac{k_{_F}\sqrt{A_{cw}}\Delta P_\tau}{q\mu} \tag{B.9}$$

$$\Delta P_\tau = P_i - P_\tau;\ _{\forall\, \tau = m,\, f,\, F} \tag{B.10}$$

$$\omega_{_F} = \frac{(\phi c_t)_F}{(\phi c_t)_t} \tag{B.11}$$

$$\omega_f = \frac{(\phi c_t)_f}{(\phi c_t)_t} \tag{B.12}$$

$$\omega_m = \frac{(\phi c_t)_m}{(\phi c_t)_t} \tag{B.13}$$

$$\omega_{_1} = \frac{(\phi c_t)_{m_1}}{(\phi c_t)_m} \tag{B.14}$$

$$\omega_{_2} = \frac{(\phi c_t)_{m_2}}{(\phi c_t)_m} \tag{B.15}$$

$$\omega_{_1} + \omega_{_2} = 1 \tag{B.16}$$

$$\omega_m + \omega_f + \omega_{_F} = 1 \tag{B.17}$$

$$\alpha_{fm} = \frac{S_{a,fm}}{l_{fm}} \tag{B.18}$$

$$\alpha_{_{Fm}} = \frac{S_{a,_{Fm}}}{l_{_{Fm}}} \tag{B.19}$$

$$\alpha_{_{Ff}} = \frac{S_{a,_{Ff}}}{l_{_{Ff}}} \tag{B.20}$$

$$\lambda_{_{AC,fm}} = \frac{\alpha_{fm} k_{m_1}}{k_{_F}} A_{cw} = \frac{12}{L_f^2} \frac{k_{m_1}}{k_{_F}} A_{cw} \tag{B.21}$$

$$\lambda_{_{AC,_{Fm}}} = \frac{\alpha_{_{Fm}} k_{m_2}}{k_{_F}} A_{cw} = \frac{12}{L_{_F}^2} \frac{k_{m_2}}{k_{_F}} A_{cw} \tag{B.22}$$

$$\lambda_{_{AC,_{Ff}}} = \frac{\alpha_{_{Ff}} k_f}{k_{_F}} A_{cw} = \frac{12}{L_{_F}^2} \frac{k_f}{k_{_F}} A_{cw} \tag{B.23}$$

B.2 Dimensionless Flow Equations

Matrix Equations

$$\frac{\partial^2 P_{_{DLm_1}}}{\partial y_{_D}^{*\,2}} = \frac{3\omega_{_1}\omega_m}{\lambda_{_{AC,fm}}} \frac{\partial P_{_{DLm_1}}}{\partial t_{_{D_{AC}}}} \tag{B.24}$$

$$P_{DLm_1}(y^*_D,\ 0) = 0 \tag{B.25}$$

$$P_{DLm_1}\Big|_{y^*_D=1} = P_{DLf}\Big|_{y^*_D=1} \tag{B.26}$$

$$\frac{\partial P_{DLm_1}}{\partial y^*_D}\bigg|_{y^*_D=0} = 0 \tag{B.27}$$

$$\frac{\partial^2 P_{DLm_2}}{\partial {x^*_D}^2} = \frac{3\omega_2\omega_m}{\lambda_{AC,Fm}}\frac{\partial P_{DLm_2}}{\partial t_{D_{AC}}} \tag{B.28}$$

$$P_{DLm_2}(x^*_D,\ 0) = 0 \tag{B.29}$$

$$P_{DLm_2}\Big|_{x^*_D=1} = P_{DLF}\Big|_{x^*_D=1} \tag{B.30}$$

$$\frac{\partial P_{DLm_2}}{\partial x^*_D}\bigg|_{x^*_D=0} = 0 \tag{B.31}$$

Taking Laplace Transforms of Matrix Equations

$$\frac{\partial^2 \overline{P}_{DLm_1}}{\partial {y^*_D}^2} - \frac{3\omega_1\omega_m}{\lambda_{AC,fm}} s\overline{P}_{DLm_1} = 0 \tag{B.32}$$

Applying Eq. B.26 and Eq. B.27 results in

$$\overline{P}_{DLm_1} = \overline{P}_{DLf}\Big|_{y^*_D=1} \times \frac{\cosh\left(\sqrt{\frac{3s\omega_1\omega_m}{\lambda_{AC,fm}}}\, y^*_D\right)}{\cosh\left(\sqrt{\frac{3s\omega_1\omega_m}{\lambda_{AC,fm}}}\right)} \tag{B.33}$$

$$\overline{P}_{DLm_2} = \overline{P}_{DLF}\Big|_{x^*_D=1} \times \frac{\cosh\left(\sqrt{\frac{3s\omega_2\omega_m}{\lambda_{AC,Fm}}}\, x^*_D\right)}{\cosh\left(\sqrt{\frac{3s\omega_2\omega_m}{\lambda_{AC,Fm}}}\right)} \tag{B.34}$$

Micro-Fracture Equations

$$\frac{\partial^2 P_{DLf}}{\partial {x_D}^2} = \frac{3\omega_f}{\lambda_{AC,Ff}} \frac{\partial P_{DLf}}{\partial t_{D_{AC}}} + \frac{\lambda_{AC,fm}}{\lambda_{AC,Ff}} \frac{\partial P_{DLm_1}}{\partial y_D^*}\bigg|_{y_D^*=1} \tag{B.35}$$

$$P_{DLf}(x_D,\ 0) = 0 \tag{B.36}$$

$$P_{DLf}\Big|_{x_D=1} = P_{DLF}\Big|_{x_D=1} \tag{B.37}$$

$$\frac{\partial P_{DLf}}{\partial x_D}\bigg|_{x_D=0} = 0 \tag{B.38}$$

Taking Laplace Transforms of Micro-Fracture Equations

$$\frac{\partial^2 \overline{P}_{DLf}}{\partial {x_D}^2} = \frac{3\omega_f}{\lambda_{AC,Ff}} s\overline{P}_{DLf} + \frac{\lambda_{AC,fm}}{\lambda_{AC,Ff}} \frac{\partial \overline{P}_{DLm_1}}{\partial y_D^*}\bigg|_{y_D^*=1} \tag{B.39}$$

Differentiating Eq. B.33 and applying Eq. B.37 and Eq. B.38 results in

$$\frac{\partial^2 \overline{P}_{DLf}}{\partial {x_D}^2} - s f_f(s) \overline{P}_{DLf} = 0 \tag{B.40}$$

$$\text{where } f_f(s) = \left\{ \frac{3\omega_f}{\lambda_{AC,Ff}} + \frac{\lambda_{AC,fm}}{s\lambda_{AC,Ff}} \sqrt{\frac{3s\omega_1\omega_m}{\lambda_{AC,fm}}}\ tanh\left(\sqrt{\frac{3s\omega_1\omega_m}{\lambda_{AC,fm}}}\right)\right\} \tag{B.41}$$

Solving Eq. B.40 and applying Eq. B.37 and Eq. B.38 results in

$$\overline{P}_{DLf} = \overline{P}_{DLF} \times \frac{\cosh\left(\sqrt{s f_f(s)} x_D\right)}{\cosh\left(\sqrt{s f_f(s)}\right)} \tag{B.42}$$

Hydraulic-Fracture Equations

$$\frac{\partial^2 P_{DLF}}{\partial {y_D}^2} = \omega_F \frac{\partial P_{DLF}}{\partial t_{D_{AC}}} + \frac{\lambda_{AC,Ff}}{3} \frac{\partial P_{DLf}}{\partial x_D}\bigg|_{x_D=1} + \frac{\lambda_{AC,Fm}}{3} \frac{\partial P_{DLm_2}}{\partial {x_D}^*}\bigg|_{x_D^*=1} \tag{B.43}$$

$$P_{DLF}(y_D,\ 0) = 0 \tag{B.44}$$

$$\left.\frac{\partial P_{DLF}}{\partial y_D}\right|_{y_D=0} = -1 \tag{B.45}$$

$$\left.\frac{\partial P_{DLF}}{\partial y_D}\right|_{y_D=y_{De}} = 0 \tag{B.46}$$

Taking Laplace Transforms of Hydraulic-Fracture Equations

$$\frac{\partial^2 \overline{P}_{DLF}}{\partial {y_D}^2} = \omega_F \left[s\overline{P}_{DLF} - P_{DLF}(y_D,\ 0)\right] + \frac{\lambda_{AC,Ff}}{3}\left.\frac{\partial \overline{P}_{DLf}}{\partial x_D}\right|_{x_D=1} + \frac{\lambda_{AC,Fm}}{3}\left.\frac{\partial \overline{P}_{DLm_2}}{\partial x_D^*}\right|_{x_D^*=1} \tag{B.47}$$

$$\left.\frac{\partial \overline{P}_{DLF}}{\partial y_D}\right|_{y_D=0} = -\frac{1}{s} \tag{B.48}$$

$$\left.\frac{\partial \overline{P}_{DLF}}{\partial y_D}\right|_{y_D=y_{De}} = 0 \tag{B.49}$$

Differentiating Eq. B.34 and Eq. B.42 and putting them into Eq. B.47 results in

$$\frac{\partial^2 \overline{P}_{DLF}}{\partial {y_D}^2} - sf(s)\overline{P}_{DLF} = 0 \tag{B.50}$$

$$\text{where } f_m(s) = \frac{3s\omega_2\omega_m}{\lambda_{AC,Fm}} \tag{B.51}$$

$$\text{and } f(s) = \omega_F + \frac{\lambda_{AC,Ff}}{3s}\sqrt{sf_f(s)}\ tanh\left(\sqrt{sf_f(s)}\right) + \frac{\lambda_{AC,Fm}}{3s}\sqrt{f_m(s)}\ tanh\left(\sqrt{f_m(s)}\right) \tag{B.52}$$

Solving Eq. B.50 and applying Eq. B.48 and Eq. B.49 results in

$$\overline{P}_{wDL} = \left.\overline{P}_{DLF}\right|_{y_D=0} = \frac{1}{s\sqrt{sf(s)}}\left[\frac{1+\ exp\left(-2\sqrt{sf(s)}y_{De}\right)}{1-\ exp\left(-2\sqrt{sf(s)}y_{De}\right)}\right] \tag{B.53}$$

$$\overline{P}_{wDL} = \frac{coth\left(\sqrt{sf(s)}y_{De}\right)}{s\sqrt{sf(s)}} \tag{B.54}$$

Appendix C

Quadrilinear Flow Model: Constant Terminal Flowing Pressure Case

C.1 Additional Dimensionless Transformations

$$P_{_{DL}} = \frac{P_i - P}{P_i - P_{wf}} \tag{C.1}$$

$$q_{_{DL}} = \frac{q(t)\mu}{k_{_F}\sqrt{A_{cw}}\,(P_i - P_{wf})} \tag{C.2}$$

C.2 Dimensionless Flow Equations

Matrix Equations

$$\frac{\partial^2 P_{_{DLm_1}}}{\partial {y^*_{_D}}^2} = \frac{3\omega_1\omega_m}{\lambda_{_{AC,fm}}}\frac{\partial P_{_{DLm_1}}}{\partial t_{_{D_{AC}}}} \tag{C.3}$$

$$P_{_{DLm_1}}(y^*_{_D},\ 0) = 0 \tag{C.4}$$

$$P_{_{DLm_1}}\Big|_{y^*_{_D}=1} = P_{_{DLf}}\Big|_{y^*_{_D}=1} \tag{C.5}$$

$$\left.\frac{\partial P_{_{DLm_1}}}{\partial y^*_{_D}}\right|_{y^*_{_D}=0} = 0 \tag{C.6}$$

$$\frac{\partial^2 P_{_{DLm_2}}}{\partial {x^*_{_D}}^2} = \frac{3\omega_2\omega_m}{\lambda_{_{AC,Fm}}}\frac{\partial P_{_{DLm_2}}}{\partial t_{_{D_{AC}}}} \tag{C.7}$$

$$P_{_{DLm_2}}(x^*_{_D},\ 0) = 0 \tag{C.8}$$

$$P_{DLm_2}\Big|_{x_D^*=1} = P_{DLF}\Big|_{x_D^*=1} \tag{C.9}$$

$$\frac{\partial P_{DLm_2}}{\partial x_D^*}\bigg|_{x_D^*=0} = 0 \tag{C.10}$$

Taking Laplace Transforms of Matrix Equations

$$\frac{\partial^2 \overline{P}_{DLm_1}}{\partial {y_D^*}^2} - \frac{3\omega_1\omega_m}{\lambda_{AC,fm}} s\overline{P}_{DLm_1} = 0 \tag{C.11}$$

$$\overline{P}_{DLm_1} = A\cosh\left(\sqrt{\frac{3s\omega_1\omega_m}{\lambda_{AC,fm}}}y_D^*\right) + B\sinh\left(\sqrt{\frac{3s\omega_1\omega_m}{\lambda_{AC,fm}}}y_D^*\right) \tag{C.12}$$

Applying Eq. C.5 and Eq. C.6 to Eq. C.12 results in

$$\overline{P}_{DLm_1} = \overline{P}_{DLf}\Big|_{y_D^*=1} \times \frac{\cosh\left(\sqrt{\frac{3s\omega_1\omega_m}{\lambda_{AC,fm}}}y_D^*\right)}{\cosh\left(\sqrt{\frac{3s\omega_1\omega_m}{\lambda_{AC,fm}}}\right)} \tag{C.13}$$

Similarly, from Eq. C.7

$$\overline{P}_{DLm_2} = \overline{P}_{DLF}\Big|_{x_D^*=1} \times \frac{\cosh\left(\sqrt{\frac{3s\omega_2\omega_m}{\lambda_{AC,Fm}}}x_D^*\right)}{\cosh\left(\sqrt{\frac{3s\omega_2\omega_m}{\lambda_{AC,Fm}}}\right)} \tag{C.14}$$

Micro-Fracture Equations

$$\frac{\partial^2 P_{DLf}}{\partial {x_D}^2} = \frac{3\omega_f}{\lambda_{AC,Ff}}\frac{\partial P_{DLf}}{\partial t_{D_{AC}}} + \frac{\lambda_{AC,fm}}{\lambda_{AC,Ff}}\frac{\partial P_{DLm_1}}{\partial y_D^*}\bigg|_{y_D^*=1} \tag{C.15}$$

$$P_{DLf}(x_D,\ 0) = 0 \tag{C.16}$$

$$P_{DLf}\Big|_{x_D=1} = P_{DLF}\Big|_{x_D=1} \tag{C.17}$$

$$\left.\frac{\partial P_{DLf}}{\partial x_D}\right|_{x_D=0} = 0 \tag{C.18}$$

Taking Laplace Transforms of Micro-Fracture Equations

$$\frac{\partial^2 \overline{P}_{DLf}}{\partial {x_D}^2} = \frac{3\omega_f}{\lambda_{AC,Ff}} s\overline{P}_{DLf} + \frac{\lambda_{AC,fm}}{\lambda_{AC,Ff}} \left.\frac{\partial \overline{P}_{DLm_1}}{\partial y_D^*}\right|_{y_D^*=1} \tag{C.19}$$

Differentiating Eq. C.13 and applying Eq. C.17 and Eq. C.18 results in

$$\overline{P}_{DLf} = \overline{P}_{DLF} \times \frac{\cosh\left(\sqrt{sf_f(s)}x_D\right)}{\cosh\left(\sqrt{sf_f(s)}\right)} \tag{C.20}$$

$$\text{where } f_f(s) = \left\{ \frac{3\omega_f}{\lambda_{AC,Ff}} + \frac{\lambda_{AC,fm}}{s\lambda_{AC,Ff}} \sqrt{\frac{3s\omega_1\omega_m}{\lambda_{AC,fm}}}\, tanh\left(\sqrt{\frac{3s\omega_1\omega_m}{\lambda_{AC,fm}}}\right) \right\} \tag{C.21}$$

Hydraulic-Fracture Equations

$$\frac{\partial^2 P_{DLF}}{\partial {y_D}^2} = \omega_F \frac{\partial P_{DLF}}{\partial t_{D_{AC}}} + \frac{\lambda_{AC,Ff}}{3} \left.\frac{\partial P_{DLf}}{\partial x_D}\right|_{x_D=1} + \frac{\lambda_{AC,Fm}}{3} \left.\frac{\partial P_{DLm_2}}{\partial x_D^*}\right|_{x_D^*=1} \tag{C.22}$$

$$P_{DLF}(y_D,\ 0) = 0 \tag{C.23}$$

$$P_{DLF}(0,\ t) = 1 \tag{C.24}$$

$$q_D = -\left.\frac{\partial P_{DLF}}{\partial y_D}\right|_{y_D=0} \tag{C.25}$$

$$\left.\frac{\partial P_{DLF}}{\partial y_D}\right|_{y_D=y_{De}} = 0 \tag{C.26}$$

Taking Laplace Transforms of Hydraulic-Fracture Equations

$$\frac{\partial^2 \overline{P}_{DLF}}{\partial {y_D}^2} = \omega_F \left[s\overline{P}_{DLF} - P_{DLF}(y_D,\ 0)\right] + \frac{\lambda_{AC,Ff}}{3} \left.\frac{\partial \overline{P}_{DLf}}{\partial x_D}\right|_{x_D=1} + \frac{\lambda_{AC,Fm}}{3} \left.\frac{\partial \overline{P}_{DLm_2}}{\partial x_D^*}\right|_{x_D^*=1} \tag{C.27}$$

$$\overline{P}_{DLF}(0,\ s) = \frac{1}{s} \tag{C.28}$$

$$\overline{q}_{_D} = -\left.\frac{\partial \overline{P}_{_{DLF}}}{\partial y_{_D}}\right|_{y_{_D}=0} \tag{C.29}$$

$$\left.\frac{\partial \overline{P}_{_{DLF}}}{\partial y_{_D}}\right|_{y_{_D}=y_{_{De}}} = 0 \tag{C.30}$$

Differentiating Eq. C.14 and solving using Eq. C.27, Eq. C.29 and Eq. C.30 results in

$$\overline{q}_{_D} = \frac{\sqrt{sf(s)}}{s\ coth\left(\sqrt{sf(s)}y_{_{De}}\right)} \tag{C.31}$$

$$\text{where } f(s) = \omega_{_F} + \frac{\lambda_{_{AC,Ff}}}{3s}\sqrt{sf_f(s)}\ tanh\left(\sqrt{sf_f(s)}\right) + \frac{\lambda_{_{AC,Fm}}}{3s}\sqrt{f_m(s)}\ tanh\left(\sqrt{f_m(s)}\right) \tag{C.32}$$

Appendix D

Quadrilinear Flow Model: Physical Meaning of Weighting Parameters

This part shows the relationship of weighting parameters (ω_1 and ω_2) to spacing aspect ratio R_{sp} ($= L_f/L_{_F}$) and the effect of R_{sp} on the reservoir.

D.1 Relationship of ω_1 to Spacing Aspect Ratio

First, ω_1 is expressed in terms of the virtual sub-matrix volumes that feed MF and HF. V_m is bulk matrix volume. V_{m1} and V_{m2} are sub-matrix 1 and sub-matrix 2 pore volumes respectively. Sub-matrix 1 and 2 have the same total compressibility (c_t).

$$\omega_{_1} = \frac{(\phi c_t)_{m_1}}{(\phi c_t)_{m_1} + (\phi c_t)_{m_2}} \times \frac{V_m}{V_m} \tag{D.1}$$

$$\omega_1 = \frac{V_{m_1}}{V_{m_1} + V_{m_2}} \tag{D.2}$$

Next the virtual sub-matrix volumes are expressed in terms of connection area between sub-matrix and fractures (MF and HF).

$$\omega_1 = \frac{A_{fm} \times \frac{L_f}{2}}{A_{fm} \times \frac{L_f}{2} + A_{_{Fm}} \times \frac{L_F}{2}} \tag{D.3}$$

$$\omega_1 = \frac{A_{fm} \times L_f}{A_{fm} \times L_f + A_{_{Fm}} \times L_{_F}} \tag{D.4}$$

The connection area between sub-matrix and fractures (MF and HF) is already defined in inter-porosity shape factors. Therefore, from Eq. B.18 and Eq. B.19

$$\alpha_{fm} = \frac{S_{a,fm}}{l_{fm}} = \frac{A_{fm}}{V \times l_{fm}} = \frac{12}{L_f^2} \tag{D.5}$$

$$\alpha_{_{Fm}} = \frac{S_{a,_{Fm}}}{l_{_{Fm}}} = \frac{A_{_{Fm}}}{V \times l_{_{Fm}}} = \frac{12}{L_{_F}^2} \tag{D.6}$$

From Eq. D.5 and Eq. D.6,

$$A_{fm} = \frac{12}{L_f^2} \times V \times l_{fm} \tag{D.7}$$

$$A_{_{Fm}} = \frac{12}{L_{_F}^2} \times V \times l_{_{Fm}} \tag{D.8}$$

Substituting Eq. D.7 and Eq. D.8 into Eq. D.4 results in,

$$\omega_1 = \frac{\frac{l_{fm}}{L_f}}{\frac{l_{fm}}{L_f} + \frac{l_{_{Fm}}}{L_{_F}}} \tag{D.9}$$

Next step involves an approximate physical description of characteristic lengths between interacting groups of binary media (matrix—MF and matrix—HF).

$$\text{If } l_{fm} \approx \frac{L_{_F}}{2} \text{ and } l_{_{Fm}} \approx \frac{L_f}{2}, \text{ then}$$

$$\omega_1 = \frac{\frac{L_{_F}}{L_f}}{\frac{L_{_F}}{L_f} + \frac{L_f}{L_{_F}}} \tag{D.10}$$

$$\omega_1 = \frac{L_{_F}^2}{L_{_F}^2 + L_f^2} \tag{D.11}$$

$$\omega_1 = \frac{1}{1 + \left(\frac{L_f}{L_{_F}}\right)^2} \tag{D.12}$$

$$\omega_1 = \frac{1}{1 + R_{sp}^2} \tag{D.13}$$

D.2 Effect of Spacing Aspect Ratio on Reservoir

Here, the discussion focuses on how the limits of spacing aspect ratio affects the reservoir behavior.

D.2.1 Case 1: $\omega_1 \longrightarrow 0$

Large MF spacing results in high spacing aspect ratios, hence low MF density with a given HF spacing. This implies low MF conductivity (Alkouh et al., 2012) such that there is more matrix—HF communication and less matrix—MF communication. Hence, the reservoir flow signature tends to that of a dual-porosity model.

D.2.2 Case 2: $\omega_1 \longrightarrow 1$

Small MF spacing results in low spacing aspect ratios, hence high MF density with a given HF spacing. This implies high MF conductivity such that there is more matrix—MF communication and less matrix—HF communication. Despite the high MF conductivity, HF being the most permeable medium still play an important role in depleting the reservoir. However, the reservoir flow signature tends to that of a sequential triple-porosity model.

Appendix E

Quadrilinear Flow Model: Analysis Equations in Laplace Space

This part simplifies the general transfer function $[f(s)]$ for the quadrilinear flow model (Ezulike and Dehghanpour, 2014a) using dimensionless rate $[q_{wDL}]$ and pressure derivative $[\partial P_{wDL}/\partial(lnt_D)]$ type-curves as guides. The simplification of the transfer functions under constant bottom-hole rate and pressure conditions yields simplifying analysis equations in Laplace space. These analysis equations are useful tools to interpret flow regions observable on field production data.

E.1 Constant Terminal Flowing Rate

The constant bottom-hole rate solution is given as :

$$\overline{P}_{wDL} = \frac{coth\left(\sqrt{sf(s)}y_{De}\right)}{s\sqrt{sf(s)}} \tag{E.1}$$

$$\text{where } f_m(s) = \frac{3s\omega_2\omega_m}{\lambda_{AC,Fm}};\ f_f(s) = \left\{\frac{3\omega_f}{\lambda_{AC,Ff}} + \frac{\lambda_{AC,fm}}{s\lambda_{AC,Ff}}\sqrt{\frac{3s\omega_1\omega_m}{\lambda_{AC,fm}}}\ tanh\left(\sqrt{\frac{3s\omega_1\omega_m}{\lambda_{AC,fm}}}\right)\right\} \tag{E.2}$$

$$\text{and } f(s) = \omega_F + \frac{\lambda_{AC,Ff}}{3s}\sqrt{sf_f(s)}\ tanh\left(\sqrt{sf_f(s)}\right) + \frac{\lambda_{AC,Fm}}{3s}\sqrt{f_m(s)}\ tanh\left(\sqrt{f_m(s)}\right) \tag{E.3}$$

Flow Region 1

ω_F is the controlling parameter ($\frac{1}{2}$ slope)

$$\text{if } \omega_F \gg \frac{\lambda_{AC,Ff}}{3s}\sqrt{sf_f(s)}\ tanh\left(\sqrt{sf_f(s)}\right) + \frac{\lambda_{AC,Fm}}{3s}\sqrt{f_m(s)}\ tanh\left(\sqrt{f_m(s)}\right);\ f(s) \to \omega_F \tag{E.4}$$

$$\text{when } \sqrt{sf(s)}y_{De} \geq 3 \text{ ; then } coth\left(\sqrt{sf(s)}y_{De}\right) \rightarrow 1; \text{ and } \overline{P}_{wDL} \rightarrow \frac{1}{s\sqrt{s\omega_F}} \tag{E.5}$$

$$\text{provided } \sqrt{sf(s)}y_{De} \geq 3, \text{ squaring both sides and dividing by } s^2 \text{ gives } \frac{9}{s^2 y_{De}^2 \omega_F} \leq \frac{1}{s} \tag{E.6}$$

Flow Region 2

Case A: ω_2, ω_m and $\lambda_{AC,Fm}$ are the controlling parameters ($\frac{1}{4}$ slope after $\frac{1}{2}$ slope)

$$\text{Provided } \frac{\lambda_{AC,Fm}}{3s}\sqrt{f_m(s)}\ tanh\left(\sqrt{f_m(s)}\right) \gg \omega_F + \frac{\lambda_{AC,Ff}}{3s}\sqrt{sf_f(s)}\ tanh\left(\sqrt{sf_f(s)}\right) \tag{E.7}$$

$$\text{and } \sqrt{f_m(s)} \geq 3 \text{ such that } tanh\left(\sqrt{f_m(s)}\right) \rightarrow 1;\ f(s) \rightarrow \sqrt{\frac{\omega_2\omega_m\lambda_{AC,Fm}}{3s}} \tag{E.8}$$

$$\text{if } \sqrt{sf(s)}y_{De} \geq 3 \text{ such that } coth\left(\sqrt{sf(s)}y_{De}\right) \rightarrow 1 \tag{E.9}$$

$$\text{then } \overline{P}_{wDL} \rightarrow \frac{1}{s\sqrt{sf(s)}} \rightarrow \frac{1}{s}\left(\frac{3}{s\omega_2\omega_m\lambda_{AC,Fm}}\right)^{\frac{1}{4}} \tag{E.10}$$

$$\text{provided } \sqrt{f_m(s)} \geq 3, \text{ squaring both sides, and dividing by } s^2 \text{ gives } \frac{3}{s^2} \leq \frac{\omega_2\omega_m}{s\lambda_{AC,Fm}} \tag{E.11}$$

Case B: ω_f and $\lambda_{AC,Ff}$ are the controlling parameters ($\frac{1}{4}$ slope after $\frac{1}{2}$ slope)

$$\text{Provided } 3\omega_f \gg \frac{\sqrt{3s\omega_1\omega_m\lambda_{AC,fm}}}{s}\ tanh\left(\sqrt{\frac{3s\omega_1\omega_m}{\lambda_{AC,fm}}}\right);\ f_f(s) \rightarrow \frac{3\omega_f}{\lambda_{AC,Ff}} \tag{E.12}$$

$$\text{Provided } \frac{\lambda_{AC,Ff}}{3s}\sqrt{sf_f(s)}\ tanh\left(\sqrt{sf_f(s)}\right) \gg \omega_F + \frac{\lambda_{AC,Fm}}{3s}\sqrt{f_m(s)}\ tanh\left(\sqrt{f_m(s)}\right) \tag{E.13}$$

$$\text{and } \sqrt{sf_f(s)} \geq 3,\ tanh\left(\sqrt{sf_f(s)}\right) \to 1; \text{ and } \sqrt{sf(s)}y_{De} \geq 3,\ coth\left(\sqrt{sf(s)}y_{De}\right) \to 1 \tag{E.14}$$

$$\text{then } \overline{P}_{wDL} \to \frac{1}{s\sqrt{sf(s)}} \to \frac{1}{s}\left(\frac{3}{s\omega_f\lambda_{AC,Ff}}\right)^{\frac{1}{4}} \tag{E.15}$$

$$\text{provided } \sqrt{sf_f(s)} \geq 3, \text{ squaring both sides and dividing by } s^2 \text{ gives } \frac{3}{s^2} \leq \frac{\omega_f}{s\lambda_{AC,Ff}} \tag{E.16}$$

Case C: ω_F and y_{De} are the controlling parameters (unit slope after $\frac{1}{2}$ slope)

$$\text{If } \omega_F \gg \frac{\lambda_{AC,Ff}}{3s}\sqrt{sf_f(s)}\ tanh\left(\sqrt{sf_f(s)}\right) + \frac{\lambda_{AC,Fm}}{3s}\sqrt{f_m(s)}\ tanh\left(\sqrt{f_m(s)}\right) \tag{E.17}$$

$$\text{and } \sqrt{sf(s)}y_{De} \leq 1 \text{ such that } coth\left(\sqrt{sf(s)}y_{De}\right) \to \frac{1}{\sqrt{sf(s)}y_{De}} \tag{E.18}$$

$$\text{then } \overline{P}_{wDL} \to \frac{1}{s^2f(s)y_{De}} \to \frac{1}{s^2\omega_F y_{De}} \tag{E.19}$$

$$\text{provided } \sqrt{sf(s)}y_{De} \leq 1, \text{ squaring both sides and dividing by } s^2 \text{ gives } \frac{1}{s^2y_{De}^2\omega_F} \geq \frac{1}{s} \tag{E.20}$$

Flow Region 3

Case A: ω_2, ω_m, ω_f, $\lambda_{AC,Fm}$, $\lambda_{AC,Ff}$ and y_{De} are the controlling parameters ($\frac{1}{2}$ slope after $\frac{1}{4}$ slope)

$$\text{Provided } 3\omega_f \gg \frac{\sqrt{3s\omega_1\omega_m\lambda_{AC,fm}}}{s}\ tanh\left(\sqrt{\frac{3s\omega_1\omega_m}{\lambda_{AC,fm}}}\right); \text{ then } f_f(s) \to \frac{3\omega_f}{\lambda_{AC,Ff}} \tag{E.21}$$

$$\text{Provided } \frac{\lambda_{AC,Ff}}{3s}\sqrt{sf_f(s)}\ tanh\left(\sqrt{sf_f(s)}\right) + \frac{\lambda_{AC,Fm}}{3s}\sqrt{f_m(s)}\ tanh\left(\sqrt{f_m(s)}\right) \gg \omega_{_F} \tag{E.22}$$

$$\sqrt{sf_f(s)} \geq 3,\ tanh\left(\sqrt{sf_f(s)}\right) \to 1;\quad \sqrt{sf(s)}y_{De} \leq 1,\ coth\left(\sqrt{sf(s)}y_{De}\right) \to \frac{1}{\sqrt{sf(s)}y_{De}} \tag{E.23}$$

$$\text{then } \overline{P}_{_{wDL}} \to \frac{1}{s^2 f(s) y_{De}} \to \frac{1}{sy_{De}}\sqrt{\frac{3}{s}}\frac{1}{\sqrt{\omega_f\lambda_{AC,Ff}} + \sqrt{\omega_2\omega_m\lambda_{AC,Fm}}} \tag{E.24}$$

$$\text{provided } \sqrt{sf(s)}y_{De} \leq 1, \text{ squaring both sides and dividing by } s^2 \text{ gives:} \tag{E.25}$$

$$\frac{1}{sy_{De}^2}\sqrt{\frac{3}{s}}\frac{1}{\sqrt{\omega_f\lambda_{AC,Ff}} + \sqrt{\omega_2\omega_m\lambda_{AC,Fm}}} \geq \frac{1}{s} \tag{E.26}$$

Case B: ω_f, $\lambda_{AC,Ff}$ and y_{De} are the controlling parameters ($\frac{1}{2}$ slope after $\frac{1}{4}$ slope)

$$\text{Provided } 3\omega_f \gg \frac{\sqrt{3s\omega_1\omega_m\lambda_{AC,fm}}}{s}\ tanh\left(\sqrt{\frac{3s\omega_1\omega_m}{\lambda_{AC,fm}}}\right); \text{ then } f_f(s) \to \frac{3\omega_f}{\lambda_{AC,Ff}} \tag{E.27}$$

$$\text{Provided } \frac{\lambda_{AC,Ff}}{3s}\sqrt{sf_f(s)}\ tanh\left(\sqrt{sf_f(s)}\right) \gg \omega_{_F} + \frac{\lambda_{AC,Fm}}{3s}\sqrt{f_m(s)}\ tanh\left(\sqrt{f_m(s)}\right) \tag{E.28}$$

$$\sqrt{sf_f(s)} \geq 3,\ tanh\left(\sqrt{sf_f(s)}\right) \rightarrow 1;\ \sqrt{sf(s)}y_{De} \leq 1,\ coth\left(\sqrt{sf(s)}y_{De}\right) \rightarrow \frac{1}{\sqrt{sf(s)}y_{De}} \tag{E.29}$$

$$\text{then } \overline{P}_{wDL} \rightarrow \frac{1}{s^2 f(s) y_{De}} \rightarrow \frac{1}{s y_{De}} \sqrt{\frac{3}{s\omega_f \lambda_{AC,Ff}}} \tag{E.30}$$

$$\text{if } \sqrt{sf(s)}y_{De} \leq 1, \text{ squaring both sides and dividing by } s^2 \text{ gives } \frac{1}{s y_{De}^2} \sqrt{\frac{3}{s\omega_f \lambda_{AC,Ff}}} \geq \frac{1}{s} \tag{E.31}$$

Case C: ω_2, ω_m, $\lambda_{AC,Fm}$ and y_{De} are the controlling parameters ($\frac{1}{2}$ slope after $\frac{1}{4}$ slope)

$$\text{Provided } \frac{\lambda_{AC,Ff}}{3s}\sqrt{sf_f(s)}\ tanh\left(\sqrt{sf_f(s)}\right) \gg \omega_F + \frac{\lambda_{AC,Fm}}{3s}\sqrt{f_m(s)}\ tanh\left(\sqrt{f_m(s)}\right) \tag{E.32}$$

$$\text{and } \sqrt{sf(s)}y_{De} \leq 1 \text{ such that } coth\left(\sqrt{sf(s)}y_{De}\right) \rightarrow \frac{1}{\sqrt{sf(s)}y_{De}} \tag{E.33}$$

$$\text{then } \overline{P}_{wDL} \rightarrow \frac{1}{s y_{De}} \sqrt{\frac{3}{s\omega_2\omega_m \lambda_{AC,Fm}}} \tag{E.34}$$

$$\text{if } \sqrt{sf(s)}y_{De} \leq 1, \text{ squaring both sides and dividing by } s^2 \text{ gives } \frac{1}{s y_{De}^2} \sqrt{\frac{3}{s\omega_2\omega_m \lambda_{AC,Fm}}} \geq \frac{1}{s} \tag{E.35}$$

Flow Region 4

Case A: ω_f and y_{De} are the controlling parameters (unit slope after $\frac{1}{2}$ slope)

$$\text{Provided } 3\omega_f \gg \frac{\sqrt{3s\omega_1\omega_m\lambda_{AC,fm}}}{s}\ tanh\left(\sqrt{\frac{3s\omega_1\omega_m}{\lambda_{AC,fm}}}\right);\ f_f(s) \rightarrow \frac{3\omega_f}{\lambda_{AC,Ff}} \tag{E.36}$$

$$\text{Provided } \frac{\lambda_{AC,Fm}}{3s}\sqrt{f_m(s)}\ tanh\left(\sqrt{sf_f(s)}\right) \gg \omega_{_F} + \frac{\lambda_{AC,Ff}}{3s}\sqrt{sf_f(s)}\ tanh\left(\sqrt{f_m(s)}\right) \tag{E.37}$$

$$\text{and } \sqrt{sf_f(s)} \leq 0.1mbox,\ tanh\left(\sqrt{sf_f(s)}\right) \rightarrow \sqrt{sf_f(s)} \tag{E.38}$$

$$\text{and } \sqrt{sf(s)}y_{_{De}} \leq 1 \text{ such that } coth\left(\sqrt{sf(s)}y_{_{De}}\right) \rightarrow \frac{1}{\sqrt{sf(s)}y_{_{De}}} \tag{E.39}$$

$$f(s) \rightarrow \omega_f \text{ and } \overline{P}_{_{wDL}} \rightarrow \frac{1}{s^2 f(s) y_{_{De}}} \rightarrow \frac{1}{s^2 \omega_f y_{_{De}}} \tag{E.40}$$

$$\text{provided } \sqrt{sf_f(s)} \leq 0.1, \text{ squaring both sides and dividing by } s^2 \text{ gives } \frac{1}{s^2} \geq \frac{300\omega_f}{s\lambda_{_{AC,Ff}}} \tag{E.41}$$

Case B: ω_1, ω_2, ω_m, $\lambda_{_{AC,Fm}}$ and $\lambda_{_{AC,fm}}$ are the controlling parameters ($\frac{1}{4}$ slope after $\frac{1}{2}$ slope)

$$\text{Provided } \frac{\sqrt{3s\omega_1\omega_m\lambda_{_{AC,fm}}}}{s} tanh\left(\sqrt{\frac{3s\omega_1\omega_m}{\lambda_{_{AC,fm}}}}\right) \gg 3\omega_f \tag{E.42}$$

$$\text{as } tanh\left(\sqrt{\frac{3s\omega_1\omega_m}{\lambda_{_{AC,fm}}}}\right) \rightarrow 1 \text{ then } f_f(s) \rightarrow \frac{1}{\lambda_{_{AC,Ff}}}\sqrt{\frac{3\omega_1\omega_m\lambda_{_{AC,fm}}}{s}} \tag{E.43}$$

$$\text{If } \frac{\lambda_{_{AC,Ff}}}{3s}\sqrt{sf_f(s)}\ tanh\left(\sqrt{sf_f(s)}\right) + \frac{\lambda_{_{AC,Fm}}}{3s}\sqrt{f_m(s)}\ tanh\left(\sqrt{f_m(s)}\right) \gg \omega_{_F} \tag{E.44}$$

$$\text{and while } \sqrt{sf_f(s)} \leq 0.1 \text{ and } \sqrt{f_m(s)} \geq 3;\ f(s) \rightarrow \sqrt{\frac{\omega_1\omega_m\lambda_{_{AC,fm}}}{3s}} + \sqrt{\frac{\omega_2\omega_m\lambda_{_{AC,Fm}}}{3s}} \tag{E.45}$$

$$\text{If } coth\left(\sqrt{sf(s)}y_{_{De}}\right) \rightarrow 1;\ \overline{P}_{_{wDL}} \rightarrow \frac{1}{s\sqrt{sf(s)}} \rightarrow \frac{1}{s}\sqrt{\frac{\sqrt{3}}{\sqrt{s}\left(\sqrt{\omega_1\omega_m\lambda_{_{AC,fm}}} + \sqrt{\omega_2\omega_m\lambda_{_{AC,Fm}}}\right)}} \tag{E.46}$$

if $\sqrt{sf_f(s)} \leq 0.1$, squaring both sides and rearranging gives $\frac{1}{s^2} \geq \frac{30000\omega_1\omega_m\lambda_{AC,fm}}{s\lambda_{AC,Ff}^{\ 2}}$ (E.47)

Flow Region 5

Case A: ω_1, ω_m, $\lambda_{AC,Ff}$ and y_{De} are the controlling parameters ($\frac{1}{2}$ slope after unit slope)

$$\text{Provided } \frac{\sqrt{3s\omega_1\omega_m\lambda_{AC,fm}}}{s}\ tanh\left(\sqrt{\frac{3s\omega_1\omega_m}{\lambda_{AC,fm}}}\right) \gg 3\omega_f \text{ and } \sqrt{\frac{3s\omega_1\omega_m}{\lambda_{AC,fm}}} \leq 1 \tag{E.48}$$

$$\text{then } tanh\left(\sqrt{\frac{3s\omega_1\omega_m}{\lambda_{AC,fm}}}\right) \rightarrow \sqrt{\frac{3s\omega_1\omega_m}{\lambda_{AC,fm}}} \text{ and } f_f(s) \rightarrow \frac{3s\omega_1\omega_m}{\lambda_{AC,Ff}} \tag{E.49}$$

$$\text{If } \frac{\lambda_{AC,Ff}}{3s}\sqrt{sf_f(s)}\ tanh\left(\sqrt{sf_f(s)}\right) \gg \omega_{_F} + \frac{\lambda_{AC,Fm}}{3s}\sqrt{f_m(s)}\ tanh\left(\sqrt{f_m(s)}\right) \tag{E.50}$$

$$\text{and } \sqrt{sf_f(s)} \geq 3 \text{ so } tanh\left(\sqrt{sf_f(s)}\right) \rightarrow 1\text{; then } f(s) \rightarrow \frac{3\omega_1\omega_m}{\lambda_{AC,Ff}} \tag{E.51}$$

$$\text{If } \sqrt{sf(s)}y_{De} \leq 1 \text{ such that } coth\left(\sqrt{sf(s)}y_{De}\right) \rightarrow \frac{1}{\sqrt{sf(s)}y_{De}} \tag{E.52}$$

$$\text{then } \overline{P}_{wDL} \rightarrow \frac{1}{s^2 f(s) y_{De}} \rightarrow \frac{1}{sy_{De}}\sqrt{\frac{3}{s\omega_1\omega_m\lambda_{AC,Ff}}} \tag{E.53}$$

provided $\sqrt{sf_f(s)} \geq 3$, squaring both sides and dividing by s^2 gives $\frac{3}{s^2} \leq \frac{\omega_1\omega_m}{s\lambda_{AC,Ff}}$ (E.54)

Case B: ω_1, ω_2, ω_m, $\lambda_{AC,Fm}$, $\lambda_{AC,fm}$ and y_{De} are the controlling parameters ($\frac{1}{2}$ slope after unit slope)

$$\text{Provided } \frac{\sqrt{3s\omega_1\omega_m\lambda_{AC,fm}}}{s}\ tanh\left(\sqrt{\frac{3s\omega_1\omega_m}{\lambda_{AC,fm}}}\right) \gg 3\omega_f \text{ and } \sqrt{\frac{3s\omega_1\omega_m}{\lambda_{AC,fm}}} \gg 3 \tag{E.55}$$

$$\text{then } tanh\left(\sqrt{\frac{3s\omega_1\omega_m}{\lambda_{AC,fm}}}\right) \to 1 \text{ and } f_f(s) \to \frac{1}{\lambda_{AC,Ff}}\sqrt{\frac{3\omega_1\omega_m\lambda_{AC,fm}}{s}} \tag{E.56}$$

$$\text{If } \frac{\lambda_{AC,Ff}}{3s}\sqrt{sf_f(s)}\ tanh\left(\sqrt{sf_f(s)}\right) + \frac{\lambda_{AC,Fm}}{3s}\sqrt{f_m(s)}\ tanh\left(\sqrt{f_m(s)}\right) \gg \omega_F \tag{E.57}$$

$$\text{and } \sqrt{sf_f(s)} \le 0.1,\ tanh\left(\sqrt{sf_f(s)}\right) \to \sqrt{sf_f(s)};\ \sqrt{f_m(s)} \ge 3,\ tanh\left(\sqrt{f_m(s)}\right) \to 1 \tag{E.58}$$

$$\text{then } f(s) \to \frac{\lambda_{AC,Ff}}{3}f_f(s) + \frac{\lambda_{AC,Fm}}{3}\sqrt{f_m(s)} \to \sqrt{\frac{\omega_m}{3s}}\left(\sqrt{\omega_1\lambda_{AC,fm}} + \sqrt{\omega_2\lambda_{AC,Fm}}\right) \tag{E.59}$$

$$\text{If } \sqrt{sf(s)}y_{De} \le 1 \text{ such that } coth\left(\sqrt{sf(s)}y_{De}\right) \to \frac{1}{\sqrt{sf(s)}y_{De}} \tag{E.60}$$

$$\text{then } \overline{P}_{wDL} \to \frac{1}{s^2f(s)y_{De}} \to \frac{1}{sy_{De}}\sqrt{\frac{3}{s\omega_m}}\left\{\frac{1}{\sqrt{\omega_1\lambda_{AC,fm}} + \sqrt{\omega_2\lambda_{AC,Fm}}}\right\} \tag{E.61}$$

$$\text{provided } \sqrt{sf_f(s)} \le 0.1,\ \text{squaring both sides twice gives } \frac{1}{s^2} \ge \frac{30000\omega_1\omega_m\lambda_{AC,fm}}{s\lambda_{AC,Ff}^{\ 2}} \tag{E.62}$$

Flow Region 6

ω_m, ω_f and y_{De} are the controlling parameters (unit slope after $\frac{1}{2}$ slope)

$$\text{If } \sqrt{\frac{3s\omega_1\omega_m}{\lambda_{AC,fm}}} \le 0.1 \text{ so that } tanh\left(\sqrt{\frac{3s\omega_1\omega_m}{\lambda_{AC,fm}}}\right) \to \sqrt{\frac{3s\omega_1\omega_m}{\lambda_{AC,fm}}};\ f_f(s) \to \frac{3\omega_f + 3\omega_1\omega_m}{\lambda_{AC,fm}} \tag{E.63}$$

$$\text{and } \sqrt{f_m(s)} \le 0.1\text{so that } tanh\left(\sqrt{f_m(s)}\right) \to \sqrt{f_m(s)} \tag{E.64}$$

$$\text{and } \sqrt{sf_f(s)} \leq 0.1 \text{ so that } tanh\left(\sqrt{sf_f(s)}\right) \rightarrow \sqrt{sf_f(s)} \tag{E.65}$$

$$\text{then } f(s) \rightarrow \omega_m + \omega_f + \omega_{_F} \rightarrow 1 \tag{E.66}$$

$$\text{If } \sqrt{sf(s)}y_{_{De}} \leq 1 \text{ such that } coth\left(\sqrt{sf(s)}y_{_{De}}\right) \rightarrow \frac{1}{\sqrt{sf(s)}y_{_{De}}} \tag{E.67}$$

$$\text{then } \overline{P}_{_{wDL}} \rightarrow \frac{1}{s^2 f(s) y_{_{De}}} \rightarrow \frac{1}{s^2 y_{_{De}}} \tag{E.68}$$

$$\text{provided } \sqrt{sf(s)}y_{_{De}} \leq 1, \text{ squaring both sides twice and rearranging gives } \frac{1}{s^2} \geq \frac{y_{_{De}}^2}{s} \tag{E.69}$$

E.2 Constant Terminal Flowing Pressure

The constant bottom-hole pressure solution is given as :

$$\overline{q}_{_{wDL}} = \frac{\sqrt{sf(s)}}{s\ coth\left(\sqrt{sf(s)}y_{_{De}}\right)} \tag{E.70}$$

Flow Region 1

$\omega_{_F}$ is the controlling parameter ($\frac{1}{2}$ slope)

$$\text{Provided } \sqrt{sf(s)}y_{_{De}} \geq 3;\ \overline{q}_{_{wDL}} \rightarrow \sqrt{\frac{\omega_{_F}}{s}} \tag{E.71}$$

Flow Region 2

Case A: ω_2, ω_m and $\lambda_{AC,Fm}$ are the controlling parameters ($\frac{1}{4}$ slope after $\frac{1}{2}$ slope)

$$\text{Provided } \sqrt{f_m(s)} \geq 3;\ \overline{q}_{wDL} \rightarrow s^{-\frac{3}{4}} \left(\frac{\omega_2 \omega_m \lambda_{AC,Fm}}{3} \right)^{\frac{1}{4}} \tag{E.72}$$

Case B: ω_f and $\lambda_{AC,Ff}$ are the controlling parameters ($\frac{1}{4}$ slope after $\frac{1}{2}$ slope)

$$\text{provided } \sqrt{s f_f(s)} \geq 3;\ \overline{q}_{wDL} \rightarrow s^{-\frac{3}{4}} \left(\frac{\omega_f \lambda_{AC,Ff}}{3} \right)^{\frac{1}{4}} \tag{E.73}$$

Case C: ω_F and y_{De} are the controlling parameters (exp trend after $\frac{1}{2}$ slope)

This is for $\sqrt{sf(s)} y_{De} \leq 1$. However, the analysis equation is unavailable because of the exponential trend observed instead of a slope.

Flow Region 3

Case A: ω_2, ω_m, ω_f, $\lambda_{AC,Fm}$, $\lambda_{AC,Ff}$ and y_{De} are the controlling parameters ($\frac{1}{2}$ slope after $\frac{1}{4}$ slope)

$$\text{Provided } \sqrt{sf(s)} y_{De} \leq 1 \text{ and } \sqrt{s f_f(s)} \leq 0.5;\ \overline{q}_{wDL} \rightarrow y_{De} \frac{\sqrt{\omega_f \lambda_{AC,Ff}} + \sqrt{\omega_2 \omega_m \lambda_{AC,Fm}}}{\sqrt{3s}} \tag{E.74}$$

Case B: ω_f, $\lambda_{AC,Ff}$ and y_{De} are the controlling parameters ($\frac{1}{2}$ slope after $\frac{1}{4}$ slope)

$$\text{Provided } \sqrt{sf(s)} y_{De} \leq 1;\ \overline{q}_{wDL} \rightarrow y_{De} \sqrt{\frac{\omega_f \lambda_{AC,Ff}}{3s}} \tag{E.75}$$

Case C: ω_2, ω_m, $\lambda_{AC,Fm}$ and $y_{De}$are the controlling parameters ($\frac{1}{2}$ slope after $\frac{1}{4}$ slope)

$$\text{Provided } \sqrt{sf(s)}y_{De} \leq 1;\ \overline{q}_{wDL} \rightarrow y_{De}\sqrt{\frac{\omega_2\omega_m\lambda_{AC,Fm}}{3s}} \tag{E.76}$$

Flow Region 4

Case A: ω_f and y_{De} are the controlling parameters (exp trend after $\frac{1}{2}$ slope)

This is for $\sqrt{sf_f(s)} \leq 0.1$. However, the analysis equation is unavailable because of the exponential trend is observed instead of a slope.

Case B: ω_1, ω_2, ω_m, $\lambda_{AC,Fm}$ and $\lambda_{AC,fm}$ are the controlling parameters ($\frac{1}{4}$ slope after $\frac{1}{2}$ slope)

$$\text{Provided } \sqrt{sf_f(s)} \leq 0.1;\ \overline{q}_{wDL} \rightarrow s^{-\frac{3}{4}}\sqrt{\frac{\sqrt{\omega_1\omega_m\lambda_{AC,fm}} + \sqrt{\omega_2\omega_m\lambda_{AC,Fm}}}{\sqrt{3}}} \tag{E.77}$$

Flow Region 5

Case A: ω_1, ω_m, $\lambda_{AC,Ff}$ and y_{De} are the controlling parameters ($\frac{1}{2}$ slope after exp trend)

$$\text{Provided } \sqrt{sf_f(s)} \geq 3;\ \overline{q}_{wDL} \rightarrow y_{De}\sqrt{\frac{\omega_1\omega_m\lambda_{AC,Ff}}{3s}} \tag{E.78}$$

Case B: ω_1, ω_2, ω_m, $\lambda_{AC,Fm}$, $\lambda_{AC,fm}$ and y_{De} are the controlling parameters ($\frac{1}{2}$ slope after exp trend)

$$\text{Provided } \sqrt{sf_f(s)} \leq 0.1;\ \overline{q}_{wDL} \rightarrow y_{De}\sqrt{\frac{\omega_m}{3s}}\left\{\sqrt{\omega_1\lambda_{AC,fm}} + \sqrt{\omega_2\lambda_{AC,Fm}}\right\} \tag{E.79}$$

Flow Region 6

ω_m, ω_f and y_{De} are the controlling parameters (exp trend after $\frac{1}{2}$ slope)

This analysis equation is unavailable because of the exponential trend observed instead of a slope.

Appendix F

Quadrilinear Flow Model: Analysis Equations in Time Space

This part inverts the analysis equations in Appendix E from Laplace space to time space.

F.1 Constant Terminal Flowing Rate

Flow Region 1

$\omega_{_F}$ is the controlling parameter ($\frac{1}{2}$ slope)

$$\text{Provided } t_{_D} \leq \frac{y_{De}^2 \omega_{_F}}{9};\ \frac{\partial P_{_{wDL}}}{\partial (lnt_{_D})} \rightarrow t_{_D} \frac{\partial P_{_{wDL}}}{\partial t_{_D}} \rightarrow \sqrt{\frac{t_{_D}}{\pi \omega_{_F}}} \tag{F.1}$$

Flow Region 2

Case A: ω_2, ω_m and $\lambda_{_{AC,Fm}}$ are the controlling parameters ($\frac{1}{4}$ slope after $\frac{1}{2}$ slope)

$$\text{Provided } t_{_D} \leq \frac{\omega_2 \omega_m}{3\lambda_{_{AC,Fm}}};\ \frac{\partial P_{_{wDL}}}{\partial (lnt_{_D})} \rightarrow \left(\frac{3t_{_D}}{\omega_2 \omega_m \lambda_{_{AC,Fm}}}\right)^{\frac{1}{4}} \times \frac{1}{\Gamma(0.25)} \tag{F.2}$$

Case B: ω_f and $\lambda_{_{AC,Ff}}$ are the controlling parameters ($\frac{1}{4}$ slope after $\frac{1}{2}$ slope)

$$\text{Provided } t_{_D} \leq \frac{\omega_f}{3\lambda_{_{AC,Ff}}};\ \frac{\partial P_{_{wDL}}}{\partial (lnt_{_D})} \rightarrow \left(\frac{3t_{_D}}{\omega_f \lambda_{_{AC,Ff}}}\right)^{\frac{1}{4}} \times \frac{1}{\Gamma(0.25)} \tag{F.3}$$

Case C: $\omega_{_F}$ and $y_{_{De}}$ are the controlling parameters (unit slope after $\frac{1}{2}$ slope)

$$\text{provided } t_{_D} \geq y_{_{De}}^2 \omega_{_F};\ \frac{\partial P_{_{wDL}}}{\partial (lnt_{_D})} \rightarrow \frac{t_{_D}}{\omega_{_F} y_{_{De}}} \tag{F.4}$$

Flow Region 3

Case A: ω_2, ω_m. ω_f, $\lambda_{_{AC,Fm}}$, $\lambda_{_{AC,Ff}}$ and $y_{_{De}}$ are the controlling parameters ($\frac{1}{2}$ slope after $\frac{1}{4}$ slope)

$$\text{Provided } t_{_D} \geq \frac{\left(\sqrt{\omega_f \lambda_{_{AC,Ff}}} + \sqrt{\omega_2 \omega_m \lambda_{_{AC,Fm}}}\right)^2 y_{_{De}}^4 \Gamma(1.5)^2}{3} \tag{F.5}$$

$$\frac{\partial P_{_{wDL}}}{\partial (lnt_{_D})} \rightarrow \frac{1}{y_{_{De}}} \sqrt{\frac{3t_{_D}}{\pi}} \frac{1}{\sqrt{\omega_f \lambda_{_{AC,Ff}}} + \sqrt{\omega_2 \omega_m \lambda_{_{AC,Fm}}}} \tag{F.6}$$

Case B: ω_f, $\lambda_{_{AC,Ff}}$ and $y_{_{De}}$ are the controlling parameters ($\frac{1}{2}$ slope after $\frac{1}{4}$ slope)

$$\text{Provided } t_{_D} \geq \frac{\omega_f \lambda_{_{AC,Ff}} y_{_{De}}^4 \Gamma(1.5)^2}{3};\ \frac{\partial P_{_{wDL}}}{\partial (lnt_{_D})} \rightarrow \frac{1}{y_{_{De}}} \sqrt{\frac{3t_{_D}}{\pi \omega_f \lambda_{_{AC,Ff}}}} \tag{F.7}$$

Case C: ω_2, ω_m, $\lambda_{_{AC,Fm}}$ and $y_{_{De}}$ are the controlling parameters ($\frac{1}{2}$ slope after $\frac{1}{4}$ slope)

$$\text{Provided } t_{_D} \geq \frac{\omega_2 \omega_m \lambda_{_{AC,Fm}} y_{_{De}}^4 \Gamma(1.5)^2}{3};\ \frac{\partial P_{_{wDL}}}{\partial (lnt_{_D})} \rightarrow \frac{1}{y_{_{De}}} \sqrt{\frac{3t_{_D}}{\pi \omega_2 \omega_m \lambda_{_{AC,Fm}}}} \tag{F.8}$$

Flow Region 4

Case A: ω_f and $y_{_{De}}$ are the controlling parameters (unit slope after $\frac{1}{2}$ slope)

$$\text{Provided } t_{_D} \geq \frac{300 \omega_f}{\lambda_{_{AC,Ff}}};\ \frac{\partial P_{_{wDL}}}{\partial (lnt_{_D})} \rightarrow \frac{t_{_D}}{\omega_f y_{_{De}}} \tag{F.9}$$

Case B: ω_1, ω_2, ω_m, $\lambda_{AC,Fm}$ and $\lambda_{AC,fm}$ are the controlling parameters ($\frac{1}{4}$ slope after $\frac{1}{2}$ slope)

$$\text{Provided } t_D \geq \frac{30000\omega_1\omega_m\lambda_{AC,fm}}{\lambda_{AC,Ff}^{\ 2}};\ \frac{\partial P_{wDL}}{\partial(lnt_D)} \rightarrow \sqrt{\frac{\sqrt{3t_D}}{\left(\sqrt{\omega_1\omega_m\lambda_{AC,fm}}+\sqrt{\omega_2\omega_m\lambda_{AC,Fm}}\right)}}\times\frac{1}{\Gamma(0.25)} \tag{F.10}$$

Flow Region 5

Case A: ω_1, ω_m, $\lambda_{AC,Ff}$ and y_{De} are the controlling parameters ($\frac{1}{2}$ slope after unit slope)

$$\text{Provided } t_D \leq \frac{\omega_1\omega_m}{3\lambda_{AC,Ff}};\ \frac{\partial P_{wDL}}{\partial(lnt_D)} \rightarrow \frac{1}{y_{De}}\sqrt{\frac{3t_D}{\pi\omega_1\omega_m\lambda_{AC,Ff}}} \tag{F.11}$$

Case B: ω_1, ω_2, ω_m, $\lambda_{AC,Fm}$, $\lambda_{AC,fm}$ and y_{De} are the controlling parameters ($\frac{1}{2}$ slope after unit slope)

$$\text{Provided } t_D \geq \frac{30000\omega_1\omega_m\lambda_{AC,fm}}{\lambda_{AC,Ff}^{\ 2}};\ \frac{\partial P_{wDL}}{\partial(lnt_D)} \rightarrow \frac{1}{y_{De}}\sqrt{\frac{3t_D}{\pi\omega_m}}\left\{\frac{1}{\sqrt{\omega_1\lambda_{AC,fm}}+\sqrt{\omega_2\lambda_{AC,Fm}}}\right\} \tag{F.12}$$

Flow Region 6

ω_m, ω_f, y_{De} are the controlling parameters (unit slope after $\frac{1}{2}$ slope)

$$\text{Provided } t_D \geq y_{De}^2;\ \frac{\partial P_{wDL}}{\partial(lnt_D)}\frac{t_D}{y_{De}} \tag{F.13}$$

F.2 Constant Terminal Flowing Pressure

Flow Region 1

$\omega_{_F}$ is the controlling parameter ($\frac{1}{2}$ slope)

$$\text{Provided } t_{_D} \leq \frac{y_{De}^2 \omega_{_F}}{9};\ q_{wDL} \rightarrow \sqrt{\frac{\omega_{_F}}{\pi t_{_D}}} \tag{F.14}$$

Flow Region 2

Case A: ω_2, ω_m and $\lambda_{_{AC,Fm}}$ are the controlling parameters ($\frac{1}{4}$ slope after $\frac{1}{2}$ slope)

$$\text{Provided } t_{_D} \leq \frac{\omega_2 \omega_m}{3\lambda_{_{AC,Fm}}};\ q_{wDL} \rightarrow \frac{1}{\Gamma(0.75)} \left(\frac{\omega_2 \omega_m \lambda_{_{AC,Fm}}}{3t_{_D}} \right)^{\frac{1}{4}} \tag{F.15}$$

Case B: ω_f and $\lambda_{_{AC,Ff}}$ are the controlling parameters ($\frac{1}{4}$ slope after $\frac{1}{2}$ slope)

$$\text{Provided } t_{_D} \leq \frac{\omega_f}{3\lambda_{_{AC,Ff}}};\ q_{wDL} \rightarrow \frac{1}{\Gamma(0.75)} \left(\frac{\omega_f \lambda_{_{AC,Ff}}}{3t_{_D}} \right)^{\frac{1}{4}} \tag{F.16}$$

Case C: $\omega_{_F}$ and y_{De} are the controlling parameters (*exp* trend after $\frac{1}{2}$ slope)

This is for $t_{_D} \geq y_{De}^2 \omega_{_F}$. However, the analysis equation is unavailable because of the exponential trend is observed instead of a slope.

Flow Region 3

Case A: ω_2, ω_m, ω_f, $\lambda_{AC,Fm}$, $\lambda_{AC,Ff}$ and y_{De} are the controlling parameters ($\frac{1}{2}$ slope after $\frac{1}{4}$ slope)

$$\text{Provided } t_D \geq \frac{\left(\sqrt{\omega_f \lambda_{AC,Ff}} + \sqrt{\omega_2 \omega_m \lambda_{AC,Fm}}\right)^2 y_{De}^4 \Gamma(1.5)^2}{3};\ q_{wDL} \rightarrow y_{De} \frac{\sqrt{\omega_f \lambda_{AC,Ff}} + \sqrt{\omega_2 \omega_m \lambda_{AC,Fm}}}{\sqrt{3\pi t_D}} \tag{F.17}$$

Case B: ω_f, $\lambda_{AC,Ff}$ and y_{De} are the controlling parameters ($\frac{1}{2}$ slope after $\frac{1}{4}$ slope)

$$\text{Provided } t_D \geq \frac{\omega_f \lambda_{AC,Ff} y_{De}^4 \Gamma(1.5)^2}{3};\ q_{wDL} \rightarrow y_{De} \sqrt{\frac{\omega_f \lambda_{AC,Ff}}{3\pi t_D}} \tag{F.18}$$

Case C: ω_2, ω_m, $\lambda_{AC,Fm}$ and y_{De} are the controlling parameters ($\frac{1}{2}$ slope after $\frac{1}{4}$ slope)

$$\text{Provided } t_D \geq \frac{\omega_2 \omega_m \lambda_{AC,Fm} y_{De}^4 \Gamma(1.5)^2}{3};\ q_{wDL} \rightarrow y_{De} \sqrt{\frac{\omega_2 \omega_m \lambda_{AC,Fm}}{3\pi t_D}} \tag{F.19}$$

Flow Region 4

Case A: ω_f and y_{De} are the controlling parameters (*exp* trend after $\frac{1}{2}$ slope)

This is for $t_D \geq \frac{300\omega_f}{\lambda_{AC,Ff}}$. However, the analysis equation is unavailable because of the exponential trend observed instead of a slope.

Case B: ω_1, ω_2, ω_m, $\lambda_{AC,Fm}$ and $\lambda_{AC,fm}$ are the controlling parameters ($\frac{1}{4}$ slope after $\frac{1}{2}$ slope)

$$\text{Provided } t_D \geq \frac{30000\omega_1 \omega_m \lambda_{AC,fm}}{\lambda_{AC,Ff}^2};\ q_{wDL} \rightarrow \frac{t_D^{-\frac{1}{4}}}{\Gamma(0.75)} \sqrt{\frac{\sqrt{\omega_1 \omega_m \lambda_{AC,fm}} + \sqrt{\omega_2 \omega_m \lambda_{AC,Fm}}}{\sqrt{3}}} \tag{F.20}$$

Flow Region 5

Case A: ω_1, ω_m, $\lambda_{AC,Ff}$ and y_{De} are the controlling parameters ($\frac{1}{2}$ slope after *exp* trend)

$$\text{Provided } t_D \leq \frac{\omega_1\omega_m}{3\lambda_{AC,Ff}};\ q_{wDL} \rightarrow y_{De}\sqrt{\frac{\omega_1\omega_m\lambda_{AC,Ff}}{3\pi t_D}} \tag{F.21}$$

Case B: ω_1, ω_2, ω_m, $\lambda_{AC,Fm}$, $\lambda_{AC,fm}$ and y_{De} are the controlling parameters ($\frac{1}{2}$ slope after *exp* trend)

$$\text{Provided } t_D \geq \frac{30000\omega_1\omega_m\lambda_{AC,fm}}{{\lambda_{AC,Ff}}^2};\ q_{wDL} \rightarrow y_{De}\sqrt{\frac{\omega_m}{3\pi t_D}}\left\{\sqrt{\omega_1\lambda_{AC,fm}}+\sqrt{\omega_2\lambda_{AC,Fm}}\right\} \tag{F.22}$$

Flow Region 6

ω_m, ω_f, y_{De} are the controlling parameters (*exp* trend after $\frac{1}{2}$ slope)

This is for $t_D \geq y_{De}^2$. However, the analysis equation is unavailable because of the exponential trend observed instead of a slope.

Copyright Permissions

Chapter 2: http://dx.doi.org/10.2118/175143-PA

License Number	4087170846261
License date	Apr 13, 2017
Licensed Content Publisher	Society of Petroleum Engineers
Licensed Content Publication	SPE Reservoir Evaluation & Engineering
Licensed Content Title	Flowback Fracture Closure: A Key Factor for Estimating Effective Pore Volume
Licensed Content Author	Obinna Ezulike, University of Alberta;Hassan Dehghanpour, University of Alberta;Claudio Virues, Nexen ULC et al
Licensed Content Date	2016
Licensed Content Volume	19
Licensed Content Issue	04
Volume number	19
Issue number	04
Type of Use	Thesis/Dissertation
Requestor type	author of the original work
SPE member	yes
SPE member number	3495174
Format	print and electronic
Portion	full article
Will you be translating?	no
Distribution	999999
Order reference number	
Title of your thesis / dissertation	Complementary Workflows for Analyzing Multiphase Flowback and Post-flowback Production Data In Unconventional Reservoirs
Expected completion date	Apr 2017
Estimated size (number of pages)	290
Requestor Location	Obinna D Ezulike 4-80-4 NREF 9105 116th St University of Alberta Edmonton, AB T6G 2W2 Canada Attn: Obinna D Ezulike

Chapter 3: http://dx.doi.org/10.1016/j.jngse.2014.05.004

License Number	4087171074685
License date	Apr 13, 2017
Licensed Content Publisher	Elsevier
Licensed Content Publication	Journal of Natural Gas Science and Engineering
Licensed Content Title	Modelling flowback as a transient two-phase depletion process
Licensed Content Author	Obinna Daniel Ezulike,Hassan Dehghanpour
Licensed Content Date	July 2014
Licensed Content Volume	19
Licensed Content Issue	n/a
Licensed Content Pages	21
Start Page	258
End Page	278
Type of Use	reuse in a thesis/dissertation
Intended publisher of new work	other
Portion	full article
Format	both print and electronic
Are you the author of this Elsevier article?	Yes
Will you be translating?	No
Order reference number	
Title of your thesis/dissertation	Complementary Workflows for Analyzing Multiphase Flowback and Post-flowback Production Data In Unconventional Reservoirs
Expected completion date	Apr 2017
Estimated size (number of pages)	290
Elsevier VAT number	GB 494 6272 12
Requestor Location	Obinna D Ezulike 4-80-4 NREF 9105 116th St University of Alberta Edmonton, AB T6G 2W2 Canada Attn: Obinna D Ezulike

Chapter 4: http://dx.doi.org/10.1016/j.jngse.2015.09.059

License Number	4087171220812
License date	Apr 13, 2017
Licensed Content Publisher	Elsevier
Licensed Content Publication	Journal of Natural Gas Science and Engineering
Licensed Content Title	A complementary approach for uncertainty reduction in post-flowback production data analysis
Licensed Content Author	Obinna Daniel Ezulike,Hassan Dehghanpour
Licensed Content Date	November 2015
Licensed Content Volume	27
Licensed Content Issue	n/a
Licensed Content Pages	18
Start Page	1074
End Page	1091
Type of Use	reuse in a thesis/dissertation
Intended publisher of new work	other
Portion	full article
Format	both print and electronic
Are you the author of this Elsevier article?	Yes
Will you be translating?	No
Order reference number	
Title of your thesis/dissertation	Complementary Workflows for Analyzing Multiphase Flowback and Post-flowback Production Data In Unconventional Reservoirs
Expected completion date	Apr 2017
Estimated size (number of pages)	290
Elsevier VAT number	GB 494 6272 12
Requestor Location	Obinna D Ezulike 4-80-4 NREF 9105 116th St University of Alberta Edmonton, AB T6G 2W2 Canada

Chapter 5: http://dx.doi.org/10.1016/j.jngse.2013.11.004

License Number	4087180785952
License date	Apr 13, 2017
Licensed Content Publisher	Elsevier
Licensed Content Publication	Journal of Natural Gas Science and Engineering
Licensed Content Title	A model for simultaneous matrix depletion into natural and hydraulic fracture networks
Licensed Content Author	Daniel Obinna Ezulike,Hassan Dehghanpour
Licensed Content Date	January 2014
Licensed Content Volume	16
Licensed Content Issue	n/a
Licensed Content Pages	13
Start Page	57
End Page	69
Type of Use	reuse in a thesis/dissertation
Intended publisher of new work	other
Portion	full article
Format	both print and electronic
Are you the author of this Elsevier article?	Yes
Will you be translating?	No
Order reference number	
Title of your thesis/dissertation	Complementary Workflows for Analyzing Multiphase Flowback and Post-flowback Production Data In Unconventional Reservoirs
Expected completion date	Apr 2017
Estimated size (number of pages)	290
Elsevier VAT number	GB 494 6272 12
Requestor Location	Obinna D Ezulike 4-80-4 NREF 9105 116th St University of Alberta Edmonton, AB T6G 2W2 Canada

Chapter 6: http://dx.doi.org/10.1016/j.petrol.2015.11.016

License Number	4087171366209
License date	Apr 13, 2017
Licensed Content Publisher	Elsevier
Licensed Content Publication	Journal of Petroleum Science and Engineering
Licensed Content Title	Capturing the effects of secondary fractures on production data using flow regime equations and specialised plots: An uncertainty analysis approach
Licensed Content Author	Obinna Daniel Ezulike,Hassan Dehghanpour
Licensed Content Date	February 2016
Licensed Content Volume	138
Licensed Content Issue	n/a
Licensed Content Pages	17
Start Page	201
End Page	217
Type of Use	reuse in a thesis/dissertation
Intended publisher of new work	other
Portion	full article
Format	both print and electronic
Are you the author of this Elsevier article?	Yes
Will you be translating?	No
Order reference number	
Title of your thesis/dissertation	Complementary Workflows for Analyzing Multiphase Flowback and Post-flowback Production Data In Unconventional Reservoirs
Expected completion date	Apr 2017
Estimated size (number of pages)	290
Elsevier VAT number	GB 494 6272 12
Requestor Location	Obinna D Ezulike 4-80-4 NREF 9105 116th St University of Alberta Edmonton, AB T6G 2W2

Chapter 7: http://dx.doi.org/10.1115/1.4032520

Confirmation Number: 11638248
Order Date: 04/ 13/ 2017

If you paid by credit card, your order will be finalized and your card will be charged within 24 hours. If you choose to be invoiced, you can change or cancel your order until the invoice is generated.

Payment Information

Obinna Ezulike
zulike2004@yahoo.com
+1 (780) 807-4237
Payment Method: invoice

Billing address:

4-80-4 NREF
9105 116th St
Edmonton, AB T6G 2W2
CA

Order Details

Special Orders

Journal of energy resources technology

Order detail ID:	70385309
Job Ticket:	501258587
ISSN:	0195-0738
Publication Type:	Journal
Volume:	
Issue:	
Start page:	
Publisher:	AMERICAN SOCIETY OF MECHANICAL ENGINEERS,
Author/ Editor:	AMERICAN SOCIETY OF MECHANICAL ENGINEERS

Permission Status: Special Order
Special Order Update: Checking availability

Permission type:
Republish or display content
Type of use:
Republish in a thesis/dissertation

Requestor type	Author of requested content
Format	Print, Electronic
Portion	chapter/article
Title or numeric reference of the portion(s)	Chapter 7 of the Thesis
Title of the article or chapter the portion is from	Implications of Characterizing Tight Reservoirs with Dual-porosity and Triple-porosity Models
Editor of portion(s)	N/A